University of Glasgow

Miniaturisation and Testing of an Optical Interference Block for Fluorescence Imaging in Capsule Endoscopy

Gianluca Melino

A Thesis submitted to

School of Engineering
University of Glasgow

in fulfilment of the requirements for the degree of

Doctor of Philosophy

September 2019

Abstract

Early detection of gastrointestinal cancer is crucial to increase the life span of patients. The implementation of new imaging modalities, such as fluorescence imaging, in traditional endoscopy is the key in the detection of early signs of cancer. Fluorescence imaging techniques for clinical applications can be divided in two groups defined as autofluorescence imaging and fluorescence-labelling imaging. The former exploits the natural green fluorescence emitted by human tissues when excited by blue or ultra-violet light. Detection of cancer through autofluorescence imaging relies on the fact that cancer tissues have a much lower autofluorescence signal than healthy tissues. On the other hand, fluorescence-labelling imaging is used when the difference in autofluorescence between cancer and healthy surroundings is too weak to detect. Therefore, external fluorescence agents are used to target and label cancer lesions. Although traditional endoscopy has been successfully equipped with fluorescence imaging capabilities, the discomfort caused in patients and the incapability to reach the small intestine represent two main limitations.

Fluorescence capsule endoscopy can enhance diagnostic accuracy with less inconvenience for patients. The optical components in traditional endoscopes are bulky and implemented outside the body of the patients. Therefore, there is a demand to develop highly miniaturised optical components for integration in capsule endoscopy. This thesis describes the design, fabrication, characterisation, and testing of a 5 mm x 6 mm x 6 mm optical interference block with the capability of fluorescence imaging in capsule endoscopy. The block accommodates ultrathin filters for optical isolation and was successfully integrated with a sensitive 64 x 64 pixels complementary metal oxide semiconductor single photon avalanche diode array to detect green fluorescence from Flavin Adenine Dinucleotide. This coenzyme is among the fluorophores responsible for autofluorescence in human tissues. The fluorescence-labelling capabilities of the imaging system were also tested to detect fluorescence from the cancer selective molecular probe ProteoGREEN-gGlu^{TM} which was used to label colorectal cancer cells. In vitro studies were also validated using a commercial Modulus^{TM} Microplate reader. The potential use of the miniaturised block in capsule endoscopy was further demonstrated by imaging healthy and malignant resected human tissues from the colon to detect changes in autofluorescence signal that are crucial for cancer diagnosis. The results obtained demonstrated that the system successfully imaged the differences in the autofluorescence signal from resected healthy and malignant human tissues from the colon. Moreover, results from the *in vitro* tests showed that the system detected changes in the fluorescence signal induced in colorectal cancer cells after labelling with ProteoGREEN-gGlu^{TM}.

Publications

Peer-reviewed Journals

Melino, G., Accarino, C., Riehle, M., Potter, M., Annese, V. F., Grant, J. P., Al-Rawhani, M., Beeley, J., Carranza, I. E., and Cumming, D. R.S. "Capsule Endoscopy Compatible Fluorescence Imager Applied to Bowel Cancer Detection". IEEE Sensors Journal

Accarino, C., Melino, G., Annese, V. F., Al-Rawhani, M. A., Shah, Y. D., Maneuski, D., & Cumming, D. R. (2019). A 64x64 SPAD array for portable colorimetric sensing, fluorescence and x-ray imaging. IEEE Sensors Journal.

Oral Presentation

Melino G. "Miniaturization of an optical interference block for fluorescence imaging in capsule endoscopy" 2nd November 2018, Senate Room, University of Glasgow

Contents

List of Figures

List of Tables

List of Acronyms

AF: Autofluorescence

ASIC: Application Specific Integrated Circuit

CE: Capsule Endoscopy

CMOS: Complementary Metal Oxide Semiconductor

FAD: Flavin Adenine Dinucleotide

GI: Gastrointestinal

LED: Light Emitting Diode

OGIB: Obscure Gastrointestinal Bleeding

RF: Radio Frequency

SPAD: Single Photon Avalanche Diode

WL: White Light

1 Introduction

1.1 Motivation

The development of miniature medical devices has become possible thanks to the rapid progress in electronics and digital systems. Capsule Endoscopy refers to the class of ingestible medical devices that has been widely used for the screening of the gastrointestinal (GI) tract [1]. The development of capsule endoscopy in 2001 was aimed at the exploration of the small bowel which was impossible to visualize by traditional endoscopy [2]. Nowadays, the use of capsule endoscopy has been expanded to the entire GI tract. Millions of endoscopic pills have been adopted worldwide for the clinical diagnosis of diseases such as obscure gastrointestinal bleeding (OGIB), Crohn's disease, polyposis syndromes and cancerous lesions [3]–[5]. Biomedical multinational companies such as Medtronic and Olympus have a large product portfolio of capsule endoscopy devices [6], [7].

Scientific research in the field of capsule endoscopy has moved forward by introducing the idea of implementing new diagnostic and therapeutic modalities within the capsules. The idea behind the Sonopill research project at the University of Glasgow is the combination of different sensing modalities in capsule endoscopy [8]. Sonopill aims to integrate ultrasound, white light (WL) imaging and autofluorescence (AF) imaging in a capsule format in order to offer a multimodal device for a more precise diagnosis of cancer in the GI tract [9].

AF is the fluorescence emitted by endogenous fluorophores naturally occurring in human tissues [10]. The excitation of endogenous fluorophores with an external source of blue light produces a bright green fluorescence signal. The metabolic activity of cancer can change the concentration of endogenous fluorophores within tissues [11]. Moreover, the formation of new blood vessels in cancerous lesions, also known as angiogenesis, leads to an increase of blood concentration which through haemoglobin strongly absorbs light in the green region of the spectrum [12]. Consequently, the AF signal is strongly attenuated in cancer with respect to healthy tissues. Clinical AF imaging relies on the detection of differences in the AF signal between cancer and healthy tissues [13]. This imaging technique was successfully implemented in traditional endoscopes and has demonstrated a higher sensitivity than traditional WL imaging for the detection of cancer in its early stages [14], [15]. However, in some cases, the difference in the AF signal between cancer and its healthy surroundings is very weak and difficult to distinguish. Therefore, cancer-specific fluorescence probes have been proposed as an 'optical aid' in the endoscopic detection of small colonies of cancerous cells [16]. The probes are specifically designed to activate their fluorescence properties only

after binding to specific receptors overexpressed on the surface of cancer cells [17]. The use of cancer-specific fluorescence probes creates a different imaging scenario with respect to AF imaging because, after binding the probe, the tumour shows a fluorescence signal much higher than the background AF signal emitted by healthy tissues.

In endoscopes with fluorescence imaging capabilities, specific excitation wavelengths are selected by using rotating optical filters that are mounted on the main unit of the instrument outside the body of the patient [18]. The excitation light is delivered inside the body by fibres that are bundled together within the endoscope tube. The fluorescence light emitted by the tissue is delivered back to the imaging detector on the main unit by a different bundle of optical fibres or imaged directly by a monochrome CCD. The main challenge in the integration of fluorescence imaging in capsule endoscopy is the miniaturization of an optical unit capable of simultaneously exciting the tissues and detecting the resulting fluorescence light emitted by them. This research is focused on the miniaturisation and testing of an optical block unit for fluorescence imaging to be coupled with an in-house very sensitive 64 x 64 Complementary Metal Oxide Semiconductor (CMOS) Single Photon Avalanche Diode (SPAD) array sensor. Its dimensions were selected for integration in capsule endoscopy along with other electronic components and sensing modalities.

1.2 Aim and Objectives

The aim of this work is the miniaturisation and testing of a capsule endoscopy optical unit as well as its application to detect cancer by measuring the differences in AF signal between cancerous and healthy tissues from the colon. The optical block must meet specific dimensions and features to fit in the Sonopill multimodality capsule. Its imaging capabilities will be investigated on unlabelled resected healthy and cancerous tissues from the human colon and colorectal cancer cells labelled with cancer-specific fluorescence probes.

The main objectives of this research work are:

- To design and simulate a miniaturised optical block with the following features:
  - A volume smaller than 200 mm^3 to be integrated in a pill with a 10 mm diameter and a length of 20 mm.
  - A capability of providing an excitation light with a wavelength between 450 nm and 490 nm.
  - Capability of successfully imaging and isolating the resulting green light, with a wavelength between 520 nm and 550 nm, from blue excitation light.

- To fabricate a miniaturised optical block with mechanical and optical specifications based on the simulations.
- To fabricate the miniaturised optical block by using "off-the-shelf" components, manufacturing techniques and high precision material processing techniques.
- To test and integrate the optical unit with a sensitive SPAD array imager capable of detecting weak AF signals from the human body.
- To characterise the integrated system with fluorophore phantom solutions.
- To perform in vitro experiments on human colorectal cells labelled with cancer-specific fluorescence probes.
- To characterise the integrated system through ex-vivo experiments on unlabelled healthy and malignant human tissues from the colon.

1.3 Thesis outline

The rest of thesis is organised as follows:

Chapter 2 begins with an introduction on the history of capsule endoscopy followed by a short description of the devices commercially available in the market. The chapter continues by presenting the science behind fluorescence. In particular, the molecular processes responsible for fluorescence are introduced through energy diagrams and important concepts such as absorption and emission spectra, and the fluorescence quantum yield. The theory behind the interaction of light with human tissues is also presented in order to introduce fluorophores and the phenomenon of AF in human tissues. The advantages of AF imaging in cancer detection are highlighted. The mechanical and optical principles of clinical endoscopes that use fluorescence imaging for the diagnosis of cancer are reviewed in order to understand how they can be applied and translated in capsule endoscopy. Finally, a review of the work that has been done by different research groups in implementing fluorescence modalities in capsule endoscopy is presented.

Chapter 3 presents the design and fabrication of the optical unit. The "off-the-shelf" light source that is integrated in the final prototype is characterised through knife edge measurements to measure the beam profile. The simulation of the light source in Zemax Optics studio is also presented and the results from the simulations are compared to the knife-edge measurements. At this point, the optical design and simulation of the entire final prototype is shown. The CAD design of the main body holding the optical components in place is also described. The optical filters and lenses that were purchased to realize the final prototype based on the results of the simulations are then presented. Furthermore, the

material processing techniques that were performed on the optical filters to make them suitable for integration in the final prototype are described. The comparison of the filters' optical properties before and after the manufacturing processes are also discussed. The chapter ends by showing the final assembled prototype with all the optical components in place.

Chapter 4 starts by presenting the characterisation of the excitation beam exiting the optical unit through knife-edge measurements. The comparison of the experimental results with simulations results is also discussed. The chapter continues by describing the integration of the optical block onto a 64 x 64 SPAD array imager. The experiments performed on fluorophore phantom solutions to characterise the optical block coupled to the SPAD in fluorescence mode are also described.

Chapter 5 describes the work that was performed in the Centre for Cell Engineering at the University of Glasgow to test the prototype on fluorescence-labelled cancer cells. The chapter begins by introducing cell lines and fluorescence probes that were used in the experiments. The full experimental protocol to culture and label the cells in 96-well plates is also shown. The experimental procedure to measure the fluorescence signal from the plates is described in detail. The results from the experiments are discussed along with the comparison between the two fluorescence probes performances. The chapter concludes with the validation of the results through comparison with a benchmark instrument.

Chapter 6 discusses the experiments performed at the Western General Hospital in Edinburgh to measure the AF signal from fresh human resected malignant and healthy tissues from the colon. The chapter begins by describing the aim of the study and the procedures that were performed to obtain fresh samples at the hospital. The imaging protocol to scan the tissues with the optical prototype is presented in detail. The algorithm to reconstruct the final AF images of the tissues from the scan is also thoroughly described. The results from each patient are discussed to show the capability of the integrated imaging system to detect changes in AF signals between cancerous and healthy tissue samples.

Chapter 7 summarizes the results from the previous chapter and presents potential future work.

2 Literature review

2.1 The gastrointestinal tract is a complex system

"*The world is a much more interesting place if we look beyond what is visible to the naked eye - there is so much more to see!"- Julia Enders.*

Julia Enders, researcher at the Institute for Microbiology in Frankfurt, chose these words to debut in her book "GUT the inside story of our body's most under-rated organ" [19]. Human gut or gastrointestinal tract (GI) is one of the most complex systems of human physiology (Fig. 2.1). GI tract consists of mouth, oesophagus, stomach, intestines, and anus with the primary purpose of digesting the food which can be easily absorbed by the body to provide energy for various metabolic processes.

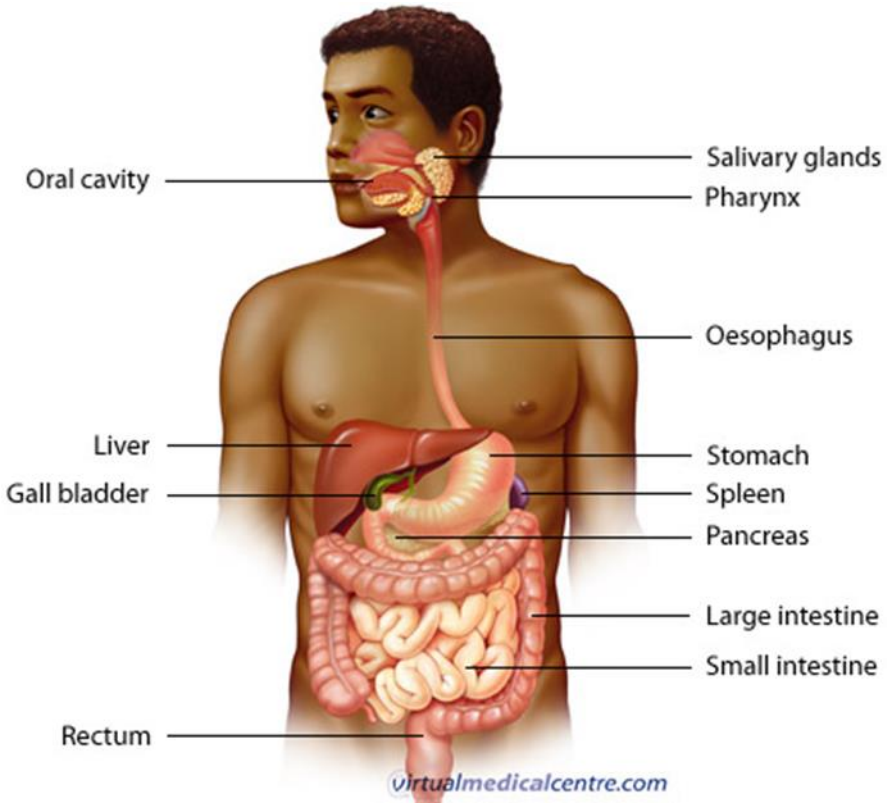

***Figure 2.1 Representation of human gastrointestinal (GI) tract* [20].**

There are several diseases associated with GI including infection, inflammation, and cancer. Several symptoms such as occult GI bleeding and ulcers can be directly related to gastric cancer, angiodysplasia, and lymphomas [21], [22]. Therefore, an early diagnosis of these symptoms is very important before these pathologies become life-threatening.

The research agency CANCERMondial stated that an estimated 14.1 million of new cancer cases arose globally in 2016 with more than 50% leading to death [22]. Cancers of the GI tract accounted for the 20% of the total cases. Although 50% of GI cancer cases were

diagnosed as colorectal cancer, mortal rates were higher in stomach and oesophageal cancer. The data showing the number of deaths in diagnosed cases for three types of cancer is shown in Fig. 2.2.

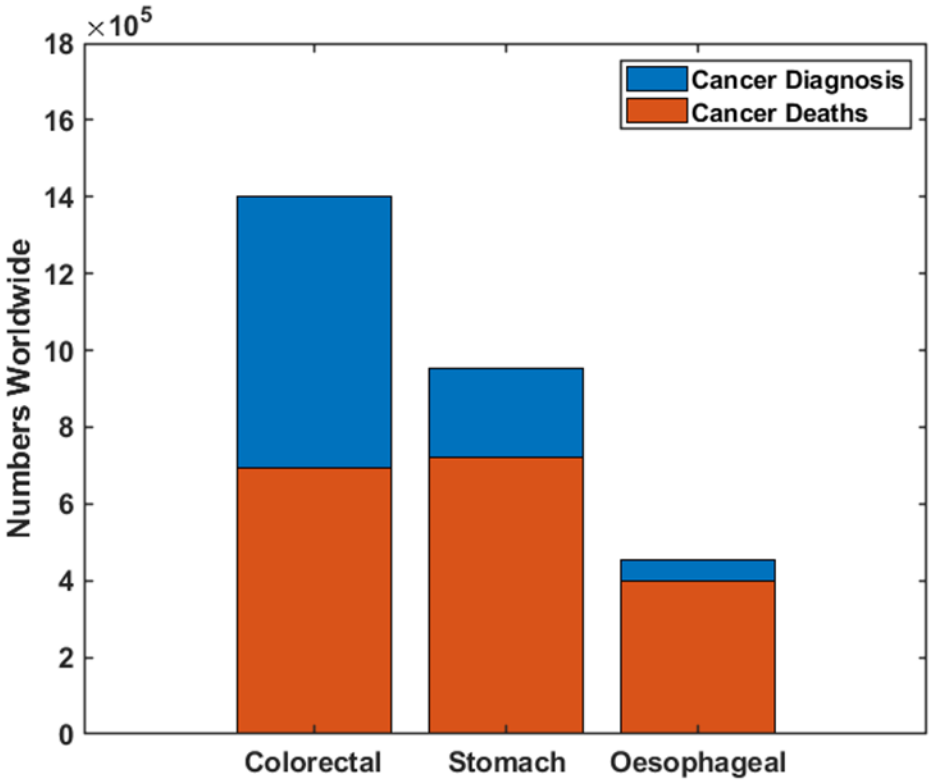

***Figure 2.2 GI cancer cases worldwide comparing the diagnosed versus mortal rates of colorectal, stomach and oesophageal cancer in 2012. Data obtained from* [23].**

Early diagnosis of cancer is quite difficult as most of the patients are asymptomatic at an early stage [24]. Moreover, many patients are referred to hospitals when the tumour has already progressed to its advanced stages [25]. The disease starts from the innermost layer of the GI walls also defined as mucosa as shown in Fig 2.3 [26]. A diagnosis can be made by means of various methods, such as physical examination, manometry, lab test, blood test, stool analysis, breath test, pH monitoring, imaging test such as Barium X-ray, computed tomography scan, magnetic resonance, endoscopy, abdominal ultrasound and other treatment options which are listed in the table 2.5 [27]. An early diagnosis of cancer is crucial to for the immediate and subsequent treatment.

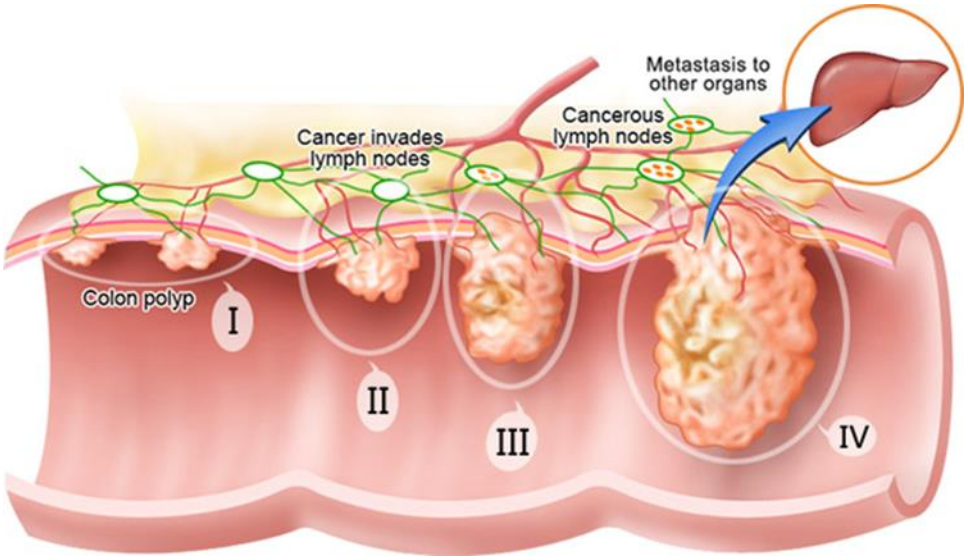

Figure 2.3 Different stages of colorectal cancer **[28].**

Table 1 Diagnosis and treatment options for gastrointestinal cancer **[27]**

Type of cancer	Screening of cancer	Treatment option
Esophageal Cancer	• Physical exam and history • Chest X-ray • Esophagoscopy • Endoscopic ultrasound • Scan (CT, MRI, PET) • Biopsy • Thoracoscopy • Laparoscopy • Ultrasound exam • Brush cytology • Balloon cytology • Chromoendoscopy • Fluorescence spectroscopy	• Surgery • Radiation therapy (External, Internal) • Chemotherapy • Chemoradiation therapy • Laser therapy • Electrocoagulation • Targeted therapy (Monoclonal antibody therapy
Stomach Cancer	• Physical exam and health history • Barium-meal gastric photofluorography • Upper endoscopy • Serum pepsinogen levels • Carcinoembryonic antigen (CEA) assay and CA 19-9 assay	• Surgery (Subtotal gastrectomy, Total gastrectomy, Endoluminal stent placement, Endoluminal laser therapy, Gastrojejunostomy) • Endoscopic mucosal resection • Chemotherapy • Radiation therapy • Chemoradiation • Targeted therapy (Monoclonal antibody therapy, Multikinase inhibitors) • Immunotherapy (Immune checkpoint inhibitor therapy

Small Intestine Cancer	• Physical exam and history • Blood chemistry studies • Liver function tests • Endoscopy (Upper endoscopy, Capsule endoscopy, Double balloon endoscopy) • Laparotomy • Biopsy • X-ray with Barium upper GI series with small bowel follow-through • Scan (CT, MRI)	• Surgery (Resection, Bypass) • Radiation therapy (External, Internal) • Chemotherapy • Biologic therapy • Radiation therapy with radiosensitizers
Colorectal Cancer	• Fecal occult blood test or FBOT (Guaiac, Immunochemical) • Sigmoidoscopy • Colonoscopy • Virtual colonoscopy • DNA stool test	• Surgery (Polypectomy, Local excision, Resection, Radiofrequency ablation, Cryosurgery, Pelvic exenteration • Radiation therapy (External, Internal) • Chemotherapy (Systemic, Regional) • Active surveillance (Digital rectal exam, MRI, Endoscopy, Sigmoidoscopy, CT scan, Carcinoembryonic antigen assay) • Targeted therapy (Monoclonal antibodies, Angiogenesis inhibitors) • Immunotherapy (Immune checkpoint inhibitor therapy)
		Colon Cancer • Surgery (Local excision, Resection of the colon with anastomosis, R esection of the colon with colostomy • Radiofrequency ablation • Cryosurgery • Chemotherapy (Systemic, Regional) • Radiation therapy (External, Internal) • Targeted therapy (Monoclonal antibodies, Angiogenesis inhibitors) • Immunotherapy (Immune checkpoint inhibitor therapy)

Gastrointestinal Stromal Tumours	• Physical exam and health history • Scan (CT, MRI, PET) • Endoscopic ultrasound and biopsy • Immunohistochemistry • Mitotic rate • Chest x-ray • Bone scan	• Surgery • Targeted therapy (Drugs, Tyrosine kinase inhibitors) • Watchful waiting • Supportive care
Gastrointestinal Carcinoid Tumours	• Physical exam and history • Blood chemistry studies • Tumour marker test • Twenty-four-hour urine test • Scan (MIBG, CT, MRI, PET) • Endoscopic ultrasound • Upper endoscopy • Colonoscopy • Capsule endoscopy • Biopsy	• Surgery (Endoscopic resection, Local excision, Resection, Cryosurgery, Radiofrequency ablation, Liver transplant, Hepatic artery embolization) • Radiation therapy (External, Internal) • Chemotherapy (Systemic, Regional) • Hormone therapy • Trageted therapy

2.2 Towards the exploration of the GI tract

How can we investigate a multifaceted and complex system as the GI tract from the inside?

In 1987, a movie called “Innerspace” introduced the idea of exploring the human body internally by taking an advantage of miniaturization. Although at that time the whole idea looked imaginary, recent advancement in the field of engineering, semiconductor industry, and wireless transmission have turned this concept into reality.

The diagnosis of gastrointestinal cancer often requires endoscopy and biopsy [29]. Endoscopy is a continuous and efficient investigative method for direct observation and detection of anatomic abnormality of the gut. The term endoscopy is derived from the Greek prefix ‘endo’ as within and the verb ‘skopein’ as to observe. It helps in the visualization and physical examination of those areas which are hidden from the external view such as the areas between body orifices. The development of wired endoscopy allowed the vision of the stomach, the upper small intestine, and colon [30]. Diseases associated with the upper gastrointestinal tract, including the esophagus, stomach, and duodenum, can also be easily visualized, diagnosed and treated using this technique.

To accomplish a safe and effective endoscopic procedure, several innovative techniques and product developments have been made in the past years. The history of visual exploration and examination inside the human body dates back to at least Egyptian and later Greco-Roman times. During that period, mechanical specula were used to examine the vagina and anus for genitourinary (GU) related problems as the cavities were short and at a relatively straight distance from the body orifice. However, progress in the development of these instruments was delayed by the lack of both suitable fabrication materials and the integration of an illumination source. In 1805, Bozzini was the first to attempt to visualize the human body internally by fabricating a device called a 'lichtleiter' (light conductor) [31]. The instrument consisted of a tin tube illuminated by a candle. Concave mirrors were placed behind the candle to reflect the illumination to the eye of the observer. The device was used to examine the genitourinary tract but it was an impractical instrument that never gained wide acceptance. Afterwards, straight metal tubes were used by Segalas in France (1826) and Fisher in Boston (1827) but the lack of an illumination source still remained a major challenge. In 1855, Desormeaux developed an instrument similar to the device of Segalas using a lamp fuelled with alcohol and turpentine which worked as a light source. Several researchers continued to develop instruments capable of delivering suitable light sources to the inaccessible areas of the human gut. In 1868, Kussmaul was the first person to perform a gastroscopy by using a straight rigid metal tube passed over a flexible obturator and a cooperative sword swallower [32]. Since then, several attempts and innovations have been made simultaneously by the scientists to develop efficient light sources and methods to rectify the problems and difficulties associated with endoscopy. The advancement of fibre optics and its application to endoscopes has truly revolutionized the diagnostic and therapeutic capabilities of endoscopy. Innovations and developments that need notable appreciation for laying the foundations of the endoscopy techniques are summarized in Table 2.1.

Table 2 Summary of the milestones leading to endoscopy **[30]–[32].**

Year	Development/innovation	Challenge/problem
1805	Bonzini developed a tin tube illuminated by a candle from which light was reflected by a mirror and named the instrument as 'lichtleiter'.	The instrument was impractical and could visualize GU tract only

1826-1827	Segalas and Fisher developed straight metal tubes	Lack of a satisfactory light source
1855	Desormeaux used a lamp fueled with alcohol and turpentine as a light source	The instrument was inadequate and unsatisfactory for the inaccessible areas of GI tract
1868	Kussmaul invented gastroscope by using a straight rigid metal tube passed over a flexible obturator and a cooperative sword swallower. For a light source, he used a mirror reflecting light from the Desormeaux device	Light illumination was inadequate and the tube had created problems to the gastric wall or gastric perforations.
1882	Bruck and Milliot introduced a loop of platinum wire charged with direct current as a light source.	Difficulties were encountered with the considerable heat generated, necessitating a water cooling system and the cumbersome batteries used for a power source
1949	The Eder-Hufford rigid esophagoscope was introduced with a straight rigid tube and a rubber finger-tipped obturator to make insertion safer. With the later addition of a 4X power lens on the proximal end and a distal incandescent bulb	The instrument was not flexible, fragile and could be easily damaged.
1911	Elsner introduced a rigid gastroscope with an outer tube through which a separate inner optical tube with a flexible rubber tip was inserted	Assitance was required to use the instrument.
1922	Schindler introduced an air channel to clear the lens of secretions	Assistance required to create a straight path for the tube into eosophagus and stomach

1932	Wolf-Schindler semiflexible introduced a gastroscope with a rigid proximal portion and and an elastic distal portion made of coiled copper wire. The instrumentended with a rubber finger and later a small rubber ball. A distal incandescent light bulb was used as a light source.	Poor quality of images
1948	Benedict introduced the Benedict Operating Gastroscope incorporating a biopsy procedure	Poor quality of images
1950	Uji, Sugiura and Fukami developed the Gastrocamera	Required more time to developed photographs and the operator could not see through the instrument directly
1962	Hirschowitz introduced Hirschowitz Gastroduodenal Fiberscope which was a very flexible side-viewing instrument with an electric light on its distal end, an air channel, and an adjustable proximal focusing lens	Fragile glass fibres, over-heating of light source causing thermal injury to the gastric mucosa and difficulty in moving the fiberscope through the pylorus and into the gut resulted in bowing in the gastric pouch
1984	Welch Allyn, Inc. (Skaneateles Falls, NY) introduced Digital Endoscopy or video endoscopy	High cost
1991	Wiersema showed that endoscopic ultrasonography (EUS) could be used to nodes and lesions of the upper and lower GI tract	Need for sedation, time taking process and need assistance during the application of the instrument

2.3 Endoscopy as the gold standard for GI tract exploration

2.3.1 White Light Endoscopy

The most diffused and standard endoscopy technique is white light endoscopy (WLE) which takes advantage of all the wavelength in the visible spectrum thanks to a xenon lamp mounted in a unit outside the body of the patients [33]. WLE detects lesions based on structural changes or discoloration of the epithelial surface and may be used to guide the acquisition of tissue biopsies. Light is carried inside the body through flexible optical fibres and shines on the gut tissues. Originally, another set of fibres was guiding back the light reflected from the gut walls outside the body to a unit where a high resolution charged coupled device (CCD) imager was placed. Nowadays, the advent of chip-on-tip endoscopes allowed the integration of CMOS image sensors directly on the distal end of the instruments [34]. An image of the mucosa on the sensor is formed thanks to an objective lens. Other lenses are often also used to magnify the areas of interest and provide a better visualization of the mucosa. In many instances, standard WLE has a miss rate of up to 25% for gastrointestinal pathology, specifically for detection of small and flat lesions within the colon [35].

2.3.2 Advanced imaging beyond white light endoscopy

Recently, a variety of new techniques have been developed and implemented in medical endoscopy with the purpose of overcoming these limitations and eventually detecting lesions that are still indiscernible under traditional white light endoscopy [36], [37]. Although there are several types of imaging systems in the market, as shown in the Table 2.3, no single imaging modality is applicable in all clinical scenarios. However, novel image-enhanced endoscopic technologies have the potential to detect polyps/neoplasms and provide real-time histological diagnosis. Some of these methods such as Narrow band Imaging (NBI) improves visibility and identification of the surface and vascular structures of colon polyps. This technique uses optical interference filters to spectrally narrow the bandwidths used in conventional white light providing more visual details of the superficial mucosal structures thus enhancing visualization of the mucosal capillaries in neoplastic tissues. NBI exploits the enhancement and optimization of the images contrast [38]. Other modalities such as magnification endoscopy (ME) allow the visualization of tissues structure at microscopic level [39]. When fluorescence is used for diagnostic purposes, two directions are generally taken to generate and then detect fluorescence information. The first method is based on autofluorescence (AF) or fluorescence emitted by the endogenous fluorophores [11]. The second method relies on detecting fluorescence emitted by exogenous fluorescence agents

[40]. Application of fluorescent probes is more invasive because these external agents pose a risk of side effects when administered to patients [41]. On the other hand, AF measurements represent a preferred method over external fluorescent probes for GI tract cancer diagnostics as they are less invasive and more suitable for endoscopy. The design and development of the fluorescence endoscopy can never be possible without understanding the basic photophysical property of light and its interaction with the tissues.

Table 3 Different types of optical imaging in endoscopy and advancement beyond WLE.

Type	***Features***	***Advantages***	***Disadvantages***
Image enhanced endoscopy or field enhancement: NBI, I-scan, FICE and autofluorescence endoscopy			
Narrow Band Imaging (NBI), [42]–[44]	It involves the placement of narrow band pass filters in front of a conventional white light source to obtain tissue illumination at selected narrow wavelength bands.	• It can detect superficial vasculature and mucosal pit patterns in real-time • Enhanced dysplasia detection • It can be used in the ablation of Barrett's, endoscopic mucosal resection, and therapeutic procedures where the assessment of the margin is critical • Highly useful in polyp's assessment in colorectal cancer	• Dimmer images as compared to WLE • Interpretation of contrast enhanced images require familiarity • The presence of blood or bile prevents optimal viewing
Blue laser imaging (BLI), [45], [46]	A 410 nm laser is used to detect vascular microarchitectures and a 450 nm laser provides white light by stimulating phosphor which is placed at the tip of the endoscope.	• It can achieve a bright and clear image even at a distant view • It produces high-contrast images in oesophageal cancer with clear vision of intrapapillary capillary loops • It predicts the histopathological of colorectal neoplasms. • It has high polyp's diagnostic sensitivity • It provides excellent vision of both microvascular and micro-surface patterns	• Physicians are not familiar with the technique • The endoscopic view is darker than with WLI
Fujinon intelligent	It uses postprocessing	• It has enhanced adenoma detection rates	• Expensive

chromoendoscopy (*FICE)* / I-Scan, [47]–[49]	algorithms to digitally convert high definition WLE images into colour images composed of various wavelength combinations.	• It provides topographical information and enhances mucosal vasculature by augmenting light contrast. • No optical filter needed	• Time-consuming • It requires experience to operate the system
Autofluorescence imaging (AF), [50]	It detects the fluorescence of naturally occurring fluorophores within the gastrointestinal mucosa.	• Less risk for the patient • It can distinguish neoplastic from non-neoplastic tissues	• Colour differentiation is poor • Low specificity • High rate of false positives
Virtual histology or point enhancement for in vivo histological examination: Confocal laser endomicroscopy, OCT, Spectroscopic endoscopy			
Confocal laser endomicroscopy (CLE), [50]	It works by focusing blue laser light through a single lens onto a specific target. The reflected light is filtered through a pinhole reducing light scattering and creating highly detailed images from a thin focal plane.	• It offers image details comparable to histopathological sections • It gives higher resolution, wider field of view and deeper imaging depth. • It provides real-time histological details	• The operator requires training in CLE image acquisition and interpretation. • It requires an additional capital investment in equipment and accessories that limits its widespread use. • Time consuming • It requires contrast agents
Optical Coherence Tomography (OCT), [51]	It uses near infrared light on the target tissue. Differential light scatter is detected and interpreted to create a cross-sectional image.	• It can scan depth of up to 2 mm below the mucosal surface. • It can visualize histologic morphology in real time, especially the epithelial structures such as villi, crypts, and squamous and intestinal epithelium	• Relatively high costs. • It needs standardized terminology and criteria for normal and neoplastic tissues • Lack of prospective data on clinical outcomes

Fluorescent Tagged Molecular Probes, [52], [53]	It employs the application of exogenous and targeted fluorescent contrast agents to highlight a biological process that is not regulated properly in the diseased area	• Dynamic as well as quantitative visualization of specific biochemical processes is possible • It has been useful for early-stage cancer diagnosis	• It lacks specificity for tumours which translates in a high background fluorescence noise and consequent difficult detection of diseased areas
Spectroscopy, [54], [55]	It uses spectral differences in the optical signals based on the microstructure and biochemical nature of the tissues.	• It can quantitatively measure the colour and intensity of reflected light • Training in image analysis is not needed • It is a rapid and almost real-time analysis • as chemical composition and nanoscale tissue structure can be assessed • It can differentiate between neoplastic and non-neoplastic tissues and can detect flat dysplasia in Barrett's oesophagus	• It has ability to only diagnose focal lesions. • It is a time-consuming process because allows for interrogation of a single point at a time and

2.4 The role of fluorescence in endoscopy

2.4.1 The physics behind fluorescence

Atoms and molecules are in their ground state in the absence of any excitation. The multiplicity of the energy levels in a molecule is given by Equation 2.1:

$$M = 2S + 1 \tag{2.1}$$

where:

S is the total spin angular momentum

Organic molecules do not have any unpaired electrons in their ground state. If the spins of the electrons in the orbitals are balanced, the total spin angular momentum is zero (S=1/2-

1/2=0), the spin multiplicity M is equal to one and the energy state is defined as singlet (S0 for the ground state) as defined by Equation 2.1.

The absorption of a photon by a molecule does not merely imply a transfer from a ground state energy level to a higher one. If the electron in the excited state is paired (opposite spin) with the electron in the ground state or retaining its antiparallel configuration the spin angular momentum is zero, the multiplicity is one and the state is still a singlet (S1) with higher energy. However, if the electron in the excited state is paired (same spin or remain parallel) with the electron in the ground state, the spin angular momentum is one, the multiplicity is three and the excited state is defined as a triplet (T1).

It must be stated that in diatomic and polyatomic molecules, there are several vibrational states within each electronic energy state. The Jablonski diagram proposed in 1935 illustrates all the molecular processes and transitions of a molecule between electronic states as shown in Fig. 2.4 [51]. When the continuous radiation passes through a chromophore, a portion of the radiation is absorbed by the molecule. As a result of light absorption, the electrons in the chromophore are excited from the ground vibrational level, S0 (low energy) to higher vibrational levels, S1 or S2 (high energy) in a very short span of time (timescale: 10^{-15} s). After the transition, molecule will undergo rapid relaxation (timescale: $<10^{-12}$ s) and return to the ground vibrational level of S1. This phenomenon is known as vibrational relaxation and can only arise within the vibrational levels of a given electronic state. On the other hand, the relaxation of a molecule from a higher electronic singlet state to a lower single state can lead either to non-radiative decays known as internal conversions (IC) (timescale: 10^{-14} to 10^{-1}1 s) or radiative decays such as fluorescence (F) (timescale: 10^{-9} s). Molecules in the excited S1 state can also transition to the first excited triplet state T1. This process is defined as intersystem crossing (ISC) (timescale: 10^{-11} to 10^{-6} s) and is linked to a spin conversion (a "flip") in the spin direction. Therefore, the electron in the excited triplet state is unpaired with the electron in the S0 state. According to the selection rules of quantum mechanics, transitions between the T1 and the S0 states have low probability of occurring and are considered as forbidden transition [52]. However, relaxation from the excited T1 state to the S0 ground state happens and the phenomenon of emission of light is named as

phosphorescence (P) (timescale: 10^{-3} to 100 s) which is weakly allowed through spin-orbit coupling.

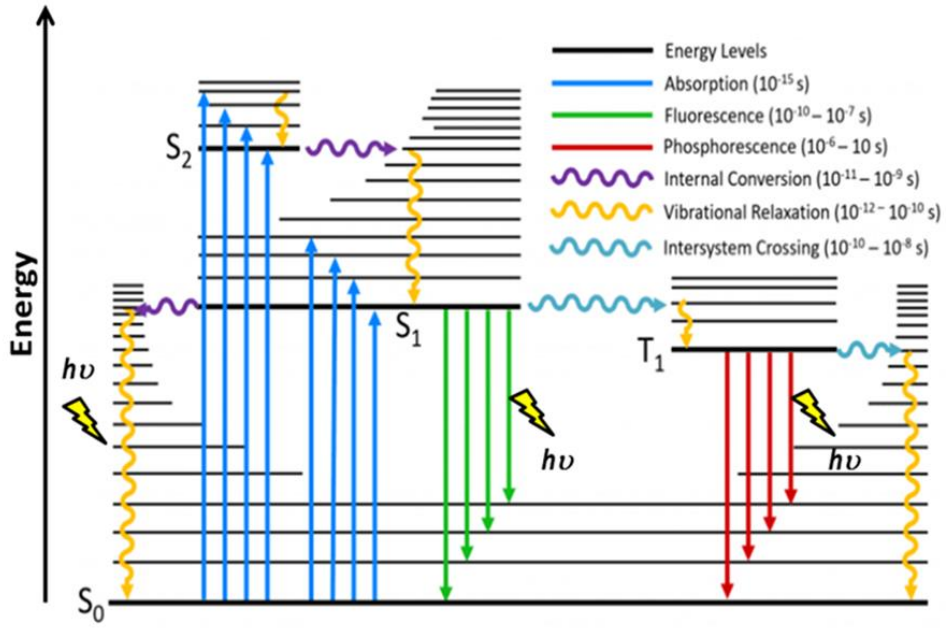

***Figure 2.4 Jablonski diagram illustrating the several molecular processes which occur between energy states* [56].** *Here: hυ is a generic term for photon energy with h = Planck's constant (6.63 × 10-34 Js) and υ = frequency of light.*

2.4.1.1 Frank Condon Principle

A deeper understanding of fluorescence phenomena can be achieved through the analysis of the Frank Condon Principle [57]. In the excited state (S_1), the internuclear distance between the atoms in the molecule is longer. This can be seen in Fig. 2.4 where the potential energy of the electronic states is plotted versus the internuclear distance and, the curve for the excited states is shifted right on the axis. When a photon is absorbed by a molecule the promotion of electrons from ground state to the excited state happens much faster with respect to vibrations of the nuclei. This is due to the fact the nuclei in molecules are enormously heavy compared to the electrons and thus they can be considered fixed. This assumption implies that there is no change in internuclear distance immediately before and after the promotion of an electron from the ground state to the excited state. Therefore, the transition can be considered vertical. Vibration levels of excited and ground state are equivalent and thus a mirror image is obtained. When a photon is absorbed, a change from one vibrational energy level to another will happen where the two vibrational wave functions overlap more significantly. As a matter of fact, during the absorption process, the molecule does not shift from v =0 to v'=0 but from v=0 to v'=2 (Fig. 2.5, *A* arrow) and starts vibrating as a spring. These vibrations occur periodically in the order of 10^{-13} or 10^{-12} s. Since the

typical lifetimes of excited electronic states are of the order of 10^{-9} s, there is enough time during the excitation period for many thousands of vibrations. The phenomenon of fluorescence occurs when the electronic deactivation from E_0 to E_1 causes the emission of a photon. As in the case of excitation, during fluorescence, the molecule does not shift from v'=0 to v=0 but from v'=0 to v=2 with some excitation energy converted into vibrational energy. This means that the fluorescence frequency is lower than the absorption frequency. Consequently, the energy of the emitted photon will be significantly lower than the absorbed photons. In other words, fluorescence light has a longer wavelength compared to the absorbed radiation. This phenomenon is known as Stokes' shift and was introduced in this chapter as it is the main cause of the human tissue emission of green fluorescence under the excitation of blue light.

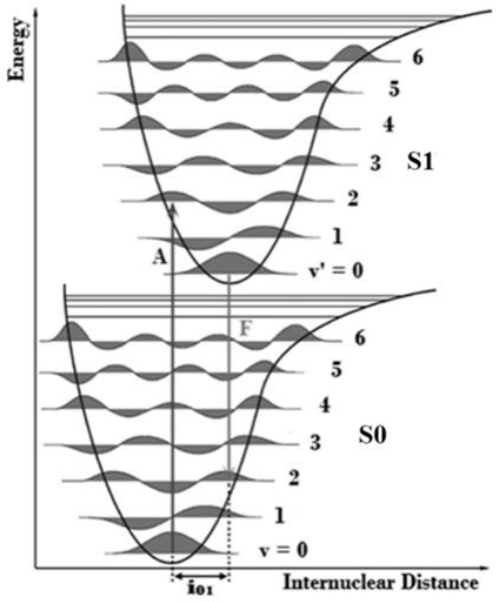

***Figure 2.5 Energy diagram showing transitions in the vibrational levels of ground and excited energy states S0 and S1* [58].** *During the absorbance of a photon (A) the molecule shifts from the vibrational level v = 0 in S0 to the vibrational level v' =2 in S1. On the other hand, during fluorescence emission the molecule has already lost some vibrational energy and shifts from v'=0 in S1 to v =2 in S0.*

2.4.2 The interaction of light with biological tissues

A deep understanding of fluorescence at tissue-level is necessary to design an efficient fluorescence optical system for medical applications. Each fluorescence measurement involves the interrogation of tissues with excitation light. This interaction is strongly dependent on the optical properties of the tissues. The absorption of a photon by a molecule can be described by the Beer's Law [59].

$$A = \log I_0/I \ = \varepsilon cl \qquad (2.1)$$

where, A = absorbance, I_0 = intensity of incident light, I = intensity of transmitted light, ϵ = molar extinction coefficient or molar absorptivity ($M^{-1}cm^{-1}$), c = molar concentration of sample (M) and l = pathlength of sample cell (cm).

However, Beer's law shows certain deviations when it comes to tissue-light interactions because the index of refraction is variable within the tissues and both absorption and scattering phenomena occur [60]. In fact, tissues can be considered as turbid media and are characterized by both absorption and scattering coefficients which express the probability of absorption and scattering occurring per unit pathlength, respectively [61]. For example, the important molecules responsible for the absorption in tissues are oxyhaemoglobing (HbO2), deoxyhaemoglobin (Hb) and water (H2O) [62]. The absorption spectra of these molecules show a lower absorption in the range of wavelengths defined as "Therapeutic Spectral Window" [63]. This region extends from 600 nm to 1000 nm and scattering prevails over absorption (Fig.2.6).

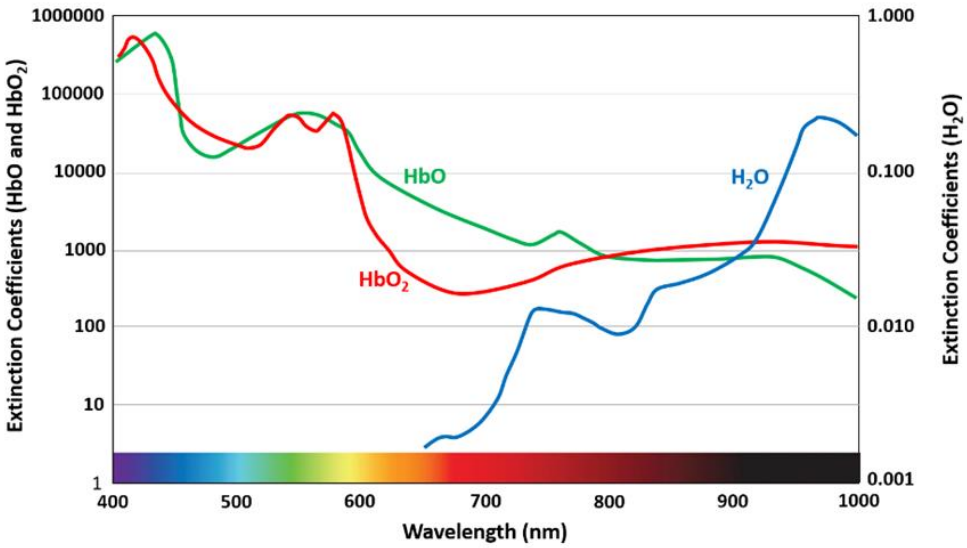

Figure 2.6 Absoption spectra of oxyhaemoglobing (HbO2), deoxyhaemoglobin (Hb) and water (H2O) **[64].** *In the region between 600 nm and 1000 nm the absorption is lower than the surrounding wavelenghts therefore scattering prevails.*

2.4.3 Fluorophore

Fluorophores can absorb visible light and reemit it at longer wavelengths. Fluorescent probes or dyes offer vast opportunities to visualize and detect different dynamic events within living cells and tissues. Moreover, they also help in the quantification of various physiological and biochemical parameters inside the cells by *in vivo*, *in vitro* and *in situ* approaches.

The efficiency of fluorescence emission from a fluorophore is defined in terms of fluorescence quantum yield (Q_f) which is described as the number of emitted fluorescence photons over the numbers of absorbed photons [65]. As reported previously, the absorption of a photon brings the molecules to a higher excited state but does not intrinsically lead to fluorescence. In fact, other process such as non-radiative decays and intersystem crossing affect the fluorescence quantum yield which can be defined as:

$$Q_f = \frac{k_f}{k_f + k_i + k_{nr}} \tag{2.2}$$

Where,

Q_f : Fluorescence quantum yield

k_f : Fluorescence decay rate; defined as the inverse of fluorescence lifetime (τ_f) or the time during which the molecule remains in the excited state before relaxation

k_i is the decay for intersystem crossing

k_{nr} is the decay rate for non-radiative transitions

If the decay rates k_i and k_{nr} are much smaller than k_f the quantum yield is closer to one. The closer the quantum yield is to one, the higher the fluorescence light emitted by the fluorophore.

The quantum yield can be precisely measured in environments where all photons in the excitation source are focused on the fluorophore solution. Commonly, the quantum yield of a fluorophore is determined in comparison to a compound with known quantum yield as a reference. However, this method is not suitable when the sample consists of multiple molecular species because quenching can occur [66]. Quenching is a decrease of fluorescence intensity due to a wide variety of processes. In this case, the fluorophore can undergo collisional quenching due to the contact between the fluorophore and other molecules in the environment.

Fluorophores can be divided broadly into two main classes - intrinsic or endogenous fluorophore and extrinsic or exogenous fluorophore. Fluorophores that naturally occur in biological tissues, such as amino acids, proteins, etc are defined as endogenous fluorophores. Exogenous fluorophores are added to the sample to provide fluorescence or change the photophysical or spectral property of the sample. Propidium iodide, dansyl, fluorescein are few examples of exogenous fluorophores that are commonly used in medical science.

Endogenous fluorophores are responsible for the phenomenon known as Autofluorescence (AF) [64]. They can absorb different wavelengths of light and emit light with longer wavelength. Although the intensity of AF light is not strong, it is often used to detect changes in the biological tissues. Fluorophores include the aromatic amino acids (tyrosine, tryptophan, and phenylalanine), enzyme cofactors (NADH, pyridoxyl phosphate), Riboflavin (Flavin mononucleotide, FMN and Flavin adenine dinucleotide, FAD), etc.

Figure 2.7 shows the absorbance and emission spectra of the endogenous fluorophore exploited in most biomedical applications [67]. Tryptophan is an aromatic amino acid with fluorescence excitation and emission wavelengths of 295 nm and 353 nm, respectively. Collagen is a constituent protein of tissues matrix and shows fluorescence emission at 400 nm when excited at 325 nm. Flavins are among the major electron acceptors and take part in the energy metabolism of cells. Flavin adenine dinucleotide (FAD) is an electron carrier and emits fluorescent light between 520 nm and 530 nm when excited at 450 nm. However, upon acceptance of two electrons, FAD is reduced to $FADH_2$ which do not show any fluorescence emission. Flavin mononucleotide (FMN) and riboflavin (Vitamin B2) are other important flavins which are present in biological tissues capable of emitting fluorescence. NADH is the reduced form of the major electron acceptor nicotinamide adenine dinucleotide (NAD). Oppositely to FAD, NAD emits fluorescence in its reduced form (NADH) with fluorescence excitation and emission maxima of 340 nm and 460 nm, respectively. The brightness of fluorescence light emitted by specific fluorophore is proportional to the product between the extinction coefficient at the wavelength of the excitation light and the quantum yield of the fluorophore.

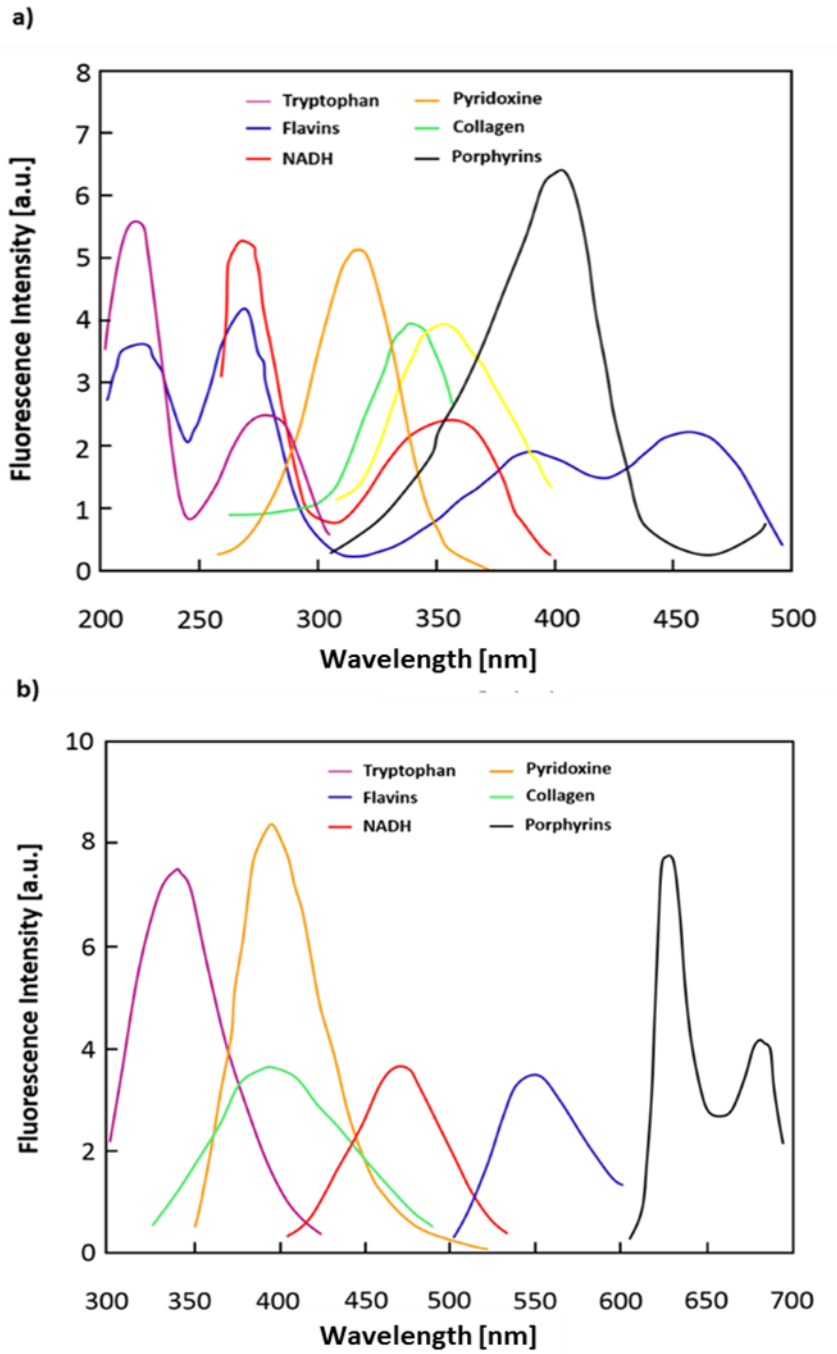

Figure 2.7 (a) Absorption spectra and (b) Emission spectra of endogenous fluorophores in human tissues **[67]**.

The photophysical property of biological samples can be employed in the detection of cancer by exploiting the naturally occurring autofluorescence (AF). These endogenous fluorophores can also be used to observe the differences in AF spectra between normal and diseased tissues. Healthy epithelial tissue generally emits green autofluorescence when excited with blue light due to the presence of elastin and collagen as endogenous fluorophores in the submucosa layer. However, the abnormal tissue emits markedly dimmer autofluorescence

with a red-shifted spectrum. Therefore, changes in the intensity of tissue autofluorescence can be used to follow pathological processes such as carcinogenesis (Fig. 2.10).

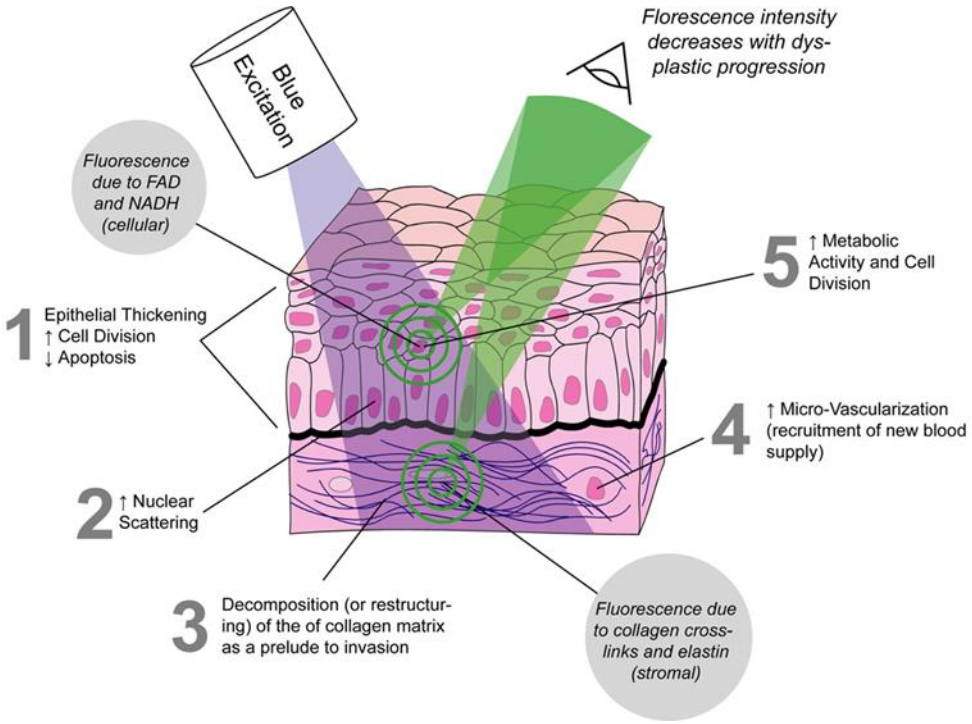

***Figure 2.8 Illustration of tissue autofluorescence of healthy and cancerous tissues upon excitation* [68].**

A comparative analysis between autofluorescence spectra of normal and pathological tissues could lead to the detection of early cancerous and precancerous lesions with an increase in fluorescence ratio between red region and green region of the fluorescence spectrum. Cancerous tissues show low fluorescence intensity and some changes in the spectral shape compared to normal tissues upon excitation with ultraviolet or visible light. The drop in fluorescence intensity in pathological tissue may be due to thickening of the epithelium. Therefore, less excitation light is delivered to the endogenous fluorophores in the submucosa and less fluorescence light is emitted by the same fluorophores. In 2019, Ehlen et al. run a pilot study on the potential of fluorescence and near-infrared spectroscopy for the discrimination of colorectal cancer malignancies. Fluorescence emission spectra of ex-vivo normal and tumour tissues of resected colorectal cancer specimen were obtained by exciting the tissues at 473 nm and recording the fluorescence emission by means of fibre optics probes. Considerable spectral differences between normal tissues and cancer were discovered in the fluorescence spectra (Fig 2.10) [69].

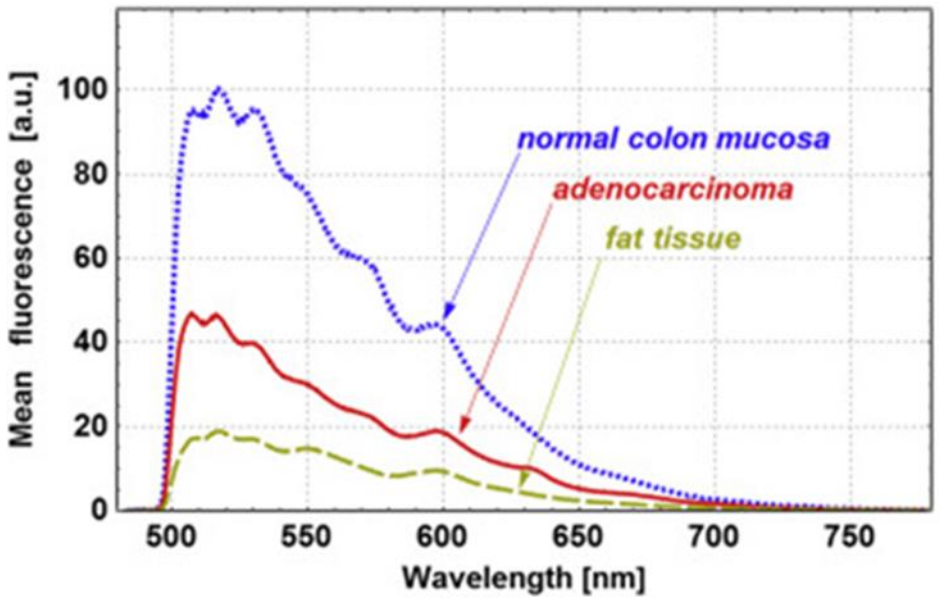

***Figure 2.9 Fluorescence behaviour representation (mean spectra) of some colorectal tissues* [69].**

2.4.4 AF imaging

The fundamental principle of AF imaging is to exploit the properties of the endogenous fluorophores within the tissues [70]. In AF imaging, tissues are excited with specific wavelengths in the blue spectrum to detect the tissues emission of longer wavelengths of light in the green spectrum. Flavins are the main targeted fluorophores. Specifically, FAD emits fluorescent light between 520 nm and 530 nm when excited at 465 nm. However, variations in the ratio between the oxidized form of FAD and its reduced form $FADH_2$, which does not emit any fluorescence, are directly linked to the metabolic activity within the tissues during carcinogenesis [71]. Therefore, $FADH_2$ is increased when cancer is present. Moreover, the growth of new blood vessels (angiogenesis) in cancerous tissues causes an increase in the levels of Haemoglobin which is responsible for a strong absorption of green wavelengths. This phenomenon leads to a strong attenuation in the autofluorescence signal in the presence of cancer [72]. Therefore, autofluorescence changes in neoplastic tissues are mainly due to three mechanisms: (1) increase in the nuclear-cytoplasmic ratio which consequently determines decreased autofluorescence as nuclei show no autofluorescence as compared with cytoplasm; (2) loss of collagen as submucosal collagen is the strongest fluorophore which disappears due to thickening of the mucosa; and (3) neovascularization: inducing increased haemoglobin concentration which absorbs autofluorescence light [72].

In AFI endoscopy, white light generated by a xenon lamp is conducted through a rotational filter wheel to continuously produce blue (395–480 nm) and green (535–550 nm) light. An emission filter is placed in the proximity of CCD imagers to reject the blue excitation light

and permit tissue autofluorescence and reflected green light to impinge the sensitive area of the imagers [73]. In the resultant images, healthy mucosa will appear as green while dysplastic and neoplastic lesions as purple [74], [75] (Fig. 2.12). The challenge in AFI systems is the weakness of the AF signal which usually has an intensity three orders of magnitude lower than the intensity of the excitation light.

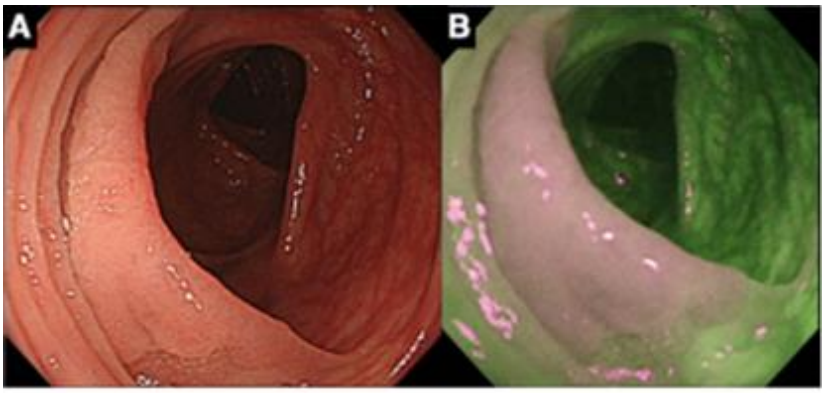

Figure 2.10 (a) White light imaging of a spreading tumour in the transverse colon. (b) Autofluorescence imaging of the lesion **[74].**

2.4.5 Confocal laser endomicroscopy (CLE)

In contrast to AFI, CLE relies on the application of fluorescence agents to create a high resolution and better contrast image. This endoscopic technique is based on the exact same principle of standard confocal microscopy in which excitation and fluorescence detection take place on the same focal plane [76]. Excitation light from a blue laser is collimated and filtered onto a dichroic beam splitter which reflects the light towards the sample at a specific point and depth. The fluorescence light emitted by the sample is then imaged by the objective lens through a confocal pinhole on the detector. The pinhole rejects fluorescence light out of focus with the purpose that only a section of the sample is imaged. The main advantage of CLE is providing a wider field of view and deeper imaging depth, therefore, allowing for better capability to investigate tissues morphology down to cellular level [77].

Implementation of confocal microscopy in endoscopy led to the development of two types of CLE systems defined as endoscope-based CLE (eCLE) and probe-based CLE (pCLE). In eCLE, a confocal scanner has been integrated into the distal tip of a flexible endoscope. This system is no longer commercially available, though, a hand-held system (FIVE1; Optiscan, Melbourne, Australia) is available for research applications [78] (Fig. 2.11). On the other hand, pCLE system (Cellvizio Endomicroscopy System; Mauna Kea Technologies, Paris, France) is commercially available and consists of a flexible miniprobe which may be introduced through the working channel of a standard endoscope [79]. In eCLE the

endoscope integrates the miniaturised confocal endomicroscope. The distal tip of the endoscope is equipped with two light guides and an objective lens for traditional endoscopy screening. The remaining volume is occupied by the confocal imaging window of the endomicroscope which is placed in contact with the tissue. The window integrates a microelectromechanical system (MEMS) scanning mirror which raster scans a beam of laser light (488 nm) delivered through a fibre from a confocal microscope placed outside the body of the patient. The fibre also works as pinhole and carries fluorescence light between 500 nm and 580 nm to the detector. The fibre acting as excitation source, objective and pinhole makes the apertures automatically aligned. The scan of consecutive points on the tissue produces sections that can be seen at variable imaging depths by controlling a z-actuator. It offers a maximum depth of scanning of 250 μm beyond the limits of the confocal imaging window surface. A special channel is used to deliver the contrast agent while another channel is equipped with a tweezer for tissues biopsies. It has a variable image collection rate of 0.8 or 1.6 frames per second. On the other hand, in pCLE (Fig. 2.12) many fibres are packed together and a small microscope objective with two scanning mirrors are placed at the proximal end of the package which has an external diameter of 2 mm and can be easily inserted in the working channel of the endoscope [80]. It has limited lifespan of only 20 procedures. This increases the maintenance cost of the pCLE system. Laser excitation light is carried by individual fibres and focused to a point in the tissue using the miniature objective. Fluoresce light is focused by the objective through the same fibre to the detector. The fluorescence light is sequentially focused on all fibres to construct an image.

The advantage of pCLE over eCLE is that the acquisition of the images is faster as well as more practical for inspecting narrow ducts due to the small diameter of the fibre bundle. On the other hand, in eCLE the user can change the depth of field as the scanner unit is integrated in the endoscope. This is not possible in pCLE which is characterized by a fixed depth of field (Table 2.4). The main exogenous fluorescence agents used in CLE can be administered either topically or systemically. The most common topical contrast agents that are applied topically by a spraying catheter are acriflavine and cresyl violet whereas the most widely used systemically administered fluorescent agent is fluorescein sodium. Fluorescein sodium is non-toxic and incapable of passing through cells nuclei [41]. On the other hand, acriflavine has been reported to be carcinogenic and thus its use must be limited [35]. Researchers have

shown that CLE could be useful in polyp assessment, microscopic colitis and Inflammatory Bowel Disease (IBD) mucosal healing in colon [81], [82].

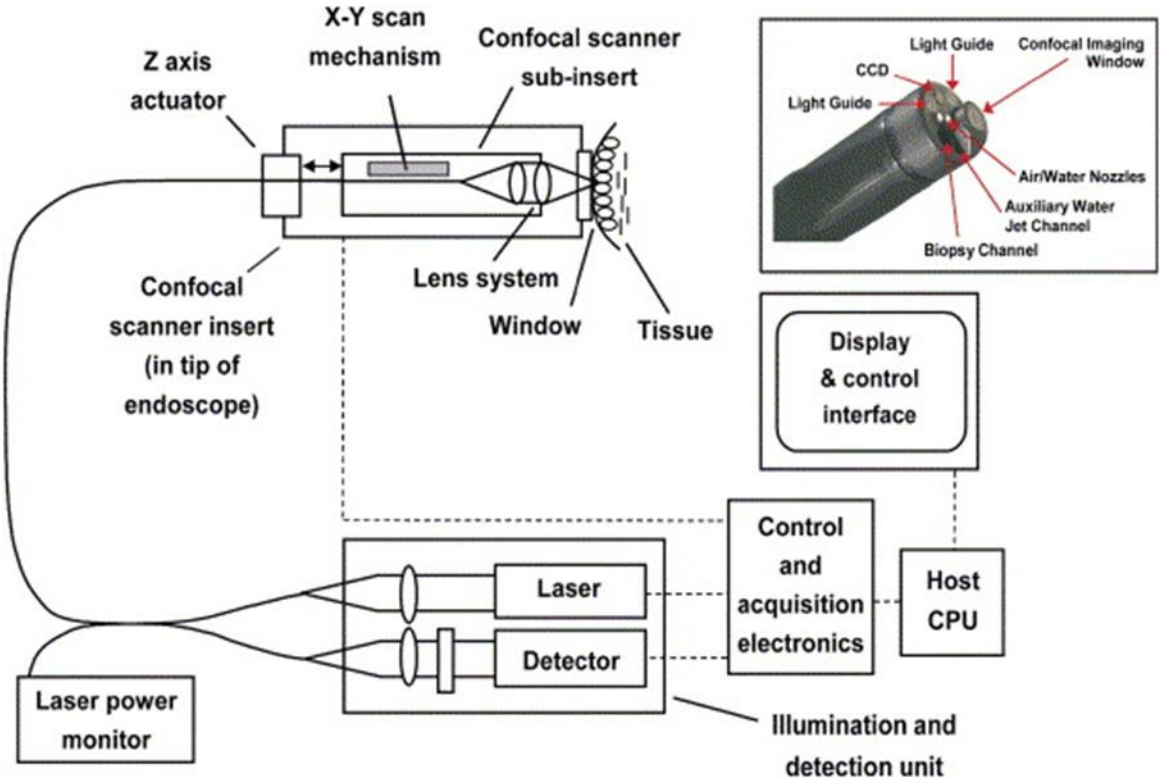

Figure 2.11 Schematic of the miniaturised confocal microscope implemented in a traditional endoscope. The mechanical and optical components on tip of the endoscope are shown on the top right pictured [78].

Figure 2.12 Confocal microscopy probe inserted through the working channel of the endoscope [79].

Table 4 Technical aspects of CLE systems **[83].**

Technical aspect	**Endoscope-based CLE (eCLE)**	**Probe-based CLE (pCLE)**
Outer diameter (mm)	12.8 (scope)	1, 2.7, 2.6*
Length (cm)	120, 180	300, 400*
Field of view (μm^2)	475 × 475	240, 320, 600*
Resolution (μm)	0.7	1, 3.5*
Magnification	× 1000	× 1000
Imaging plane depth (μm)	0-250 (dynamic)	40-70, 55-65, 70-130 (fixed) *
Acquisition rate	Slow	Fast
Maintenance	Less maintenance cost	High maintenance cost
Use or application	Less use or limited application	More practical for inspecting narrow ducts

*depending on the probes

2.4.6 Fluorescence imaging using molecular probes

Two crucial points for a successful detection of cancer in the GI tract are the intensity of the fluorescence signal to be detected and the sensitivity of the detector used in the measurements. These aspects can be addressed and tailored through an optimal combination of chemical, electronic and optical engineering. The application of a exogenous and targeted fluorescent contrast agent, consisting of a fluorescent dye conjugated to a targeting moiety, designed to highlight a biological process that is not regulated properly in the diseased area, is referred to as "optical molecular imaging" (OMI). OMI was found to be promising in terms of better endoscopic inspection of the gastrointestinal tract [84]. The use of fluorescence agents for the enhancement of contrast in the images dates to 1960s when the FDA approved the use of Fluorescein isothiocynate (FITC), Indocyanine green (ICG) and Rhodamine B for medical applications [85]. However, the main drawback of generic fluorescence agents for medical screening is the lack of specificity for tumours which translates in a high background fluorescence noise and consequent difficult detection of diseased areas [86]. In the last decade, specific fluorescence molecular probes were engineered with the aim of aiding endoscopy by providing a higher specificity and sensitivity for tumours [67]. The strategy behind the engineering of these probes is to target precise biological pathways occurring at cellular and molecular level. This means that the probes do not show any fluorescence emission unless they are "fluorescently switched on" or activated

by specific cellular environments or by the presence of receptors overexpressed on the surface of cancer cells. This approach solves the problem of high background fluorescence noise allowing visualization of small lesions in dark background. In 2013, the peptide ASYNYDA was labelled with FITC and synthesized for selectively binding to esophageal neoplasia. *Ex vivo* and *in vivo* studies performed using confocal endomicroscopy confirmed the specificity of the probe with a maximum excitation wavelength of 471 nm and fluorescence emission of 519 nm. The peptide was also found to be safe for all the 25 patients in the study [87]. In 2014, the company Goryo chemical commercialized the Gamma-glutamyl transpeptidase (GGT) selective fluorescence probe γ-glutamyl hydroxymethyl rhodamine green (gGlu-HMRG) with the name of ProteoGREEN-gGlu^{TM} [88]. The probe worked by reacting with the enzyme GGT which acts as catalyst in the cellular glutathione homeostasis. GGT expression is high on the membranes of several cancer cells and low in normal tissues. The probe (gGlu-HMRG) does not emit any fluorescence signal under low levels of GGT. However, the reaction with GGT on the membranes of cancer cells causes the hydrolysis of gGlu-HMRG into hydrophobic HMRG which emits fluorescence signal with a peak at 525 nm. The new fluorescence product permeates cells membranes and accumulates in lysosomes making the cells fluorescent (Fig. 2.13). The probe was successfully tested on several cancerous cells lines with promising results. *Ex vivo* experiments performed on colon tissues showed the capability of the probe to successfully bind to the tumours [53]. However, since GGT is also present in non-cancerous environment the probe is not efficient on the excised tissue specimen. As a result, in 2016 the same research group proposed a different probe (HMRef- βGlcNAc) for targeting human colorectal cancer [89]. The probe targets the enzyme hexosaminidase which is overexpressed in breast and colorectal carcinomas. The reaction of the probe with hexosaminidase leads to a highly fluorescence compound with excitation maxima of 479 nm and fluorescence emission of 518 nm. Tests carried out on excised specimen revealed the selectivity versus tumour lesions which showed a high fluorescence signal with respect to the lower fluorescence background of healthy tissues (Fig. 2.14). However, the probe is not available in the market.

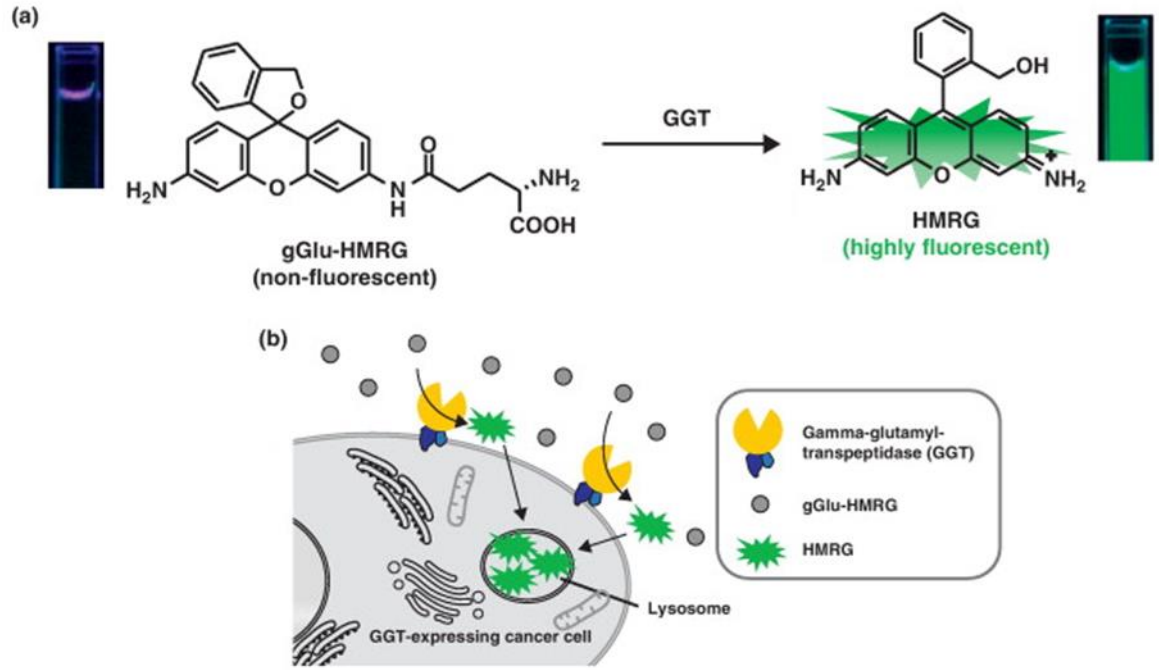

Figure 2.13 Schematic illustration of the chemical reaction of the probe in the presence of GGT. (a) *The fluorescence capabilities of the probe are activated by GGT.* ***(b)*** *After the reaction, the probe accumulates in the lysosomes of cells* [89].

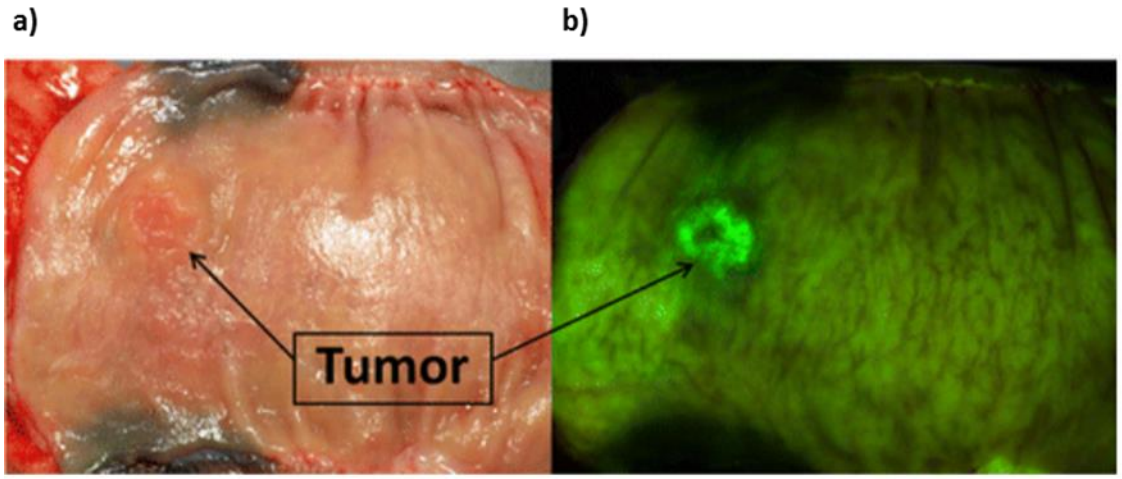

Figure 2.14 Application of HMRef-βGlcNAc to excised colorectal cancer tissues. (a) *WL image of the tumour in the rectum.* ***(b)*** *Optical image of the excised tissue under WL* [89].

2.4.7 Optical sensors for fluorescence imaging

2.4.7.1 Single Photon Avalanche Diodes

Imaging detectors along with the type of excitation source and optical components are the most important part of a fluorescence imaging system. In fluorescence medical applications, the choice of detectors depends on the type of fluorescence signal to target (Table 2.5). If fluorescence from exogenous fluorophores is investigated, multichannel detectors like photodiode arrays (PDAs) can be used as the quantum yield of external fluorescence agents or molecular probes is usually high and close to unity [90]. On the other hand, in autofluorescence imaging the quantum yield of endogenous fluorophores is between 0.015 and 0.030 and the use of more sensitive devices is necessary. In this scenario, charge coupled devices (CCDs) are recommended as they require lower electrical charges with respect to PDAs and have higher charge-to-voltage conversion efficiency. Therefore, CCDs are ideal for low-light-levels detection. The quantum efficiency of CCDs is quite high as compared to PDAs and can successfully read out by the devices for each incoming photon. This property is especially important for low-light imaging applications such as fluorescence microscopy where emission photon wavelengths are often in the 375-550 nm range and have a relatively high absorption coefficient in silicon.

In endoscopes equipped with AF modalities, the optical sensors are used to detect the signal of autofluorescence light from the tissues. A filter is used to integrate the autofluorescence image over a range of wavelengths in which the autofluorescence intensity for normal tissues is different from that of diseased tissues. In AF endoscopy, CCD arrays are being used with the powerful xenon excitation lamps operating at 300 W [91]. Endoscopes are usually electrically connected to an external unit and power consumption does not represent a constraint. In the case of medical devices operating from inside the body power considerations must be made and high-power excitation sources would be unrealistic.

Battery-powered light emitting diodes (LEDs) could be a solution. However, the use of a lower intensity excitation source results in a weaker autofluorescence signal which can only be measured by using very sensitive detectors. Photomultiplier tubes (PMTs) have been used to detect very weak light signals; however, high size cost and power make these devices unsuitable for applications in miniature medical devices [92].

CCDs or CMOS image sensors can be integrated into the tip of the endoscope to record and transmit a video image [93]. However, the problem with integrating these image sensors into the small space at the tip of an endoscope often affects the resolution of the images.

Single photon avalanche detectors (SPADs) can detect single photons and easily substitute CCDs [94]. Moreover, SPADs are characterized by lower power consumption and can be fabricated by using commercially available CMOS technologies, while CCDs require precise and expensive silicon fabrication procedures [95]. The working principle behind SPADs can be understood by first describing Avalanche Photodiodes (APDs).

APDs are reverse biased p/n or n/p silicon junctions functioning at high electric fields and thus characterized by an internal gain. The bias voltage can be applied either at the anode or at the cathode and the electric field increases with the voltage. In this configuration, if a photon with energy (E_{photon}) higher than the energy gap between the valence and conduction bands of the bonding electrons in the lattice atoms hits the active area of the APD, an electron-hole pair will be generated. The high electric field will accelerate the new electron-hole pair resulting in an avalanche of carriers. The value of the reverse bias voltage is critical in determining how to operate the APD. If the reverse bias is lower than the breakdown voltage ($V_{breakdown}$), the number of generated electron-hole pairs is finite and proportional to the number of photons impinging the active area of the APD. On the other hand, if a bias voltage higher than $V_{breakdoww}$ is applied to the cathode ($V_{breakdown}+V_{excessbias}$) or to the anode ($-(V_{breakdown}+V_{excessbias})$) the APD functions in Geiger mode and the electric field becomes very high. In this configuration, a single carrier injected in the depletion region can trigger a self-sustaining avalanche. This phenomenon results in a sharp increase in the current (Fig. 2.15 (a)). The only way to extinguish the avalanche is to reduce the bias voltage below $V_{breakdown}$. Although a decrease in the voltage is already achieved, thanks to the internal resistance of the diode, quenching circuits are used to decrease the voltage across the photodiode once a current pulse occurs. The simplest quenching circuit consists of a resistor placed in between the SPAD anode and the ground (Fig. 2.15 (b)). When an avalanche is triggered, the current passes through the resistor producing an electric potential which reduces the bias voltage. At this point the SPAD is out from the Geiger mode configuration and no current passes through the resistor. The bias voltage can, therefore, be raised above $V_{breakdown}$ again to detect another photon. The fundamental difference between SPADs and APDs is that SPADs are specifically designed to operate with a reverse bias voltage well above the breakdown voltage (on the contrary APDs operate at a bias lesser than the breakdown voltage). All SPADs are characterized by a noise component defined as dark count rate (DCR) which is independent from the signal. Specifically, DCR is defined as the number of counts per second recorder by the SPAD in the absence of any light source. The counts are not caused by incident photons but by other internal phenomena such as thermal

noise. SPADs were used in several applications including point of care diagnostic tools [95], fluorescence life-time imaging [96], proximity sensors [97] and X-ray detection [98].

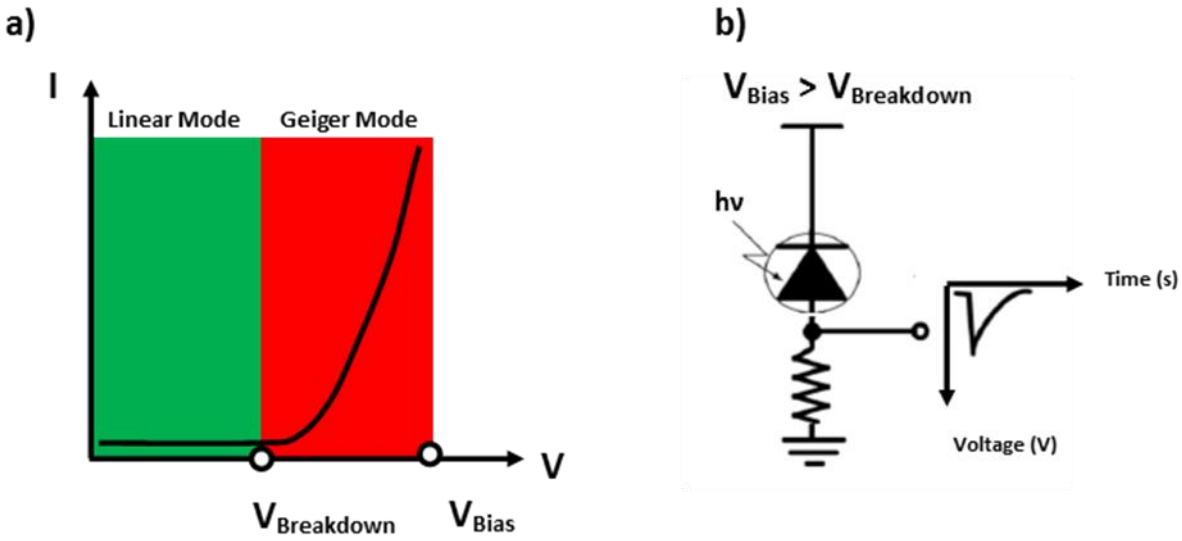

Figure 2.15 SPAD operation mechanism (a) *Voltage versus current curve showing linear and Geiger mode.* ***(b)*** *Passive quenching circuit* [99].

Table 5 Different types of optical sensors used in endoscopy.

Type	***Features***	***Advantages***	***Disadvantages***
Image enhanced endoscopy or field enhancement: NBI, I scan, FICE and autofluorescence endoscopy			
Charge coupled devices (CCDs)	Metal oxide semiconductors (MOS) are attached with an insulating oxide coating to silicon. MOS are photosensitive and convert light to electricity in. The accumulated electrical charge is proportional to the intensity of the incident light on the active area of the device.	• It is ideal for low-light-level detection • It gives improved resolution and high quality of the images	• It is often cooled to increase signal to noise ratio and corresponding sensitivity • It is cumbersome and power hungry • It is insensitive to UV light.
Photodiode arrays (PDAs)	It is a type of semi conducting device with PN junction and designed to operate in reverse bias.	• Photon saturation charge is greater than CCD so the detection range of PDA is larger than CCD • It delivers lower noise than CCD. • It is applicable where higher	• It is less sensitive than CCD

		output accuracy is needed. • It offers peak measurement at all wavelengths	
Single photon avalanche detectors (SPADs)	It is solid-state detector that offers imaging capabilities at the level of individual photons. The device is also known as Geiger-mode APDs (GmAPDs). It exploits avalanche multiplication as an internal gain mechanism.	• It can be implemented in industry-standard CMOS technology • It is small with high sensitivity. • It can tolerate longer acquisition times due to scanning	• It has lower photon detection efficiencies at longer wavelengths

2.5 Capsule endoscopy to overcome the limits of traditional endoscopy

The purpose behind the invention and fabrication of capsule endoscopy was to investigate the unreached and unexplored zones of the GI tract for efficient and extensive diagnoses [100].

The first ingestible capsule emerged in 1957 and relied on radio frequency transmission for obtaining values of pressure and temperature from within the body [101]. Three years later, an easily ingestible pill capable of detecting pH variations within the stomach was developed by Noeller [102].

In 2000, Iddan et al. successfully developed the first wireless capsule endoscopy [100]. The dimension of the pill was 11 x 30 mm. The device was equipped with an optical dome, encasing Light Emitting Diodes (LEDs) and lenses, a complementary metal–oxide–semiconductor (CMOS) image sensor and an application specific integrated circuit (ASIC) transmitter. Once ingested by the patient, the capsule coated with special slithery material, was driven through the GI tract by peristalsis. The gut tissues were illuminated by the LEDs and images were taken via the CMOS image sensor using the respective short focal length lenses. Images were radiotelemetry transmitted by means of the ASIC transmitter and antenna to an array of aerials attached to the body. The elementary significance of telemetry is the transmission of data from one location to another by means of some medium or channel. Three characteristic constituents of a telemetry system are the transmitter, the channel, and the receiver. The measured signal is converted into a compatible format by the transmitter to be sent through the channel. The channel, consecutively, carries the signal and conveys it to the receiver sited in another spatial position with respect to the transmitter. In

capsule endoscopic configuration, there is no physical channel for the signal between the capsule and the data recorder. Therefore, the simplest way to transmit data from the device to the receiver is utilizing the concept of radiofrequency (RF) communication technology and its application. The transmitted data was then visualised in an image format. The images can be saved in the memory of a small transportable video recorder and can also be downloaded for further analysis. During these processes, the capsule was powered by two silver oxide batteries providing up to 5 hours of autonomy. The Food and Drug Administration (FDA) approved the clinical use of CE as a complementary method for the investigation of small intestine which was only visible up to half of its length with the traditional wired endoscopic techniques [103]. In the following years, the use of endoscopic pills has been expanded to the whole GI tract. Table 2.6 shows the advantages and disadvantages introduced by endoscopic capsules.

Table 6 Advantages and disadvantages of capsule endoscopy [48].

Advantages	Disadvantages	Promising solution
• Convenience • No need for sedation • Simple examination for patient • Less invasiveness • High diagnostics yield comparable to other imaging modality	• Low quality image • Uncontrolled air insufflation • Retention or delayed transition • Limited battery life • Location • Impossibility of manoeuvre • Therapeutic or biopsy capability	• 3D reconstruction • Untethered controlled CO_2 insufflation • External real-time image viewer • Frame rate modulation, video compression • Impulse Radio-Ultra-Wideband • Software using 3D triangulation and Capsule-odometer • A magnetic navigation system and Mobile robotic platform • Tagging • Targeted drug delivery • Integration of miniaturised biopsy and therapeutic equipment within the capsule

• Delayed time of the interpretation	• Software which excludes useless frames and optimize summarization of the findings

2.5.1 Capsules launched in the market

There are several CE available commercially in the market as shown in Figure 2.19. Information related to the commercially available capsules for endoscopy is summarized in the Table 2.2. The first pill available in the market was the Mouth to Anus (M2A) which was manufactured by Given Imaging with a field of view of 156° and named as PillCam Small Bowel (SB) in all its following generations [6](Fig. 2.19(a)). Other companies developed similar capsules for the small bowel such as the Olympus EndoCapsule, (Fig. 2. 19 (b)) and the Jianshan OMOM pill (Fig. 2. 19 (e)) with the unique difference of using a Charge Coupled Device (CCD) as an image sensor instead of a CMOS [7], [104]. On the other hand, the Intromedic Miro pill (Fig. 2. 19 (d)) was developed with a system found on the original type of telemetry technology identified as electric-field propagation [104]. This method takes advantage of the human body as a conductive medium for the transmission of the data. A different capsule called CapsoCam (Fig. 2. 19 (c)) was manufactured by Capovision and overcame two problems associated with the other models which were insufficient battery life, resulting in an incomplete examination, and impossibility of visualizing the side walls of the bowel [105]. CapsoCam is equipped with four cameras placed on the sides of the capsule's body and a special motion technology that powers the capsule only during movement allowing the battery to last up to 15 hours. Interest towards exploiting endoscopic capsules was showed for determining both locations and causes of OGBI [105]. Traditional wired endoscopy often fails in this task because of the inability to reach the small bowel, the region from which the pathology usually originates. The advantage of capsule endoscopy in the diagnosis of OGIB is the capability of obtaining a complete view of the small bowel as well as providing high resolution images for recognition of small lesions at vascular level associated with patients suffering from OGIB. Other diseases that can be investigated using capsule endoscopy in the small bowel include Crohn's Disease, malignant or benignant neoplastic lesions (polyps) and celiac disease [106]–[108]. CE enables the early diagnosis of Crohn's disease due to its ability to detect superficial mucosal lesions, which often go unnoticed by radiology or cannot be accessed with ileocolonoscopy. Therefore, these characteristics of CE and its excellent level of safety,

define it as the best exploratory method for the study of inflammatory activity in the mucosa of the small intestine with Crohn's disease [109].

The next generation of capsules (Fig. 2. 19 (f)) was developed to screen the oesophagus and look for signs of diseases such as gastroesophageal reflux disease, Barret's oesophagus and oesophageal varices [110]. Finally, Pillcam Colon® marked the advent of a painless and sedative-free technique for colon screening (Fig. 2. 19 (g)). The capsule carries two optical domes with a total angular field of view of 344° and travels without requiring insufflation of the colon [109].

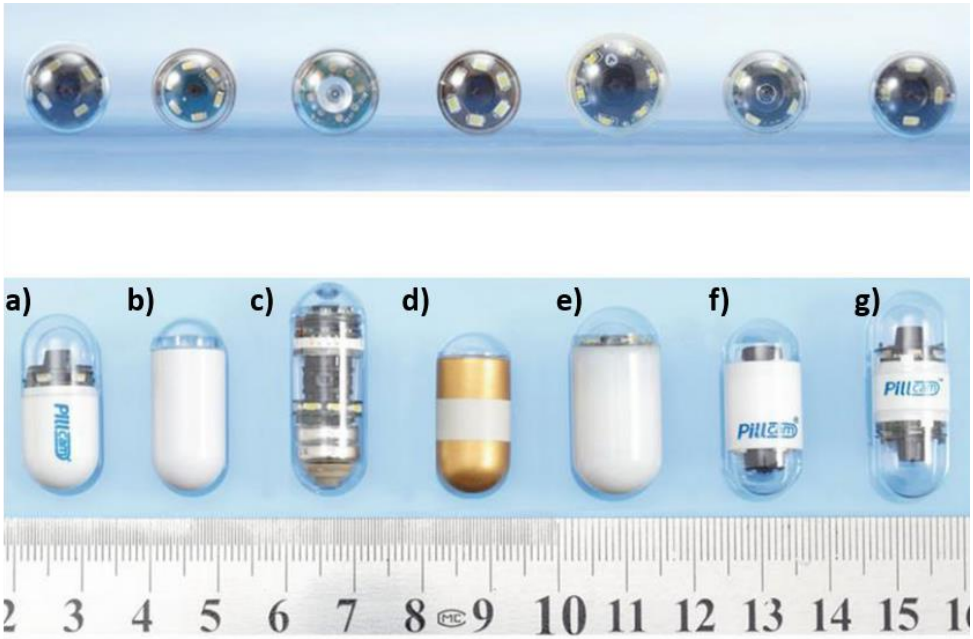

Figure 2.16 Comparative image of capsules for endoscopy available in the market **[111].** *(a) PillCam. (b) EndocCapsule. (c) CapsoCam. (d) Miro pill. (e) OMOM pill. (f) PillCam ESO®. (g) PillCam Colon®.*

Table 7 Commercially available capsule endoscopes

Name of the product (Launched by)	**Year of launching**	**Product specification**	**Reference**
PillCam SB (Company: Given Imaging)	2001	• Capsule (size: 11 mm × 26 mm, weight: 3.64 g) consist of CMOS chip imager, a short focal lens, 6 white light-emitting diode illumination sources, 2 watch	[103], [112]

PillCam SB (Company: Given Imaging)	2001	batteries, and ASIC transmitter is present. • Image features include a 140° field of view, 1:8 magnifications, 1 to 30 mm depth of view, and a minimum size of detection of about 0.1 mm. • It provides images at a frequency of 2 frames per second (f/s) until the battery expires, after about 8 h, which enables the device to take up to 55000 still images. • Approved by FDA in 2001.	
PillCam ESO (Company: Given Imaging)	2004	• Capsule (size: 11 mm × 26 mm; weight: 3.64 g) is similar to PillCam. • It has the capability of capturing 18 f/s, the field of view is 169°, CMOS image sensor and its continuous working time is observed to be 20 ± 5 minutes. • Approved by FDA in 2004.	[113]
PillCam COLON (Company: Given Imaging)	2006	• Capsule (size: 11 mm × 31 mm; weight: 2.9 g) is equipped with two image sensors on both ends and provides a near 360° view of the colon. • It has a bidirectional communication between the CE and the data recorder. Therefore, the image capture rate can be adjusted in real time from 4 f/s up to 35 f/s to maximize colon tissue coverage. • It can keep working approximately for 10 h.	[113]

		• Approved by CE in 2006.	
EndoCapsule (Company: Olympus)	2005	• Capsule (size: 11 mm × 26 mm; weight: 3.8 g) is equipped with 6 white LEDs, a supersensitive CCD image sensor and an external real-time image viewer (External Viewer) monitor. Radiofrequency is used for transmission of the data. • It has frame rate at 2 f/s. • VCE software has a Multiview capability added for reading the VCE recordings. This allows for the simultaneous display in adjacent windows of four consecutive images from the VCE recordings. • It also includes software that detects the colour red, which may help to identify bleeding in the small bowel. • Approved by FDA in 2007.	[7], [103], [114]
OMOM pill (Company: Jianshan Science & Technology (Group) Co., Ltd)	2005	• Capsule (size: 11 mm × 25.4 mm; weight 6 g) is equipped with a field of view of 140° and radiofrequency is the transmission mode. • The frame rate is 2 f/s, and the longest operation time is 6~8 h. • Approved by CE in 2007.	[7], [103], [114]
MiRoCam (Company: IntroMedic)	2007	• Capsule (size: 11 mm × 24 mm; weight 3.3 g) is equipped with a field of view of 150°. • It has a CMOS image sensor and a high-resolution image capture (102,000 pixels), with the highest	[115]

		frame rate that can be 3 f/s, and a system of data transmission using E-field propagation instead of a high-frequency transducer. • It has the longest operation time reaches more than 11 h. • Approved by CE in 2007.	
Norika (Company: RF System Lab)	2001	• Capsule (size: 9 mm × 23 mm) is equipped with a CCD image sensor with the frame rate of 30 f/s. • Its 4 illumination LEDs have different light wavelengths, which can generate simulative 3D images. The focus of the camera lens can be adjusted to obtain more clear images. • Wireless power transmitter (WPT) technique is used in Norika. • It is used in the *in vivo* drug delivery and sample extraction.	[116]
CapsoCam SV-1 (Company: CapsoVision)	2011	• Capsule (size: 11 mm × 31 mm) employs 4 CMOS cameras, each with an approximately 90° field of view, facing the sides of the capsule. • It provides a 360-degree panoramic lateral image. Each camera obtains 5 f/s for the first 2 h and thereafter 3 f/s, resulting in 20 and 12 f/s, respectively. • It has a battery life of 15 h. • Approved by FDA in 2016.	[105]

2.6 Steps towards a fluorescence endoscopic capsule

Nowadays, a revolutionary perspective has emerged since the scientific community has introduced the concept of multimodality in CE. The idea of smart pills capable of performing diagnosis and treatment of the GI tract tissues is simultaneously brilliant and convenient, though complex. The devices are supposed to supply a wide range of functions while maintaining a miniaturization approach to be easily ingested by the patients. The concept of multimodality can be simply thought as a partition of the capsule in several "compartments" each one devoted to a defined duty; literally 'a lab in a pill'. The challenge is to develop a device which is able to perform a specific function while simultaneously responding to the criteria of low-power consumption and miniaturization. Smaller components lead to an easier ingestion of the devices by the patients. Moreover, low-power consumption allows for longer inspection of the tissues and thus the acquisition of more data.

Diagnosis and therapy are essentially two main fields of research for the development of multimodality capsules. The therapeutic field is related to the capacity of the pills to perform actions such as targeted drug delivery and biopsy directly on the inspected tissues [117]. On the other hand, the diagnostic aspect is surely the most developed and involves the application of several imaging techniques coupled with the acquisition of other important physiological parameters (such as pH, temperature etc.) in order to achieve a better examination of the GI tract.

Presently, all the endoscopic capsules available in the market use WL imaging to inspect the GI tract. As previously mentioned, the implementation of fluorescence imaging in traditional endoscopes has reported to improve the detection of cancerous lesions [118]. Therefore, the integration of new imaging modalities in endoscopic capsules could merge an enhanced diagnostic accuracy with a less painful procedure for patients.

With the possibility of improving the current capsule endoscope, researchers have been attempting to incorporate the concept of fluorescence phenomenon.

In 2008 Kfouri et al. proposed the first proof of concept of a wireless fluorescence imaging diagnostic system in cylindrical shape with a diameter of 20 mm and length of 100 mm [119], (Fig. 2.21(a)). The optics in the device consisted of eight LEDs placed circularly around two achromatic imaging lenses. Four LEDs emitted UV light at 360 nm whereas the other four shined white light with a wavelength spectrum between 400 nm to 700 nm. A conical mirror was placed at the top of the capsule, before the LED and the lenses, to project

the excitation light on the GI tract lumen. Autofluorescence emission was imaged by the two lenses on the active area of a CCD imager. An aperture with an adjustable diameter (0 to 2 mm) was inserted between the two lenses to change the depth of view. Fluorescence imaging was performed by using two filters positioned in succession before the CCD imager. A long-pass filter was used to reject any light with a wavelength higher than 300 nm preventing any excitation light to hit the CCD detector (Fig. 2.21 (b)). A band pass filter was placed immediately before the image sensor to select only specific fluorescence wavelengths even though its transmission properties were not disclosed. The study was useful because two types of LEDs with centre wavelength of 365 nm and different power consumption were tested for integration in the platform. The first LED was characterized by a power of 100 mW when biased at 500 mA. The second LED had an optical power of 2 mW and 20 mA bias current. The tests revealed an elevated heating of the device when the LED with higher power was used. The potential use of the system for detection of fluorescence was validated by imaging fresh porcine skin labelled with FITC. However, the size of the prototype was too large for further validations in human tissues.

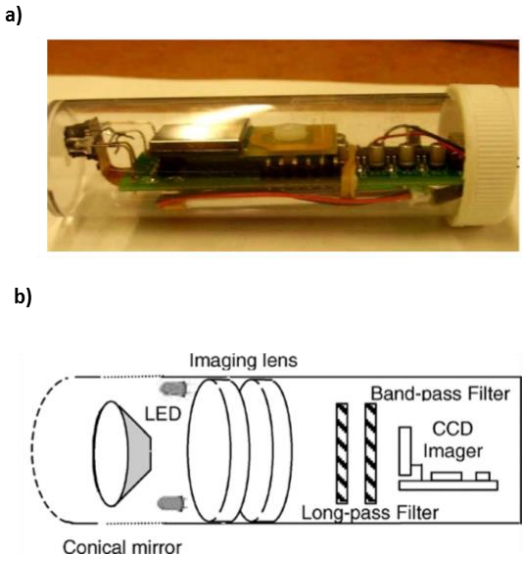

Figure 2.17 First proof of concept fluorescence pill proposed in 2008. ***(a)*** *Assembled prototype* ***(b)*** *Schematic of the optical component within the prototype* [119].

Ferreira *et al*. addressed the issue of miniaturisation in 2011 proposing optical microsensors for detection of dysplasia in the GI tract [120]. The sensors were based on thin-film optical filters and CMOS photodiodes to collect fluorescence and tissues reflectance originated by collagen in the tissue matrix. The filters were realized with dielectric materials arranged in multilayer Fabry-Perot structure. The validation of the microsensors was performed by using spectroscopy data from cancerous and healthy GI tissues that were fitted through a

mathematical model using the transmittance properties of the filters. The idea of using thin film filters was very promising from a miniaturisation point of view. However, the fabricated fluorescence filters showed a transmittance lower than 50%. As discussed previously in the chapter, autofluorescence signals are usually very weak and the use of photodiodes coupled with low transmittance optical filters might lead to unsuccessful detection of the signal.

Another approach was taken by Thomas D. O'Sullivan *et al*. who developed a tethered implantable biosensor for targeting fluorescence from the exogenous fluorophore Cyanine 5.5 (Cy 5.5) which emits fluorescence at 710 nm when excited at 684 nm and can be bound to specific receptor for tumour targeting [121]. The device consisted of a vertical cavity surface emitting laser (VCSEL) with wavelength of 670 nm and optical power of 2 mW, two GaAs photodiodes, fluorescence filter and a readout circuit assembled on PCB (Fig. 2.22 (a)). A lens was placed on top of the sensor to collimate the laser. Furthermore, biocompatible epoxy was used to coat the whole body of the device. The advantage of targeting NIR fluorophore is the low signal to background noise since autofluorescence from tissues is very low in this spectral region. The system was validated by implanting the sensor subcutaneously in a nude mouse injected with Cy5.5 (Fig. 2.12 (b)). The biosensor could detect a minimum concentration of 50nM.

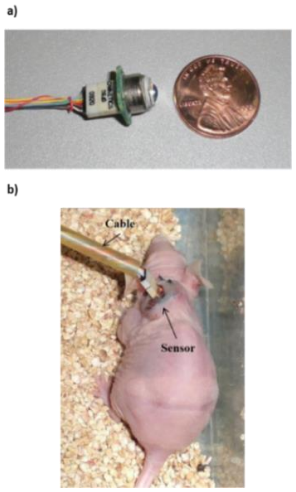

Figure 2.18 Tethered implantable biosensor for fluorescence detection of Cyanine 5.5 (Cy 5.5) (a) *Assembled device.* ***(b)*** *Implantation of the sensor in a living mouse* [121].

In 2013, a wireless capsule for autofluorescenec detection in biological tissues was proposed by Al-Rawhani *et al* [122]. The capsule consisted of one LED, three optical filters and a single pixel SPAD biased in Geiger Mode via a charge pump integrated on an ASIC (Fig 2.23 (a)). The capsule was 15 mm in diameter and 40 mm long (Fig. 2.23 (b)). The optics in the capsule were chosen to successfully detect fluorescence emission from FAD at 520 nm.

The optical components comprisisng LED, optical filters and a SPAD were tested and characterized in two separate setups before full integration in the capsule. Firstly, a band-pass excitation filter with a central wavelength of 460 nm, a bandwidth of 25 nm and maximum transmission of 85% was placed before the LED to meet the required 450 nm wavelength to excite FAD. Both LED and filter were placed above the SPAD. Furthermore, two identical long-pass filters with cut-off wavelength of 510 nm were positioned on top of the SPAD to reject any scattered excitation light allowing only fluorescence light detection (Fig. 2.24 (a)). An important figure of merit, defined as LED crosstalk, was measured by switching the LED on and evaluating the efficiency of the fluorescence filter thus measuring the LED photons impinging the active area of the detector. The illumination from the LED was responsible for an increase in the noise from 4000 counts/s, which was the experimentally measured dark count of the detector, to 89000 counts/s. A tissue specimen from an adult sheep's small intestine with thickness of 100 μm was then placed between the LED and the SPAD in order to verify the capability of the system to generate and detect autofluorescence from the tissue (Fig. 2.24 (b)). The introduction of the specimen caused an increase in the number of events with a total of 737000 counts /s, suggesting that autofluorescence signal with equal spectral properties to the transmission band of the fluorescene filter was being detected. After this preliminary characterisations, the LED and SPAD with the corresponding filters were integrated next to each other on a PCB to simulate the optical setup chosen for integration in the capsule format. Both DCR and LED crosstalk were measured. As it was expected, the DCR matched the value obtained in the previous measurements. However, the LED crosstalk was 6500 counts/s thus an order of magnitude lower than in the previous setup. The small intestine of an adult sheep was positioned above the optical system and parallel to the PCB. The filter and the LED were tilted with respect to the PCB at an angle of 20° to better excite the tissue area under the SPAD detector (Fig. 2.24 (c)). The same experiment was repeated for measuring autofluorescence fom a piece of lamb intestine. During the experiments the LED current supply was sequentially increased from 0 mA to 10 mA in order to determine the power consumption required to produce an autofluorescence emission from the tissues which could be distinguished from the background noise. Results showed that at 1mA current the autofluorescent response started to become noticeable with a clear distinction from the noise at 6mA (Fig. 2.25) . Moreover, further validation of the system was perfomed by placing aluminum foil to evaluate the detector's response to any reflected excitation light. At current supplies higher than 1mA the reflected excitation light caused a signal higher than background noise. Autofluorescence signals from both animal tissues were higher and clearly distinguishable.

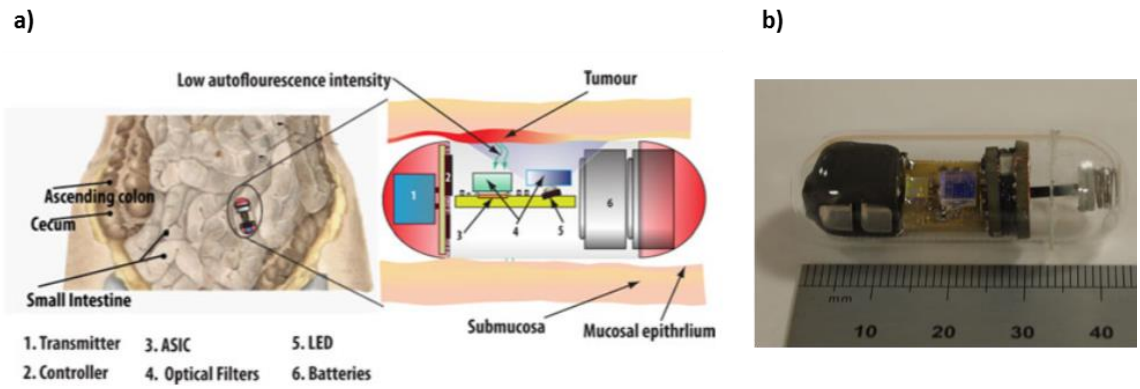

Figure 2.19 Al-Rawhani wireless capsule for AF detection in biological tissues. (a) *Potential use of the pill in the human body.* ***(b)*** *Final assembled prototype* [122].

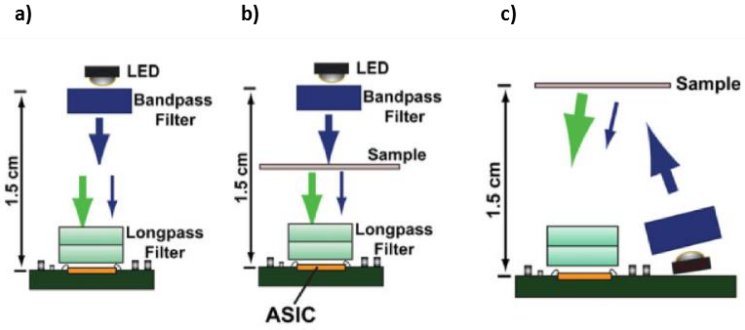

Figure 2.20 Optical setup (a) *Setup with LED on top on the SPAD without sample.* ***(b)*** *Setup with LED on top on the SPAD with sample.* ***(c)*** *Setup with LED and SPAD integrated side to side on the PCB and LED and filter tilted at 20°* [122].

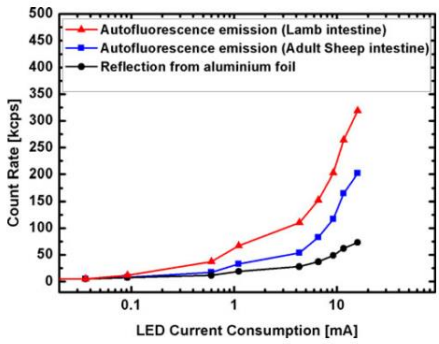

Figure 2.21 AF signal measured from animal small intestine at different LED current supplieS. Reflected light from aluminium foil is also showed in black [122]**.**

One limitation of this system is that only one side of the GI tract lumen would be inspected during examination and implementation of the same optics on the other side of the pill might increase the power consumption of the device. From an optical point of view, the system is limited to one single pixel thus a higher resolution array would improve the imaging

capabilities. The use of a higher resolution system would require a lens to focus the image on the detector. Therefore, more calculations would have to be done in order to find the exact tilting angle for the LED in order to take into account the focal length of any lens added to the optical setup.

In 2015 the same author proposed another proof of concept of a fluorescence wireless endoscopic pill [123]. The device changed from a single pixel to a SPAD array of 32 x 32 pixels biased by a charge pump. The device also incorporated a radio transmitter, an antenna, two silver oxide batteries and a filed-programmable gate array (FPGA) for converting the SPAD counts into images. The caspule body had a 16 mm diameter and was 48 mm long (Fig. 2.26). As in the previous device, the optics were designed to target green fluorescence from FAD. An LED with peak wavelenght of 460 nm and a convex lens were placed before a circular excitation band-pass filter with transmission band from 430 nm to 490 nm. An objective lens was also used to image fluorescence light emitted by the sample down to the SPAD before passing through a circular fluorescence filter with transmission band between 513 and 555 nm . Specifically, 11 mm in height, 9.6 mm in length and 8.6 mm in width were occupied by the aluminium casing holding the optical components. Both excitation and fluorescence filters have diameters of 5 mm. The main drawback of this system is the size of the pill and the optical block. As a matter of fact, the FDA released a document as guidance on the physical attributes of capsules [124]. They cannot be longer than 30 mm and the diameter must be kept shorter than 12 mm for easy ingestion. Therefore, important steps are required to further shrink the size of the optics while maintaining a good optical efficiency and sensititvity.

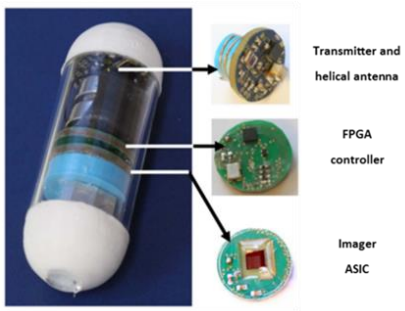

Figure 2.22 Assembled proof of concept of AF capsule **[123].**

A wireless capsule that met the dimension requirements released by FDA was developed by Nemiroski et al. in 2015 [125]. The device measured 11 mm x 27 mm and was specifically designed to detect GI bleeding after injection of fluorescein in the blood stream (Fig. 2.27(a)). The fluorometer optics in the capsule were not designed to achieve imaging

capabilities but to detect minimum concentration of fluorescence agents in the body. This approach relied on faster screening without the requirement of performing any image analysis. Two pinholes were mounted perpendicularly with respect to each other in the optical tip of the capsule to define a minimum 0.2 μM volume of detection. One pinhole guided the light from a blue LED (460 nm) whereas the other directed the fluorescence emission down to a photodiode (Fig 2.27 (b)). Bench experiments demonstrated the potential use of the sensor with a minimum concentration of 20 nM fluorescein detected in aqueous solution. A similar approach was taken in 2018 by Demosthenous who developed a pill prototype capable of detecting infrared (IR) fluorescence from indocyanine green (ICG) exogenous fluorophore [126], (Fig. 2.28). The prototype was equipped with six excitation laser diodes and six photodiodes coupled with both a long-pass filter and six operation amplifiers to detect low concentrations of ICG at the nanomolar scale. The capsule measured measured 11 x 26 and met the standard requirements. The main drawback of the system is the inability to detect AF wavelengths from the human body.

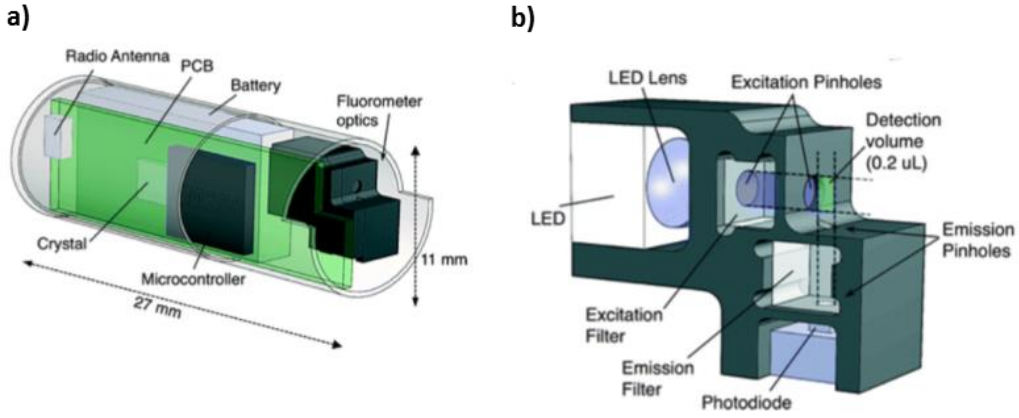

Figure 2.23 Nemiroski capsule. (a) *3D prototype of the fluorometric capsule for detection of GI bleeding.* ***(b)*** *Fluorometric optical setup* [125].

Figure 2.24 Fluorometric capsule for detection of infrared fluorescence with six LEDs in the front end **[126].**

2.7 Summary

The aim of this chapter is to highlight the importance of studying the GI track. The chapter begins by introducing the problems caused by GI tract cancer worldwide. A brief history of wired endoscopy was discussed to introduce the current technologies for gut investigation. The different imaging systems currently used in clinics to make a diagnosis were described and compared in depth. Particular attention was given to fluorescence imaging by explaining fluorescence measurements already implemented in traditional endoscopy for the detection of GI cancer along with their advantages and limitations.

Therefore, fluorescence theory was explained to understand the physical principles behind this phenomenon and how they are applied in cancer detection. Furthermore, changes in fluorescence signal from the GI tract in the presence of cancer were discussed by highlighting a distinction between the natural fluorescence emitted by biological tissues (AF) and fluorescence induced by external agents. For this purpose, Cancer-selective fluorescence molecular probes were presented as a beneficial tool for increasing fluorescence signal from malignant lesions.

Suitable detectors for fluorescence imaging were introduced with a deeper focus on SPADs. SPADs are specifically suited for this type of application because they can detect single photons of light and thus image weak changes in AF signals from the human body.

The chapter introduces then capsule endoscopy by covering its history since the implementation of the first capsule in 1957 to modern products available in the market that rely on WL imaging. Therefore, the potential implementation of fluorescence imaging in CE endoscopy is introduced by highlighting the increased diagnostic accuracy of this imaging technique in traditional endoscopy.

Finally, works done by other research groups on the implementation of fluorescence sensing modalities in capsule endoscopy were presented. The main challenge lays in developing systems which meet the dimension requirements released by FDA. Proof of concepts prototypes implemented with fluorescence imaging modalities revealed to be too bulky. On the other hand, the devices that met the dimensions requirements are based on simple fluorometric measurements that would not allow doctors to have a complete scenario of the disease.

The aim of this research work is to realize an optical interference block to be coupled with a sensitive SPAD array imager for AF and fluorescence labelling imaging in the GI tract. The block must meet specific dimensions to fit in a pill equipped with other sensing modalities.

All the limitations highlighted in the previous works both in terms of size and sensitivity need to be overcome. Therefore, the optical unit presented in this work must be the first fluorescence imaging system for CE capable of imaging human colorectal cancer cells and resected human tissues from the colon.

3 Simulation, measurements, and set-up of the optical block

The chapter describes the steps undertaken to finalise the design of the optical block, as well as the experiments performed to process the individual parts of the block and assemble them. Table 3.1 summarises the requirements for the fluorescence optical block. As the block had to be fabricated to fit the Sonopill capsule, the final volume of the prototype was the first requirement of this research. During the brain storming sessions among the different universities working on the project, a volume of 200 mm^3 was assigned to the fluorescence unit in the capsule by taking into considerations all the circuitry and components dedicated to the other sensing modalities. Therefore, the following choices were influenced by this constraint. A timeline of three years was assigned to realize and test the optical unit. Therefore, a choice to use off-the-shelf components was made to focus also on testing the prototype on a large and variable range of biological samples. Excitation and fluorescence wavelengths of operations were chosen based on AF imaging systems used in traditional endoscopy. Therefore, a small light source with a narrow footprint and a wavelength between 460 and 480 nm was researched to fit in the block and excite fluorescence between 520 and 550 nm. Different filters were investigated for the implementation of the unit. Since the fluorescence light excited by a small power source could be low in intensity, a detector high sensitivity for the wavelengths of interest and low noise was investigated.

Table summarises the requirements for the fluorescence optical block.

Table 8

Volume	200 mm^3
Components	Off the shelf
Excitation wavelength	460 - 480 nm
Fluorescence wavelength	520 - 550 nm
Light source	Narrow footprint (small illumination angle)
Collimating Lens	Adequate diameter to gather all the light coming from the source
Objective Lens	
Detector	High sensitivity and low noise
Spatial resolution	2000 µm

The software used to simulate the optical components of the set-up will be introduced. Simulations of different optical filters will be showed to justify the choice of the final set of

filters used in the prototype. The results from the characterisation of the optical source will then be presented, followed by the implementation of the final design for the entire optical block. The chapter will conclude by detailing the processes used to make the optical block, and the results from the characterisation of each optical filter needed in the block.

3.1 Zemax Optics Studio

Zemax Optics Studio is a software commonly used for the design and analysis of optical systems [127]. The software can be operated in two different modalities:

- **Sequential ray tracing**. In this mode, rays are traced from the surface of an object to another surface in a predetermined sequence. Surfaces are also automatically numbered in sequence. Therefore, if four objects are modelled, rays are traced from one to two, two to three etc. It is not possible to trace rays from two to four or from four to two.
- **Non-sequential ray tracing**. In this mode, rays can only be traced along a possible physical path until they intercept an object, with which some interaction takes place, e.g. refraction, reflection, or absorption depending upon the properties of the object. Rays then continue along a new path striking any group of objects in any order, or the same object repeatedly.

The main difference between the two modes is that in the non-sequential mode, all the optical components are treated as three dimensional objects and thus it is possible to import CAD designs realised with other software tools such as SolidWorks.

3.2 Optical Design in Zemax

3.2.1 Light Source: Considerations

The design for the miniaturised optical block for capsule endoscopy was realised in non-sequential mode. The first step in the design was the choice of a light source for the system, and several aspects needed consideration. The main aspect was that the block needed to fit into a capsule with a diameter of approximately 10 mm and a length of 20 mm, thus dimensions and power consumption were the main constraints. With regard to the fluorescence aspect, the wavelength of the source was crucial.

As discussed in the previous chapter, endogenous and exogenous fluorophores have different maxima excitation wavelengths. In order to excite tissue AF, illumination at wavelengths between 380 nm and 475 nm (violet-blue colour) is needed. Moreover, fluorescence light in

the green, with wavelength between 515 nm and 530 nm, resulted to be the highest attenuated fluorescence component in malignant tissues. Therefore, a choice to limit the operation of block to only a specific wavelength range was made. In this way, it was easier to meet the dimension requirements and limit power consumption by working at a specific band instead of the whole visible spectrum. Flavin adenine dinucleotide (FAD) was chosen as the target endogenous fluorophore. The maximum excitation wavelength of FAD is 450 nm with fluorescence emission at 530 nm.

A commercially available Indium Gallium Nitride (InGaN) based sub-miniature LED was purchased (part no. ASMT-BB20 PCB). As shown in Figure 3.1 (a), the LED is 2.4 mm x 3.2 mm x 2.4 mm and is characterised by a peak wavelength of 468 nm (Figure 3.1 (b)) and a narrow print with a viewing angle of 7.5° (Figure 3.1 (c)). The LED operates at a bias of 3.2 V with a forward current of 20 mA [128]. The output beam of the LED was first characterised by using the knife-edge technique (explained in the next paragraph) to confirm its emission was best approximated by a Gaussian beam and determine the beam size. The light source was then simulated in Zemax Optics Studio to compare the simulated and experimental beam profile and validate the simulations.

3.2.2 Light Source: Knife-edge measurements

A knife-edge measurement allows to obtain the size of a light beam (the so-called beam *waist*) by transversally scanning a blade. To perform the measurement, first the light source is placed at a fixed distance from a detector. A blade moving by fixed steps (Figure 3.2) then gradually shields the beam until it is completely obscured and the detected power drops to zero. In this case, the LED and the detector were fixed to an optical table at 2 mm from each other, and the blade was mounted between them. In the experiments, a pedestal pillar post held a manual translational stage to which the blade was mounted (Figure 3.3), and the stage was used to move the blade in steps of 200 µm, recording the power of the beam at every step. The exact same measurements were performed on both x and y directions.

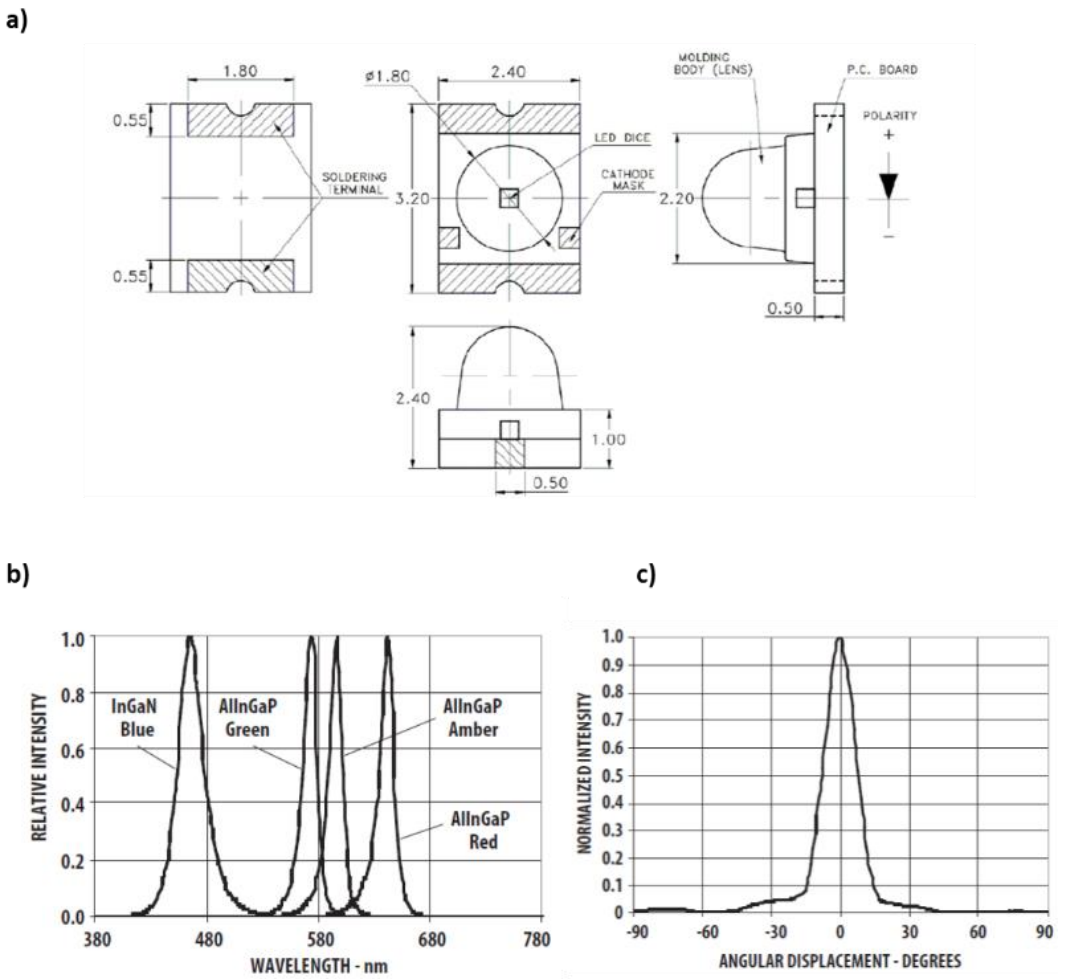

Figure 3.1 Light source specifications. *(**a**) Technical drawing of the sub-miniature LED lamp in four different planes. (**b**) Relative intensity versus wavelengths for the InGaN LED chosen for the design, and the other type LEDs available for purchase. (**c**) Radiation pattern of the LED. All figures were imported from the LED data sheet.*

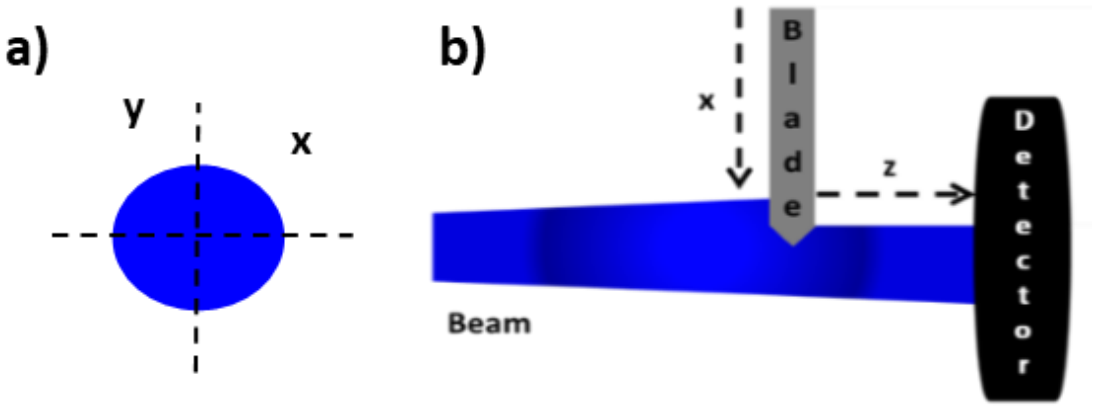

Figure 3.2 Conceptual diagram for knife-edge measurement. *(**a**) Front view of the beam showing x and y directions for knife-edge measurements (**b**) Top view of the knife-edge setup with the blade shielding the beam in the x direction.*

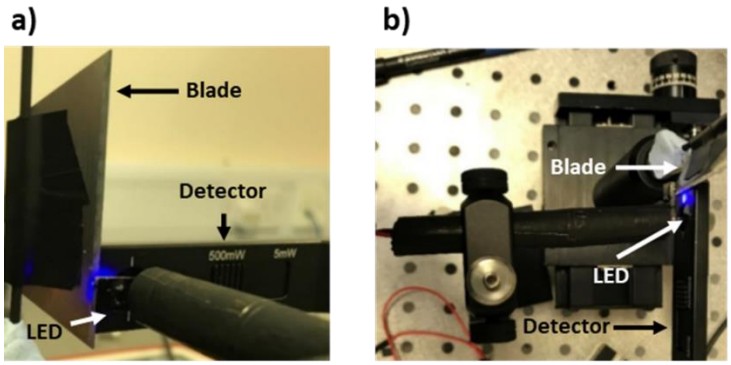

Figure 3.3 Knife-edge measurements setup. ***(a)*** *Front view of the setup with LED blade and detector* ***(b)*** *Top view of setup.*

Following the measurement, the power scanned along one direction was plotted versus the distance travelled by the blade. As Figure 3.4 shows, the detected power progressively decreased until dropping to zero once the blade covered the whole beam. The experimental data were fitted to the power distribution model for the Gaussian beam:

$$P = P_0 + \frac{P_{max}}{2}\left(1 - \text{erf}\left(\frac{\sqrt{2}(x - x_0)}{w}\right)\right) \quad (5)$$

Where

P_0 and P_{max} are the minimum and the maximum measured powers, respectively.

x_0 is the position in the x direction where the power is equal to half the maximum power.

w is the waist of the beam.

erf is the standard error function.

The results from the fitting model showed an R^2 higher than 99% in both x and y directions (Figure 3.4 (a) and (b)). Therefore, the waists (w_x, w_y) and the centres (x_0, y_0) of the beam were computed by using the coefficients from the fitting model in eq. 5. Calculations showed that the centre of the beam in the x direction was at 3.76 mm and the beam had a waist of 1.17 mm. In the y direction, the beam was centred at 4.085 mm with a waist of 1.17 mm.

The Gaussian beam profile was also directly derived by using the experimental data points into the following equation:

$$\frac{dP}{dx} = P(x_n - x_{(n-1)})/(x_n - x_{(n-1)}) \quad (6)$$

Where

Px_n is the measured power of the LED when the blade was at a position x_n.

The experimental data were fitted to the equation for the intensity of the Gaussian beam:

$$I = I_{max} e^{\left(-\left(\frac{2(x-x_0)^2}{w^2}\right)\right)} \quad (7)$$

Where

I_{max} is the maximum intensity (W/m).

Figure 3.5 shows the Gaussian curve obtained by applying equation 6 to the experimental data superimposing the fitted Gaussian beam intensity distribution model from eq. 7. Table 1 compares the R^2 values between the experimental results and the fitting models. The parameters w_x, w_x, x_0 and y_0 are also used as figures of merit for both models. Both models provided an excellent fit to the experimental data and the difference between them was negligible.

Table 9 Comparison between parameters obtained from the two fitting models.

	R^2		**Waist (mm)**		**Centre (mm)**	
	x direction	*y direction*	*x_0*	*y_0*	*x_0*	*y_0*
$\boldsymbol{P = P_0 + \frac{P_{max}}{2}(1 - \mathrm{erf}(\frac{\sqrt{2}(x - x_0)}{w}))}$	99%	99%	1.17	1.17	3.76	4.08
$\boldsymbol{I = I_{max} e^{\left(-\left(\frac{2(x-x_0)^2}{w^2}\right)\right)}}$	99%	99%	*1.17*	*1.13*	*3.85*	4.18

a)

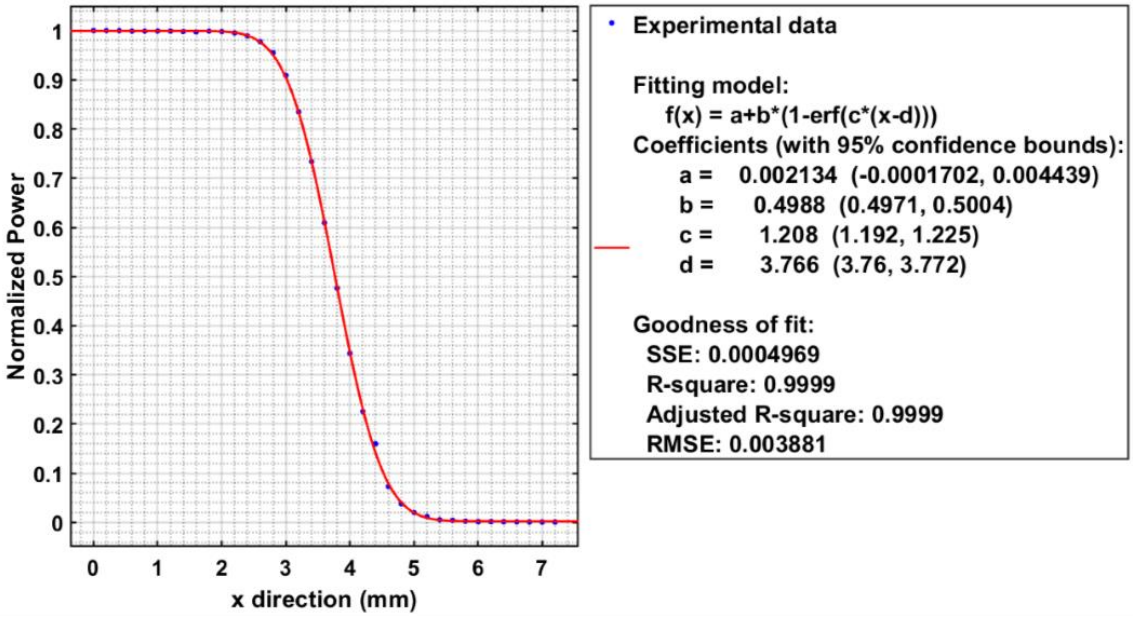

b)

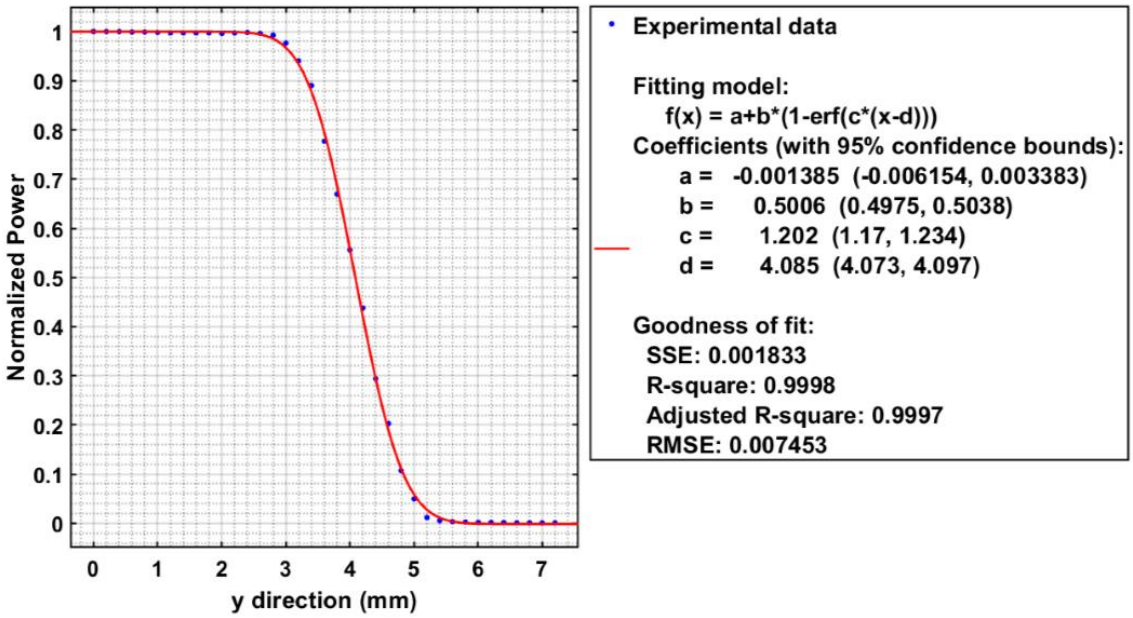

Figure 3.4 Normalised power versus distance. *(**a**) x direction. (**b**) y direction. Data were normalised with respect to the maximum value of 1.1 mW measured in both directions.*

a)

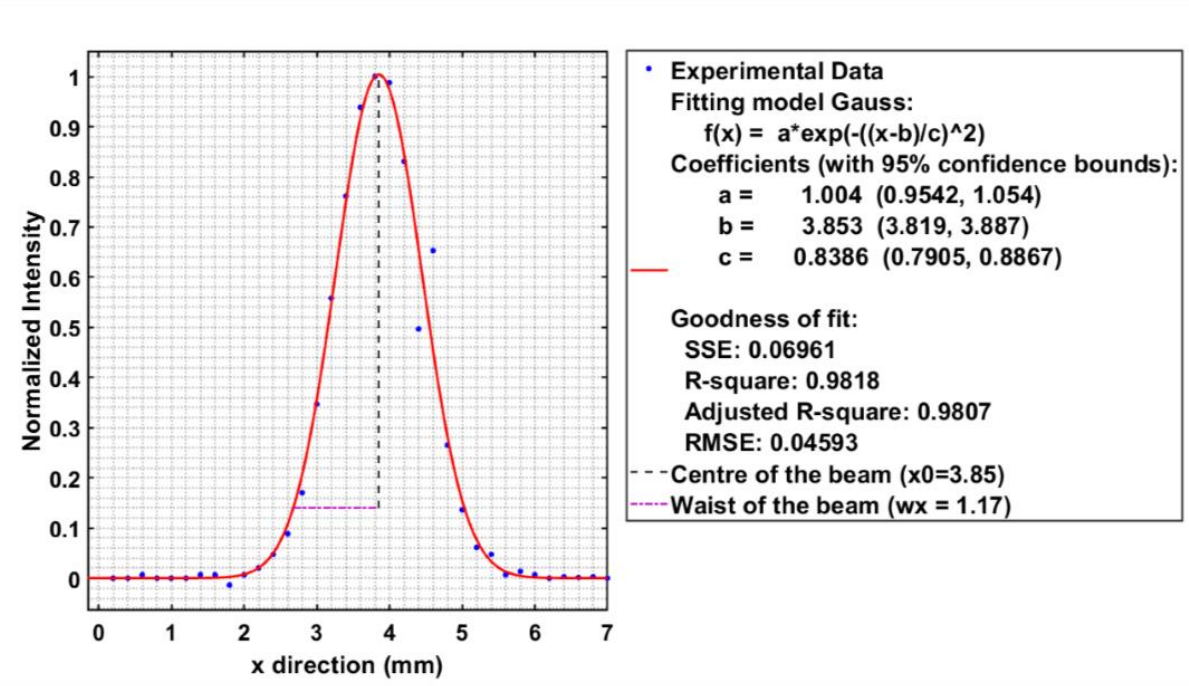

b)

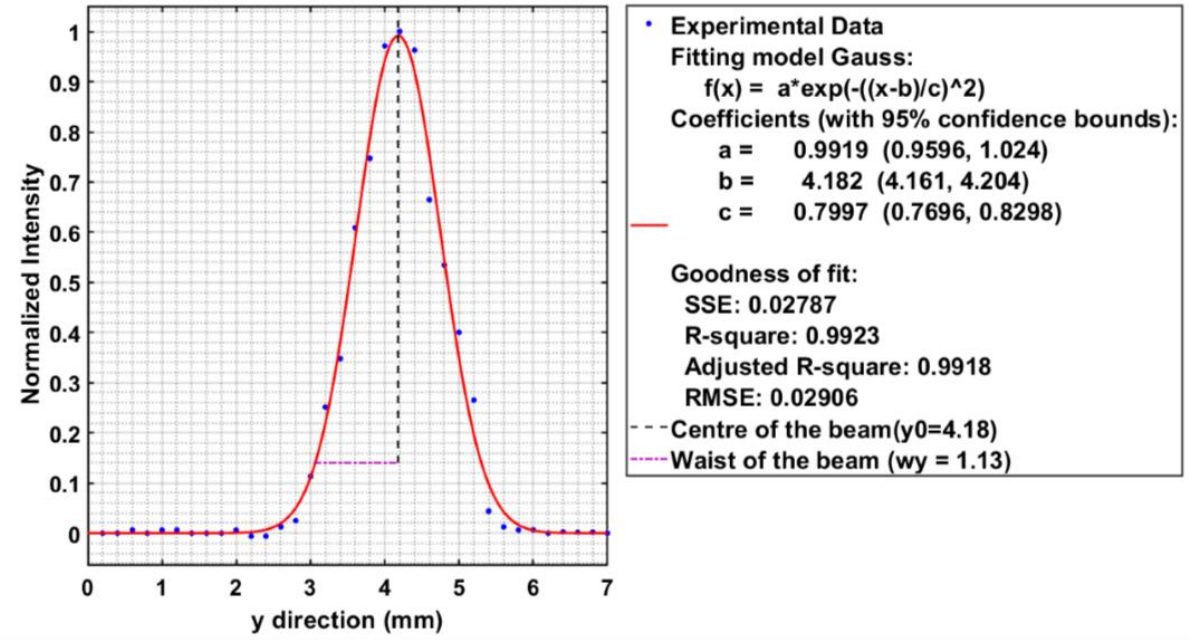

Figure 3.5 Gaussian beam profile. *(**a**) x direction. (**b**) y direction. Data were normalised with respect to the maximum value obtained by applying equation 6 to the experimental data.*

3.2.3 Light Source: Simulation in Zemax Optics Studio

Zemax Optics Studio was used to simulate the emission from the LED. The necessary data for the simulation were extracted from the datasheet of the LED. The interface of Zemax Optics Studio makes it straightforward to use. Figure 3.6 shows the typical interface of the software in non-sequential mode with a non-sequential component (NSC) editor window

(Figure 3.6 (a)), and an NSC shaded model window (Figure 3.6 (b)). The former window allows the user to choose the components in the design, whereas the latter shows the components in a three-dimensional space as they are added to the design. The non-sequential component editor is structured as a table. New rows are added to the table as components are introduced in the design by the user. Each row hence represents an object. The first cell of each row is the '*Object Type'* (Figure 3.6 (a)). There are a different number of cells for each object depending on the parameters characterising the object itself. Photometric units and wavelengths can be changed through the System Explorer Window, shown in Figure 3.6 (c).

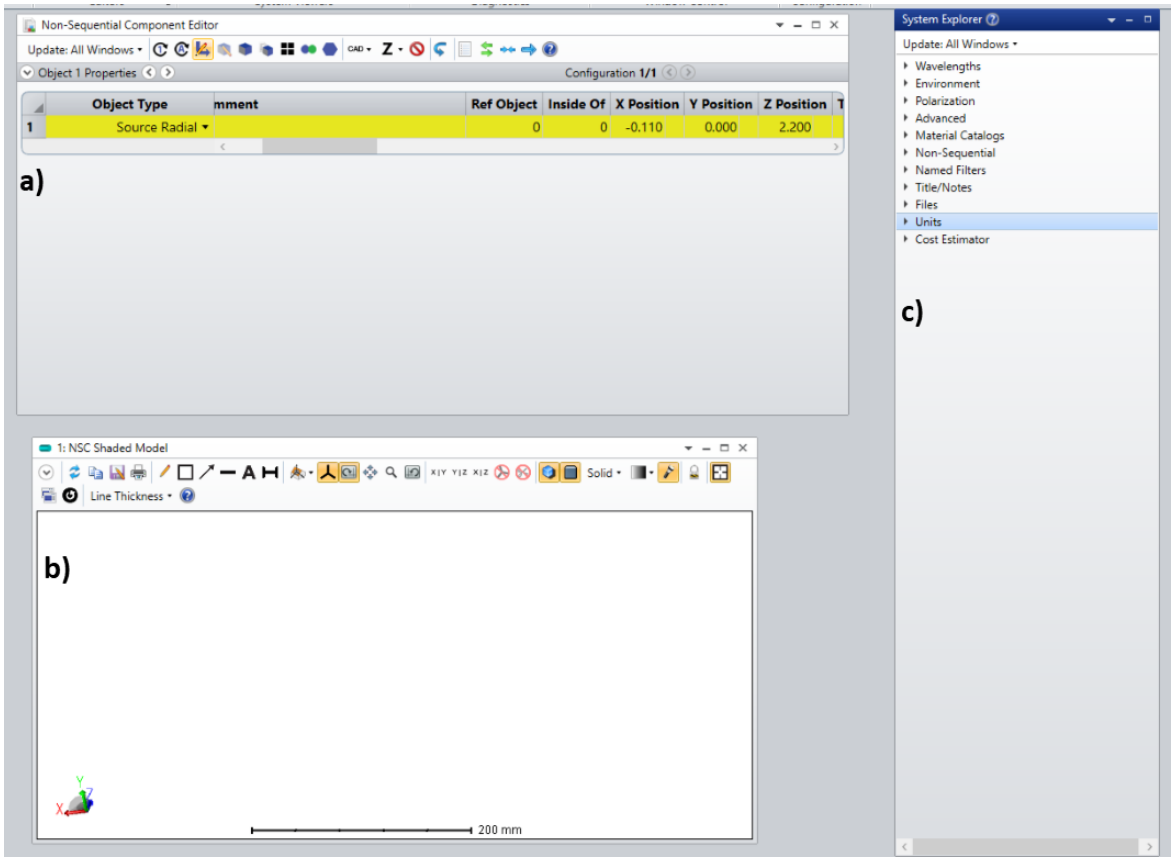

Figure 3.6 Zemax interface in non-sequential mode. (a) *Non-sequential component editor (NSC).* ***(b)*** *NSC shaded Model.* ***(c)*** *System explorer windows.*

Zemax offers different type of sources among the objects available. In this case, the '*Source Radial*' object was chosen as model for simulating the LED (Figure 3.7 (a)). A fixed number of points were used to reproduce the same angular displacement radiation pattern of the LED. As we can see in Figure 3.7 (a), the maximum and minimum angle in the simulation model were inserted under the cells '*Minimum Angle*' and '*Maximum angle'*. The values of normalised intensities for each angle were retrieved from the LED radiation pattern diagram, previously shown in Figure 3.1 (c). In fact, the data points were extracted from the diagram

by using the online software *WebPlotDigitizer*. Moreover, since the intensity in the datasheet diagram is normalised from zero to one, each value was multiplied by a hundred to match the normalisation in the simulation software. As we can see from Table 2, a total of nineteen angles were introduced in the model with the respective normalised relative intensities.

Table 10 Angles with respective relative intensities retrieved by the LED datasheet radiation pattern and inserted in the model.

Points	Angle (º)	Relative Intensity
1	0	100
2	5	78
3	10	26
4	15	8
5	20	4
6	25	3.2
7	30	1.9
8	35	1.83
9	40	1.46
10	45	0.6
11	50	0
12	55	0
13	60	0
14	65	0
15	70	0
16	75	0
17	80	0
18	85	0
19	90	0

The normalised intensities for each angle were inserted in the cells '*I 0.0*', '*I 5.0'*, '*I 10.0*' etc. with each point corresponding to an angle from 0 º to 90º (Figure 3.7 (a)). In the datasheet of the product, 1.8 mm was the diameter of the source. Therefore, 0.9 mm was introduced as value in the cells with names '*X halfwidth'* and '*Y halfwidth'* to give a size to the simulated source (Figure 3.7 (a)). Other parameters that were used in the model were the LED peak wavelength and the power emitted by the source. The maximum value of power emitted by the source that was measured during the knife-edge measurements was 1 mW. The peak wavelength of 468 nm was specified in the system explorer window under the panel '*Wavelength'*. At this point, a '*Rectangular detector'* object was created and placed 2 mm away in front of the source (Figure 3.7 (b)). The detector had 16384 pixels (128 x 128) and measured 7 mm on both sides. The three-dimensional model including both LED and detector is showed in Figure 3.7 (c). The model simply consists of several rays hitting the surface of the detector exactly in the centre.

a)

	Object Type	Power(Watts)	X Half Width	Y Half Width	Minimum Angle	Maximum Angle	# Of Points	I(0.00)
1	Source Radial	0.064	0.700	0.700	0.000	90.000	19	100.000

b)

	Object Type	X Half Width	Y Half Width	# X Pixels	# Y Pixels
2	Detector Rectangle	3.500	3.500	128	128

c)

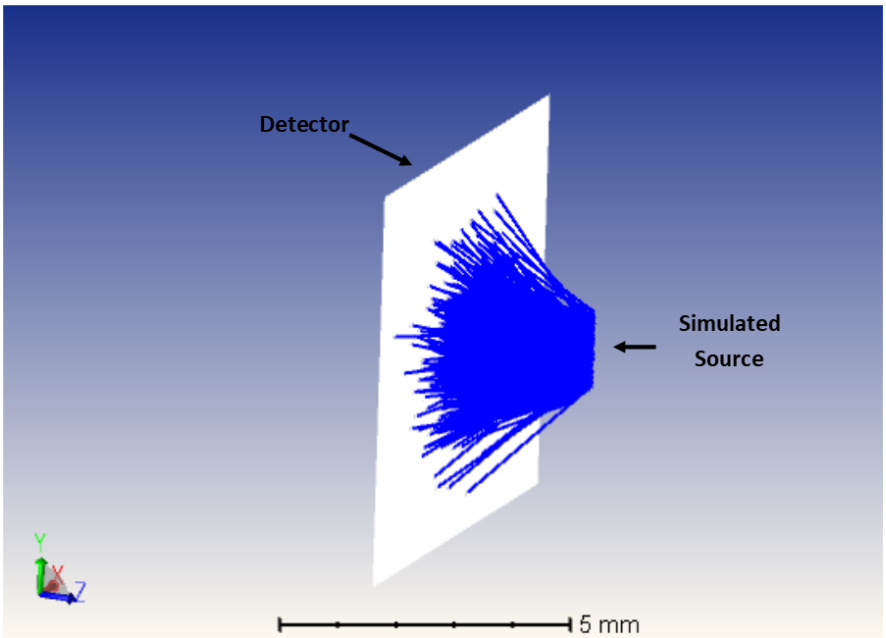

Figure 3.7 Zemax interface I. *(**a**) Source radial object interface, (**b**) Detecor object interface. **(c)** Three- dimensional NSC model.*

Once all parameters were set, a ray trace was launched to evaluate the simulated beam profile (Figure 3.8(a)). The '*Split NCS rays*' and '*Use Polarization*' boxes in the ray trace control window were both checked to allow rays splitting during the ray trace. At the end of the ray trace analysis, the simulated beam was obtained, and is shown in Figure 3.8 (b). Zemax uses the value of Irradiance (W/cm^2) as photometric unit to describe the spatial distribution of the beam. The detector viewer in Zemax also allowed separating the analysis of the irradiance along each transversal direction. Therefore, data for x and y directions were separately exported in a text file and fitted to a Gaussian beam intensity distribution model in eq. 7 using Matlab. As Figure 3.9 (a) shows, the R^2 of 99.8 % suggests an excellent match between the simulated beam and the Gaussian model. The simulations provided a beam waist value of 1.17 mm, corresponding to the value obtained from the knife-edge measurements. Simulations were also carried out to obtain the radiant intensity of the beam, and evaluate the angular radiation pattern along thex and y directions to compare them to the diagram in the data sheet. In the LED datasheet, 7.5 º is reported as the device viewing angle, which is defined as the angle at which the intensity is half of the peak intensity. The viewing angle obtained from the simulations is shown in Figure 3.9 (b), and again an excellent match between the simulated data and the angular radiation pattern given in the datasheet can be seen.

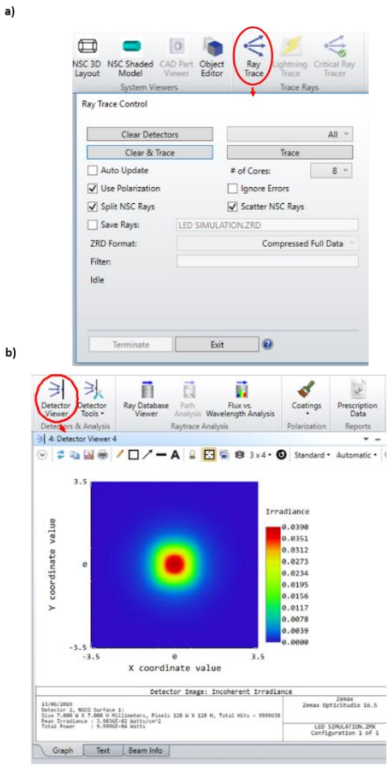

Figure 3.8 Zemax object interface II. ***(a)*** *Ray trace window in Zemax* ***(b)*** *Detector viewer window showing the beam spot on the detector along two dimensions.*

a)

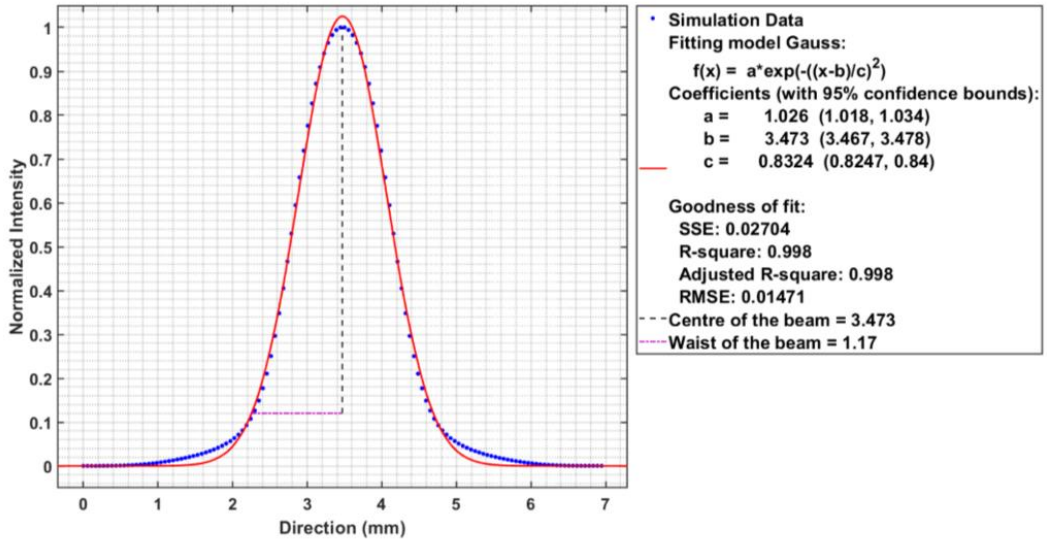

b)

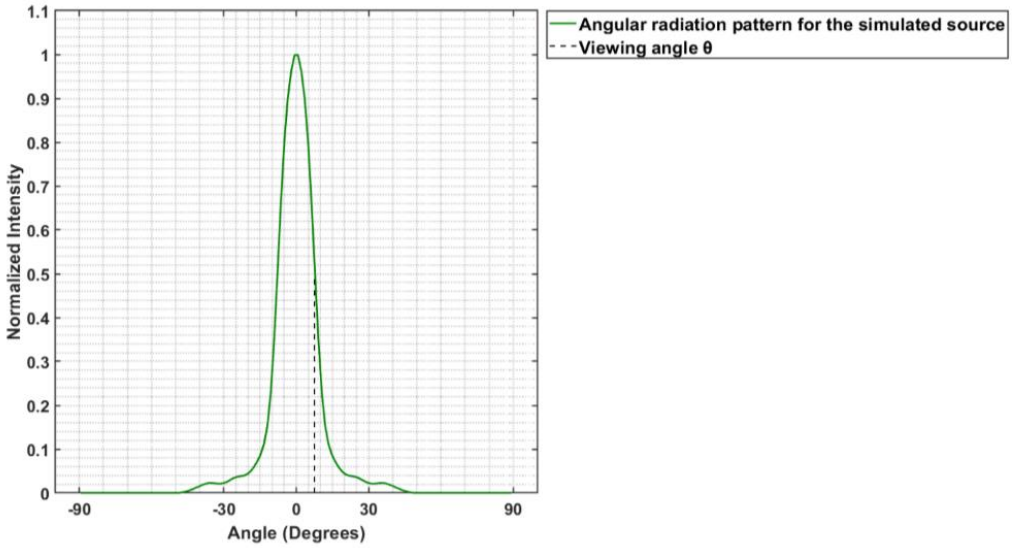

Figure 3.9 Beam profiles from simulation. *(**a**) Gaussian beam profile of the simulated source is identical in both x and y directions. The diagram was normalised with respect to the maximum value of irradiance given in the simulation (**b**) Angular radiation pattern of the simulated source showing the viewing angle of 7.5 º. The diagram was normalised with respect to the maximum value of radiant intensity given in the simulation.*

3.2.4 Optical configuration

The optical design for the miniaturised block was inspired from a typical in-line fluorescence microscope setup (Figure 3.10). The typical components in a fluorescence microscope are certainly the excitation, emission and dichroic filters. Most fluorescence microscopes use a

dichroic beam splitter that reflects shorter wavelengths to excite fluorophores and transmits longer fluorescence wavelengths. The combination of these optical filters avoids non-fluorescent light hitting the microscope sensor. The most important parameters of a filter are the centre wavelength (CWL), transmission percentage, optical density (OD), and bandwidth. The choice of the filters for the setup was mainly based on these optical characteristics.

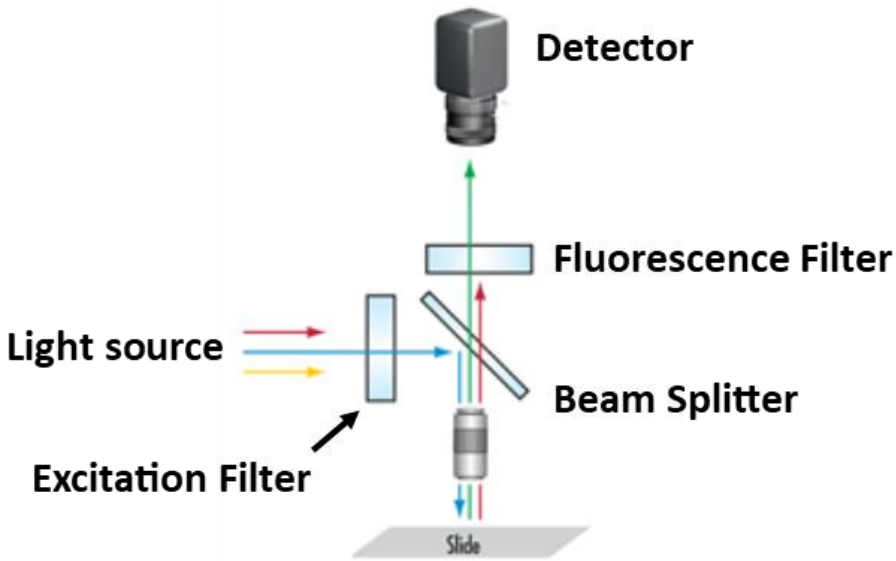

Figure 3.10 In-line fluorescence microscope setup.

The initial goal of the optical design was to maintain all the optical components in a cube with a volume of 25 mm^3 and sides of 5 mm in each dimension. This choice was made to leave space for other electrical components within the capsule. Although the LED had a very small angle of view, dichroic beam splitters are designed to work with collimated light. Therefore, the first object that was added to the optical design after the light source was a lens to collimate the light from the LED. The lens was chosen by considering the size of the LED as well as the size of the lenses available in the market. A commercially available plano-convex lens from Edmund Optics, with diameter and focal length of 2 mm was chosen. The 3D CAD design of the lens was obtained from the manufacturer and imported in Zemax Optics Studio, where of the type of glass used for the lens (N-LASF9) was also specified. The lens was placed in front of the light source with the flat face facing the LED at 1.57 mm which is the back focal length of the lens.

3.2.5 Choice of filters

Filters were chosen based on the results from optical simulations. The setup for the simulations was created by placing a rectangular volume object with sides of 5 mm and

2 mm and thickness of 500 µm was after the collimating lens. The object was used to model an excitation filter. The next element added to the optical design was the dichroic beam splitter. The beam splitter was placed at a 45º angle in front of the light source, collimating lens, and excitation filter to deflect all the light coming from the source upward at 90º. The dichroic beam splitter thickness was fixed at 200 µm whereas the sides of the filter measured 2.1 mm and 5 mm. An objective lens with a diameter of 2 mm and a focal length of 3 mm was then positioned above the beam splitter at 1.1 mm from its centre. The purpose of the lens was to direct the excitation light on the sample as well as imaging any fluorescence light coming from the specimen. Finally, the fluorescence filter was modelled with a thickness of 500 µm and placed under the beam splitter and objective lens at 3 mm from the end of the lens facing the beam splitter. In the simulations, a detector was placed in front of the objective lens at a distance equal to its focal length to determine the irradiance of the excitation source. Another detector was placed under the excitation filter to measure the level of noise as irradiance of the excitation source passing through the fluorescence filter (Fig. 3.11). Since Zemax allows to specify coatings for each object surface, the transmission properties of bandpass filters available in the market were simulated. Filters from three different manufactures were investigated as it is shown in table 11. In the case of excitation filters, two types of filter for each manufacturer were chosen. One type with a larger band and another type with a narrower band. In the case of beam splitters, two types of filter for each manufacturer were also investigated.

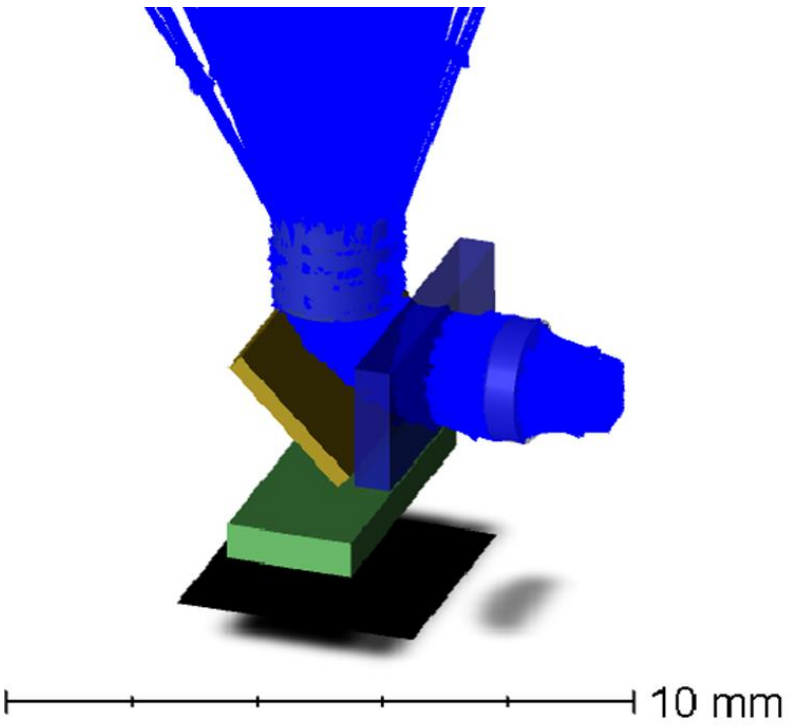

Figure 3.11 Optical setup in the Zemax Simulation.

The simulations were performed by using all the possible combinations of filters. In each simulation the average irradiance value of light hitting the detector on top of the objective lens was calculated. As it is showed in figure 3.12, the filters with larger band showed similar results. As it was expected a higher number of wavelengths can pass through the filter. However, among the filters with narrow band the substrate manufactured by Chroma showed better results in terms of light transmission.

Table 11 Excitation and Beam splitter filters used in the simulations (For the excitation filters, the first number refers to centre wavelength, the second number refers to full width at half-maximum (FWHM)).

	EXCITATION		**BEAM SPLEATTER**	
	Type 1	***Type 2***	***Type 1 (cut-off)***	***Type 2 (cut-off)***
ALLUXA	**447-60 nm**	**470-10 nm**	**498 nm**	**505 nm**
CHROMA	**450-50 nm**	**470-40 nm**	**495 nm**	**505 nm**
SEMROCK	**452-45 nm**	**480-17 nm**	**495 nm**	**506 nm**

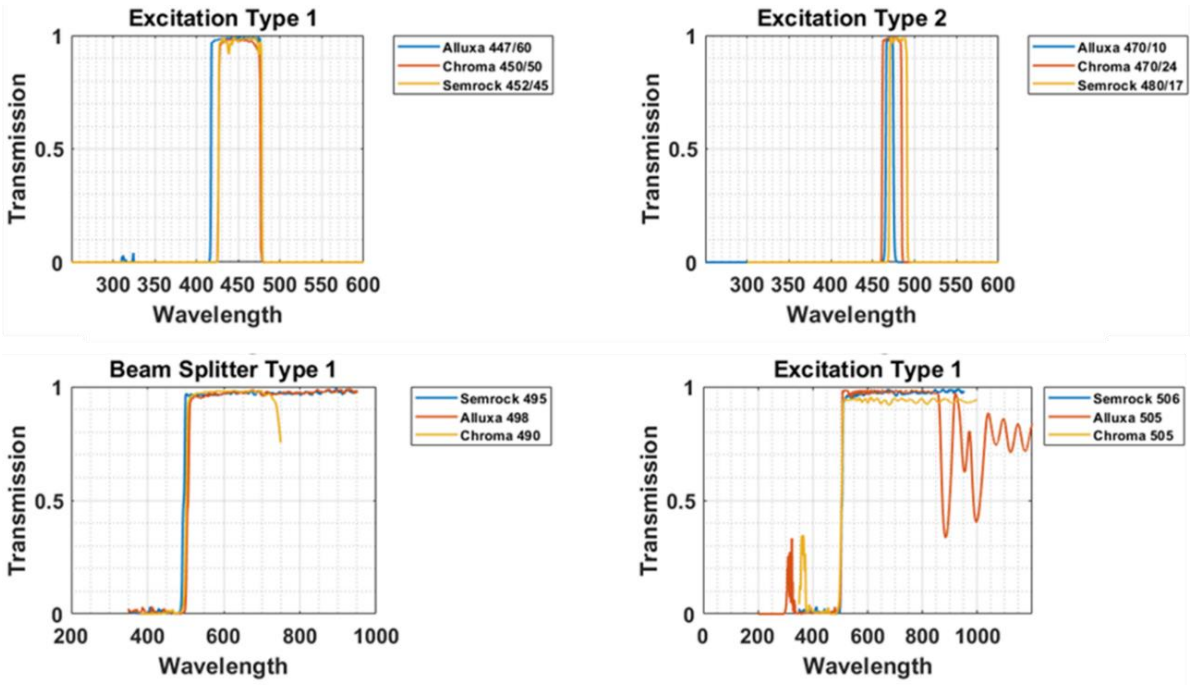

Figure 3.12 Transmission band of excitation filters and beam splitters chosen for the simulations.

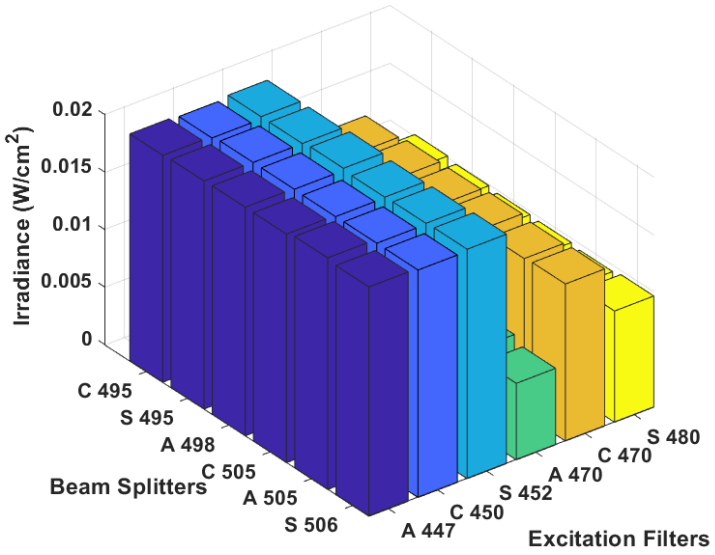

Figure 3.13 Values of average irradiance simulated on the detector placed on top of the objective lens in the optical setup.

The second set of simulations involved the investigation of the crosstalk light hitting the detector placed under the fluorescence filter. Specifically, simulations were run similarly to the previous experiments. In this case several fluorescence filters were also added to the simulation to measure the level of excitation light passing through the fluorescence filter thus allowing to estimate the best fluorescence filter for our application. In the best scenario the excitation light passing through the fluorescence filters should be close to zero. A total of five fluorescence filters were investigated. The substrates of investigation are produced by Semrock, Alluxa and Chroma and their transmission properties are showed in figure 3.14. Transmission properties were chosen by taking into consideration the emission spectra of FAD which is the man fluorophore responsible of green AF in human tissues.

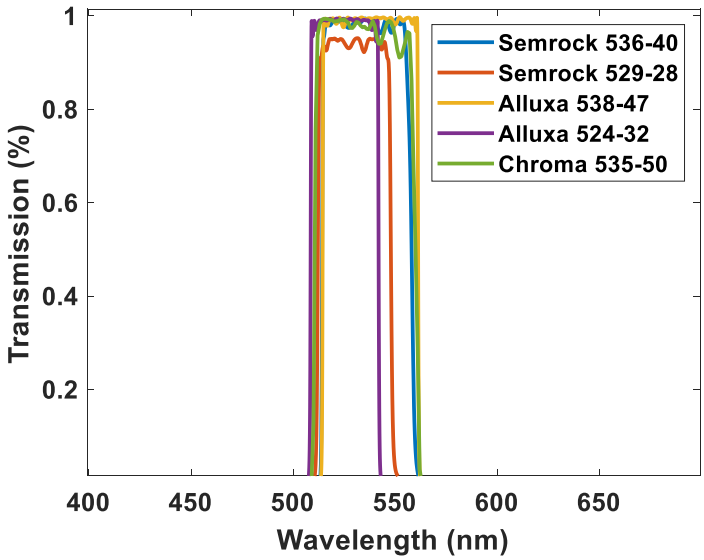

Figure 3.14 Transmission properties of fluorescence filters used in the simulations.

As it showed in figure 3.15, the level of light irradiance were one order of magnitude lower in Semrock and Chroma substrates with respect to the fluorescence filters manufactured by Alluxa. Both Chroma and Semrock were contacted to ask for quotes. The budget available for the filters was only 2000 £ and Semrock offered to provide the filters with the same dimensions of the simulations except for the thickness. The company reported that the manufacture process to make the substrates in that thicknes was around 20000 £. Therefore, the filters were bought by semrock with standard dimensions at 250 £ pounds each.

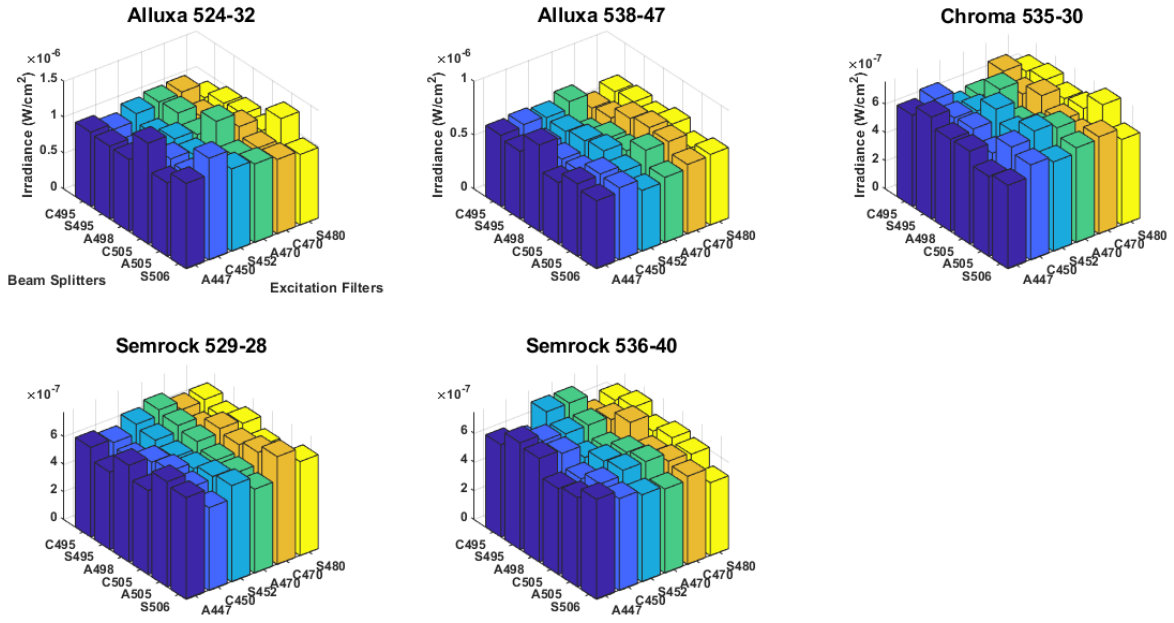

Figure 3.15 Values of average irradiance simulated on the detector placed under the fluorescence filter in the optical setup.

3.3 Post-processing of optical filters

3.3.1 Lapping and polishing process

Semrock was contacted to request filters with the optical properties highlighted on the website and custom-made dimensions for fitting the miniaturised unit. Semrock provided filters with the same width and length chosen in simulation. On the other hand, the requested thickness was too small for the company that asked for a large batch outside the research budget limit. Therefore, lapping, and polishing techniques were adopted to reduce the thickness of the filters and make them compatible with the designed slots. As previously mentioned, two types of excitation filters and two types of fluorescence filters were purchased. The filters were provided with a width of 2 mm, a length of 5 mm and a thickness of 2 mm. In the case of the beam splitter, the original thickness of the filter was 1.1 mm whereas the width and length were 2.5 mm and 5 mm, respectively. Lapping and polishing

processes were carried out by using a Logitech machine that pushes an abrasive slurry across the surface of the filter to remove material and uniformly reduce its thickness (Fig. 3.21). The goal was to reduce the thickness of excitation and fluorescence filters to 0.5 mm and the thickness of the dichroic beam splitter to 0.2 mm.

Filters were fixed to a support using vacuum. Support blocks of alumina loaded epoxy were used to protect the filters during the lapping process. The blocks were fabricated such that they had the same original thickness of the filters. The presence of the support blocks increased the surface area of the sample, reducing shear forces on the sample surface and promoting uniform removal of material (Fig. 3.22). A 3 µm Aluminium oxide powder was used in the process to remove material from the filters.

The lapping process carried out to thin the filters can be summarised as follows:

1) Measurement of the starting thickness of the filter.
2) Assessment of the coated side of the filter under the optical microscope.
3) Positioning of a glass substrate onto a hotplate atapproximately 75°.
4) Deposition of a temporary bonding agent (Quartz wax) onto the substrate (melting point ~70°).
5) Mounting of the filter and support blocks onto the wax to secure the filter onto the substrate.
6) Assembly assessment, as the coated side of the filter must be in contact with the glass plate surface to avoid the coating being lapped and removed.
7) Even distribution of the wax beneath the filter by gentle pressure.
8) Substrate removal from the hotplate and substrate secure placement under the pressure jig in order to apply consistent pressure to the filter and wax, as the wax cooled and adhered to the filter securely
9) Mounting of the glass substrate on the lapping jig via vacuum, after cooling of the wax and secure positioning of the filters (Fig. 3.22).
10) Spreading of an even layer of the 3 µm alumina abrasive onto the lapping plate
11) Placement of the lapping jig on the lapping plate to position the glass plate such that the abrasive slurry was pushed between the surface of the filter and the lapping plate, removing material from the filter.
12) Sample thickness measurement during lapping.
13) Stopping of the process when the desired quantity of material was removed.
14) Measurement of the thickness of the filter.
15) Cleaning of the filters with Isopropyl Alcohol in ultrasonic bath.

16) Polishing of the filters by using a polishing solution on a velvet plate (different from the plate used for lapping).

In the process the filters were lapped at a velocity of 25 rpm with a resulting removal rate of 0.8 µm/min. Table 3 shows the dimensions of the filters before and after lapping. Fig. 3.24 shows an excitation filter under the optical microscope before and after the lapping process.

Figure 3.16 Logitech machine. (1) Lapping plate wet with aluminium oxide powder solution to decrease the thickness of materials secured on the (2) glass plate through the (3) lapping jig.

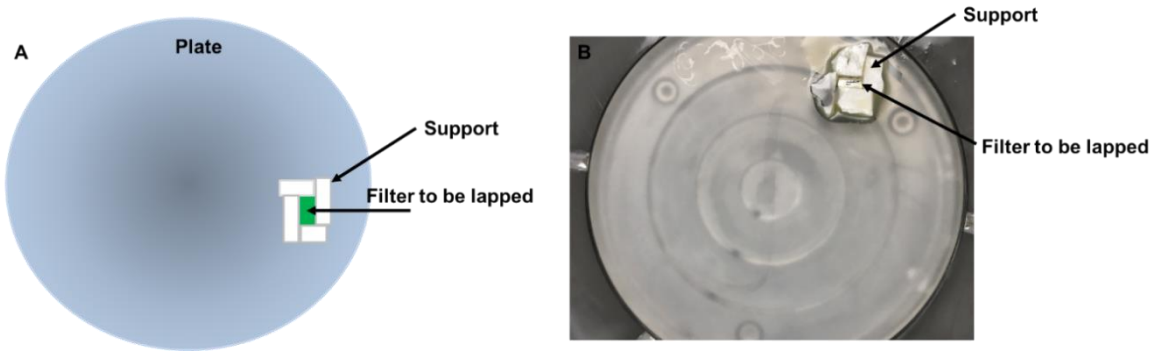

Figure 3.17 Filters secured through wax on the glass plate of the lapping jig along with epoxy supports. (a) *Schematic picture.* ***(b)*** *Real picture of the filter and support on the plate.*

Table 12 Filters dimensions before and after the lapping process

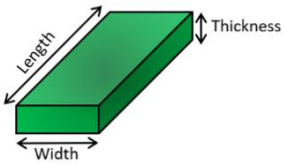

	Excitation Filter		Fluorescence Filter		Dichroic Beam Splitter	
	Before	**After**	**Before**	**After**	**Before**	**After**
Length (mm)	5	5	5	5	5	5
Thickness (mm)	2	0.5	2	0.5	1.1	0.2
Width (mm)	2	2	2	2	2.5	2.5

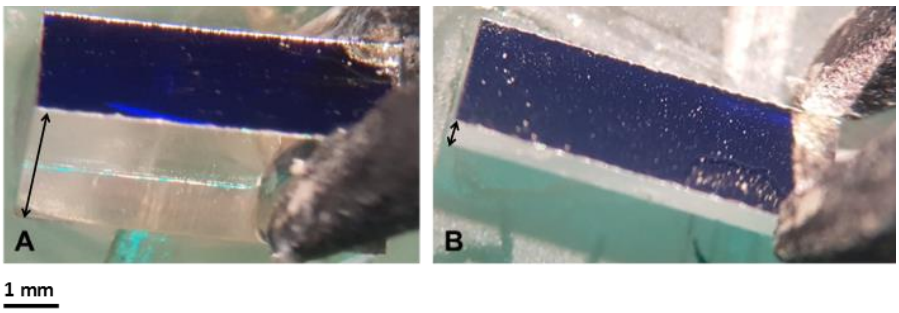

Figure 3.18 Optical microscopy image of the excitation filter. (a) *Before the lapping process.* ***(b)*** *After the lapping process.*

3.3.2 Optical characterisation of the filters

The optical transmission properties of the filters were measured before and after the lapping process by using a micro-spectrophotometer (Foster + Freeman ffTA/MS). Among the two excitation filters, the filter with an original broader bandwidth lost its transmission properties showing even a larger bandwidth after lapping (Fig. 3.24 (a)), suggesting possible damage to the coating during lapping. On the other hand, the transmission properties of the excitation filter with the narrower band were not affected (Fig. 3.24 (b)). The fabrication process did not alter the reflection and transmission properties of the dichroic beam splitter (Fig. 3.25). As in the case of the excitation filters, the original bandwidth of the fluorescence emission filter with centre wavelength of 536 nm changed after the lapping process showing a higher transmission in the 400 nm region (Fig. 3.26 (a)). On the contrary, the transmission properties of the fluorescence emission filter with narrower bandwidth and central

wavelength at 529 nm did not change after the lapping process (Fig. 3.26 (b)). Since Semrock did not disclose the coating-layers that were deposited on the substrates to achieve the desired transmission properties, it was not possible to give further information about the causes of the altered transmission bandwidths after lapping.

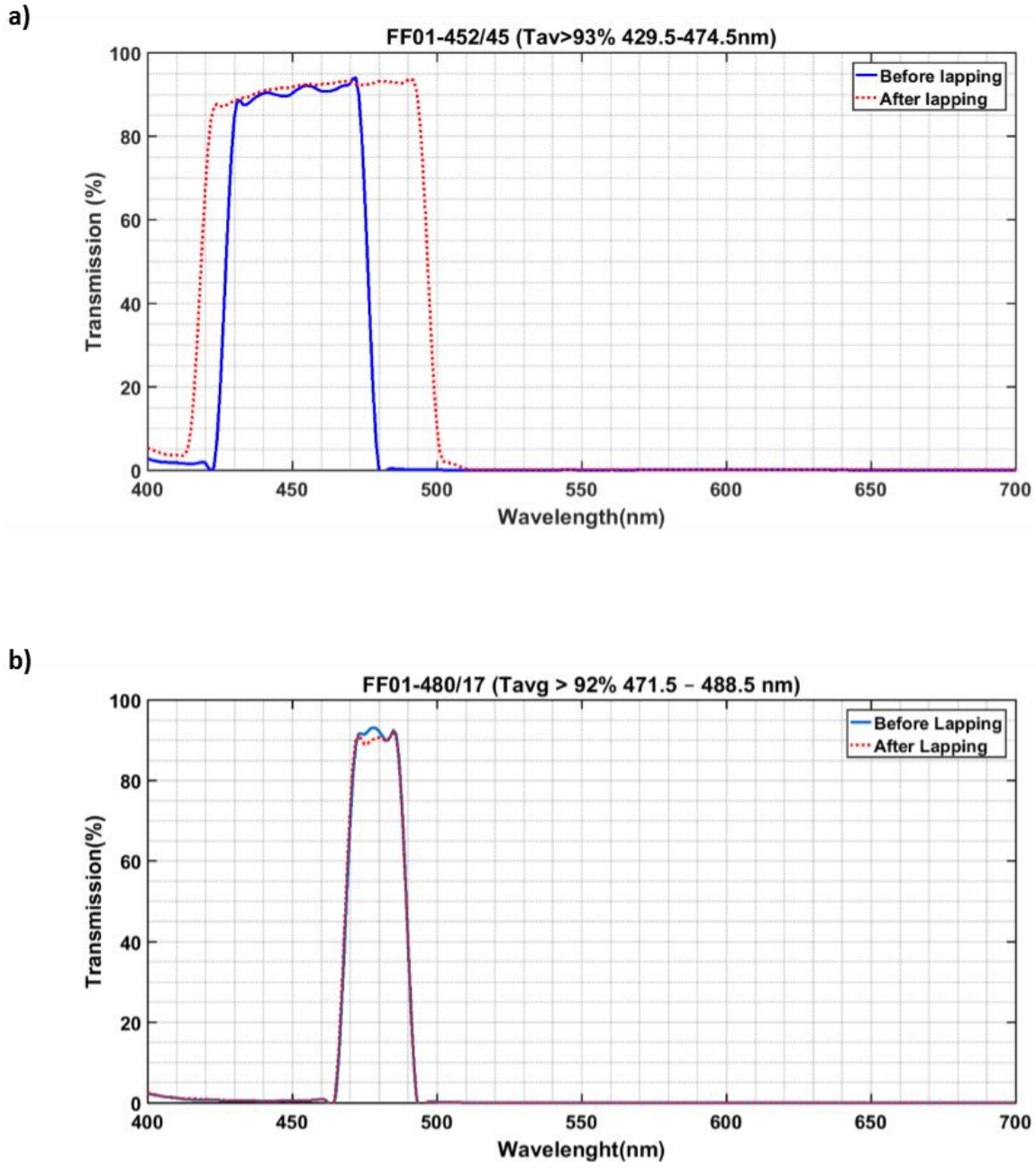

Figure 3.19 Transmission properties of excitation filters before and after lapping. (a) *FF01 452-45.* ***(b)*** *FF01 480-17.*

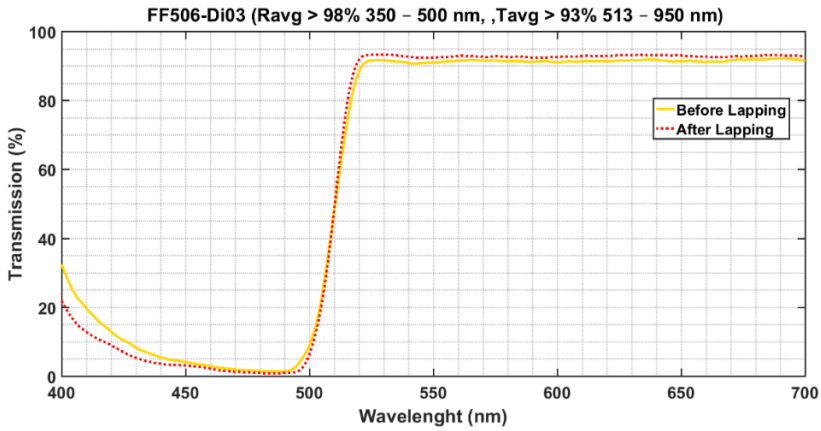

Figure 3.20 Dichroic beam splitter transmission properties before and after lapping.

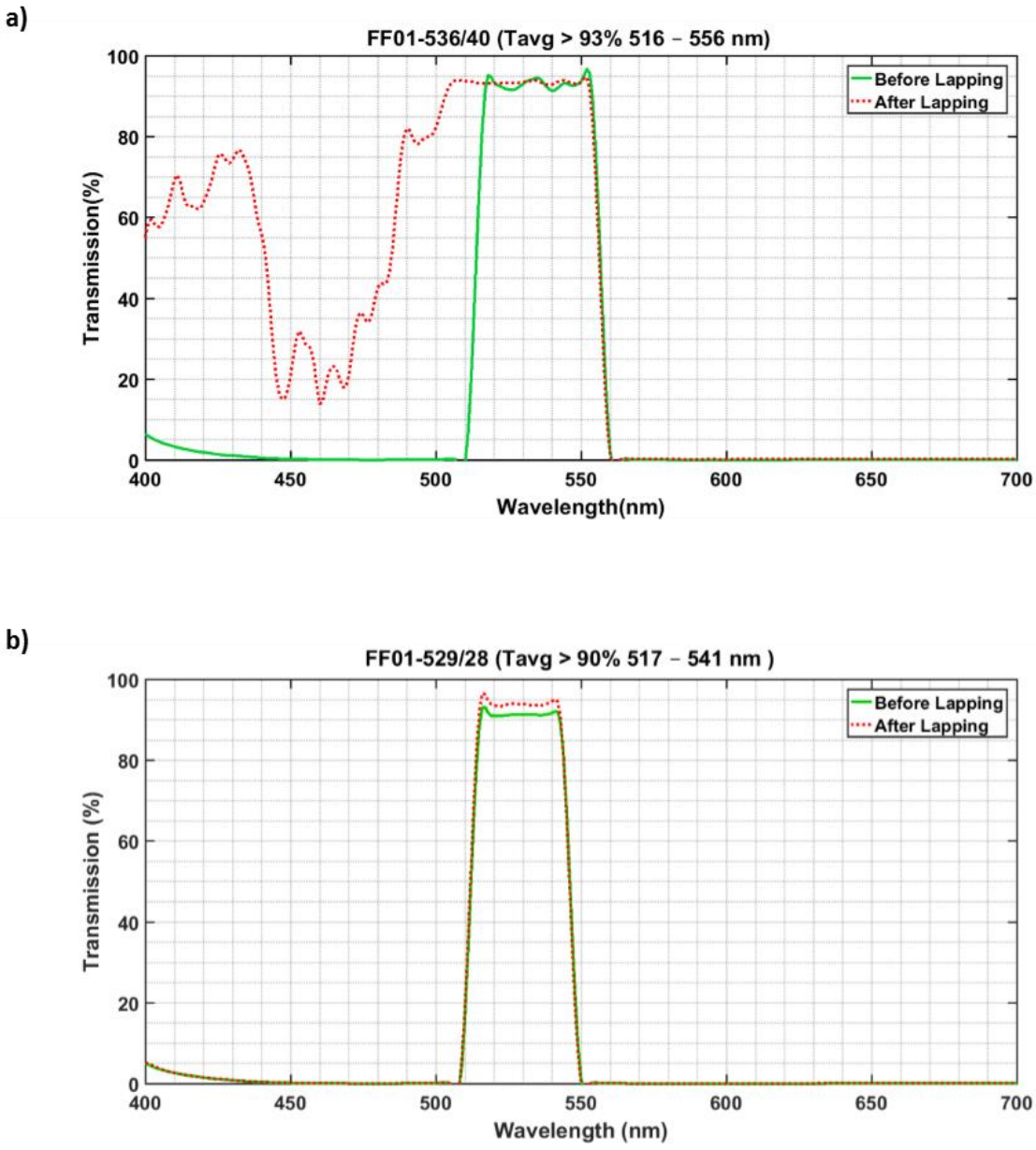

Figure 3.21 Transmission properties of fluorescence emission filters before and after lapping. (a) *FF01 536-40.* ***(b)*** *FF01 529-28.*

3.4 CAD design of miniaturised unit for the optical components

The body that held the optical components in place was designed in Solidworks. The 3D optical components were imported from Zemax to Solidworks to maintain the dimensions exact and consistent. Fig. 3.17 shows different views of the unit that measured 6 mm x 5 mm x 6 mm (Fig. 3.17 (a)). A square of 2.5 mm x 2.5 mm was designed on the front face of the block (Fig. 3.17 (b)). The square was extruded by 1.45 mm to create the space for accommodating the LED package (Fig. 3.17 (b)). The next step involved the creation of a counterbore [1] for inserting the collimation lens. The counterbore was designed with an external diameter of 2.1 mm, an internal diameter of 1.9 mm and a depth of 1 mm (Fig. 3.17 (b)). The dimensions were chosen to keep the lens with a diameter of 2 mm and a thickness of 0.8 mm in place. The slots for the filters were extruded along the whole width of the body, measuring 5 mm to allow easy insertion and removal of the filters (Fig. 3.17 (d)). The slots for the filters were designed with 0.1 mm tolerance. In fact, both slots for excitation and fluorescence filters measured 0.6 mm and 2.1 mm to accommodate filters with a thickness of 0.5 mm and a width of 2 mm. The same choice was made for the beam splitter slot which measured 0.3 mm x 2.60 mm for accommodating a filter with thickness of 0.2 mm and width of 2.5 mm. Another counterbore for accommodating the objective lens was created on top of the slot for the beam splitter (Fig. (3.17 (e)). Finally, a cylindrical opening with diameter of 1.9 mm matching the inner diameter of the counterbore was extended along the whole height of block passing through the slot for the fluorescence filter. The opening was designed to allow any fluorescence light imaged by the objective lens to pass through the fluorescence filter and hit the area of any imager sensor coupled with the block (Fig. 3.18 (e)).

3.5 Fabrication of the miniaturised block

The block was fabricated by wire erosion at the spark erosion centre in Glasgow. The technique was chosen because the features in the units were very difficult and complex to machine. In a wire erosion processes, specific shapes are created out of a workpiece by using electrical discharges or more literally sparks. A wire is fed through a metal workpiece that is usually immersed in a dielectric fluid. The wire is held between two guides which move in x and y direction. The application of a voltage between the wire and workpiece allows the generation of the sparks and hence the removal of material from the workpiece (Fig. 3.18). The final unit was fabricated out of aluminium. After fabrication, the final piece was

[1] A cylindrical flat-bottomed hole that enlarges another coaxial hole

anodised and painted black to prevent any reflection within the optical path. Fig. 3.19 shows the miniaturised holder after deionisation and black paint coating. The slots for the filters where imaged with an optical microscope to assess the precision of the fabrication process. Fig. 3.20 shows that all of the feature sizes were between 50 µm and 60 µm larger than the designed values.

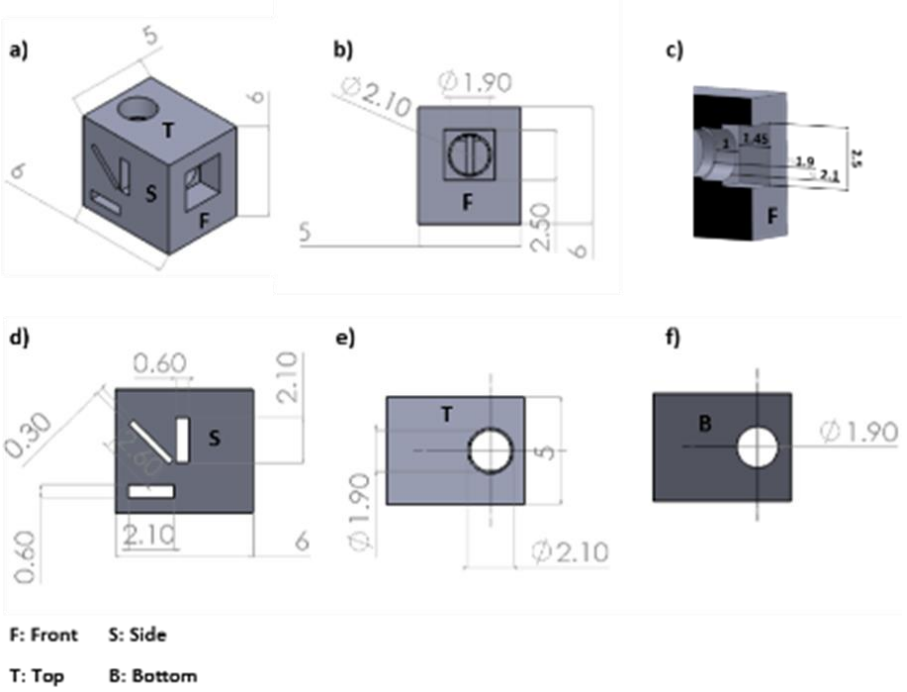

Figure 3.22 Figure 3.22 Technical drawing of the unit designed to accommodate the optical components. ***(a)*** *3D view of the block.* ***(b)*** *Front view of the block.* ***(c)*** *3D section of the block highlighting the square-opening for the LED and the counterbore for accommodating the collimation lens.* ***(d)*** *Side view of the block showing the slots for the filters* ***(e)*** *Top view of the block showing the counterbore for accommodating the objective lens* ***(f)*** *Bottom view of the block showing the exit pupil. All data are in millimetres.*

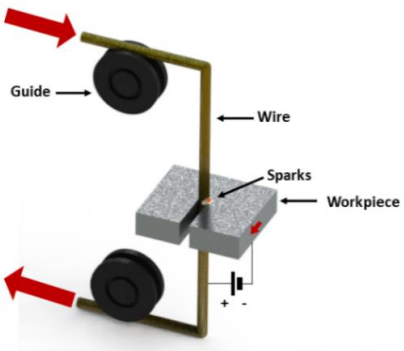

Figure 3.23 Schematic model of wire erosion technique.

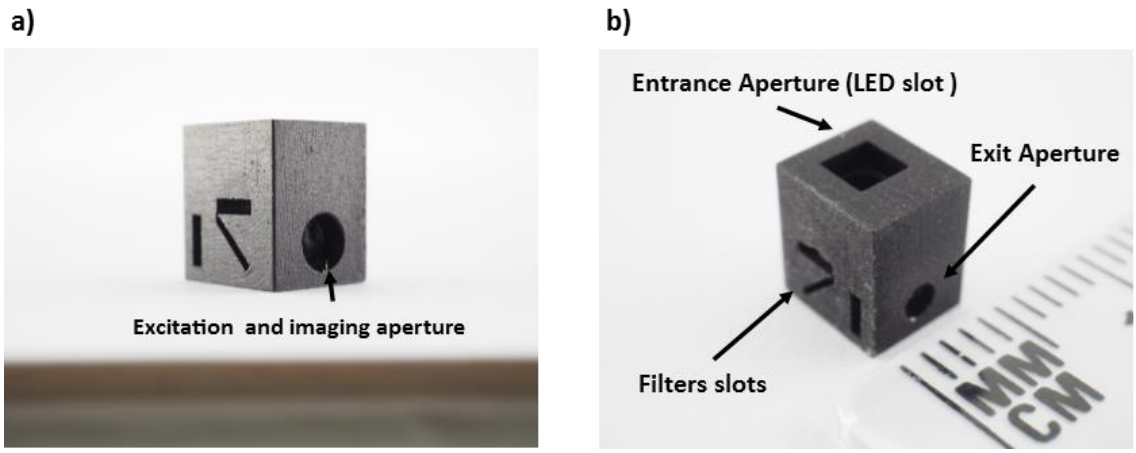

Figure 3.24 Fabricated unit. *(**a**) Objective lens counterbore and filter slots. (**b**) LED slot, exit pupil and filter slots.*

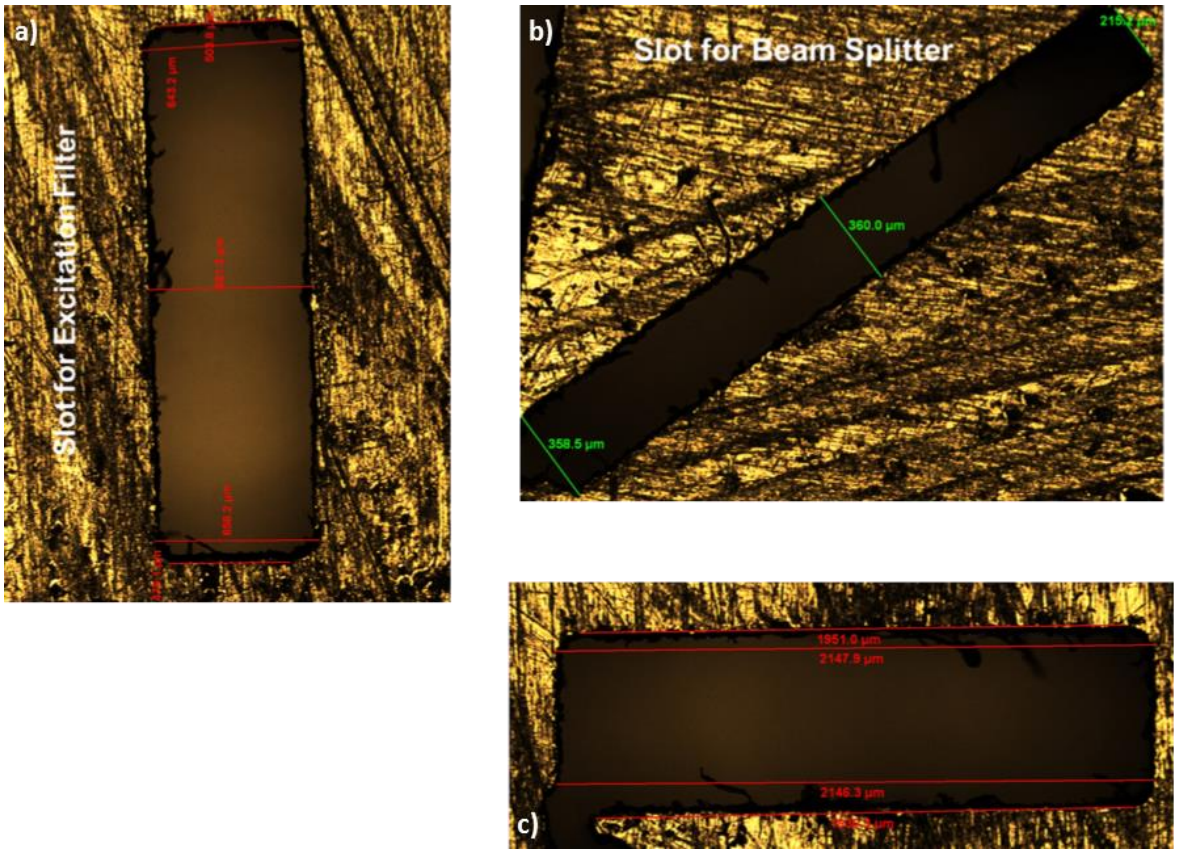

Figure 3.25 Optical microscopy image of the wire-eroded slots. ***(a)*** *Excitation filter slot.* ***(b)*** *Fluorescence filter slot.* ***(c)*** *Beam splitter filters slot.*

3.6 Assembly of the optical components within the miniaturised unit

The filters that did not show any change in transmission properties after post-processing were integrated within the miniaturised unit. Filters and lenses were manually inserted within the designated slots under the optical microscope by using tweezers with carbon-fibre tips to avoid scratching or damaging (Fig. 3.27). The LED package was inserted inside the designed aperture. The body of the lamp was initially secured to the unit by using blue-tack and successively glued by using cyanoacrylate-based glue (Fig. 3.27 (d)).

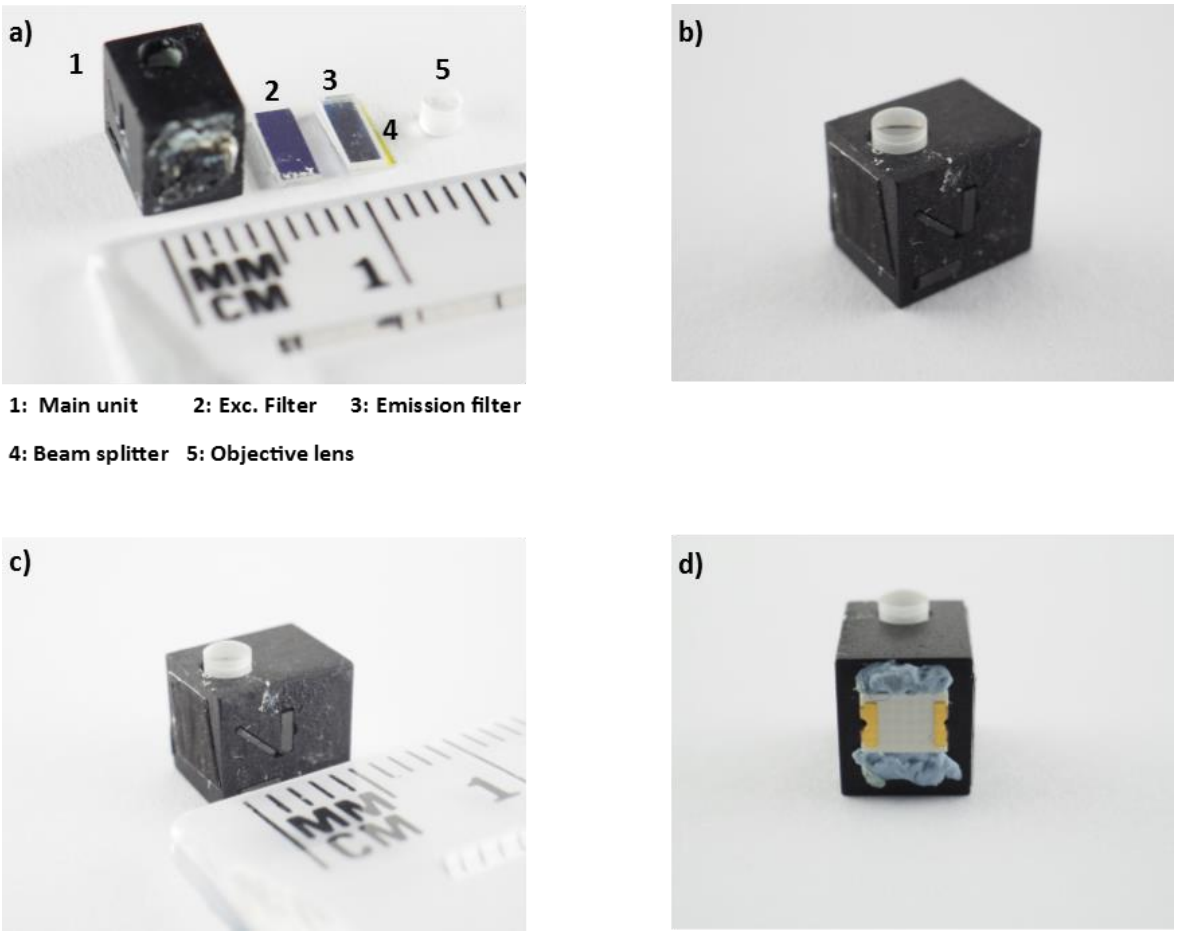

Figure 3.26 Miniaturised unit coupled with the optical components. (a) Real optical components outside unit. *(**b**) Final assembled device (**c**) Final assembled device placed next to a ruler to show real dimensions (**d**) Front view of the device showing the sub-miniature PCB-lamp integrated within the unit.*

3.7 Summary

The aim of this chapter was to describe the software and techniques that were employed to design, fabricate and assemble the miniaturised optical unit. The optical design of the device was performed in Zemax Optics Studio. The light source that was purchased for integration in the device was simulated. The results from the simulations were compared with knife-edge measurements performed on the actual device. The CAD design and the fabrication processes used to create the unit for holding the optical components were also addressed. Post-processing techniques performed on the off-the-shelf optical filters purchased for the optical setup were explained, and their effects on the optical properties of the filters were discussed. Finally, the assembly of the device was briefly described and the final unit equipped with the optical components was shown.

4 Integration and characterization of the optical unit

As discussed in the previous chapter, the miniaturised optical unit operated in two different modalities defined as excitation and fluorescence modes. In excitation mode, the beam from the LED was collimated, filtered and then reflected by the beam splitter through the objective lens to excite the sample. In fluorescence mode, fluorescence light emitted by the sample was imaged by the objective lens through the fluorescence filter on the detector. Although, the two modalities were synchronous and mutually dependent, two different strategies were employed for characterizing the optical module in excitation and fluorescence modes.

4.1 Excitation mode

The shape and size of the excitation beam incident was characterized by knife-edge measurements (Fig. 4.1 (a)). The protocol for these measurements was discussed in detail in section 3.2.2. As in the case of the excitation source, the shape of the beam was also studied in Zemax by placing a detector on top of the optical unit at a distance equal to the focal length of the optical system, in order to compare the experimental data with simulated results (Fig. 4.1 (b)).

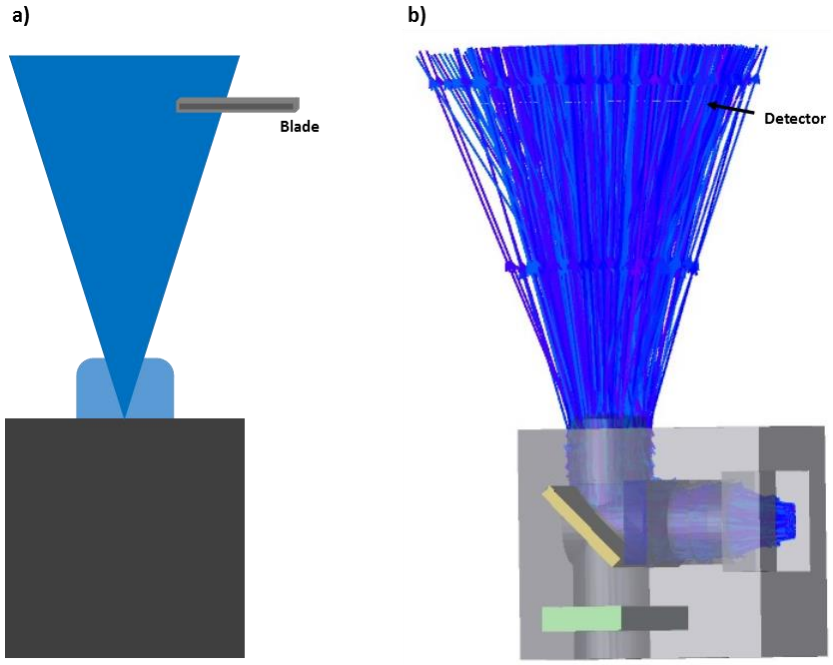

Figure 4.1 Characterisation of the excitation beam. *(**a**) A blade was placed on top of the optical unit and knife-edge measurements were performed on the excitation beam. (**b**) The miniaturised unit for holding the optical components was simulated and a detector was placed on top of the unit to study the shape and size of beam.*

Gaussian beam profiles in x and y directions were extracted from knife-edge measurements by appling equation 2.2 to the data. The profiles were then compared to those obtained from the simulations (Fig. 2.2). The results showed a strong correlation (> 95%) between the simulated and the experimental results. In fact, the waist of the simulated beam was approximately 1.09 mm in both x and y directions against the 1.13 mm obtained from the experiments.

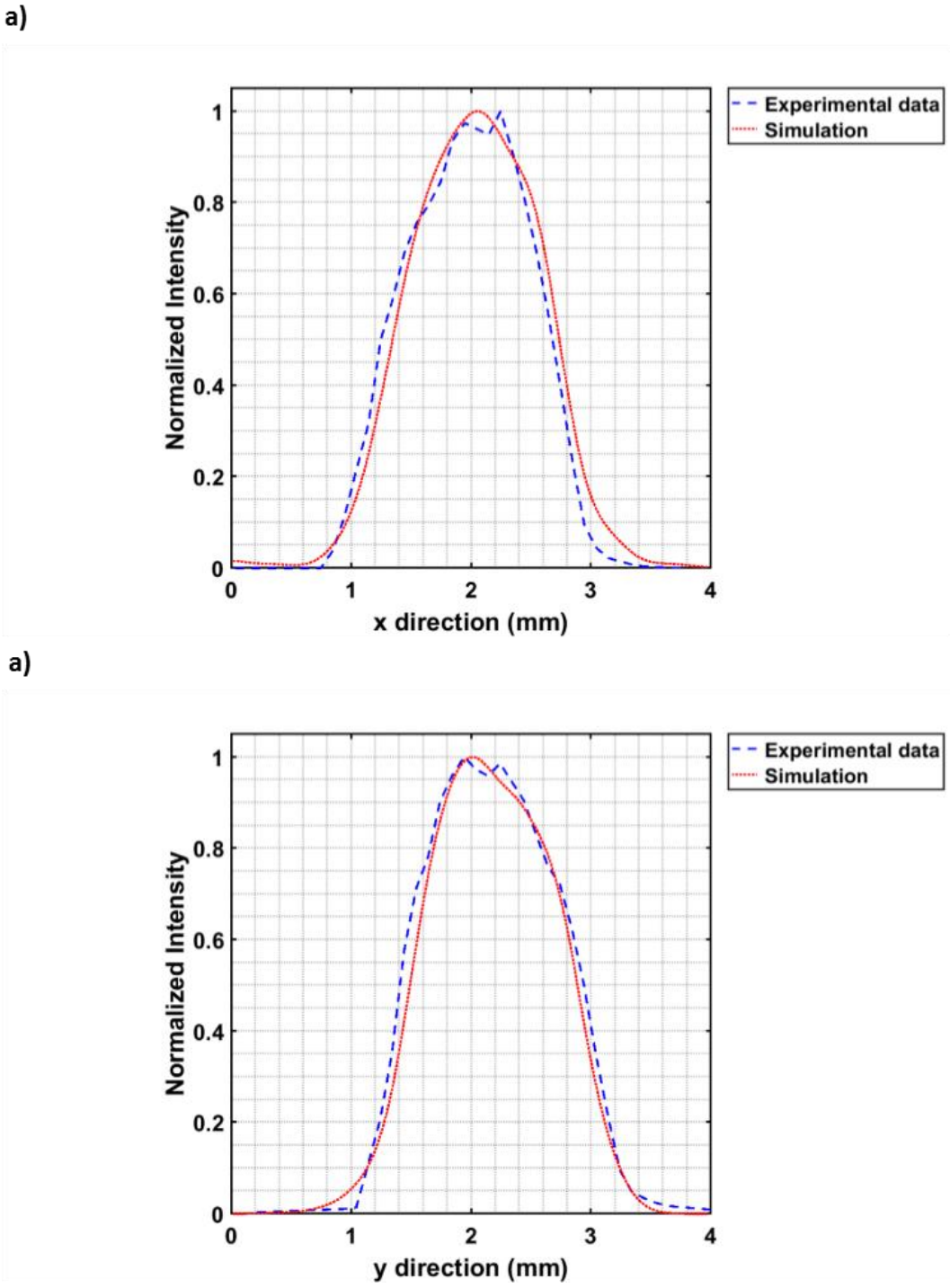

Figure 4.2 Gaussian beam profiles in (a) x and (b) y directions obtained from knife-edge measurements and Zemax simulation.

4.2 Fluorescence mode

4.2.1 CMOS 64 x 64 SPAD array

The characterization in fluorescence mode was performed by coupling and integrating the optical unit with a 64 x 64 pixels SPAD array designed by another PhD candidate in the microsystem and technology (MST) group at University of Glasgow [129]. The array had a pixel pitch of 61.5 µm in both horizontal and vertical directions and a fill factor of 3.5%. The imager was designed with a global shutter architecture and operated with a power supply of 1.8 V (VDD) and a ground supply of 0 V (GND). The chip was coupled to a CPGA 208 socket and integrated on a custom-made PCB board which interfaced a F334R8 microcontroller (Mbed). The microcontroller was connected to a laptop via a USB cable and was programmed to provide the inputs and read the outputs of the chip (Fig. 4.3). A Matlab graphical user interface (GUI) was also developed to acquire data and reconstruct the image through the Mbed. The interface allowed to select several sample intervals, also defined as integration times or gate times. Another feature of the graphic user interface was the capability of creating software masks and subtracting them from the data of interest in order to remove noise sources that could be misguiding in the measurements. The maximum frame rate was limited to 3 fps because of the USB serial protocol used to transfer data between the chip and the laptop.

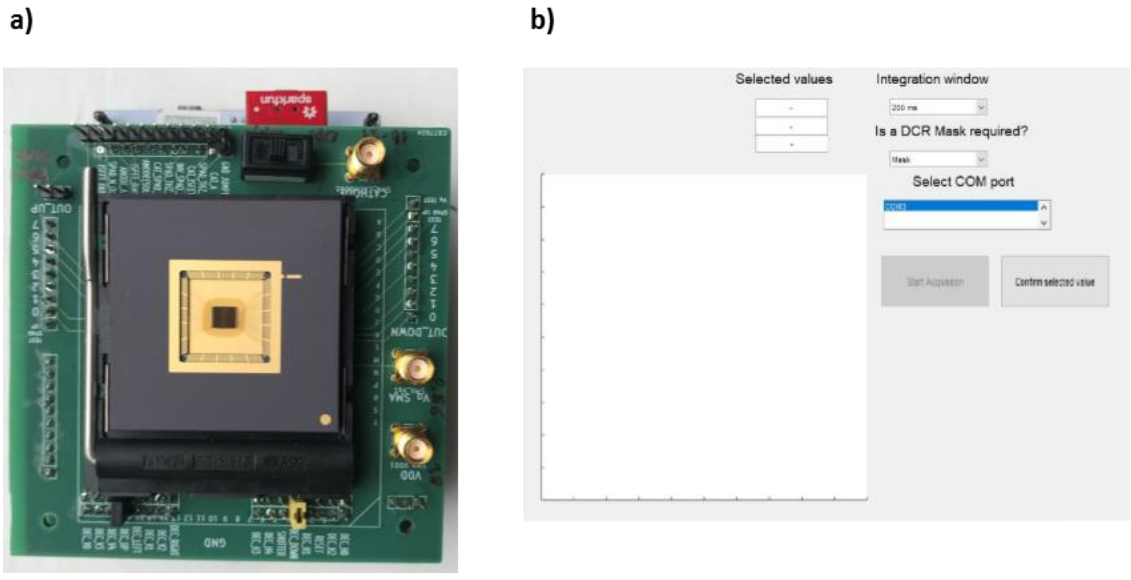

Figure 4.3 64 x 64 CMOS SPAD array. (a) *Imager chip mounted on the PCB and Mbed board.* ***(b)*** *GUI interface for data acquisition. The interface was designed to select the integration window, the port that was connected to the imager and also to allow the user to load a DCR mask previously created. When loaded, the mask was subtracted in real time from the images during data acquisition.*

4.2.2 Integration of the optical unit on the chip

The SPAD chip was mounted on to the side of the optical block using a black-nylon disk. The disc was designed in Soidworks and 3D printed with a diameter of 40 mm and a thickness of 0.2 mm in order to sit on the 1849 mm^2 chip carrier (Figs 4.4(a) and (b)). A square aperture with sides of 2 mm was also designed in the centre of the disc to match the exit pupil of the optical unit (Figs 4.4 (c) and (d)). Two wings were realized around the aperture at a distance of 5.5 mm from each other to accommodate and hold the optical unit firm in position. Two small copper-clad boards were also glued onto the wings of the spacer to facilitate soldering of the LED's anode and a cathode wires. Black nylon was chosen as the printing material in order to avoid any stray fluorescence light from hitting the active area of the imager. The whole imager assembly was then attached to an optical breadboard. Moreover, three transitional optical stages (Thorlabs, MTS50/M-Z8) were also secured on the breadboard in order to position and manipulate objects to be imaged with respect to the fluorescence imaging unit (Fig. 4.5 (a) and (b)). Several object holder arms were also 3D printed depending on the size of the samples to be imaged.

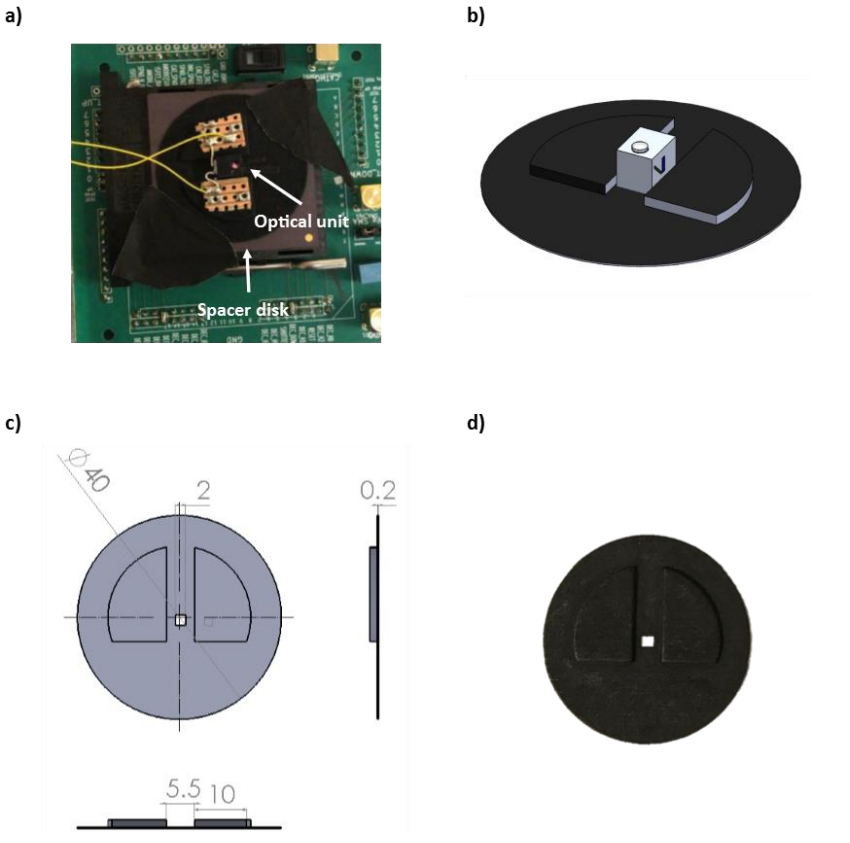

Figure 4.4 Spacer disk for integration of the optical unit on the SPAD array chip. (a) *Optical unit assembled on the SPAD chip through the disk.* ***(b)*** *3D assembly model of the optical block sitting on the disk.* ***(c)*** *Technical drawing showing disk's dimensions in millimetres.* ***(d)*** *3D printed spacer-disk.*

a)

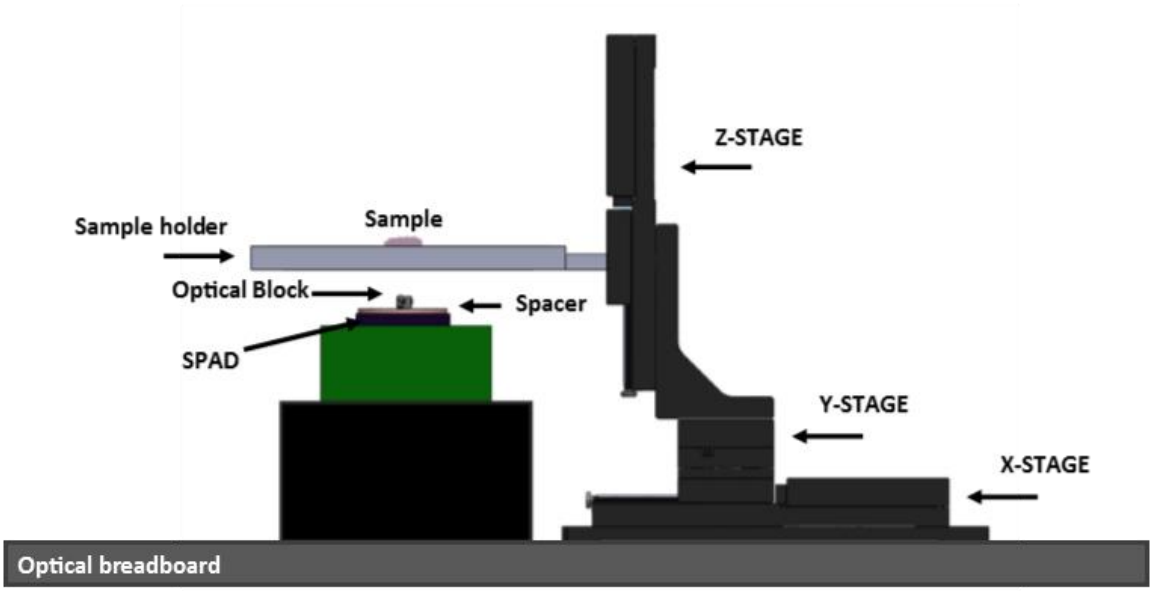

b)

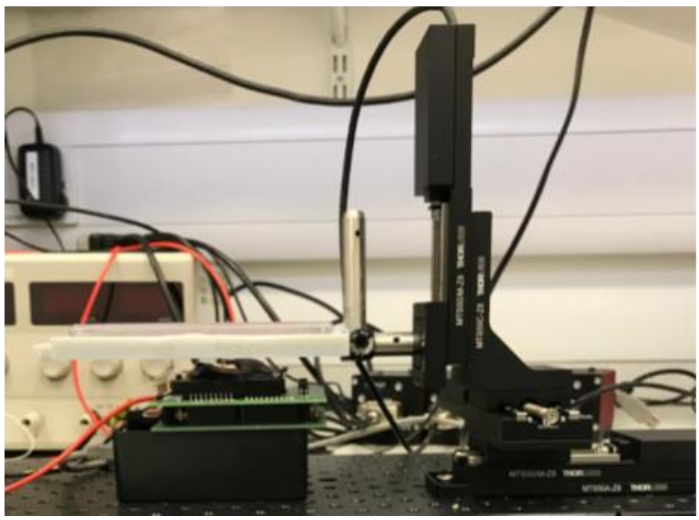

Figure 4.5 Experimental setup for the measurements. (a) *3D model of the setup.* ***(b)*** *Measurements setup in the laboratory.*

4.2.3 Software mask

As previously mentioned, the exit pupil of the optical block was 1.9 mm in diameter, whereas the SPAD imaging array was 3.9 mm x 3.9 mm. Therefore, after the integration of the optical unit on the imager, a mask was created to exclude the pixels in the outer region of the array. The experimental procedure for determining the diameter of the system's circular field of view was performed by placing a petri dish containing a high concentrated FTCI solution (100 µM) on top of the imaging unit, at the focal length of the system (6 mm) (Fig. 4.6 (a)). The field of view of the system was determined by imaging the fluorescence. A Matlab

algorithm was written to create a software mask to use in all the experiments. The algorithm set all the pixels outside the field of view to zero and created a circle around the region with high fluorescence signal. The diameter of this circular region was 2.1 mm which covered exactly 37 pixels. Finally, all the pixels within the circle were set to one to create the software mask (Fig. 4.6 (c)). Since images are treated as matrices of numbers in Matlab, all obtained imaging data in the following experiments were multiplied by the software mask to account only for the pixels within the field of view.

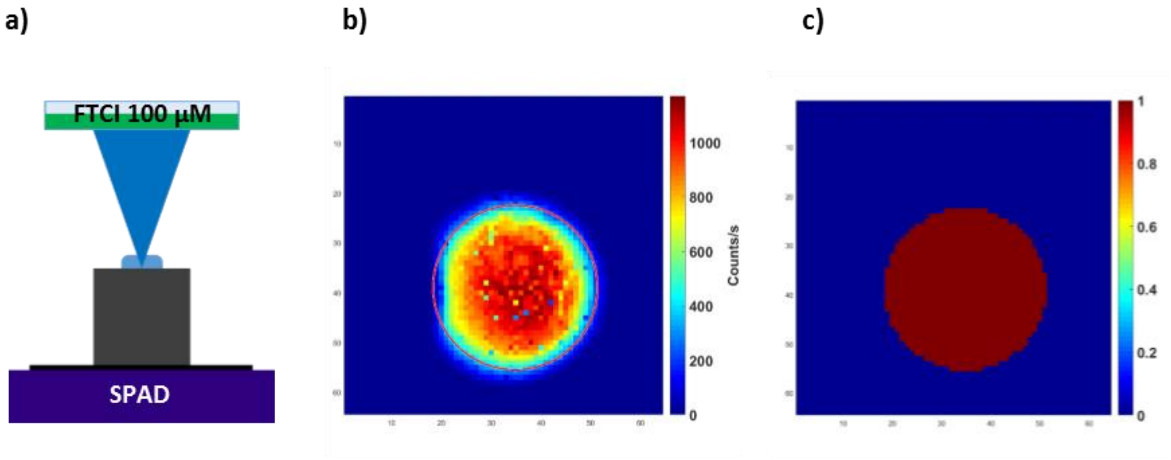

Figure 4.6 Software Mask. ***(a)*** *A 100 µM FCTI solution placed on top of the imaging system* ***(b)*** *Signal from the solution delineated the field of view.* ***(c)*** *Created software mask by setting all pixels within the field of view to one and the pixels outside the circle to zero.*

4.2.4 DCR and LED-crosstalk measurements

Before imaging any sample, the optical setup was placed in a closed dark space to evaluate the effect of the noise sources. As stated in section 2.5.4, the DCR is the number of events a SPAD reads in the absence of light arising from thermal excitation and band-to-band tunnelling. In the imaging system, another component of noise was the cross-talk as a consequence of the small amount of excitation light coming from the LED that is scattered on to the SPAD. The DCR was measured at fourteen different integration times by acquiring the same number of frames for each integration time with the LED turned off. The integration time is defined in ms and indicates the time window used by the digital counter in the circuit to count the pulses generated in the detector during photons arrivals. Specifically, ten frames were acquired for each integration time. A Matlab code was written to create an average DCR frame by averaging the ten frames. The algorithm also computed the average value of all the pixels in the frame to determine the DCR at each integration time. The standard deviation between the values of all pixels was also computed. The procedure was performed only for the pixels within the field of view of the system by applying the software mask. The

same process was repeated with the LED turned on to evaluate the noise introduced by the LED into the system. As it is shown in Fig. 4.7, the average DCR of the system increased with the increase of the gate time. Specifically, at low gate times the noise introduced by the LED is similar in unit to the DCR. However, as the integration time increases the crosstalk noise from the LED increases. This means that for signal with high fluorescence intensity short integration times must be used to prevent saturation of the counter. On the other hand, in the case of weak fluorescence signal, longer integration time windows must be chosen.

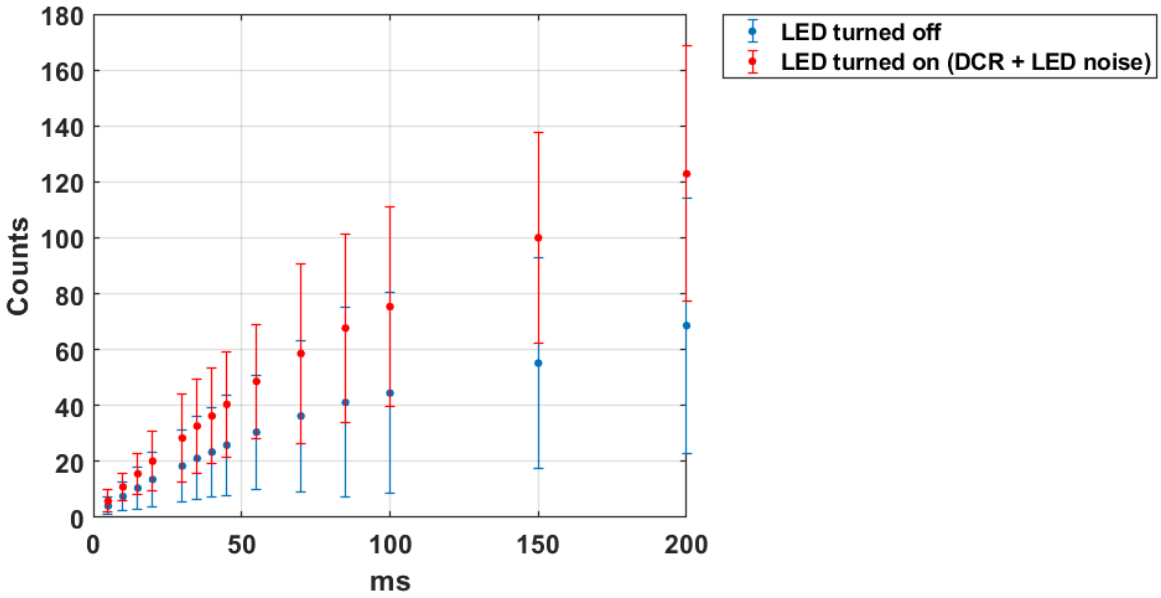

Figure 4.7 Noise sources in the imaging system.

4.2.5 FAD phantom solutions

As discussed in section 2.4, FAD is an endogenous fluorophore expressed in human tissues that plays an important role in carcinogenesis. In fact, the oxidation of FAD to $FADH_2$ in cancerogenic environment is one of the factors responsible for the decrease in the fluorescence signal from cancerous tissues. Measurements were carried out to determine the minimum concentration of fluorophore in solution which can be detected by the system. The protocol for the experiments involved the dissolution of FAD salt hydrate (molecular mass 829.5 g/mol, purity> 95%, Sigma Aldrich) in Phosphate Buffer Saline (PBS) to obtain six separate solutions at concentrations of 250 µM, 125 µM, 60 µM, 30 µM, 15 µM, and 7.5 µM respectively. For this purpose, a 7.6 cm x 7.6 cm positive fluorescent, 1951 USAF target mask (57-894, Edmund Optics) was used. The mask consisted of a layer of chrome into which transparent features were etched (Fig. 4.8(a)). A specific holder-stage was 3D printed for accommodating the target (Fig. 4.8(b)). The holder-stage was fixed to the Z motorized stage so that the target was placed on top of the imaging system. Using a 625 µm x 625 µm

feature in an USAF to form a regular mask (Fig. 4.8(c), the imaging system was tested to measure the fluorescence signal as a function of fluorophore's concentration. 10 µL of solution were pipetted on to the 625 µm x 625 µm region of interest on the USAF mask (Fig. 4.8 (d)). The chrome coated surface reflected the incident radiation while the fluorescence signal from the solution in the etched feature was imaged by the optical unit and the SPAD. The process was repeated three times for all the six separate solutions with different concentrations. The average of all the pixels within the fluorescence feature was computed for each concentration. Experiments were replicated three times per concentration. The average software mask constructed considering the LED noise, as previously, described in section 4.2.3, was subtracted from the images to account only for the fluorescence signal emitted by the phantom solutions. As clearly illustrated in Fig. 4.9, data were reliably calculated indicating that the smallest measurable concentration was as low as 7.5µM. The data obtained was also fitted to the exponential model with a resulting R^2 higher than 99% in the concentration region of the experiments. However, it is expected that the average fluorescence intensity in pixel saturates at higher concentrations of the fluorophore. Since the main aim of at this experiment was to assess the sensitivity of the imaging system for this specific fluorophore, a higher number of data points was acquired at lower concentrations.

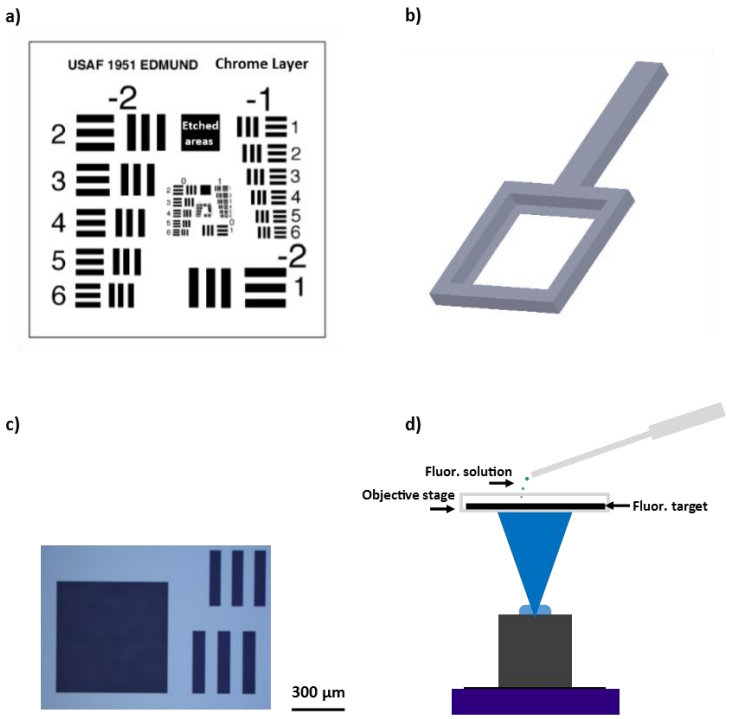

Figure 4.8 Setup for fluorescence phantom solutions experiments. (a) *USAF 1951 target with features etched on the chrome layer* ***(b)*** *3D-printed holder-stage to accommodate the*

target ***(c)*** *Microscopy image of the feature used to image the fluorescence solutions* ***(d)*** *Schematic drawing of the experimental procedure.*

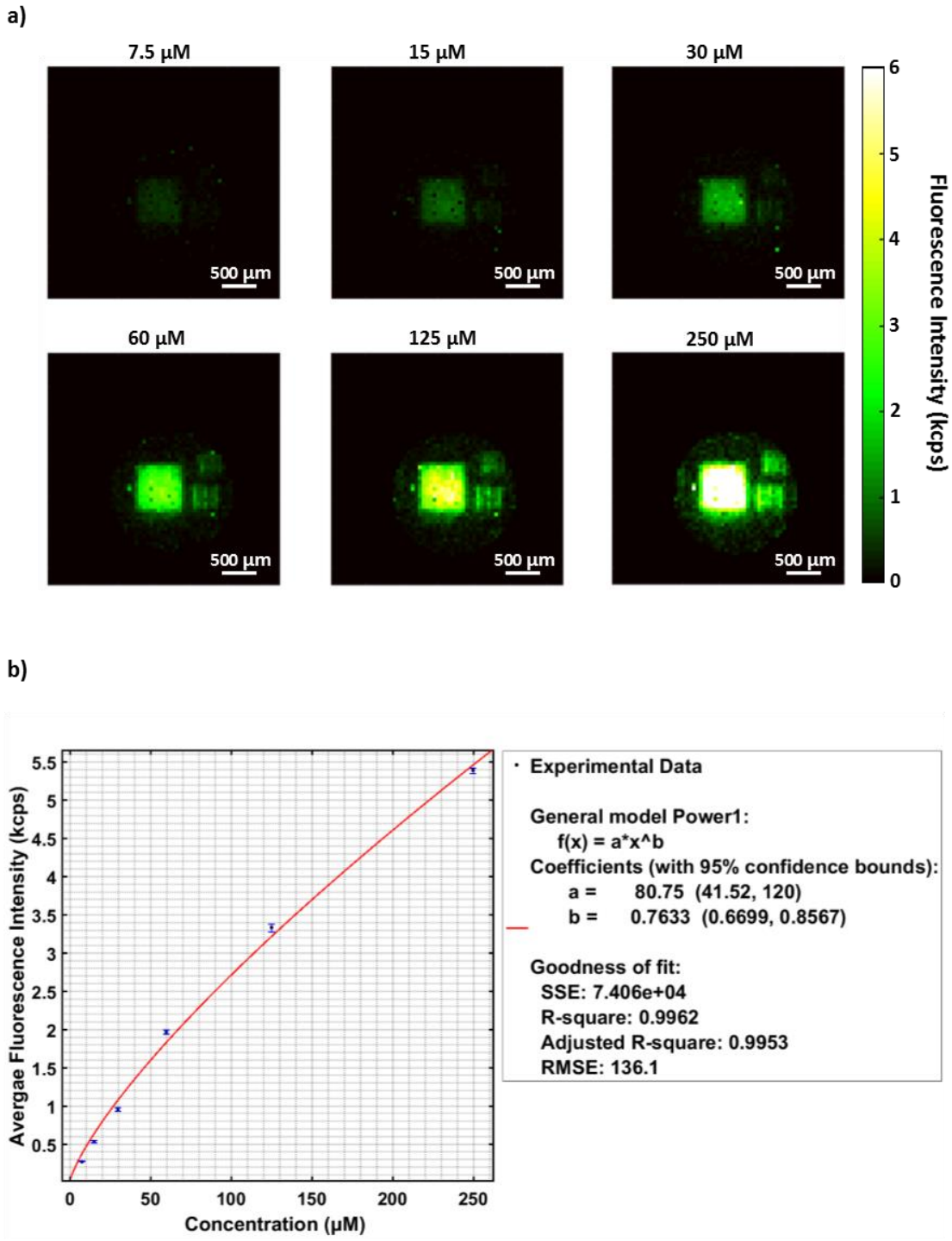

Figure 4.9 Response of the optical system to FAD at six different concentrations. *(**a**) Images of FAD solutions masked by the feature of the USAF target at concentrations of 7.5 µM, 15 µM, 30 µM, 60 µM, 125 µM, 250 µM. (**b**) Average fluorescence intensity of the pixels within the square feature for each concentration was computed to assess the optical sensitivity of the system as a function of concentration. The data shows the mean of independent experiments (n = 3) and the error bars show the standard deviation (SDT).*

Experimental data was fitted to the exponential model $f(x) = a^x + b$ *with an* R^2 *> than 99 %.*

4.2.6 FTCI phantom solutions

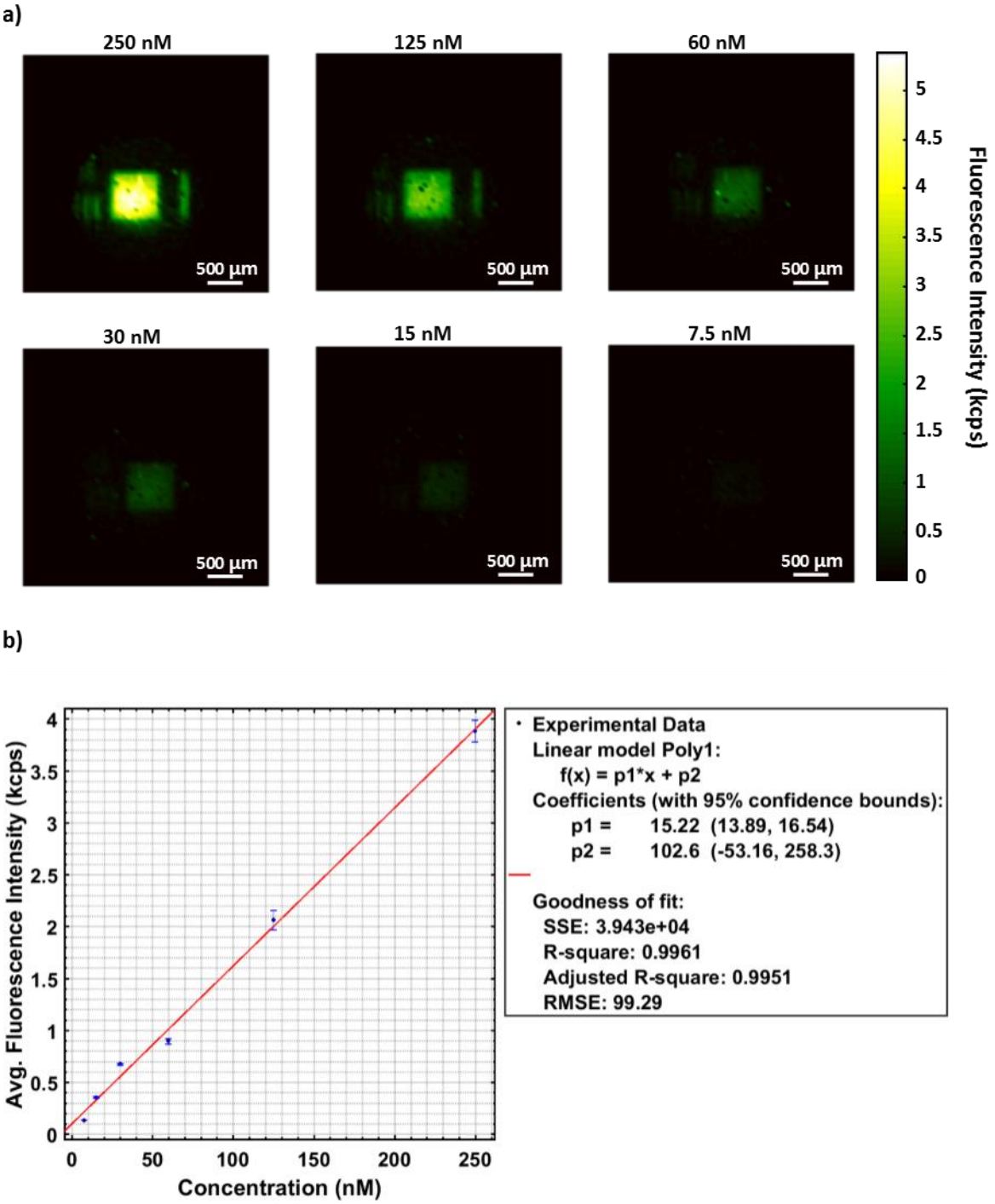

Figure 4.10 Response of the optical system to FTCI at six different concentrations*.* ***(a)*** *Images of FAD solutions masked by the feature of the USAF target at concentrations of 7.5 nM, 15 nM, 30 nM, 60 nM, 125 nM, 250 nM.* ***(b)*** *Average fluorescence intensity of the pixels within the square feature for each concentration was computed to assess the optical sensitivity of the system as a function of concentration. The data shows the mean of*

independent experiments (n = 3) and the error bars show the standard deviation (SDT). Experimental data were fitted to the exponential model f(x) = ax+b with an R2 > than 99 %.

The same experimental procedure was repeated by using FTCI to compare the performance of the two fluorophores. In contrast to FAD, FTCI is an exogenous fluorophore usually introduced as fluorescence agent to increase the contrast of specific lesions with respect to the autofluorescence background from tissues. As shown in Fig. 4.10, the experiments were performed in the nanomolar region because FTCI has a quantum yield of 0.79 in contrast to FAD that has a quantum yield of 0.025. The minimum detectable concentration was 7.5 nM. In this case, the results were displayed using a Matlab script that varied the colour in each line segment of the image matrix by interpolating the values across the line in order to obtain the images with higher resolution. In fact, in contract to the FAD images, each individual pixel in the images was indistinguishable from its neighbour pixels. This post-processing choice was made to show that higher quality images can be achieved also by using a low-resolution system. Moreover, the average value of all the pixels within the fluorescence square-feature did not increase exponentially with increasing FTCI concentration and rather was fitted to a linear model with a resulting R^2 higher than 99%. Linear behaviour can be due to fact that in this particular case the investigation was done in the nanomolar range. An exponential behaviour might appear at higher concentrations. The FDA approved 500 mg of FTCI at concentration of 300mM as the safe dosage in adults. However, side effects span from nausea to bronchospasm and cardiac arrest. The potential use of the imaging system in capsule endoscopy would require a lower dosage of the dye and hence a higher safety for patients.

4.3 Summary

The aim of this chapter was to describe the characterization of the imaging system in excitation and fluorescence mode. The excitation beam was characterized through knife-edge measurements to determine the shape of the excitation beam and the results were compared to Zemax simulations. The detection of weak fluorescence signals from within the body in autofluorescence imaging is the main drawback of this technique. Therefore, the characterization of the module in fluorescence mode was performed by evaluating the minimum fluorescence signal detectable by the system. For this purpose, fluorescence phantoms solutions were prepared by using FAD and FCTI fluorophores to mimic endogenous fluorescence from the human body and exogenous fluorescence induced by external agents. Results showed that the system could reliably detect FAD in the micromolar

range and FTCI in the nanomolar range. The findings were expected as FTCI has a quantum yield one order of magnitude higher than FAD.

5 In vitro experiments

Accuracy in assessing tumour lesions is critical to cancer diagnosis and treatment [130]. A precise early detection of cancer can be achieved by targeting specific cells or molecules that are overexpressed and metabolized in tissues undergoing carcinogenesis. This approach of targeting specific cells aims at inducing a fluorescence signal in cancerous lesions [16]. This method produces much higher and distinguishable signal from that of typical tissue autofluorescence. If the contrast agent is characterized by a high specificity towards cancer, it becomes easy to detect small colonies of cancerous cells and restrict progression of the disease resulting into better survival rate of patients. As discussed in section 2.5.3, several molecules were engineered for selectively binding to tumours. The target mechanisms span from simple antibody-based immunostaining methods to more complex chemical reactions [131], [132]. Another important aspect related to molecular probes for cancer detection is the molecule's ability of 'switching on' after binding to the target. The use of probes that are 'always on' showing fluorescence properties before reaching the target can sometimes be misleading because the time of binding or binding kinetics can vary from patient to patient as well as from condition to condition. Therefore, switchable probes have an ability to provide a more precise detection [133]. In this chapter, the optical module and the SPAD array were used to detect the fluorescence signal emitted by colorectal cancer cells cultured at different seeding densities and labelled with a gamma-glutamyl transpeptidase (GGT) selective fluorescence probe γ-glutamyl hydroxymethyl rhodamine green (gGlu-HMRG) that is sold as ProteoGreenGlu™ [88], [134]. At first, we tried to find the probe HMRef-GlcNAc which was used to target human colorectal cancer and whose results were published in 2016 [89]. However, after no response from the researchers who engineered the probe, we decided to buy off-the-shelf ProteoGreenGlu™ which was engineered by the same group. The chemical reaction that describes the activation of the probe has been discussed in detail in section 2.5.3 and relies on targeting GGT that is an enzyme expressed on the membranes of cells and overexpressed on the surface of cancer cells. The fluorescence product of the reaction accumulated in cells with a maximum fluorescence emission peak at 525 nm when excited between 460 nm and 480 nm. The same cell line was also stained with CellTracker™ Green which is a fluorescence dye for monitoring cells location designed to work with all cell types [135]. This choice was made to compare the performance of the two molecular fluorescence probes and further characterise the system. All the measurements were carried

out simultaneously to benchmark the system comprising optical block and the SPAD array with a commercial microplate reader. The experiments were performed at the Center for Cell Engineering at the University of Glasgow after completing all the training required to use the tissue culture laboratory. The instrumentation for the measurements was placed in the room adjacent to the cells incubators to maintain the best possible conditions for the cells while performing the measurements.

5.1 Cell lines

5.1.1 LS 174T (ATCC® CL-188™) colorectal adenocarcinoma

Cells were purchased from LGC STANDARD. The cell line CL-188™ was initiated from a Duke's type B adenocarcinoma of the colon of a 58 years old Caucasian human female after mincing and culturing the tissues without transfer for 10 months. Studies on nude mice revealed that tumours advanced in 20 days upon injection of 10^7 cells. The cells were delivered in frozen vials. The vials were thawed in 37°C water bath for approximately 2 minutes and then removed from the water bath and decontaminated by spraying with 70% ethanol. The vial contents were transferred to a centrifuge tube with 9.0 mL of tissue culture Eagle's minimum essential medium (EMEM) (ATCC® 30-2003™) and centrifuged at approximately 1400 rpm for 7 minutes. After centrifugation the supernatant was decanted from the tube and the cell pellet was suspended with 9 mL of new medium. Three separate cell solutions of 3 mL each where then dispensed in 75 cm^2 culture flasks to obtain three separate cultures. Fig. 5.1 shows the appearance of the cells under the microscope at both low- and high-density conditions.

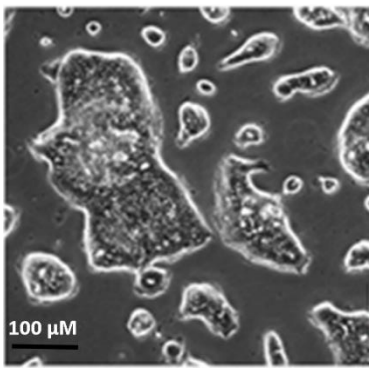

Figure 5.1 ATCC® CL-188™ colorectal adenocarcinoma cells at high density.

5.1.2 BJ-5ta (ATCC® CRL-4001™) foreskin

This specific cell line was purchased to work as a negative control for the cancer-selective probe. The hTERT-immortalized foreskin fibroblast cell line, BJ-5ta was derived by transfecting the BJ foreskin fibroblast cell line with the pGRN145 hTERT-expressing

plasmid (ATCC MBA-141) at population doubling 58. Cells were cultured in medium containing hygromycin B until stable clones were selected. The thawing process involved the steps described above for the previous cell line with the only exception that the medium was a 4:1 mixture of Dulbecco's medium and Medium 199. Fig. 5.2 shows the appearance of the cells under the microscope at both low- and high-density conditions.

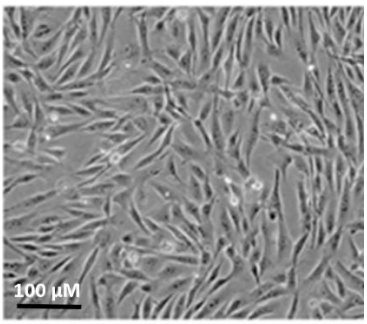

Figure 5.2 BJ-5ta ATCC® CRL-4001™ foreskin fibroblasts high densities.

5.2 Experimental Protocol

The aim of the experiments was to detect fluorescence signal from cells cultured in 96 well plates at four different seeding densities and separately labelled with two different fluorescence probes.

5.2.1 Measurement setup

The measurement setup for the experiments discussed in the previous chapter was used with the sample holder designed and 3D printed to accommodate a 96 well plate (Figs. 5.3 (a)). The sample holder was mounted on the Z-motorized-stage to lay parallel on top of the imaging system ((Figs. 5.3 (b)). A spirit level was used to ensure that the holder was aligned with respect to table where the measurement setup was mounted (Figs. 5.3 (c)). The motorized stages were programmed to move the plate with respect to the imaging system. The scanning and acquisition imaging methods will be discussed later in this chapter. The whole imaging system was enclosed in a black hardboard optical enclosure to create a dark environment during the measurements

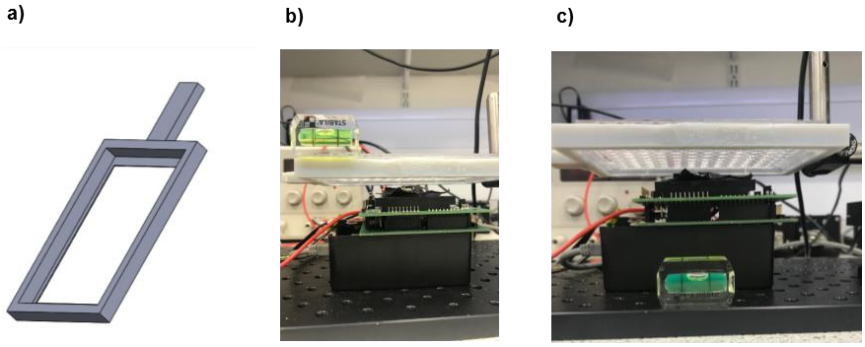

Figure 5.3 96-well plate holder. ***(a)*** *3D CAD model of the sample holder.* ***(b)*** *The holder with spirit-level was mounted on the Z-stage to lay parallel to the imaging setup.* ***(c)*** *Spirit level was placed on the optical breadboard to ensure the alignment of the system.*

5.2.2 Subculture protocol: Cells counting

The cells were incubated in the 75 cm^2 flasks for 48 hours to reach high confluency. The subculture protocol was performed as follows:

1) The culture medium was removed from the flask and the flask surface in contact with the cells was rinsed with 5mL of hepes saline to remove any traces of cell growth medium from the flask.
2) A trypsine/versene solution was prepared by mixing 20 mL of versene and 0.5 mL of trypsin together.
3) Hepes saline was removed from the flask and the flask surface was rinsed with 5mL of the trypsine/versene solution to allow cells to detach from the surface.
4) 5mL of culture medium was added to have a 10 mL cell suspension.
5) The cell suspension was removed from the flask and pipetted into a sterile plastic universal pipette.
6) Cell suspension was centrifuged at 1400 rpm for 4 minutes
7) Once the centrifugation process finished, the liquid part was poured off and substituted with 5 mL of medium to give a single cell suspension.
8) The cell suspension was pipetted in and out of the vial to break the clumps of cells
9) 10 µL of the solution is a device were taken and pipetted into the haemocytometer

The haemocytometer was used for counting these cells. It contained two separate counting chambers with two supports on either side of the counting chamber (Fig. 5.4 (a)). A microscope slide was placed on top of the supports to create a depth of 0.1 mm in the chamber (Fig. 5.4 (b)). Each chamber was etched with a carefully crafted grid with exact and known dimensions. The grid consisted of 9 squares with areas of 1 mm^2 (Fig. 5.4 (c)). Since the depth of the chamber was 0.1 mm, the volume in each square was 0.1mm^3 or

0.001mL. For these experiments the calculations were performed by considering the four outer squares which are in turn dived in 16 smaller square with side of 0.25 mm. After counting the cells in each of the four squares, the average number of cells was computed and used in the following equation

$$\boldsymbol{Cell\ Density} = \frac{\boldsymbol{Average\ cells\ per\ small\ sqaure}}{\boldsymbol{Volume\ of\ a\ square(mL)}} \tag{5.1}$$

If for instance the average number of cells was 93 as depicted in fig. 5.4 (d)), then the cell density was 9.3 x 10^5 cells/mL.

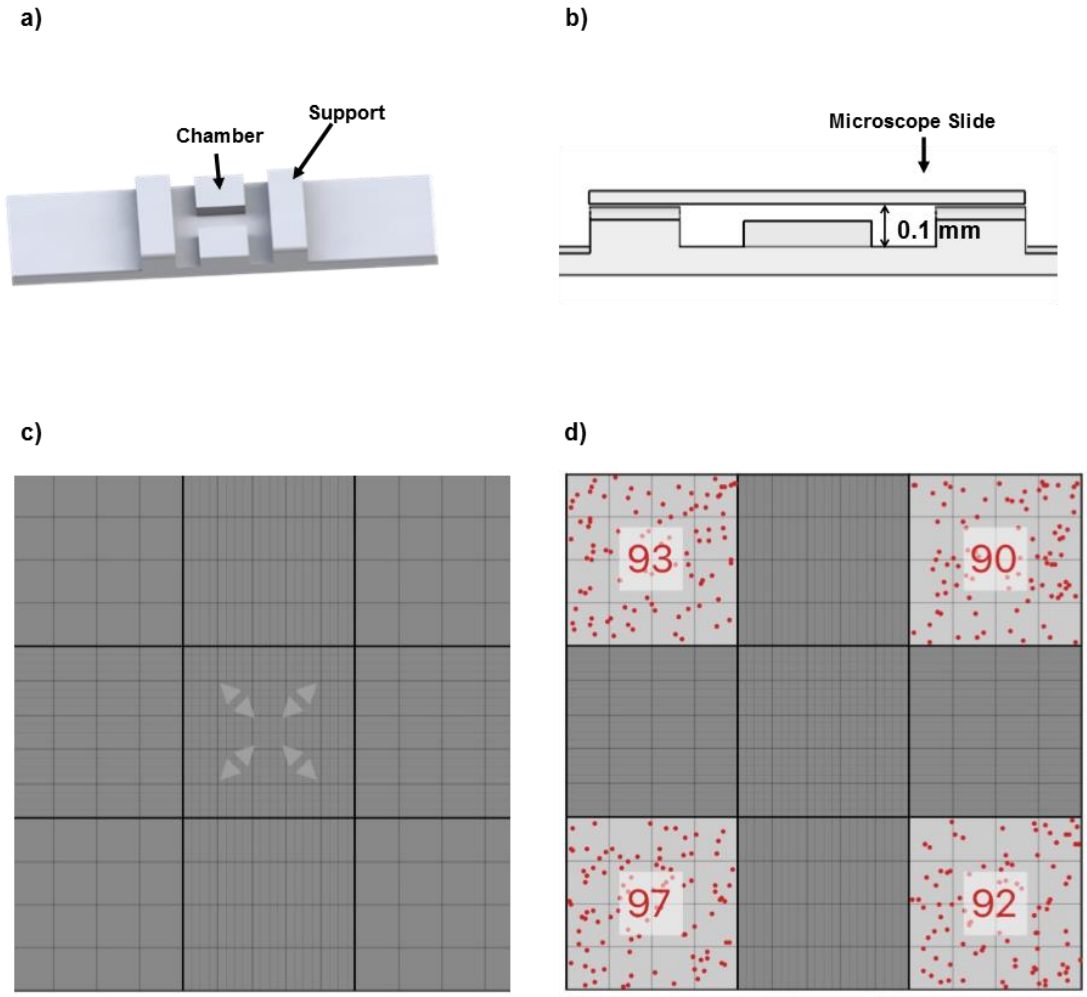

Figure 5.4 Counting cells with the haemocytometer. ***(a)*** *3D model of the device.* ***(b)*** *Cross-sectional view of the microscope slide on top of the device creating a depth of 0.1mm.* ***(c)*** *Square-grid patter etched on the two chambers* ***(d)*** *Cells were counted on the four outer squares.*

5.2.3 Subculture protocol: 96-well plate cultures

96-well plates were chosen for the experiments because the wells of these plates had the smallest diameter available. Each plate had 96 wells distributed in 8 rows and 12 columns with a bottom internal diameter and of 6.25 mm and an area of growth of 0.316 cm^2. The centre-to-centre distance between the plates was also 6.25 mm. Each well can contain a volume of media from 0.1 ml to 0.2 ml. Cultures with specified seeding densities of 100000 cells/well, 25000 cells/well, 6250 cells/well, and 1562 cells/well were replicated four times each within a 96 well plate (Fig. 5.5). Four additional wells per plate were pipetted with culture medium only, for control purposes. The seeding densities in each well was evaluated by following a simple calculation. Each well had to be filled with a volume 150µL containing both medium and cell suspension. Therefore, the total volume for four wells was 600 µL. At this point, the volume aliquots of cells suspension and medium to make the total volume of 600 µL were pre-estimated depending on the seeding density. Equations 5.2 and 5.3 shows the calculations for 100000 cells/well.

$$\boldsymbol{Cell\ suspension} = \frac{\boldsymbol{Seeding\ density\ x\ number\ of\ wells}}{\boldsymbol{Cells\ density}} = \frac{100000\ cells\ x\ 4}{9.2x10^5 cells/mL} = 430\ \mu L \quad (5.2)$$

$$\boldsymbol{Medium = Tot\ volume - cells\ suspension} = (650 - 430)\ \mu L = 220\ \mu L \quad (5.3)$$

Each of the four wells with same seeding density represented a technical replicate for that specific seeding density. A total number of four technical replicates were prepared for each seeding density. After all the wells were cultured, the plates were incubated for 48 hours to allow the cells to attach to the surface of the plate.

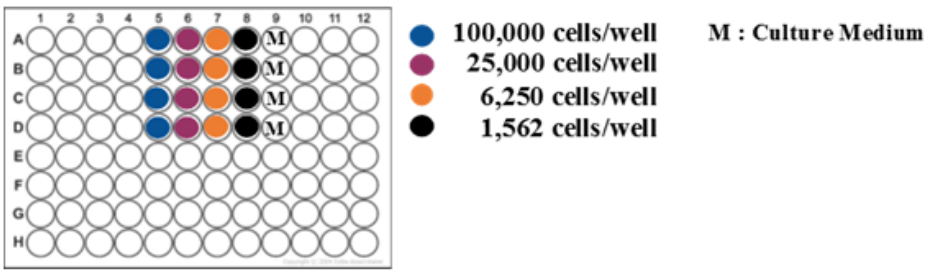

Figure 5.5 Culture protocol for the experiments. *Four different seeding densities were cultured four times in a 96 well plate with a total of four technical replicates per seeding density.*

5.2.4 Fluorescence labelling with unselective Celltracker-greenTM

The product purchased off-the shelf in the form of vials containing 50µg of the lyophilized powder was dissolved in 10.76µL of DMSO to prepare a 10mM stock solution. The stock solution was diluted to obtain three solutions at concentration of 1µM, 2µM and 5µM. For each concentration of probe three plates were cultured following the aforementioned protocol in order to have three experimental replicates per concentration of probe. The staining process involved pipetting 75µM of the stain solution in each well and incubating the plates for 30 minutes. The plates were rinsed with PBS after incubation and filled with culture medium. In this case no negative control was needed because the product worked with all the cells types.

5.2.5 Fluorescence Labelling with Cancer Selective Proteogreen-gGluTM

The product was available off-the shelf as vials containing 10µg of the lyophilized powder probe and these were dissolved in 29.7µL of DMSO to prepare 1mM stock solution. The stock solution was diluted to obtain three solutions at concentration of 1µM, 2µM and 5µM. For each concentration of probe three plates were cultured following the protocol (described before) in order to have three experimental replicates per concentration of probe. The same process was performed for hTert cells that served as negative control. The staining process involved pipetting 75µM of the stain solution in each well and incubating the plates for 30 minutes. The plates were rinsed with PBS after incubation and filled with culture medium.

5.2.6 Measurement protocol

The optical fluorescence signal from the cells stained with the fluorescence probes was expected to vary as a function of the cell density in the wells. Since the field of view of the imager was 2 mm and the well diameter was 6.25 mm, it was necessary to scan the wells over the imager to capture a representative signal. A matlab code was written to move the 96 well plates so that each well was scanned as shown in Fig. 5.6. During the scan, frames were acquired continuously through the GUI of the imager. A message appeared as soon as the scan was completed, and frame acquisition was stopped. At this point the x-y stage moved to the next well on top of the imaging system and a new scan was performed. The procedure was repeated until all 20 wells per plate were scanned.

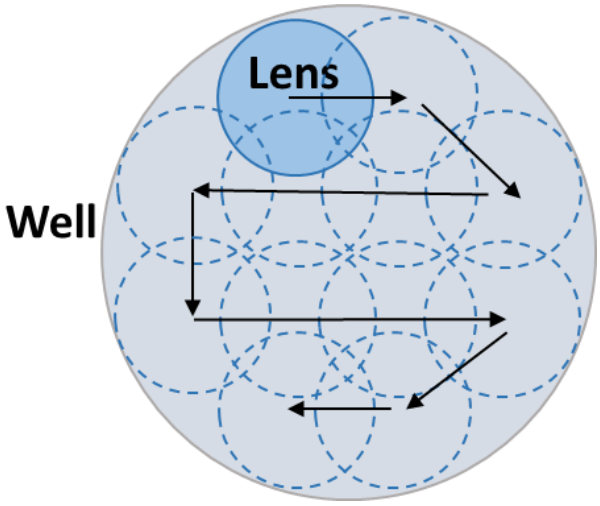

Figure 5.6 Scanning pattern. *Each well of interest for the measurements was scanned by using an optical lens of the optical unit on top at the focal length of the system in order to capture fluorescence signal from all the areas of the well. Frames were continuously acquired during scanning.*

The data from each pixel in each of the frame that made a single scan were averaged together. This procedure was also carried out for the wells containing only culture medium to determine control replicate $\bar{\boldsymbol{M}}$ which was subtracted from the data. For each plate, the average fluorescence value $\bar{\boldsymbol{\mu}}_{(\boldsymbol{s})}$ where s denotes the seeding density was calculated by averaging the values from all four wells cultured with the same seeding densities within the same plate. Three plates for each concentration of dye were measured. The final fluorescence value for each seeding density at a specific dye concentration was computed by averaging the values obtained from the three experiments for each seeding density. The procedure was also performed on three plates without any labelling probes to assess the fluorescence from the unstained cells cultured at the four seeding densities.

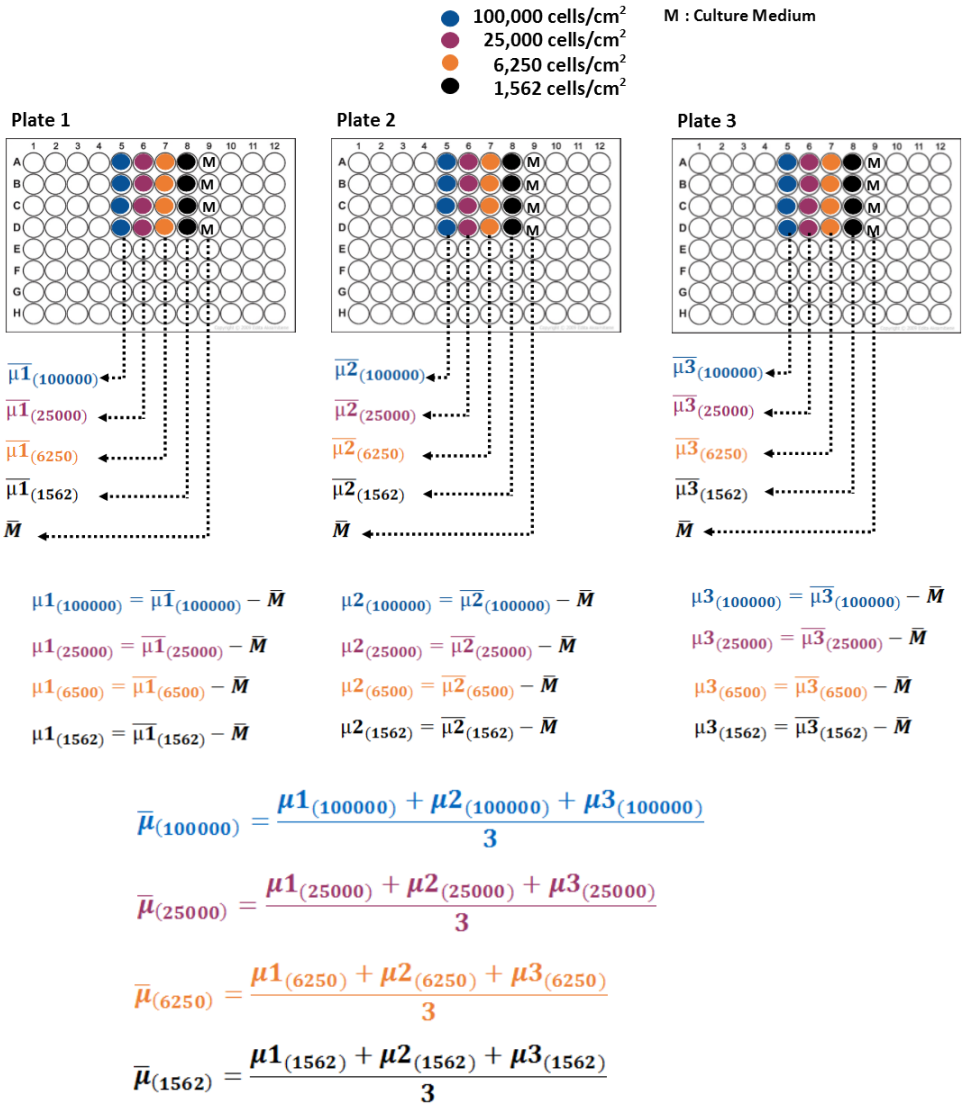

Figure 5.7 Measurement protocol*. For each concentration of dye, three plates were prepared. Each plate was considered as an experimental replicate and the fluorescence value from each seeding density was forecasted as the average values of the four technical replicates within the same plate for the specific seeding density.*

All the plates were measured by using the optical block with the SPAD array (Fig. 5.8) and also a benchmark Modulus™ II Microplate Reader to validate the results (Fig. 5.9 (a)). In this case, no scanning of the wells was required as the system directly provided a representative fluorescence signal from each well. The instrument was specifically designed to perform fluorescence readings from wells in 96-well plates. The microplate reader also worked in luminescence, absorbance and UV-vis absorbance detection modes. As it is shown in fig. 5.8 (b), the interface of the instrument was designed to give the user the choice of selecting or deselecting the wells. The wells of interest were selected simply by touching the squares on the screen corresponding to the wells. In fluorescence mode, the light source was an LED with a spectral range between 400 nm and 800 nm. The instrument was coupled

with a kit of filters that were manually inserted by the user depending on the nature of the experiment. In these experiments the blue kit provided excitation at 490 nm and fluorescence detection between 510 and 570 nm. The instrument was equipped with a PiN photodiode as a detector and results were displayed in Relative Fluorescence Units (RFU) on the screen in the squares corresponding to the wells.

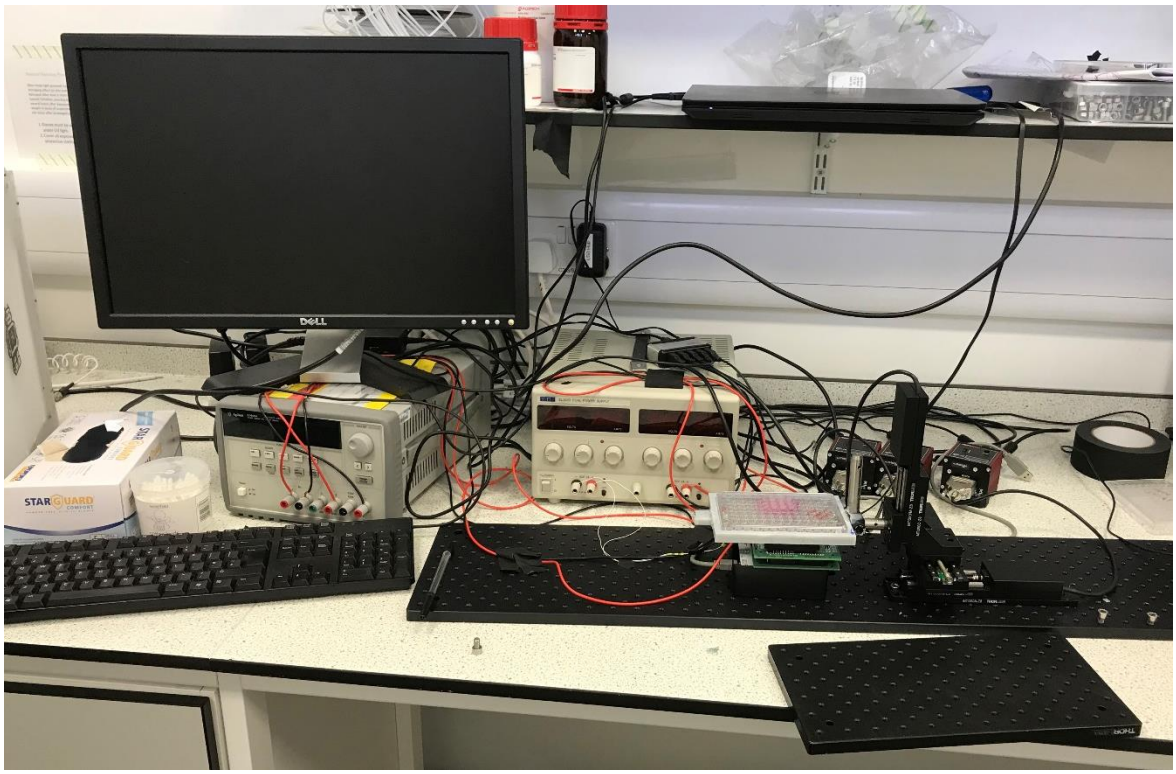

Figure 5.8 Measurements setup. *The measurements setup was powered using two power supplies. A laptop connected to a monitor allowed the control of both the stages and the imaging system. A black optical enclosure was placed on the optical breadboard covering the stages and the imager to ensure that all the experiments were performed in dark conditions.*

a) b)

***Figure 5.9 Modulus™ II Microplate Multimode Reader**. **(a)** Physical Instrument **(b)** Graphic interface to select specific wells in the measurements.*

5.3 Results

Table 1 summarizes the conditions and cell types used for all the experiments that were carried out as a part of this thesis and performed in the Centre for Cell Engineering. The aim of these experiments was not to image single cells but to determine the minimum concentration of the labelled cells required to obtain detectable signal by the system. The results from the four technical replicates after staining in each single plate, after staining, will be displayed. The results from the technical replicates in the plates without any fluorescence probe will be also shown. Finally, the results obtained by averaging the values from the three plates for each concentration of dye will be also shown. Single frames acquired during scanning of the wells will be also displayed to demonstrate that the imaging system was capable of imaging the cells after performing fluorescence labelling.

Table 13 Total number of experiments

Condition	**Cell type**	**Number of experimental replicates**
No labels	*hTert-fibroblasts*	3 plates
	Adenocarcinoma colon	3 plates
Generic CellTracker Green™	*Adenocarcinoma colon*	3 plates
Cancer-selective Proteogreen-gGLU™	*Adenocarcinoma colon*	3 plates
	hTERT-fibroblasts	3 plates

5.3.1 CellTrackerGreenTM (CTG)

After performing the labelling protocol, the dye freely permeated the cells membranes and accumulated into the cells. At this point, a chemical reaction inside the cells made the product impermeant to cell membranes. Therefore, CTG was retained in the living cells. Each well from well plate was scanned on top of the imaging system as described previously in the chapter. Each scan comprised a total number of 153 frames. Fig. 5.10 shows single frames from the wells before and after labelling the plate with 5μM of CTG. The decrease in the number of fluorescence cells and hence fluorescence intensity on the surface of the well is clearly visible from higher to lower seeding densities after labelling. Cells without fluorescence probe were not fluorescing and hence were not visible. Because of limited resolution of the imager, multiple frames were acquired from each pixel instead of depending on single frame measurements. Therefore, the average value of the pixels from all the frames of each well was evaluated to obtain a representative fluorescence value of the whole well. The four values from the wells with same seeding density were averaged and plotted versus the number of cells per well as it was shown in figs. 5.11, 5.12, and 5.13. The figs. show the average fluorescence signals from the plates labelled with CTG dye concentration of 5μM, 2μM, and 1μM respectively. The seeding densities were plotted on a logarithmic scale for better visualization of the data trend. The error bars were also plotted to show the standard deviation between the four technical replicates in each plate.

5.3.1.1 5 μM

As it is shown in fig. 5.11 (a), (c), and (e) there was no difference in the fluorescence signals from the four seeding densities without the presence of any fluorescence label. In fact the average fluorescence value from the seeding densities was around 120 cps and the values for the standard deviations were not higher than 4 cps. On the other hand, after labelling the plates with 5μM of the probe, a distinctive increase in the fluorescence signal was noticeable in all the four seeding densities (Fig. 5.11 (b), (d) and (f)). Specifically, the fluorescence signal from the wells cultured with 1562 cells was triplicated. The wells cultured with 6250 cells showed also an increase in the fluorescence signal that changed from 120 cps in no-stain condition to around an average of 420 cps after staining. The same outcome was observed for the wells with 25000 that showed an increase of 500 cps in the fluorescence signals. Finally, the highest seeding density showed a fluorescence signal one order of magnitude higher after staining. The highest standard deviation was measured in plate 1 at seeding density of 100,000 cells. An uneven uptake of the dye in the wells cultured with 100000 cells in plate 1 might have caused a high variation of the data. However, this variation in standard deviation was less in the other plates for the same seeding density.

5.3.1.2 2µM

As it is shown in fig. 5.12 (b), (d), (f) the increase of the fluorescence signal in each of the four seeding densities was lower when 2µM of the probe were used to label the plates. However, the trend of the data in the plot is similar to the trend in the experiments with 5µM. The highest fluorescence value of 738 cps was measured in the wells with 100,000 cells.

5.3.1.3 1µM

The same data trend was again noticed at the lowest concentration of the probe in figs. 5.13 (b), (d), (f). In this case the highest increase in the fluorescence signal was only three times higher than the fluorescence measured in no-stain condition.

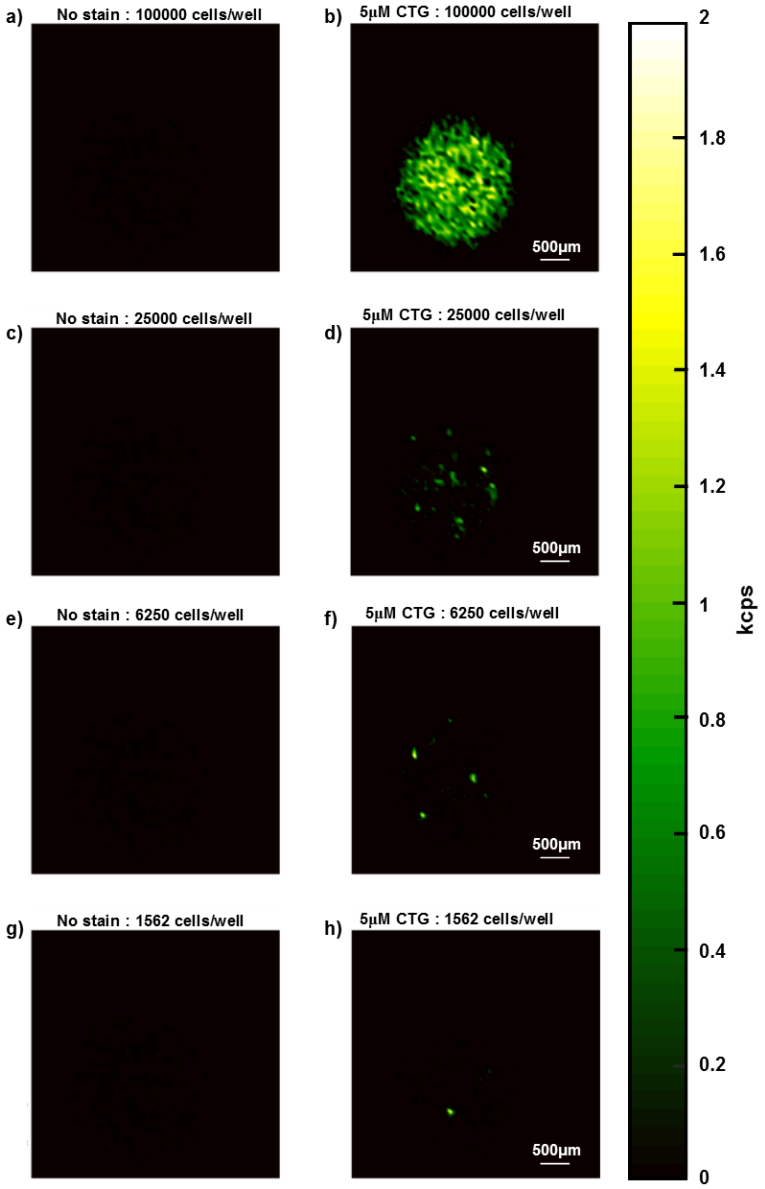

Figure 5.10 Single frames acquired before and after labelling the wells with 5µM of CTG. ***(a)****,* ***(b)*** *100000 cells/well.* ***(c)****,* ***(d)*** *25000 cells/well.* ***(e)****,* ***(f)*** *6250 cells/well.* ***(g)****,* ***(h)*** *1562 cells/well.*

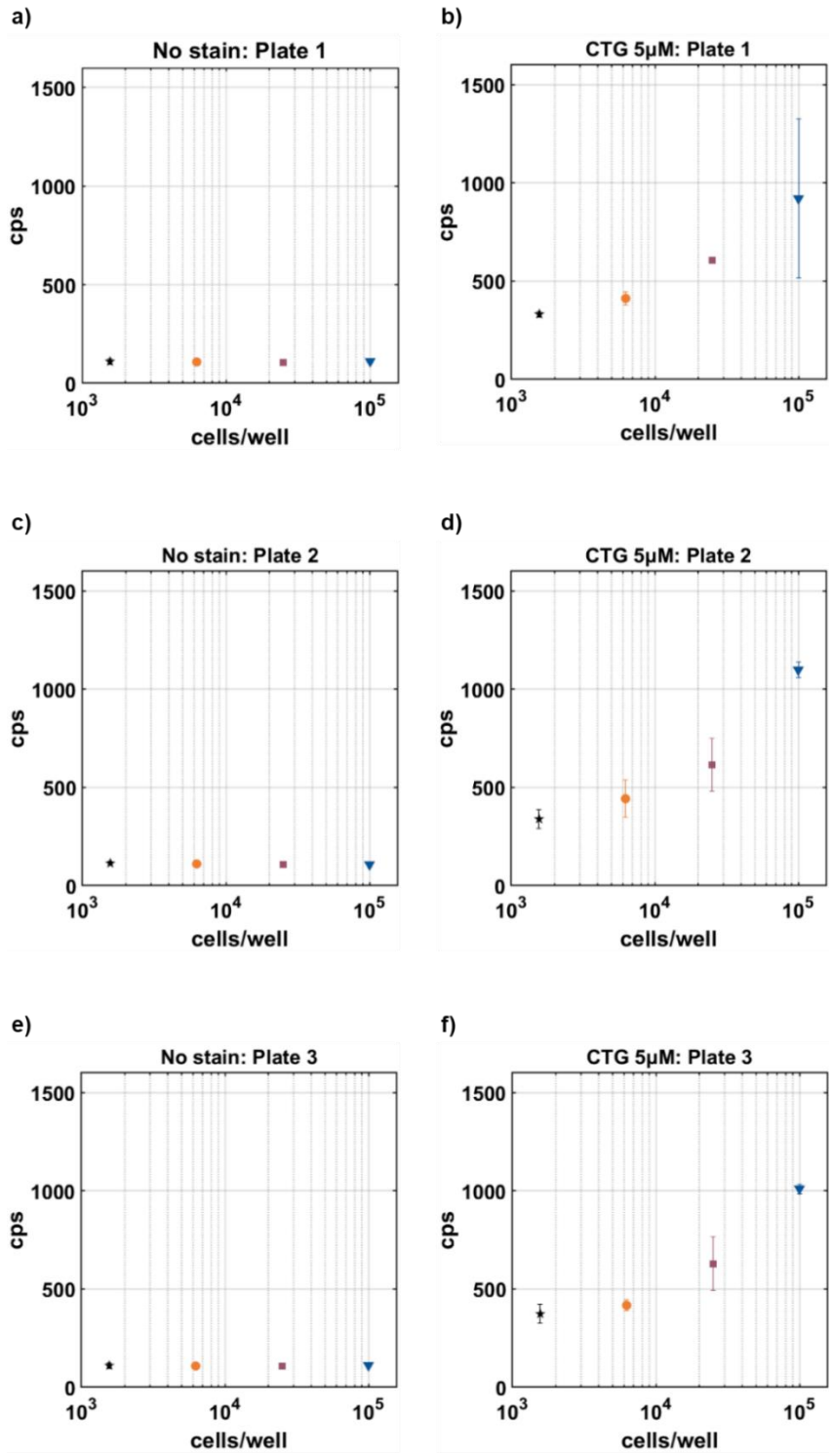

Figure 5.11 CTG 5µM. ***(a)***,***(c)***,***(e)*** *Fluorescence signals from three 96-well plates cultured with colon adenocarcinoma cancer cells at seeding densities of 1562 cells/well, 6250 cells/well, 25000 cells/well and 100000 cells/well without any labelling probe.* ***(b)***,***(d)***,***(f)*** *Fluorescence signals from three 96- well plates cultured with colon adenocarcinoma cancer cells at seeding densities of 1562 cells/well, 6250 cells/well, 25000 cells/well and 100000 cells/well and labelled with the fluorescence probe CellTrackerGreen™ at concentration of 5µM. Each seeding density was replicated four times within the plate.*

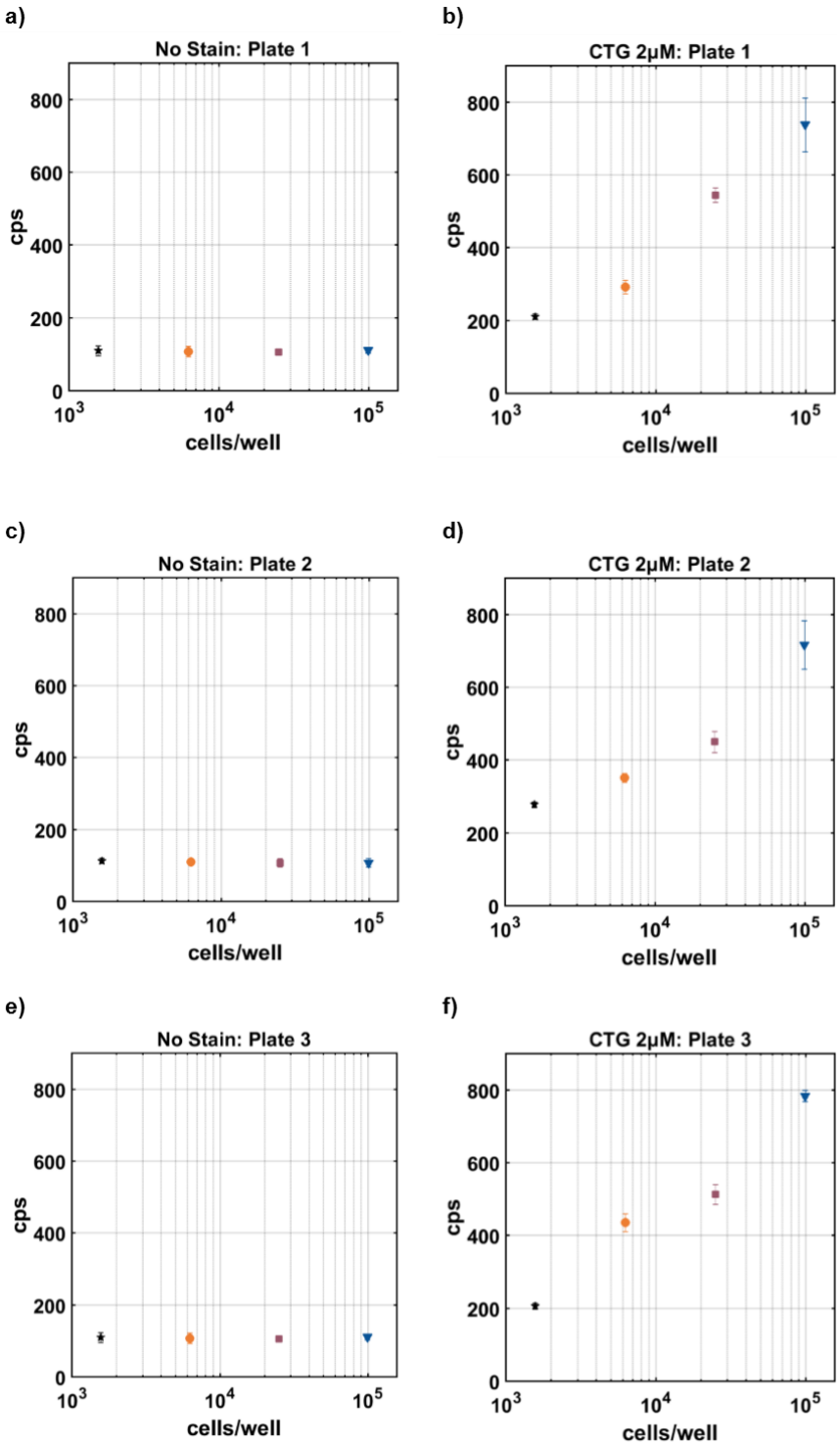

Figure 5.12 CTG 2μM. (a),(c),(e) *Fluorescence signals from three 96-well plates cultured with colon adenocarcinoma cancer cells at seeding densities of 1562 cells/well, 6250 cells/well, 25000 cells/well and 100000 cells/well without any labelling probe.* ***(b)****,* ***(d)****,* ***(f)*** *Fluorescence signals from three 96- well plates cultured with colon adenocarcinoma cancer cells at seeding densities of 1562 cells/well, 6250 cells/well, 25000 cells/well and 100000 cells/well and labelled with the fluorescence probe CellTrackerGreen™ at concentration of 2μM. Each seeding density was replicated four times within the plate.*

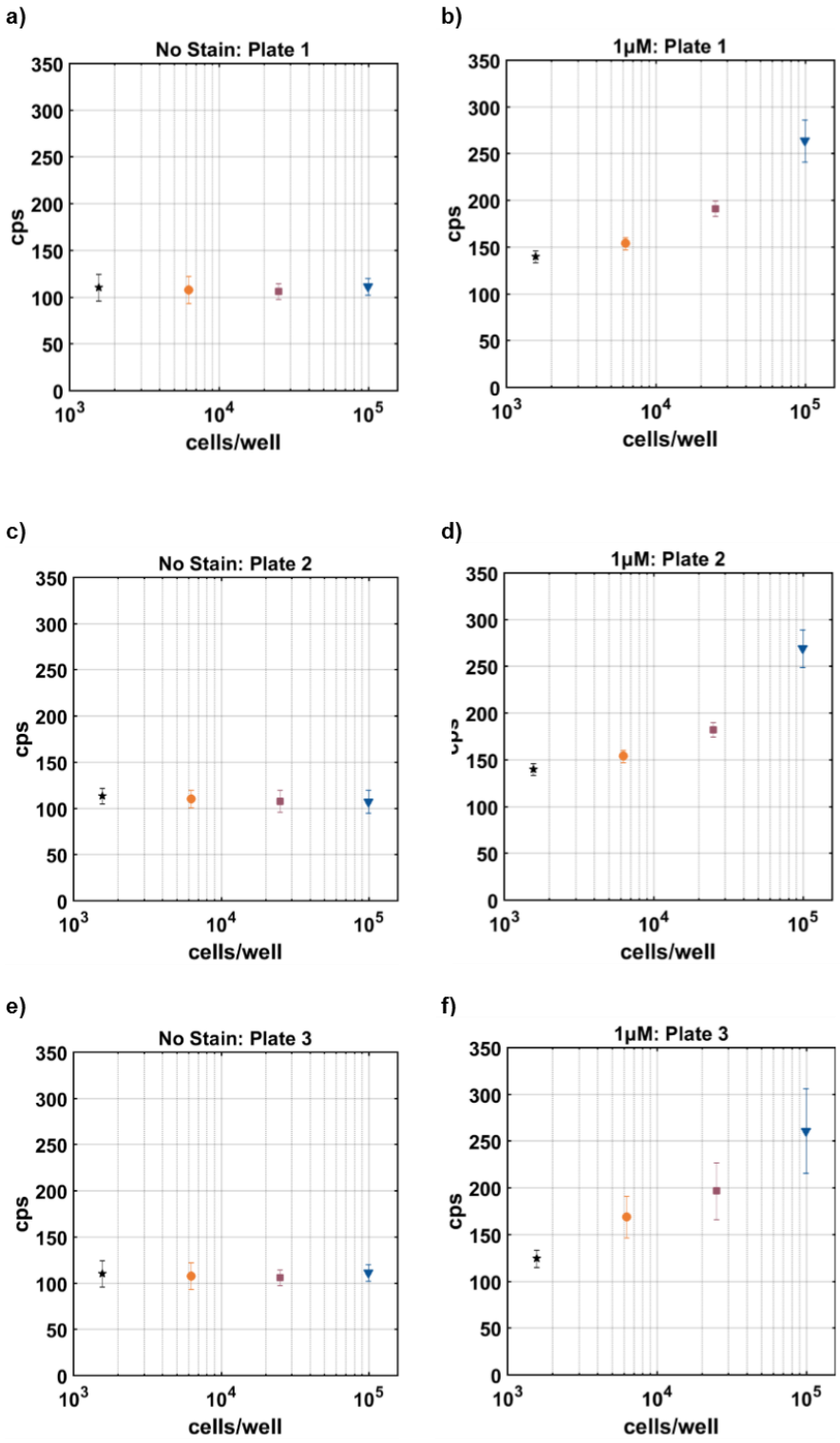

Figure 5.13 CTG 1µM. ***(a),(c),(e)*** *Fluorescence signals from three 96-well plates cultured with colon adenocarcinoma cancer cells at seeding densities of 1562 cells/well, 6250 cells/well, 25000 cells/well and 100000 cells/well without any labelling probe.* ***(b), (d), (f)*** *Fluorescence signals from three 96- well plates cultured with colon adenocarcinoma cancer cells at seeding densities of 1562 cells/well, 6250 cells/well, 25000 cells/well and 100000 cells/well and labelled with the fluorescence probe CellTrackerGreen™ at concentration of 1µM. Each seeding density was replicated four times within the plate.*

5.3.2 Cancer-selective ProteogreenTM g-Glu

Proteogreen^{TM} gGlu is a molecular probe that shows fluorescence properties only upon reaction with the enzyme GGT that naturally exists on the membranes of all cell types (cancerous and non-cancerous). An overexpressed GGT activity was noticed in several types of human cancer tumours such as colorectal cancer. Therefore, Proteogreen^{TM} gGlu was engineered and sold to visualize cancer cells.

5.3.2.1 Colorectal cancer cells (Positive Control)

Colorectal cancer cells were used as positive control to assess the performance of the probe. As in the case of CTG, Figs. 5.14 5.15 and 5.16 show the average fluorescence signals from the plates labelled with Proteogreen^{TM} gGlu at concentration of 5μM 2μM and 1μM respectively. In contrast to CTG, the effect of Proteogreen^{TM} gGlu was only remarkably evident at the highest seeding density of 100000 cells/well. However, the increase in the fluorescence signal of the cells was little compared to the previous results obtained using CTG. As it can be seen from figs. 5.14 (b), (d) and (e), 5 μM of the probe produced an average increase of the fluorescence signal of 150 cps in the wells with 100000 cells. The same seeding density showed a less increase in the fluorescence signal with 2 μM and 1μM (Figs. 5.15 (b), (d) (e) and 5.16 (b), (d) (e)). High values of standard deviations were observedfor the wells with the highest seeding density of 100000 cells suggesting that the probe was not as stable as CTG. The wells with the lowest seeding density of 1562 cells almost did not show any increase in fluorescence signal for all three concentrations of the probe tried. A slight increase in the fluorescence signal of the wells cultured with 6250 and 25000 cells was noticed in the experiments with 5μM while no remarkable changes were observed at 2 μM and 1μM.

5.3.2.2 Negative Control (hTert fibroblasts)

hTert fibroblasts were labelled with 5μM of Poteogreen^{TM} gGlu. A slight increase in the fluorescence signal of the fibroblasts was noticed at all four seeding densities after labelling (Fig. 5.17 (a), (c) and (e)). In the wells with 100000 cells, the increase in the fluorescence signal in the cancer cells was much higher than the signal increase in the fibroblasts after staining. Particularly, the signal in the wells with 100000 cells increased from 110 cps to almost 250 cps in plate 1 whereas almost 200 cps were measured in plate 2 and 3 for the same seeding density (Fig. 5.17 (b), (d), (f)). The fluoresce signal in cancer cells at seeding densities lower than 100000 cells/well in plate 2 after labelling increased gradually with the seeding density and was higher than the fluorescence increase in fibroblasts. However, in plate 1 and 3, the increases in fluorescence signal of both cell populations at densities lower than 100000 cells after staining were very similar.

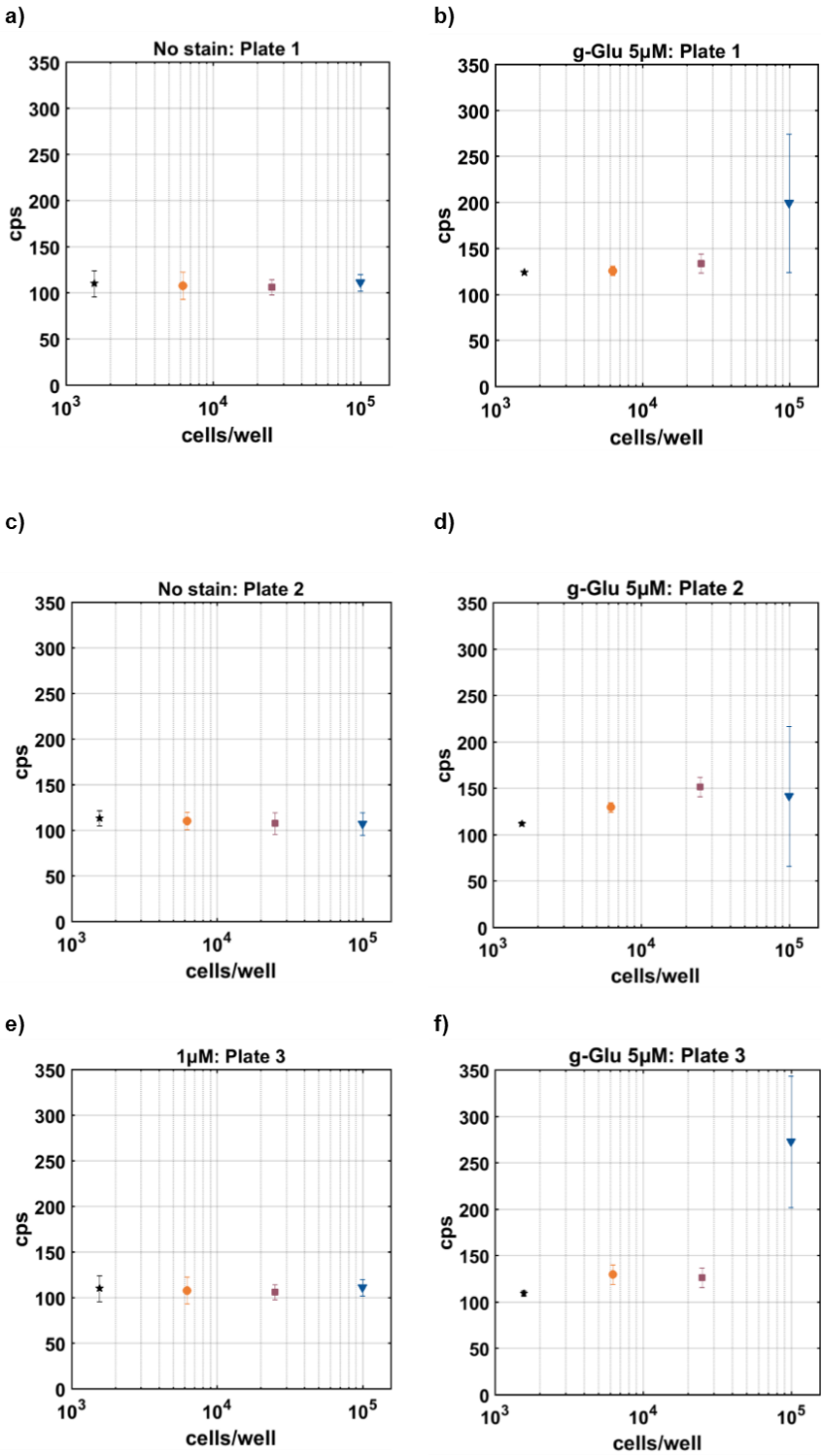

Figure 5.14 ProteoGreen™ gGlu 5µM (a),(c),(e) *Fluorescence signals from three 96-well plates cultured with colon adenocarcinoma cancer cells at seeding densities of 1562 cells/well, 6250 cells/well, 25000 cells/well and 100000 cells/well without any labelling probe.* ***(b),(d),(f)*** *Fluorescence signals from three 96- well plates cultured with colon adenocarcinoma cancer cells at seeding densities of 1562 cells/well, 6250 cells/well, 25000 cells/well and 100000 cells/well and labelled with the fluorescence probe Proteogreen™ gGlu at concentration of 5µM. Each seeding density was replicated four times within the plate.*

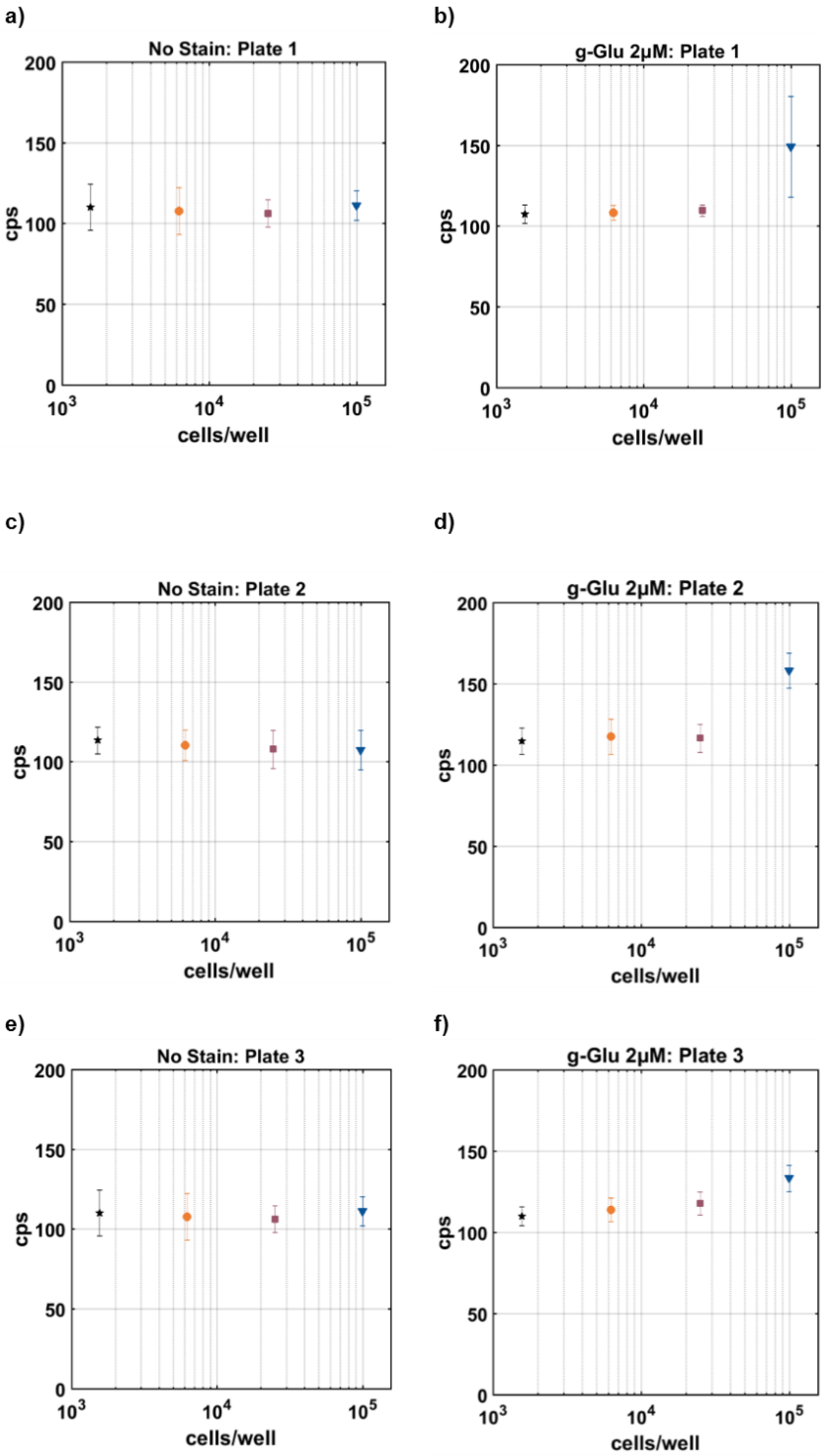

Figure 5.15 ProteoGreen™ gGlu 2µM (a),(c),(e) *Fluorescence signals from three 96-well plates cultured with colon adenocarcinoma cancer cells at seeding densities of 1562 cells/well, 6250 cells/well, 25000 cells/well and 100000 cells/well without any labelling probe.* ***(b),(d),(f)*** *Fluorescence signals from three 96- well plates cultured with colon adenocarcinoma cancer cells at seeding densities of 1562 cells/well, 6250 cells/well, 25000 cells/well and 100000 cells/well and labelled with the fluorescence probe ProteogreenTM gGlu at concentration of 2µM. Each seeding density was replicated four times within the plate.*

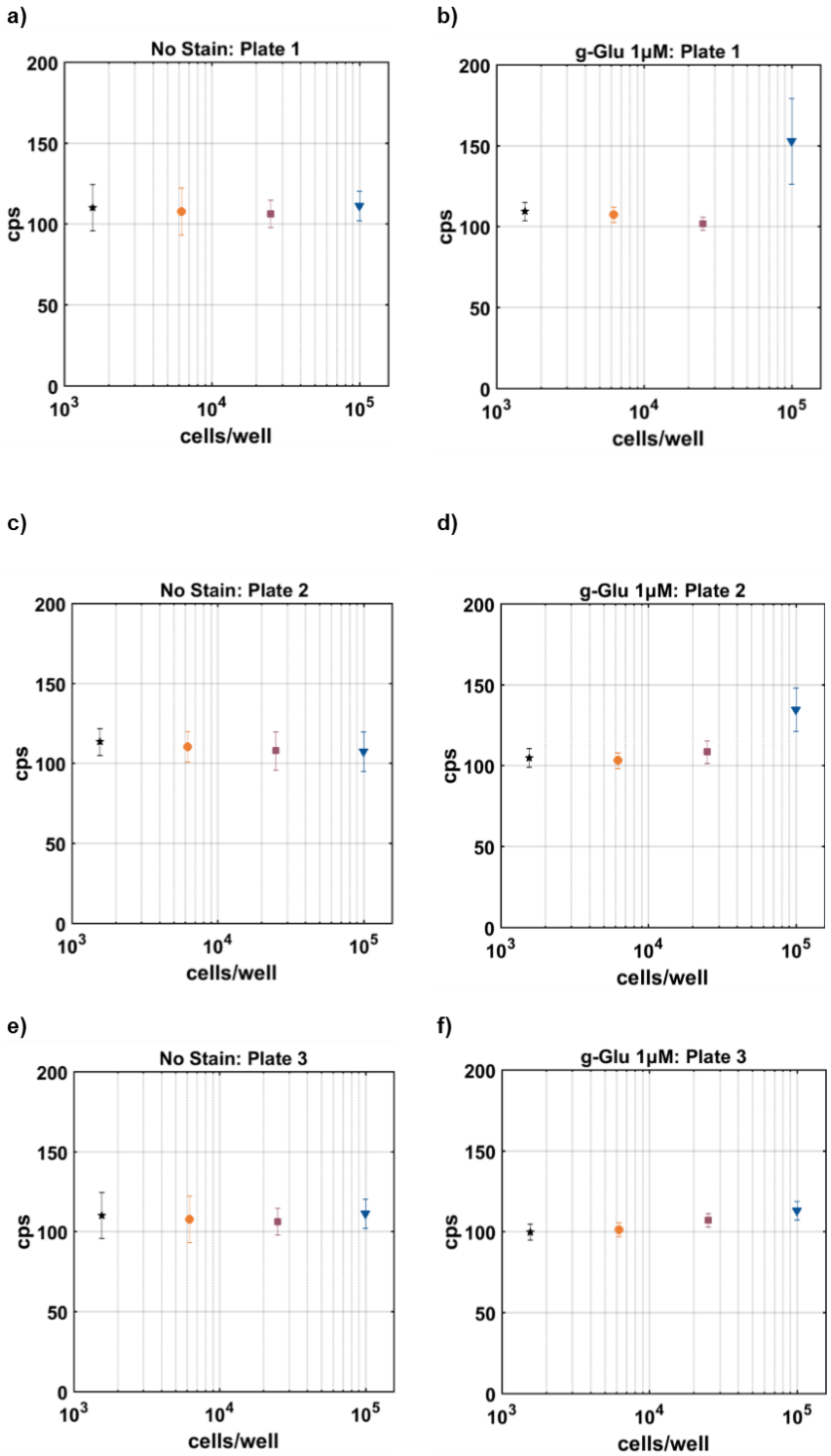

Figure 5.16 ProteoGreen™ gGlu 1µM (a),(c),(e) *Fluorescence signals from three 96-well plates cultured with colon adenocarcinoma cancer cells at seeding densities of 1562 cells/well, 6250 cells/well, 25000 cells/well and 100000 cells/well without any labelling probe.* ***(b),(d),(f)*** *Fluorescence signals from three 96- well plates cultured with colon adenocarcinoma cancer cells at seeding densities of 1562 cells/well, 6250 cells/well, 25000 cells/well and 100000 cells/well and labelled with the fluorescence probe Proteogreen™ gGlu at concentration of 1µM. Each seeding density was replicated four times within the plate.*

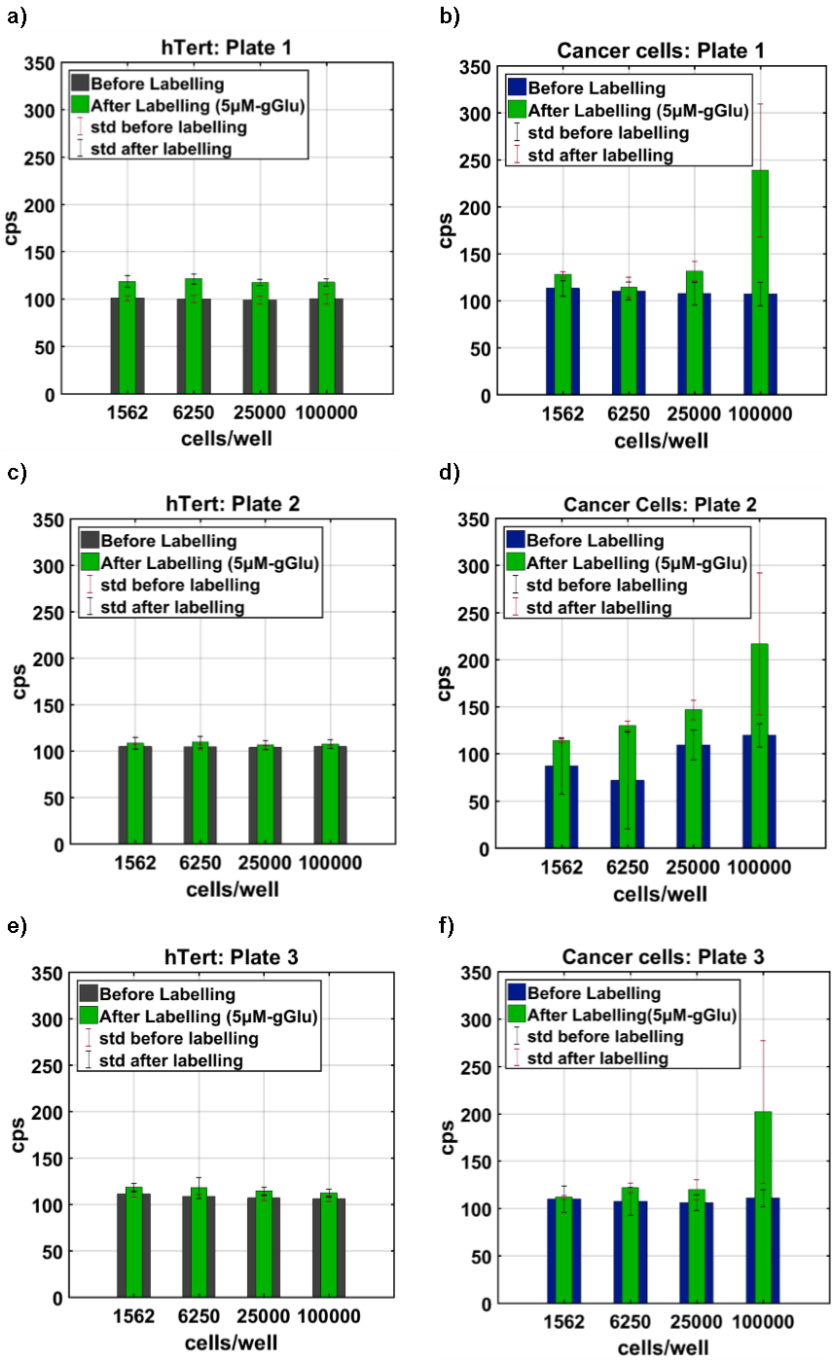

Figure 5.17 Fluorescence signals from hTert fibroblasts (negative control) and cancer cells (positive control) before and after labelling with 5μM of Proteogreen gGlu™ to assess the specificity of the probe towards cancer. (a),(c), (e) *Fluorescence signals from three 96-well plates cultured with hTert finroblasts at seeding densities of 1562 cells/well, 6250 cells/well, 25000 cells/well and 100000 cells/well before and after labelling the cells with the fluorescence probe Proteogreen™ gGlu at concentration of 5μM.* ***(b),(d), (f)*** *Fluorescence signals from three 96-well plates cultured with colon cancer cells at seeding densities of 1562 cells/well, 6250 cells/well, 25000 cells/well and 100000 cells/well before and after labelling the cells with the fluorescence probe Proteogreen™ gGlu at concentration of 5μM.*

5.3.3 Comparison with benchmark instrument

Fluorescence intensities from the same plates were also measured by using a Modulus^{TM} Microplate reader as reference instrument for the validation purpose. Fig. 5.18 shows the fluorescence intensities of cells separately labelled with 5μM, 2μM and 1μM of CellTrackerGreen^{TM} and ProteoGreen-gGlu^{TM} measured by using the optical block coupled with the SPAD and the reference instrument. As described in the measurement protocol, the final data points for each seeding density at each concentration of dye were simply evaluated by averaging the values obtained from three plates labelled with the same concentration of probe. Although the results were displayed in two different units, the trends of the data points measured by the two instruments for the same probe were very similar. In the case of CellTrackerGreen^{TM}, as it was previously discussed showing the results from single plates, an increase in the fluorescence signal of the cells at all four seeding densities was produced by all the three concentration of the probe. A more accurate and direct comparison between the instruments was performed by plotting the values measured by the microplate reader versus the values obtained by using the optical block and the SPAD array at each concentration of dye as it is shown in fig. 5.19. The data points were also fitted to a linear model with a resulting R^2 fit with more than 90% for all the three concentrations of CTG. The fluorescence signal produced by CTG increased with increase in seeding density. At concentration of 2 μM an overlap between the standard deviations of signals measured by the reference instrument at seeding densities of 25000 cells/well and 6250 cells/well was noticed (fig. 5.19(b)). On the other hand, this overlap was not observed for the fluorescence intensities measured by the optical block and the SPAD at the same seeding densities. The exact same correlation was studied for the fluorescence intensities of cells labelled with ProteoGreen-gGlu^{TM}. As it can be seen from fig. 5.20, the linear correlation between the two instruments was higher than in the previous case with values of R^2 equal to 99 % for all three concentrations of probe. As discussed previously, a remarkable increase in the fluorescence signals of the highest density of cells was produced by the probe. The reference instrument also confirmed that ProtoGreen-gGlu^{T,M} was not as stable as CellTrackerGreen^{TM} at seeding densities of 1562 cell/well, 6250 cells/well and 25000 cells/well. In fact, in fig. 5.20 the differences between data points corresponding to these seeding densities were minimal at all the three concentrations of the dye. It must be considered that the two instruments were characterized by different optical components and different photodetectors. Moreover, the microplate was designed to directly provide the user with a representative fluorescence signal of the well. On the other hand, a scanning measurement protocol was implemented in

the case of the imaging system comprising the optical block and SPAD array to give comparable fluorescence signal.

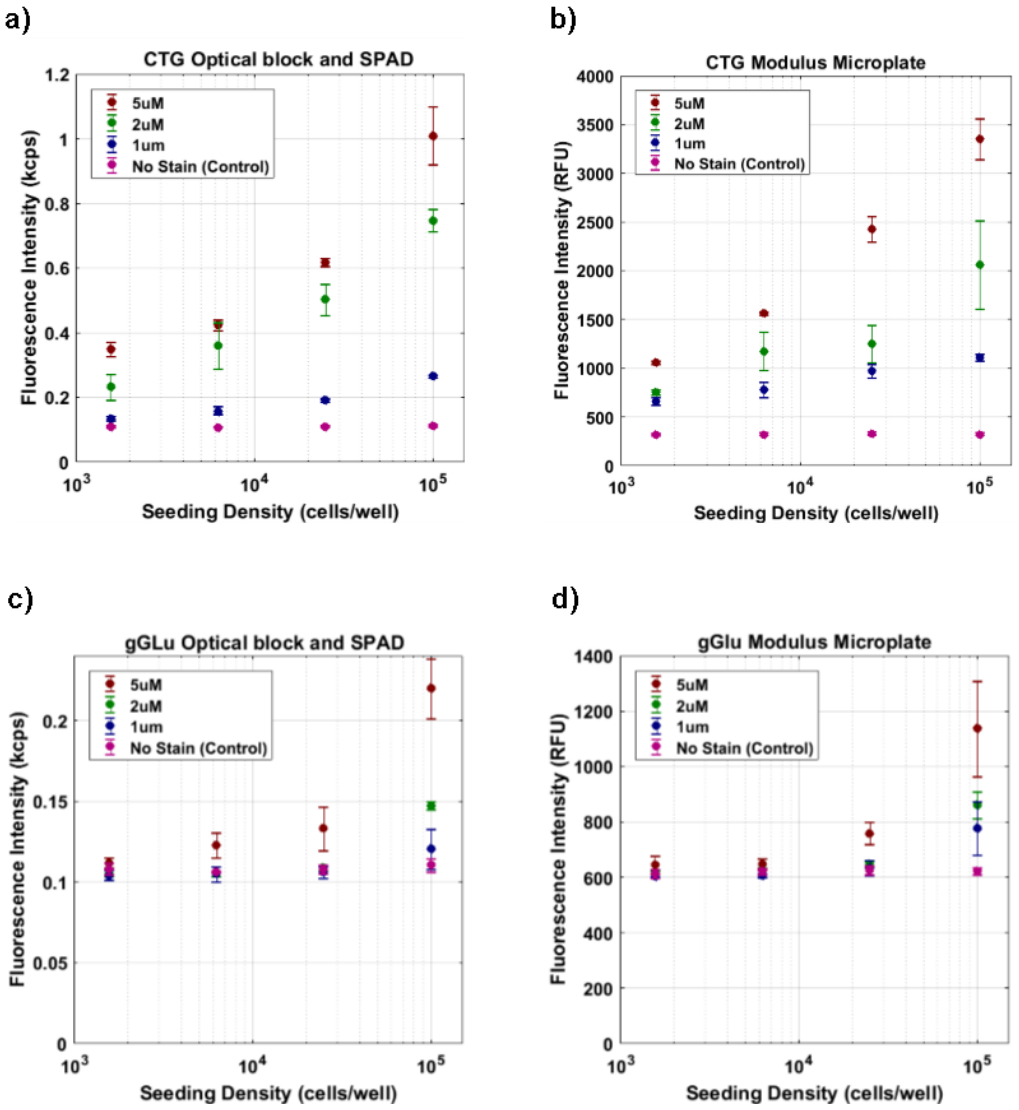

Figure 5.18 Comparison of optical block and SPAD with Modulus™ microplate for detection of fluorescence from colorectal cancer cells at seeding densities of 1562 cells/cm², 6250 cells/cm², 25,000 cells/cm², 100,000 cells/cm² separately labelled with generic fluorescence probe (CellTrackerGreen™) and cancer-selective fluorescence probe (Proteogreen gGlu™). (a), (b) *Detection of fluorescence from colorectal cancer cells labelled with fluorescence probe CellTrackerGreen™ at concentration of 5µM, 2µM and 1µM using the imaging system and the Modulus™ microplate respectively.* ***(c), (d)*** *Detection of fluorescence from colorectal cancer cells labelled with cancer-selective fluorescence probe Proteogreen gGlu™ at concentration of 5µM, 2µM and 1µM using the imaging system and the Modulus™ microplate respectively. The data points were obtained by averaging the fluorescence intensities from three plates labelled with same concentration of dye.*

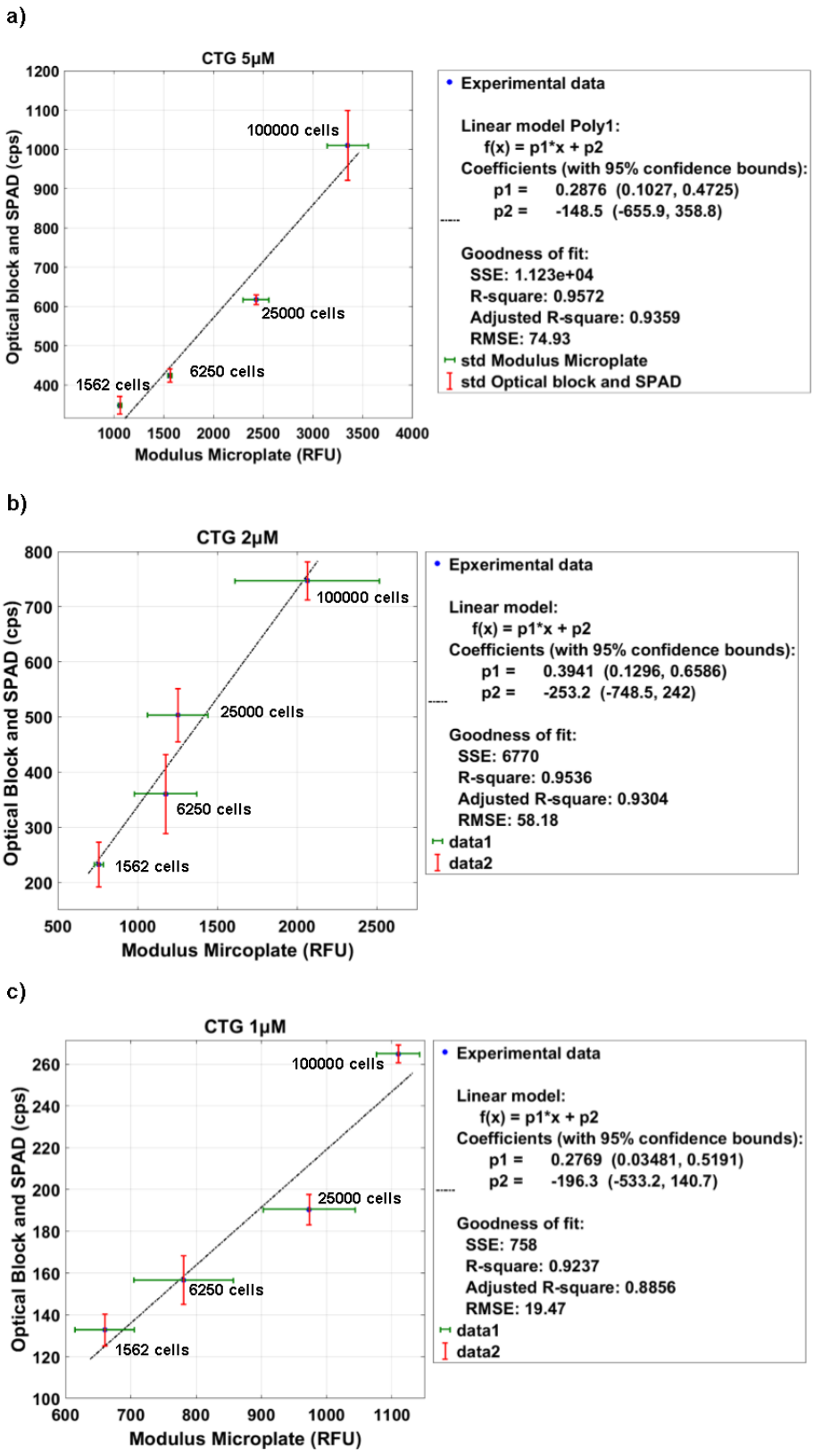

Figure 5.19 Correlation between Modulus Microplate™ and Optical block and SPAD in the measurement of fluorescence from cells at seeding densities of 100000 cells/well, 25000 cells/well, 6250 cells/well and 1562 cells/well labelled with (a) 5µM (b) 2µM and (c) 1µM of CellTrackerGreen™. *Data points refer to each of the four seeding densities and were forecasted by averaging the results from the three plates.*

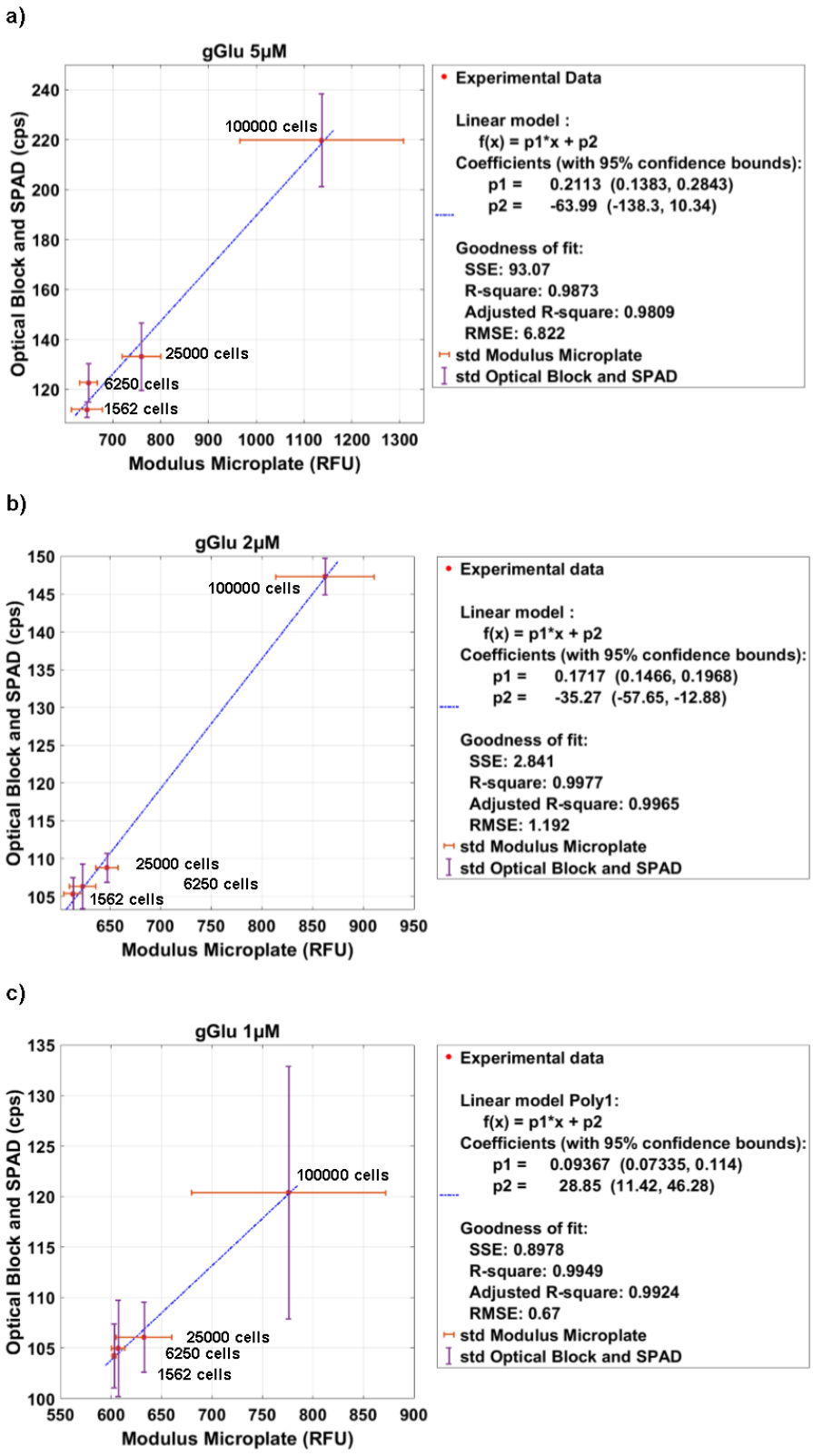

Figure 5.20 Correlation between Modulus Microplate™ and Optical block and SPAD in the measurement of fluorescence from cells at seeding densities of 100000 cells/well, 25000 cells/well, 6250 cells/well and 1562 cells/well labelled with (a) 5µM (b) 2µM and (c) 1µM of Proteogreen-gGlu™. *Data points refer to each of the four seeding densities and were forecasted by averaging the results from the three plates.*

5.4 Summary

The aim of this chapter was to describe the capability of optical block coupled with the SPAD array for the detection of fluorescence from cells labelled with a generic and a cancer-selective fluorescence probe. A colorectal cancer cell line was used as a positive control for the cancer-selective fluorescence probe whereas a fibroblast cell line was cultured and labelled to work as a negative control. The measurement protocols to culture the cells in 96 well plates at four different seeding densities and measure the fluorescence signals from the wells were described in detail. Each experiment was replicated three time in three different plates. Results from the single plates were discussed for both fluorescence probes. Finally, the performance of the imaging system was compared to a benchmark or validate the instrument. An almost linear correlation between the two instruments was observed confirming the capability of the imaging system to perform fluorescence measurements on labelled cells. In conclusion, the generic fluorescence probe was more stable producing a distinguishable fluorescence signal in all the four seeding densities. On the other hand, the cancer-selective fluorescence probe produced a lower fluorescence signal in the cells that was clearly distinguishable at the highest seeding density of 100000 cells/well.

6 Ex vivo experiments

The development of fluorescence imaging systems has improved the clinical evaluation of cancer lesions in the gastrointestinal tract [136]–[138]. However, the knowledge of the microscopic, biochemical and biomolecular mechanisms behind tissue AF is still incomplete. An optimal design of fluorescence diagnostic imaging systems requires comprehension of the differences in AF signals associated with both different anatomical sites and disease stage. Moreover, a deep understanding of all the processes involved in the alterations of AF from the human body could be crucial for the development of precise algorithms to process images and achieve an early detection of cancer [139]. As discussed in section 2.4, AF from tissues is the results of a combination of numerous fluorophores that naturally occur within tissues at different depths and concentrations. Therefore, structural changes in the morphology of tissues including variations in blood levels are considered the main factors contributing to the differences in fluorescence intensity between normal and cancerous tissues.

The intestinal walls consist of three main tissue layers defined as mucosa, submucosa and muscolaris propria [140]. The composition of fluorophores varies within the three layers. Although the mucosa is the outermost layer, fluorophores from the other layers also contribute to the fluorescence signal measured at the intestinal epithelium which is in outer layer of the mucosa. Excitation light does not pass beyond the submucosa that has usually a thickness between 0.5 and 1.5 mm and shows a strong autofluorescence intensity between 500 and 550 nm [141]. The increase in thickness of the mucosa layer as a consequence of dysplasia is responsible for an overall decrease in the green autofluorescence intensity. Specifically, the increased thickness of the mucosa contributes to the reduction of excitation light delivered to the submucosa [142]. In this work, optical block and the SPAD array were used to image resected human healthy and malignant colon tissues. All the human tissue samples were also imaged by using a commercial portable microscope to make a comparison between autofluorescence imaging and white light imaging. The experiments were performed at the Western General Hospital in Edinburgh as part of an honorary contract offered to access material of confidential or sensitive nature. The experiments were performed under the supervision of consultant colorectal surgeon Mark Potter and consultant histopathology Paul Fineron. The instrumentation for the measurements was placed in the pathology laboratory to ensure that all the experiments were performed on fresh samples within 30 minutes from hemicolectomy procedures.

6.1 Materials and Methods

6.1.1 Samples collection and preparation

This study involved the use of excised human healthy and malignant colon tissue samples. Appropriate institutional ethical consent and pre-operative patient consent were obtained for the acquisition of the tissue specimens. A total of 10 adult consenting patients were included. All the patients in this study were diagnosed with adenocarcinoma of the colon and underwent hemicolectomy procedures at the Western General Hospital in Edinburgh. The surgical operation involved the removal of the side of the colon that was affected by cancer. A cut in the abdomen of the patient was performed by the surgeon. The diseased side of the colon was removed and the small intestine was attached to the remaining healthy part (Fig. 6.1). The sample was delivered immediately after the operation from the theatre to the pathology division. The pathologist assessed the size of the cancerous lesion (Fig. 6.2). If the lesion was large enough, portions of cancer tissue and normal colon mucosa with areas of approximately 1 to 2 cm^2 were resected and used for the experiments. Lesions that were not big enough were not available for research purposes. For those cases only healthy portions of colon were available for investigation.

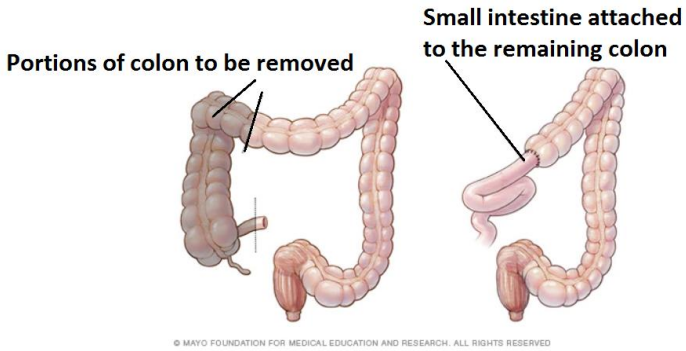

Figure 6.1 Schematic drawing of hemicolectomy procedure.

Figure 6.2 Colon sample of a 60 years old man with adenocarcinoma of the colon. *Hemicolectomy was performed at Western General Hospital in Edinburgh. The sample was prepared by the pathologist.*

6.1.2 Measurement setup

The setup for the measurements included the motorized stages equipped with a 3D printed arm to hold standard plastic petri dishes (Fig. 6.3). Healthy and cancer tissues from the same colon samples were placed in the same petri dish in succession in order to image both tissues at the same time. Optical images of the tissues were also acquired by using a portable Dino-Lite AM3113T USB digital microscope as it is shown in fig. 6.4.

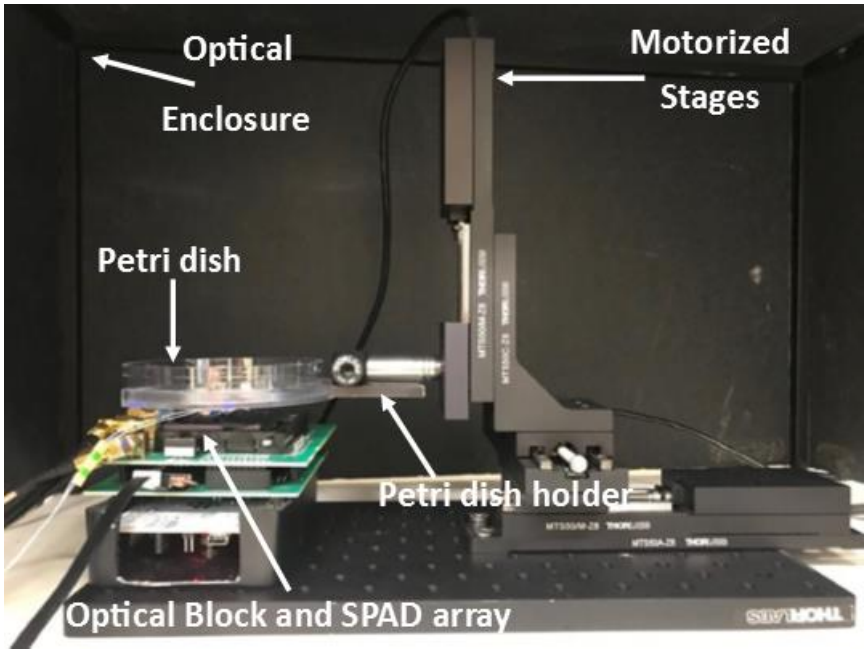

Figure 6.3 Imaging Setup for the experiments comprising three motorized optical stages mounted on an optical breadboard along with the PCB accommodating SPAD array and optical block. *A special arm was 3D printed to hold the petri dish with the tissues on top of the imaging system.*

Figure 6.4 Portable digital microscope mounted on the specific support to image the surface of the petri dish.

6.1.3 Image acquisition

Tissue samples were adjusted on the petri dishes immediately after resection without any pre-processing in order to maintain the physiology of the specimens. All the petri dishes in the experiments were placed at a height of 6 mm from the lens of the optical block in order to ensure that images were acquired at the exact focal length of the system. In each experiment, images of the surface of the empty petri dishes were acquired before imaging any tissue to account for any reflection from the dish. The average of the frames of the petri dish surface was saved to use as a mask to subtract from each frame during the scan. A MATLAB code was written to move the Thorlabs motorized stages in x and y directions. The motion of the stages followed a rectangular pattern that comprised the same number of horizontal and vertical movements. The longest side of the rectangular area surrounding the samples was measured before image acquisition by using a stainless steel ruler. Each petri dish containing the tissue samples was scanned on top of the optical block and SPAD array. Frames were continuously acquired during the movement of the plate with a SPAD gate time of 45 ms and a frame rate of 1 frame/s. An assumption was made to consider the direction of the horizontal scans as the x direction and the direction of the vertical scans as the y direction (Fig. 6.5). Tolerance was always taken into account to make sure that all tissue surfaces were imaged. If the side of the area was 10 mm long, the motor would perform 10 horizontal movements of 10 mm at a speed of 0.5 mm/s. Each horizontal movement was then followed by a vertical motion of 1mm at 0.5 mm/s except for the last horizontal movement with a total of 10 horizontal scans and 9 vertical scans. The start and finish times of each motion were saved as well as the times at which each frame was acquired. This particular scanning mechanism was performed in order to write a code that reconstructed the images by stitching all the frames acquired during each horizontal motion and successively join the horizontal scans vertically.

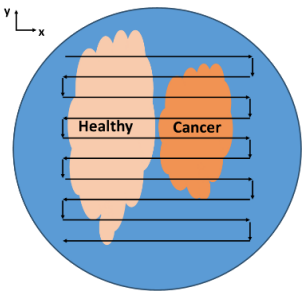

Figure 6.5 Movement pattern followed by the stages. *Bottom surface of the petri containing dish was moved on top of the imaging system. The length of the horizontal path travelled by stage was set equal to the longest side of the rectangular area covered by the tissues. The length of the vertical movements was always set to 1 mm.*

6.1.4 Image Processing

6.1.4.1 Horizontal Reconstruction

In horizontal scans the motor moved at 0.5 mm/s and the image acquisition rate was 1 frame/s. The number of frames in each scan was estimated by using equation 6.2 which was in turn derived by equation 6.1.

$$\boldsymbol{Scan\ Length(mm)} = \left(\boldsymbol{Field\ of\ view\ (mm)}\right) + \left(\frac{\boldsymbol{Motor\ Velocity}\left(\frac{\boldsymbol{mm}}{\boldsymbol{s}}\right)}{\boldsymbol{frame\ rate}\left(\frac{\boldsymbol{frame}}{\boldsymbol{s}}\right)}\right) \times (\#\boldsymbol{frames} - \mathbf{1}) \tag{6.1}$$

$$(\#\boldsymbol{frames\ in\ a\ scan} - \mathbf{1}) = ((\boldsymbol{Scan\ Length(mm)} - (\boldsymbol{Field\ of\ view\ (mm)}) \times \frac{\boldsymbol{frame\ rate}\left(\frac{\boldsymbol{frame}}{\boldsymbol{s}}\right)}{\boldsymbol{Motor\ Velocity}\left(\frac{\boldsymbol{mm}}{\boldsymbol{s}}\right)}) \tag{6.2}$$

In equation 6.1 the first term refers to the field of view of the imaging system in one frame. In fact, the movement of the motors started after that the imaging system acquired the first frame. The following frames were acquired during movement. Therefore, the path travelled by the motor after acquiring the first frame was calculated by multiplying the total number of frames minus the first frame by the ratio between the motor velocity and the frame acquisition rate. Following equation 6.2, if the length of the scan was 10 mm a total number of 17 frames was acquired in each of the horizontal scans. Each frame captured an additional area different from the previous frame after a step of 0.5 mm. The horizontal field of view of the system was 37 pixels and each pixel was 61.5 μm in length. While moving from one frame to the next frame only 8 pixels (492 μm) in the x direction captured a different area. Images were acquired by the imaging system as 64 x 64 pixels frames (Fig. 6.6 (a)). The algorithm removed the zero pixels outside the field of view of the system creating 37 x 37 pixels frames (Fig. 6.6 (b)). In fig. 6.8 three consecutive frames from a horizontal scan were stitched together. In this example, the scan was performed from left to right.

1) Firstly, the algorithm selected a 29 x 37 pixels area from frame 1 as shown in fig. 6.7 (a). The 29 pixels along x direction were selected from pixel 9 to pixel 37 of frame 1.
2) An equivalent 29 x 37 pixels area was also selected from frame 2 as shown in fig. 6.7 (b) . In this case, the 29 pixels along x direction were selected from pixel 1 to pixel 29 of frame 2.
3) The selected areas were averaged. The remaining 8 x 37 pixels areas from frame 1 and frame 2 were stitched together through the resulting average 29 x 37 pixels area to obtain a final 45 x 37 pixels frame as shown in fig. 6.7 (c).

4) A 29 x 37 pixels area from a new frame was selected as shown in fig. 6.8 (d). The 29 pixels along x direction were selected from pixel 1 to pixel 29 of frame 3.
5) An equivalent 29 x 37 pixels area was also selected from the 45 x 37 pixels frame obtained by stitching frame 1 and frame 2 together as shown in fig. 6.7 (e). The 29 pixels along x direction were selected from pixel 17 to pixel 45.
6) The selected areas were averaged. The remaining 16 x 37 pixels area from the frame obtained by joining frame 1 and frame 2 was stitched together with the 8 x 37 pixels area of the new frame 3. This was done through the 29 x 37 pixels average area to obtain a final 53 x 37 pixels frame as shown in fig. 6.7 (f).
7) The procedure was carried out until all frames in the scan were joined.

The horizontal resolution of the final image was forecasted by using equation 6.3.

$$H\ Resolution = (8\ pixles * \#frames) + 29\ pixels \tag{6.3}$$

The first term in the equation refers to the areas of pixels in x direction that were not shared between two consecutive frames. These region are highlighted in green in both fig. 6.7 and the formula. The second term of the equation 6.3 refers to the 29 pixels in x direction that were always shared between two consecutive frames. These region are highlighted in red in both fig. 6.7 and the formula. The same reconstruction steps were followed for scans that were performed from right to left. The only difference was how the 29 x 37 pixels areas were selected before stitching the frames. In fact, with reference to the previously mentioned steps, if the scan happened from right to left the 29 pixels along x direction were selected from pixel 1 to pixel 29 in frame 1 and from 9 to 37 in frame 2. After each horizontal scans were reconstructed, the algorithm stitched all the horizontal scans vertically.

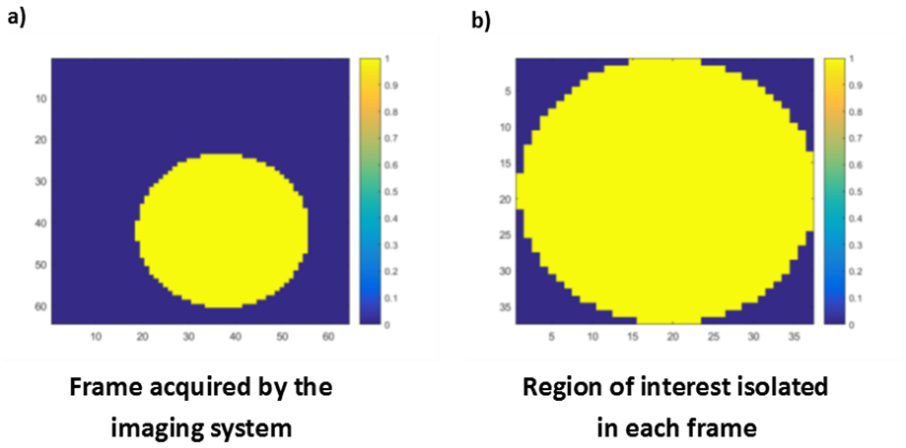

Figure 6.6 Single frames. ***(a)*** *Each frame was acquired by the imaging with a resolution of 64 x 64 pixels.* ***(b)*** *37 x 37 pixel frame created from the original frame by the algorithm.*

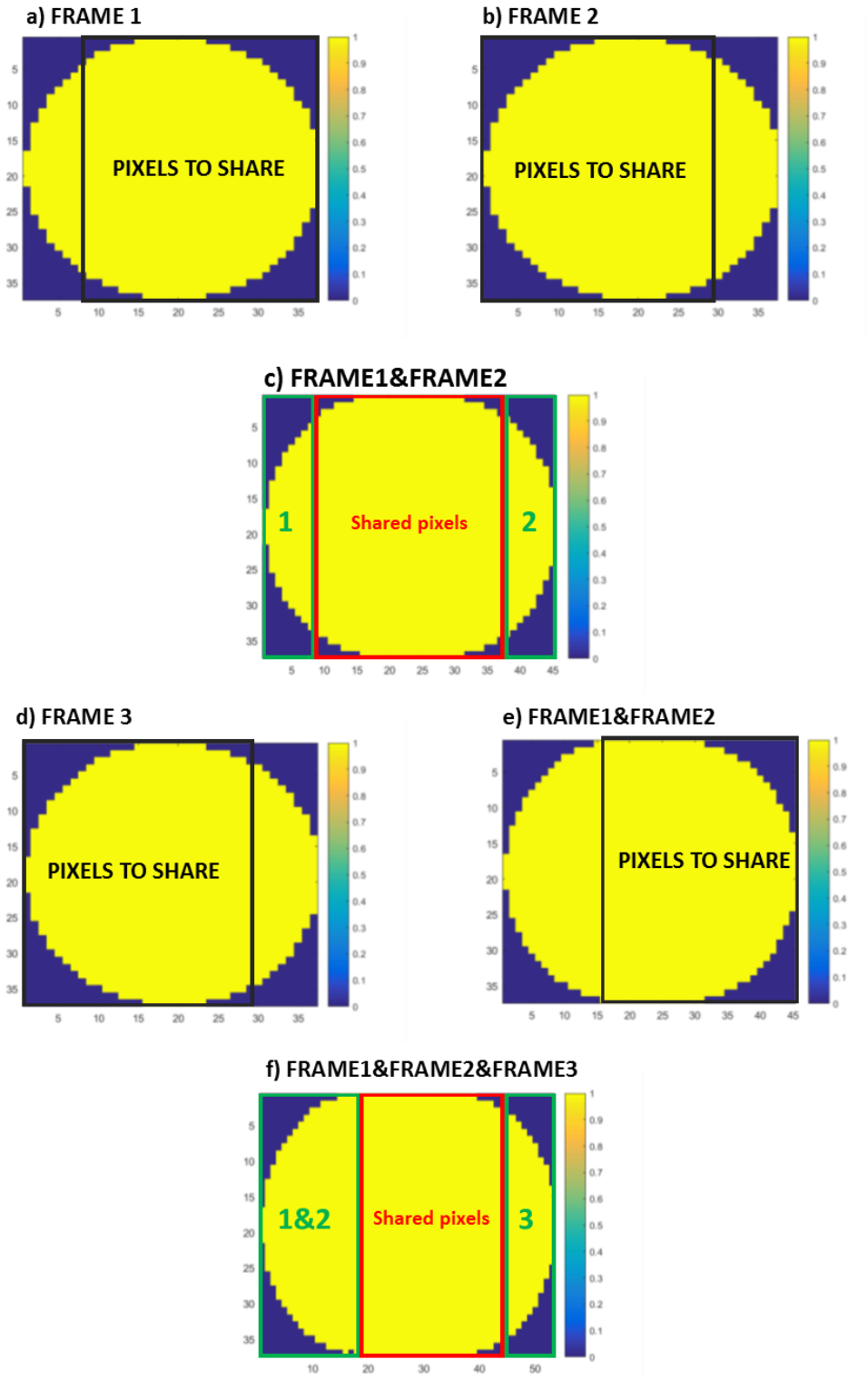

Figure 6.7 Horizontal reconstruction. ***(a)*** *Frame 1.* ***(b)*** *Frame 2. The 29 x 37 areas are highlighted in black as pixels to share in both frames.* ***(c)*** *Final 45 x 37 pixels image obtained by stitching frame 1 and frame 2. The average 29 x37 pixels area that was used to join 8 x 37 pixels areas from frame 1 and frame 2 is highlighted in red.* ***(d)*** *The new frame 3 with 29 x 37 area is highlighted in black.* ***(e)*** *A 29 x 37 area in frame obtained by joining frame 1 and 2 is highlighted in black.* ***(f)*** *Final image containing frame 1, frame 2 and frame 3.*

6.1.4.2 Vertical Reconstruction

Following the previous example, each of the ten horizontal scans was followed by a vertical scan with step of 1 mm except for the last horizontal scan for a total of 10 horizontal scans and 9 vertical scans. The step of the vertical scans was always equal to 1 mm. Since the diameter of the lens in the optical block was 2 mm, the step of the vertical scans was always set to 1 mm to make sure not to miss any surface of the tissue from imaging. The translation speed of the stage and the image acquisition rate were maintained to 0.5 mm/second and 1 frame/second respectively. The vertical field of view of the system was also 37 pixels and each pixel was 61.5 μm in length. In this case, while moving from one scan to the next scan only 17 pixels in y direction (1045 μm) were capturing a different area. In fig. 6.8 three consecutive horizontal scans were stitched together vertically. Each horizontal scan comprised 17 frames joined together as it was previously described for a horizontal scan length of 10 mm. Vertical scans were always performed from the top to the bottom. Therefore, each horizontal scan was stitched on the bottom of the previous horizontal scan.

1) The algorithm selected the bottom 165 x 20 pixels from horizontal scan 1 as shown in fig. 6.8 (a).
2) The algorithm selected the top 165 x 20 pixels from horizontal scan 2 as shown in fig.6.8 (a).
3) The selected areas were averaged. The remaining 165 x 17 pixels areas from frame 1 and frame 2 were stitched together through the resulting average 165 x 20 pixels area to obtain a final 165 x 54 pixels frame as shown in fig. 6.8 (c).
4) The top 165 x 20 pixels area from a new frame was selected as shown in fig. 6.8 (d).
5) The bottom 165 x 20 pixels area was also selected from the 165 x 54 pixels frame obtained by stitching horizontal scan 1 and horizontal scan 2 together as shown in fig. 3.7 (d).
6) The selected areas were averaged. The remaining 165 x 34 pixels area from the frame obtained by stitching horizontal scan 1 and horizontal scan 2 was stitched together with the 165 x 17 pixels area of the new horizontal scan. This was done through the 165 x 20 pixels average area to obtain a final 165 x 71 pixels frame as shown in fig. 7.7 (e). The procedure was carried out until all horizontal scans were joined and the final image was obtained. The vertical resolutions of the images was forecasted using equation 6.3.

$$V\ Resolution = [17 pixels * \#vertical\ scans] + 20\ pixels \quad (6.3)$$

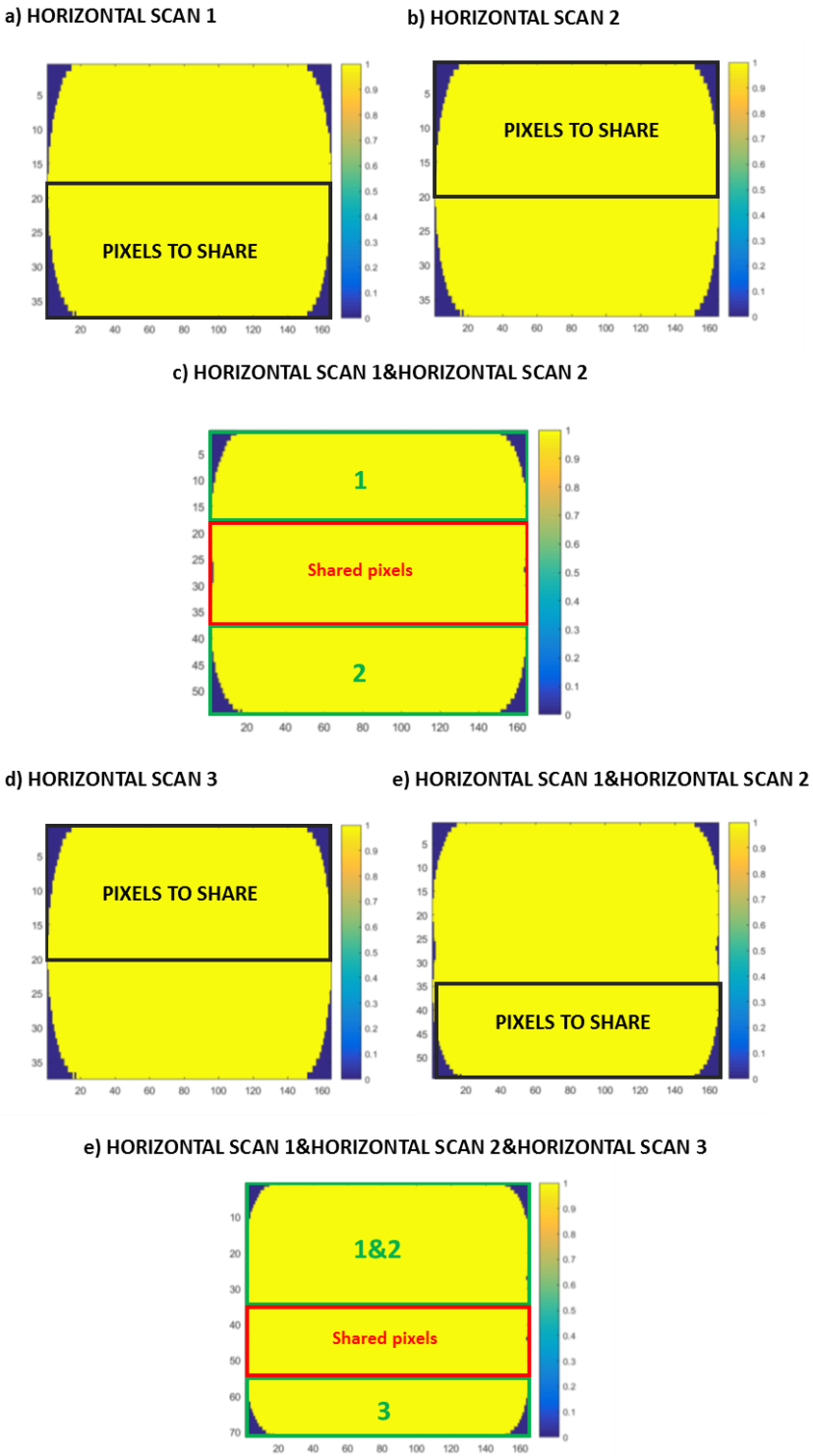

Figure 6.8 Vertical image reconstruction. ***(a)*** *Horizontal scan 1.* ***(b)*** *Horizontal Scan 2. The 165 x 20 areas are highlighted in black as pixels to share in both the scans.* ***(c)*** *Final image 165 x 54 obtained by stitching horizontal scan 1 and horizontal scan 2. The average 165 x 20 pixels area used to join 165 x 17 pixels areas from scan 1 and scan 2 is highlighted in red.* ***(d)*** *The new horizontal scan 3 with the top 165 x 20 area is highlighted in black.* ***(e)*** *A 165 x 20 area in the image obtained by joining scan 1 and scan 2 is highlighted in black.* ***(f)*** *Final image containing horizontal scan 1, horizontal scan 2 and horizontal scan 3.*

6.2 Results

6.2.1 Healthy colon mucosa (Patients 1 to 6)

In six cases the tumour lesion was too small, and it was not possible to obtain any malignant tissue for research. Therefore, tissues from the healthy colon mucosa of six different patients were scanned. Images were reconstructed from the scans to assess the AF signal emitted by the tissues. Each patient was identified by a unique identification number confidential to the hospital. However, in this work patients were numbered starting from 1 in increasing order as they are presented in the text to avoid any confusion for the reader. Specimens from healthy colon mucosa were resected to include all the three structural layers of the colon. The consistency of the tissues from healthy colon was relaxed and deformable. Therefore, the pathologist was not able to strictly maintain the same dimensions for each sample during resection. The tissues were adjusted with the mucosa facing the surface of the petri dish. The dimension of the samples varied from patient to patient. The dimensions of the tissues were measured by using a stainless ruler and the software implemented in the portable microscope to add scale bars to the images. Figs. 6.6 – 6.11 refer to patients 1 to 6 respectively. Each figure comprises the white light image of the specimen acquired with the portable microscope and the corresponding AF image. AF images were reconstructed from the frames acquired by using the optical block and the SPAD array. Each AF image was characterized by a different resolution depending on the distance travelled by the motor during the scan. As discussed previously, the higher the horizontal length of the scan, the higher the number of frames acquired and thus joined to reconstruct the final AF image. All the AF images were displayed using the same intensity scale to directly compare the AF signals from each sample. Regions of interest in each figure were numbered to make a comparison between white light images and AF images. In this section, we will refer to bright and dark regions to make a difference between the regions who show pixels with values from 1000 to 2500 cps and region who shows pixels from 0 to 1000 cps respectively. In fig. 6.9 (a) and (b) the white light image and the AF image of the colon mucosa of patient 1 are shown, respectively. In this case, the length of the horizontal path travelled by the motor to move the sample on top of the imaging system was 20 mm. Therefore, according to equation 6.2, a total number of 37 frames were acquired in each horizontal scan with an acquisition frame rate of 1 frame/s and motor velocity of 0.5 mm/s. Three areas of higher AF intensity were highlighted in fig. 6.9 (b) with the numbers 2 3 and 4. Other two regions in the tissue were characterized by a noticeable decrease in the fluorescence signal. These regions were identified by the numbers 1 and 5. The same regions appeared darker in the withe light image of fig. 6.9 (a). The darker colour might be associated with a higher quantity of blood in those particular

areas of the sample. This would also explain the decrease in the fluorescence signal in fig. 6.9 (b) for those same regions. In fact, as previously mentioned, haemoglobin strongly absorbs green fluorescence. On the other hand, a higher fluorescence signal in the other areas could be related to a higher quantity of fluorophore FAD. Moreover, in region 4 of fig. 6.9 (a), the optical reflection of the microscope objective on surface of the tissue was noticed as a consequence of the petri dish surface interfacing between the microscope and the tissue. In fact, as it was previously mentioned, the bottom surface of the petri dish containing the tissues was imaged by the portable microscope.

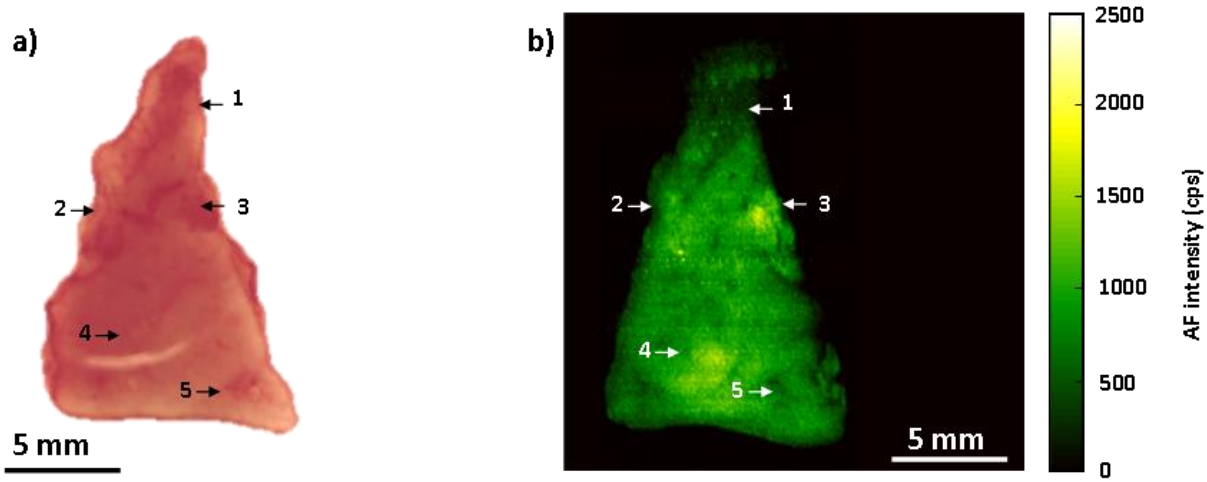

Figure 6.9 Colon mucosa sample from patient 1. (a) *White light image.* ***(b)*** *AF image.*

The number 1 in both figures' 6.10 (a) and (b) points at a region of high AF intensity whereas numbers 2, 3 and 4 refer to regions where a decrease in the AF signal was noticeable. In the white light image of fig. 6.10 (a), the areas associated with a low AF signal appear darker in colour as it was noticed in the sample from the previous patient. In this case the length of the scan was 22 mm and thus the resolution of the final AF image was higher.

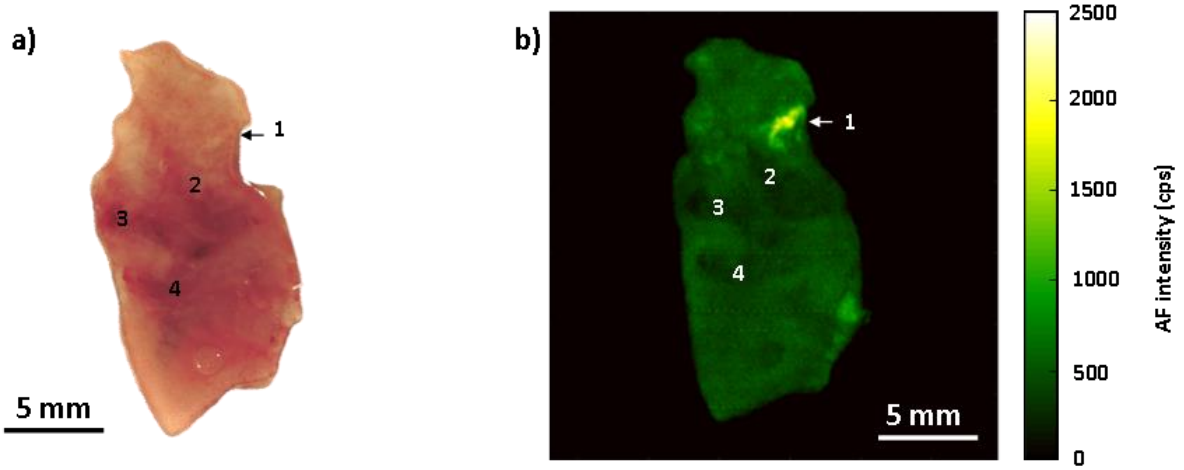

Figure 6.10 Colon mucosa sample from patient 2. (a) *White light image.* ***(b)*** *AF image.*

In the AF images of colon mucosa of patient 4 and 5, regions of low AF signal were noticed (fig. 6.10 (b) and 6.11 (b)). The resolution of the AF image in fig. 6.11 (b) was smaller than the previous images because the size of the sample was smaller. In fact, the total distance travelled by the motor was 18 mm. Both white light images of patients 3 and 4 in fig. 6.9 (a) and 6.10 (a) confirmed the previous findings. In fact, the areas characterized by low signal in the AF images appeared as darker regions in the white light images. Moreover, longitudinal folds of the mucosa layer were noticeable in the white light images of the tissues (figs. 6.9 (a) and 6.10 (a)).

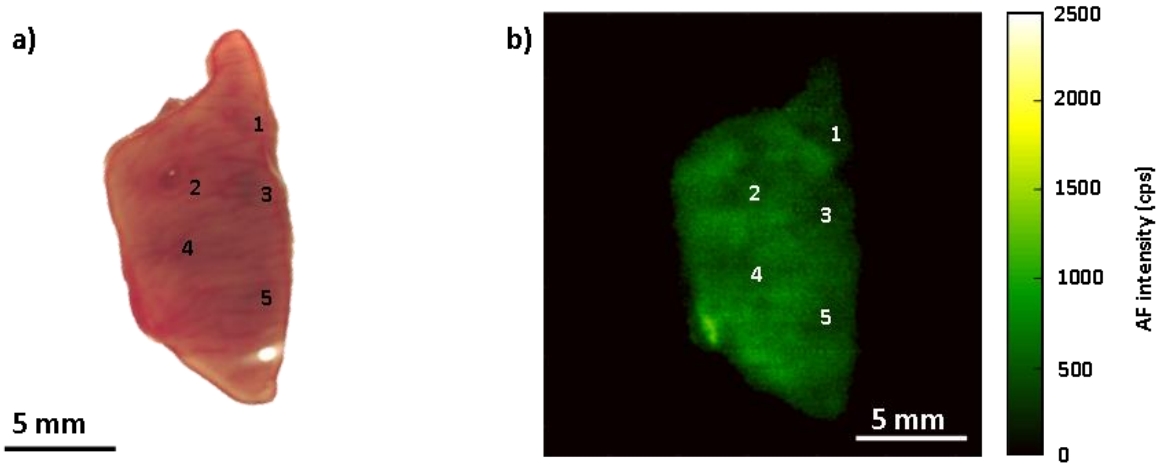

Figure 6.11 Colon mucosa sample from patient 4. (a) *White light image.* ***(b)*** *AF image.*

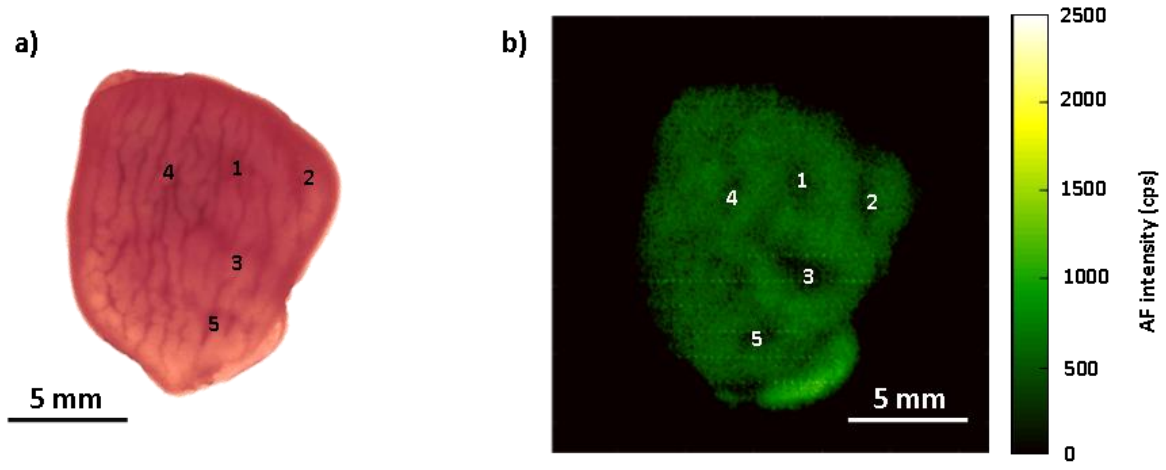

Figure 6.12 Colon mucosa sample from patient 4. (a) *White light image.* ***(b)*** *AF image.*

The resolution of the AF image of the colon mucosa of patient 5 in fig. 6.13 (b) has a higher resolution than the previous images. The length of the horizontal scans that were performed to image the surface of the sample was 26 mm. An area of high AF intensity was highlighted

with the number 1. Two areas of lower AF signal were also noticeable and marked with numbers 2 and 3.

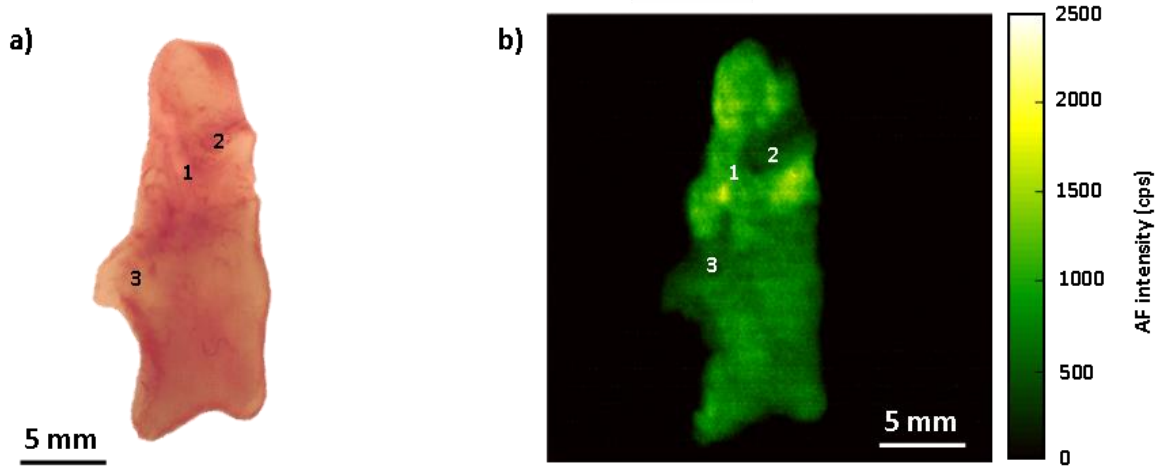

Figure 6.13 Colon mucosa sample from patient 5. (a) *White light image* ***(b)*** *AF image.*

The sample from patient 6 was characterized by an area of high AF 6.14 (b). Three regions of lower AF intensity were also detected. As in the previous cases, the areas in the corresponding white light image of fig. 6.9 (a) appeared darker than the surrounding regions.

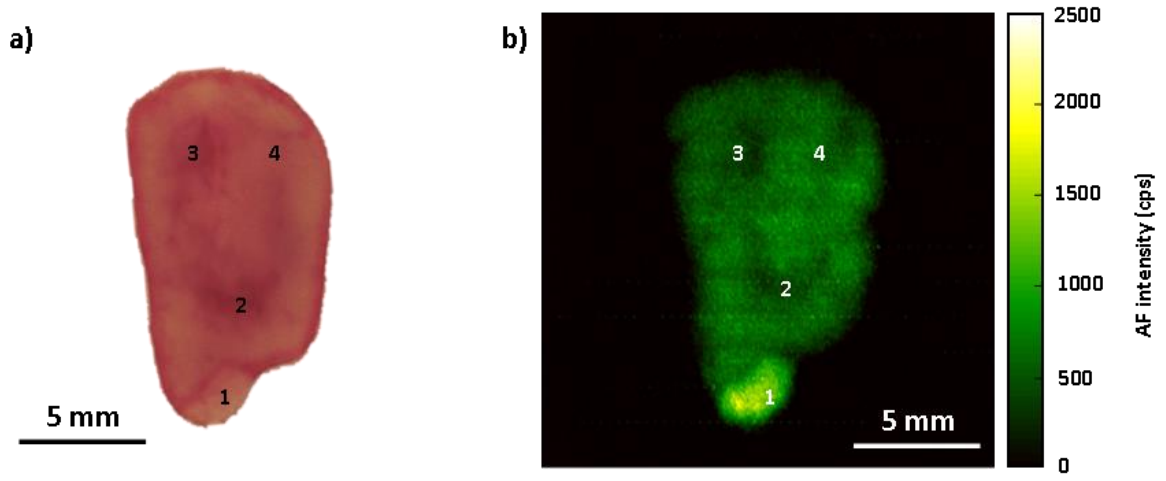

Figure 6.14 Colon mucosa sample from patient 6. (a) *White light image.* ***(b)*** *AF image.*

The average AF intensity values for each sample are shown in fig. 6.15. The results were estimated by writing a code that accounted only for the pixels with values higher than 0 cps because zero values could have been misleading on the estimate of the final average fluorescence intensity values. The highest average AF intensity value of 1656 cps was measured in the sample from patient 5. On the contrary, the specimen from patient 2 showed the lowest AF signals of 1351 cps. The standard deviations of all the pixels in the estimate were also calculated for each patient. The highest value of standard deviation from patient 1

was of 296 cps. Standard deviations of patients 2 and patients 5 were 250 and 225, respectively. The values of standard deviations from the other patients were lower and ranged from 144 cps for patient 4 to 162 cps and 174 cps for patients 3 and 4, respectively.

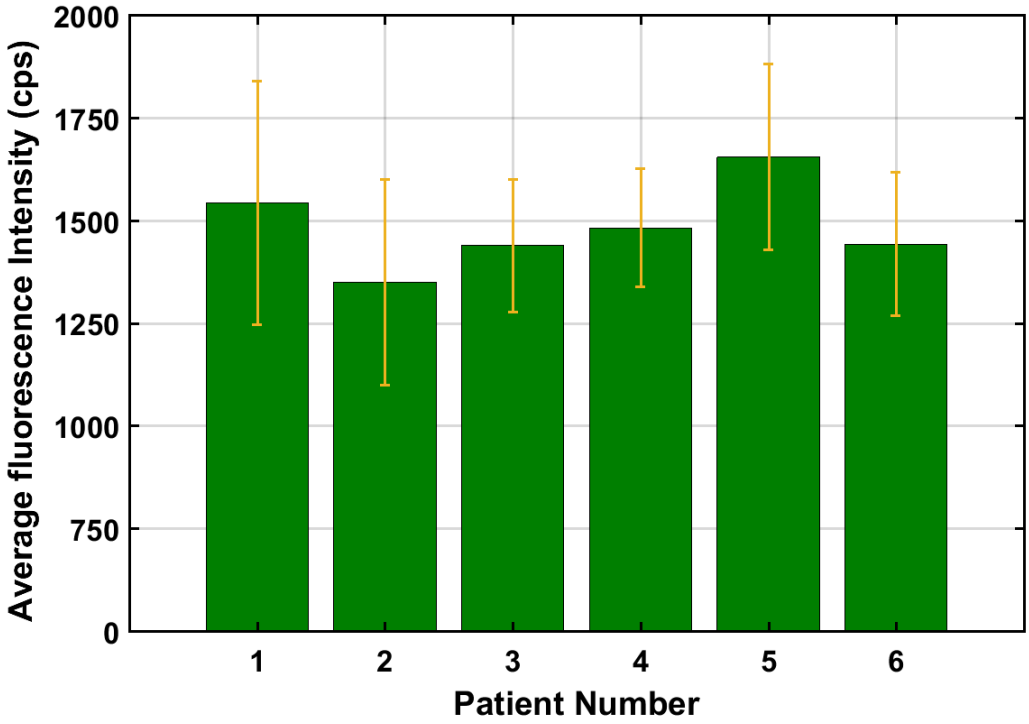

Figure 6.15 Average AF intensity values measured from the AF images of fresh colon mucosa samples from six different patients.

6.2.2 Healthy colon mucosa and cancer tissues (Patients 7 -10)

In four patients the size of the cancerous lesion was large enough to use some of the tissue for research. The experimental procedure previously described for the healthy colon mucosa samples remained unchanged except for the fact that two pieces of tissues were adjusted on the same petri dish. In fact, the tissue from the cancerous lesion was placed with the cancer side facing the surface of the petri dish at a distance of approximately 5 mm from the sample of healthy colon mucosa. This protocol was performed in order to maintain the same environmental conditions for the tissues. Both tissues were imaged at the same time to directly compare the AF signals between healthy colon and cancerous lesion. The length of the horizontal path travelled by the motor in the scans increased because two pieces of tissues had to be imaged. The length of the horizontal scans in the experiments in all the four cases was 28 mm. In this case, numbers were not use to refer to specific regions in order to allow the reader to fully capture the differences in the AF signals from the two tissues. In fig. 6.16 (a) and (b) the white light image and the AF image of the colon mucosa and cancer tissues samples of patient 7 are shown, respectively. In the white light image of fig. 6.16 (a) no

difference between the two tissues samples was perceived by naked eyes. In the AF image of fig. 6.16 (b), the AF signal from the healthy colon mucosa sample allowed to recognize the morphology of the tissue. In fact, the AF signal from the healthy colon mucosa was uniform apart from two regions where the AF intensity was higher. On the contrary, the AF signal from cancer was lower and the profile of the tissue sample was not clear to visualize. The difference in the AF signals between healthy colon mucosa and the cancerous lesion was detected by the imaging system.

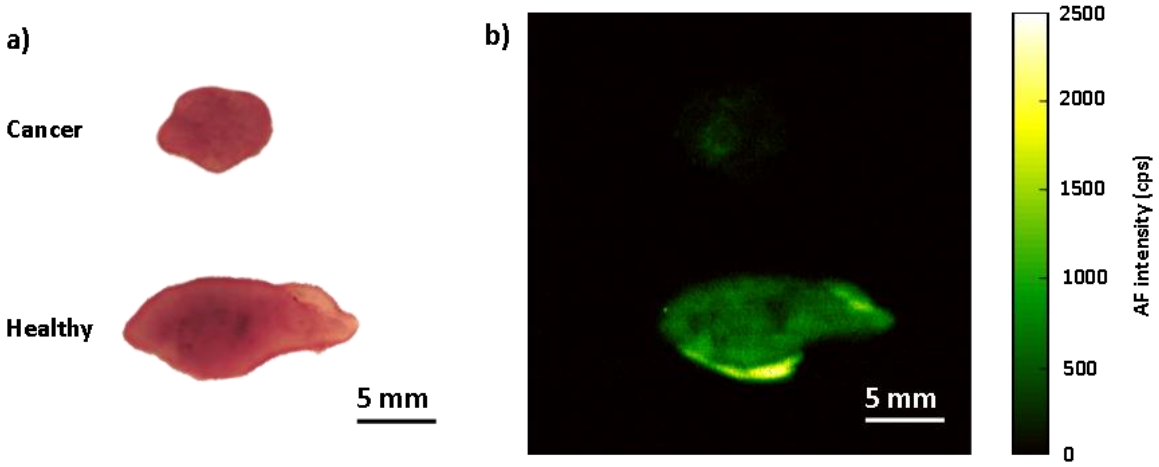

Figure 6.16 Cancer tissue and colon mucosa samples from patient 7. (a) *White light image.* ***(b)*** *AF image.*

In the AF image of fig. 6.17 (b), the shape of the tissue samples from patient 8 was distinguishable. However, the AF signal from the cancer tissues was again lower than in the healthy colon mucosa. In patients 7 and 8 the size of the tumour sample was similar.

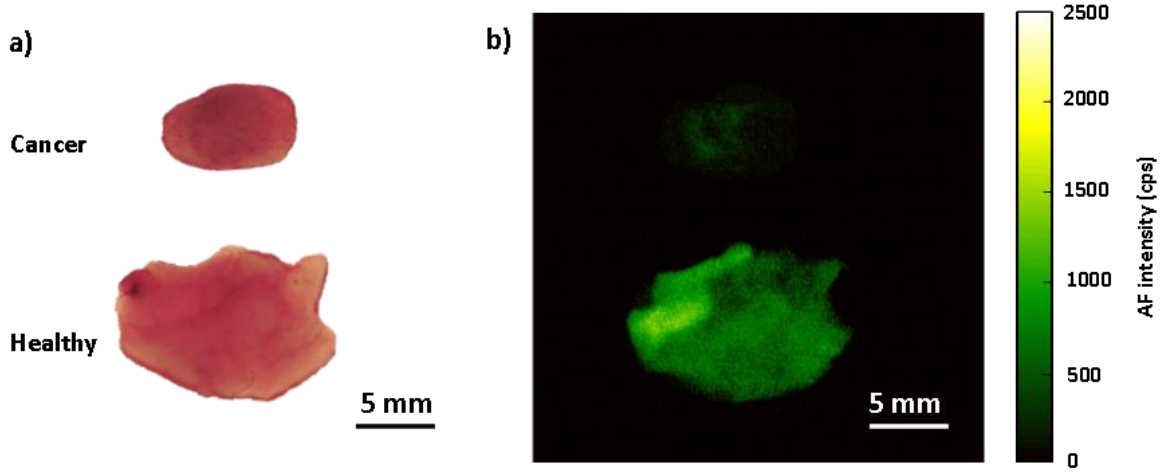

Figure 6.17 Cancer tissue and colon mucosa samples from patient 8. (a) *White light image.* ***(b)*** *AF image.*

The cancer tissue sample from patient 9 was larger in size than the previous cancer samples. As in the previous two cases, no difference between cancer and healthy mucosa was visible from the white light image of fig. 6.18 (a) that was acquired with the portable microscope. On the contrary, a difference in the AF intensities of the two samples was perceived in fig. 6.18 (b). In this case the shape of the malignant tissue was clearly perceivable. This could be due to the fact the tissue sample was bigger in size and thus it was easier for the naked eye to recognize.

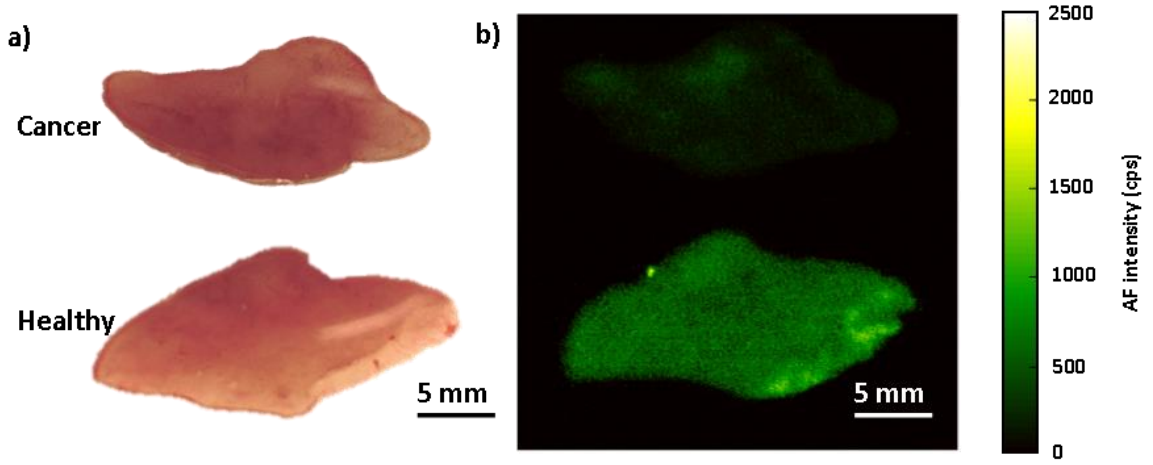

Figure 6.18 Cancer tissue and colon mucosa samples from patient 9. (a) *White light image.* ***(b)*** *AF image.*

In patient 10, the cancer tissue sample was barely visible in the AF image of fig. 6.19 (b). The AF signal from the healthy mucosa was higher than in the cancer tissue. Moreover, a region of high AF signal was noticed in the top left corner of the healthy sample. The AF signal of the healthy mucosa was not evenly distributed as in the other healthy samples.

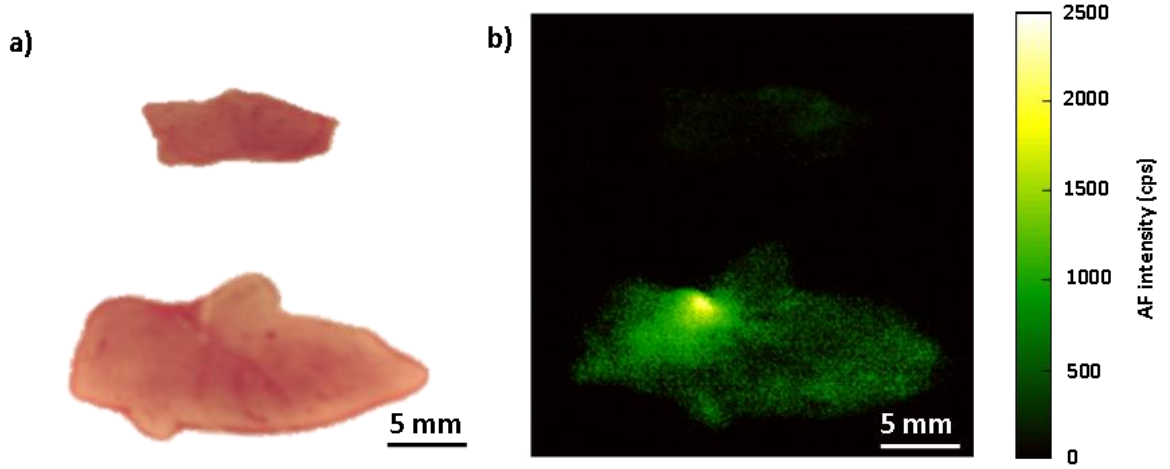

Figure 6.19 Cancer tissue and colon mucosa samples from patient 10. (a) *White light image.* ***(b)*** *AF image.*

The average AF intensity values and the standard deviations for each tissue sample were estimated in cps as in the previous six patients. Only non-zero pixels were taken into account in the estimate of the final values. The final values were divided in two groups: cancer and healthy. Results are shown in fig. 6.20. As it was expected, each cancer sample showed a lower average AF intensity than the respective healthy sample. The highest average AF intensity value from cancer was 661 cps in the sample from patient 9. This result was predictable because the shape of the malignant tissue from patient 9 was clearly perceivable in the AF image of fig. 6.18 (b). On the contrary, the specimen from patient 1 showed the lowest AF signals of 415 cps. In fact, it was not possible to distinguish the shape of the sample in the AF image of fig. 6.16 (b). AF intensities from the cancer tissues of patients 8 and 10 were 513 and 554, respectively. On the other hand, AF intensities from healthy samples were all between 1200 cps and 1500 cps for all patients. Similar values were also measured in patients 1 to 6 when only healthy samples were available (Fig. 6.155).

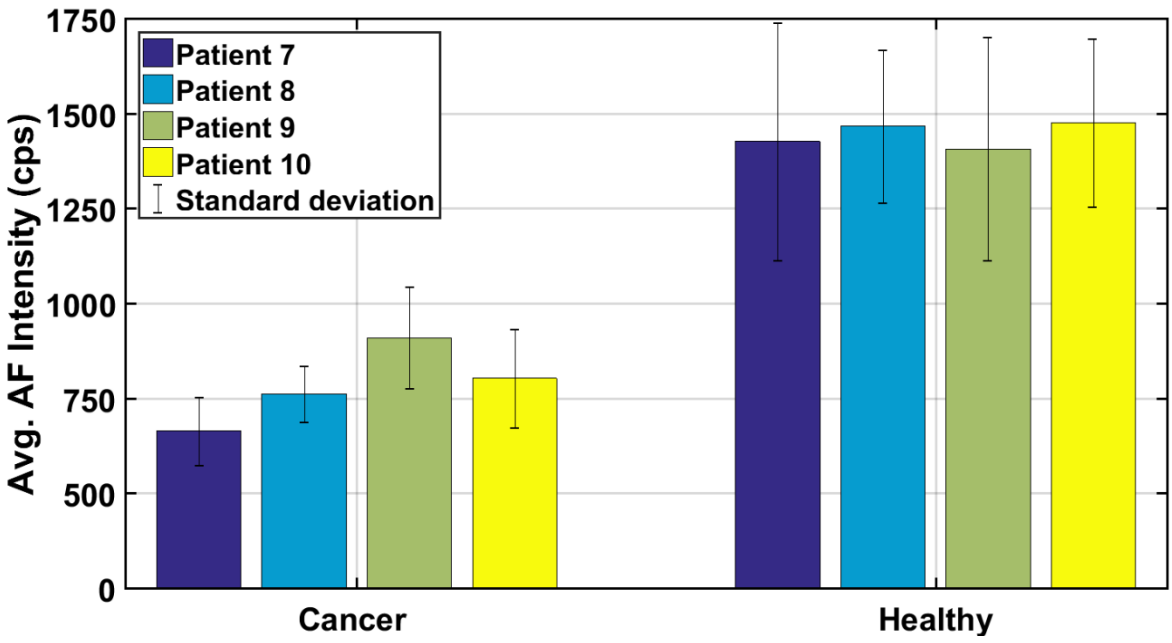

Figure 6.20 Average AF intensity values measured from the AF images of cancer samples and fresh colon mucosa samples of patients 7-10.

6.3 Summary

The aim of this chapter was to discuss a study that was performed at the Western General hospital in Edinburgh. The aim of the study was to assess the capability of the optical block coupled with the SPAD array for the detection of endogenous fluorescence emitted from resected healthy and malignant ex vivo human tissues from the colon. A total of 10 patients participated in the study. The samples were obtained within 30 minutes from hemicolectomy procedures involving the removal of a portion of the patient colon. All the specimens were prepared by a pathologist consultant. Only in four cases the size of the tumour lesion was large enough to use tissue sample for research. In the other six cases only the AF signal from healthy colon mucosa samples was imaged. In the experiments, the petri dishes with the tissues were scanned on top of the optical block. A Matlab code was written to reconstruct the full image of the tissues from the scan. White light images of the tissues were also acquired by using a portable microscope. The AF images from the samples showed changes in the clinically assessed autofluorescence intensities between healthy and malignant tissues. No changes were detected in the white light images. The AF signal from cancer samples was always lower. The decrease in the signal can be due to either reduction of FAD to $FADH_2$ or to the increased thickness of the mucosal layer either of which is linked to the presence of cancer. An increase in the levels of haemoglobin as a result of vascularization in tumours may also have been a possible cause.

7 Conclusions and future work

7.1 Conclusions

In this work a prototype of a miniaturised optical interference block for fluorescence imaging in CE has been designed, fabricated, assembled and characterised. The block consisted of an LED, two lenses and three optical filters to isolate the LED excitation light from green fluorescence light.

The main achievements of this research work are listed below:

- The optical design of the miniaturised optical unit was performed in Zemax optics studio.
- The design of the main body accommodating the optical components was realized in Solidworks.
- The results from the optical simulations were validated through knife-edge experiments.
- It was not possible to find off-the-shelf filters with the thicknesses of few hundred microns specified in the simulations. Therefore, standard filters with the optical transmission properties of interest were purchased and their thickness was reduced through lapping and polishing processes.
- The optical transmission properties of the filters in the optical setup remained unchanged after the lapping and polishing processes. This was proven by characterising the filters with a spectrophotometer before and after reducing their thickness.
- The fabrication of the block's body was realized by wire erosion. The process created precise slots and apertures out of aluminium for keeping all the optical components in place according to the simulations.
- All the components were manually assembled into the main body to create a final prototype of 5 mm W x 6 mm L x 6 mm H.
- The final prototype was then integrated onto a 64 x 64 SPAD array imager that was specifically designed by the MST group at the University of Glasgow for the detection of green fluorescence light.
- The final system comprising optical unit and SPAD imager was characterised by imaging fluorophore phantom solutions in two sets of experiments.
  - The first set of experiments was performed on FAD salt hydrate dissolved in phosphate buffer saline to define the minimum concentration of fluorophore in solution measureable by the system. FAD is the endogenous fluorophore responsible for green AF (515-520 nm) in human tissues. Solutions of FAD at different

concentrations were pipetted in a feature of an USAF target and the imaging system was tested to measure the fluorescence signal within the feature as a function of concentration. The lowest detectable concentration was as small as 7.5μM.

- The second set of experiments was performed on FITC that is an exogenous fluorophore with emission maxima of 519 nm. The results of the experiments showed a lowest detectable concentration of 7.5 nM confirming that FICT has higher fluorescence quantum yield than FAD.

- In vitro experiments were performed at the centre for cell engineering at the University of Glasgow to test the capability of the system to detect colorectal cancer cells labelled with the commercialized cancer-specific fluorescence probe ProteoGreen gGlu^{TM}. The cells were cultured in 96 well plates at four different seeding densities and stained with the probe at concentrations of 5 μM 2 μM and 1 μM. The whole surface of each well was scanned on top of the imaging system. An algorithm was written to forecast a representative fluorescence intensity from each scan. The specificity of the cancer selective probe was also validated by using fibroblasts as negative control. Moreover, the performance of ProteoGreen-gGlu^{TM} was also compared to the general CellTrackerGreent^{TM} fluorescence dye that was designed to work with all cell types. All the results were validated against a gold standard Modulus^{TM} microplate reader for benchmarking. An almost linear correlation between the two systems was found. Final results showed that the cancer–selective probe was responsible for a lower increase in the cells fluorescence signal with respect to the generic fluorescence probe.
- Ex vivo experiments on resected healthy and malignant human tissues from the colon were performed at the Western General Hospital in Edinburgh. Pieces of healthy colon mucosa and adenocarcinoma tissues were obtained fresh, within 30 minutes, from four patients scheduled for partial colon removal. Optical images of the tissues were acquired by using a portable optical microscope. Each petri dish with the specimens was also scanned on top of the imaging system comprising optical block and SPAD array. Frames were acquired for the full duration of the scan. The final AF images for each patient were created by superimposing frames acquired the scan. AF images from the eight specimens revealed differences in the detected AF signal between healthy and malignant tissues. The AF from healthy colon mucosa was always higher. On the other hand, WL images from the optical microscope did not show any difference between healthy and cancerous tissue specimens.

7.2 Future work

Potential improvements that could benefit the research work described in this thesis are listed below.

- Fig. 7.1 shows the CAD design of the final multimodality SonoPill prototype with the optical block for fluoroscopy at the top of the pill. The integration of the optical block and the SPAD array in capsule format would require integrating the SPAD imager chip into a circular PCB with dimensions suitable for incorporation in the pill.

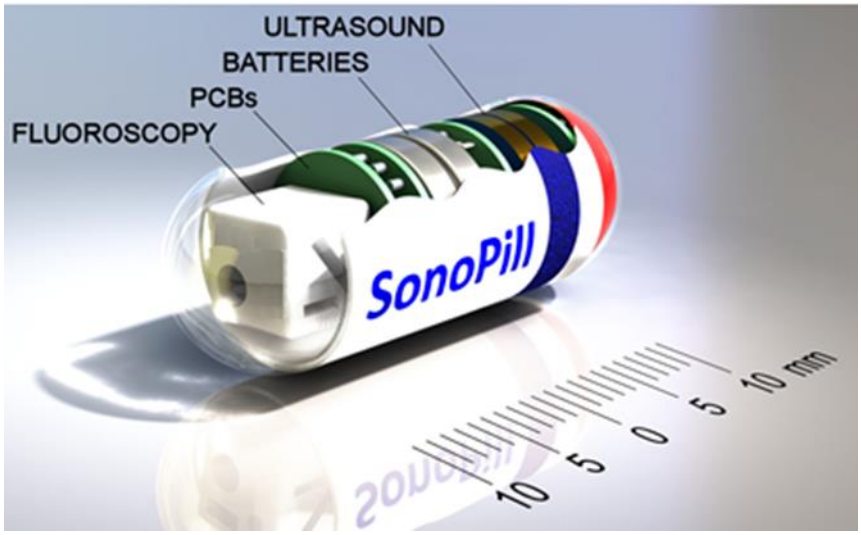

Figure 7.1 CAD prototype of the multimodality SonoPill device **[89].**

- The final size of the optical block could be further shrunk by monolithically integrating the fluorescence green filter directly on top of the SPAD imager thus reducing the height of the block of approximately 1.5 mm.
- Progress in nanophotonics could also be useful to produce fluorescence emission plasmonic filters with narrow transmission bands that could be tuneable for one or more fluorophores [143]. The integration of plasmonic filters on CMOS chips was successfully demonstrated [144], [145]. This choice would be advantageous because the size of these filters is in the nm range.

- The LED power consumption could also be minimized by performing fluorescence life-time measurements instead of steady state measurements. Micro-LED lamps have been developed to provide subnano-second pulses which are ideal for fluorescence life time measurements [146], [147]. SPAD imagers for fluorescence life time measurements were also proposed and showed interesting results in medical

applications [148]–[150]. Another solution could be the integration of a pulsed-laser diode into the block. However, this solution is impractical due to the bulkiness of the devices.

- The angular field of view is currently limited by the dimension of the optical block. Endoscopy technologies used in the clinical environments have large fields of view close to 360 degrees while the angular field of view of the current optics is only 23 degrees. However, since the optics must be used in a multimodality capsule, the other sensing modalities could compensate for the small field of view for a better diagnosis. A promising solution can be found in metalenses that could be used to achieve a better resolution and angular field of view [151]–[153]. The use of metalenses would also be beneficial in terms of size. In fact, metalenses are usually comprised of multiple metasurfaces that could be potentially monolithically stacked together on the block through lithography. A metalens was already successfully integrated in an endoscopy catheter for optical coherence tomography resulting in improved resolution and higher depth of focus [154].
- A structural change could also be applied to the main body by smoothing the edges of the cube thus creating a cylindrical shape which would improve the incorporation of the unit in CE.
- Finally, the main body of the block could be realized with a biocompatible material easy to micro-machine [155]. This choice would benefit the final pill in case of rupture of the external biocompatible casing.

Appendix: Matlab Codes

Software Mask code

```
gate_time = 0.2;
load('Field of view');
image_raw1 = image_archived_DCR_correction;
clearvars -except image_raw1 gate_time;

%First
data_2=cell2mat(image_raw1);

pixels=size(data_2,1); %Number of pixels is equal to the
Number of rows

L=size(data_2,2);% number of columns

n_frames=L/64;   %By dividing the number of columns by
64 you obtain the number of frames

image1=zeros(pixels,pixels,n_frames); %Create a 3d
matrix of zeros

for i = 1:n_frames

   image1(:,:,i)= data_2(:,64*(i-1)+1:64*i); % this
command is written so that when i=1 the 2D matrix in the
3D matrix has the columns from 1 to 64 of the matrix
data, and its respective 64 rows (this means we are
storing the frame 1 in the 3D matrix). When i=2 the 2D
matrix in the 3D matrix has the columns from 65 to 128
of the matrix data, and its respective 64 rows (this
means we are storing the frame 2 in the 3D matrix.
end

clearvars -except image1 image_raw1 image_raw2
image_raw3 gate_time;



n_frames = size(image1,3);

for i = 1:n_frames

   imagef(:,:,i)= image1(:,:,i)/gate_time;
end

image_mean = mean(imagef,3);
```

```
clearvars -except imagef image_mean image_raw1
gate_time;

imagesc(image_mean);
h = colorbar;
ylabel(h, 'Counts/s')
colormap(jet);
axis square;


[centers, radii] = imfindcircles(image_mean,[1 64]);

viscircles(centers, radii,'EdgeColor','r');

imaegSize=size(image_mean)

[xx,yy] = ndgrid((1:imaegSize(1))-
centers(2),(1:imaegSize(2))-centers(1));
mask = (xx.^2 + yy.^2)<radii^2;
mask_final = double(mask);
```

Code to scan the well on top of the optical block

Code to forecast the average value from a well

```
%First Technical Replicate
% load('mask_final_cells');
load('a8f');
A8f= saved_data.images_DCR_corrected;
n_frames1 = size(A8f,2);
for i = 1:n_frames1
    A8f{1,i}= A8f{1,i}.*mask_final_cells;
end

for z  = 1:n_frames1
           a = A8f{1,z};
    A8f{1,z}= fillmissing(a,'linear');

end

a8f_avg_vectors_fluo = zeros(1,n_frames1);
count1 =0;
```

```
sum1 = 0;
  for z = 1: n_frames1
      a = A8f{1,z};
   for i = 1:64
       for j = 1:64
           if (a(i,j)>0)
               sum1 = sum1+a(i,j);
               count1 = count1+1;
           end
       end
       avg = sum1/count1;
```

Code to scan the tissue samples on top of the optical block

Code to reconstruct AF image of the tissues from the scan

```
% Horizontal Reconstruction left to right

frame1 = data{1,n_frames};

frame2 = data{1,n_frames-1};

cv =frame2(24:60,19:55);

bv =frame1(24:60,19:55);


keep1 =bv(:,1:end-8);

cut1 = bv(:,end-7:end);

keep2 =cv(:,9:end);

cut2 = cv(:,1:8);


coloms = size(cut1,2);

rows = size(cut1,1);


interface = zeros(size(cut1));


for j = 1:rows

   for z = 1:coloms
```

```
        if cut1(j,z) == 0
            if cut2(j,z) == 0
            interface(j,z) = 0;
            end
            if cut2(j,z) ~=0
            interface(j,z) = cut2(j,z);
        end
    end

    if cut1(j,z) ~= 0
        if cut2(j,z) == 0
        interface(j,z) = cut1(j,z);
        end
        if cut2(j,z) ~=0
          if cut2(j,z)> cut1(j,z)
              interface(j,z) = cut2(j,z);
            else
              interface(j,z) = cut1(j,z);
            end
        end
     end

    end
end

join2 = [keep1,interface,keep2];

% figure
% imagesc(join1)
% colormap(jet)

%% remaining frames
```

```
for frame = n_frames-2:-1:1

frame1 = join2;
frame2 = data{1,frame};
cv =frame2(24:60,19:55);


keep1 =frame1(:,1:end-8);
cut1 = frame1(:,end-7:end);
keep2 =cv(:,9:end);
cut2 = cv(:,1:8);

coloms = size(cut2,2);
rows = size(cut2,1);

interface = zeros(size(cut2));

for j = 1:rows
   for z = 1:coloms

      if cut1(j,z) == 0
         if cut2(j,z) == 0
         interface(j,z) = 0;
         end
         if cut2(j,z) ~=0
         interface(j,z) = cut2(j,z);
      end
   end

   if cut1(j,z) ~= 0
```

```
        if cut2(j,z) == 0
        interface(j,z) = cut1(j,z);
        end
        if cut2(j,z) ~=0
          if cut2(j,z)> cut1(j,z)
              interface(j,z) = cut2(j,z);
            else
              interface(j,z) = cut1(j,z);
            end
        end
     end

    end
end

join2 = [keep1,interface,keep2];

end
% Horizontal Reconstruction right to left
frame1 = data{1,1};
frame2 = data{1,2};
cv =frame2(24:60,19:55);
bv =frame1(24:60,19:55);

keep1 =bv(:,1:end-8);
cut1 = bv(:,end-7:end);
keep2 =cv(:,9:end);
cut2 = cv(:,1:8);

coloms = size(cut1,2);
rows = size(cut1,1);
```

```
interface = zeros(size(cut1));

for j = 1:rows
   for z = 1:coloms

      if cut1(j,z) == 0
         if cut2(j,z) == 0
         interface(j,z) = 0;
         end
         if cut2(j,z) ~=0
         interface(j,z) = cut2(j,z);
      end
   end

   if cut1(j,z) ~= 0
      if cut2(j,z) == 0
      interface(j,z) = cut1(j,z);
      end
      if cut2(j,z) ~=0
        if cut2(j,z)> cut1(j,z)
           interface(j,z) = cut2(j,z);
        else
           interface(j,z) = cut1(j,z);
         end
      end
    end

   end
end

join1 = [keep1,interface,keep2];
```

```
% figure
% imagesc(join1)
% colormap(jet)

%% remaining frames


for frame = 3:n_frames

frame1 = join1;
frame2 = data{1,frame};
cv =frame2(24:60,19:55);


keep1 =frame1(:,1:end-8);
cut1 = frame1(:,end-7:end);
keep2 =cv(:,9:end);
cut2 = cv(:,1:8);

coloms = size(cut2,2);
rows = size(cut2,1);

interface = zeros(size(cut2));

for j = 1:rows
   for z = 1:coloms

      if cut1(j,z) == 0
         if cut2(j,z) == 0
         interface(j,z) = 0;
         end
```

```
        if cut2(j,z) ~=0
        interface(j,z) = cut2(j,z);
      end
   end

   if cut1(j,z) ~= 0
      if cut2(j,z) == 0
      interface(j,z) = cut1(j,z);
      end
      if cut2(j,z) ~=0
       if cut2(j,z)> cut1(j,z)
           interface(j,z) = cut2(j,z);
        else
           interface(j,z) = cut1(j,z);
        end
      end
    end

   end
end

join1 = [keep1,interface,keep2];


end
% Vertical Reconstruction
row1 = size(join1,1);
col1 =size(join1,2);

row2 = size(join2,1)
col2 = size(join2,2)

to_cut1 = join1(1:20,:);
to_keep1 =join1(21:end,:);

to_cut2 =join2((row2-19):row2,:);
to_keep2 = join2(1:(row2-20),:);
```

```
to_keep_interface = zeros(size(to_cut2));

row = size(to_cut1,1);
col = size(to_cut1,2);

for j = 1:row
for z = 1 : col

    if to_cut1(j,z) == 0
        if to_cut2(j,z) == 0
        to_keep_interface(j,z) = 0;
        end
        if to_cut2(j,z) ~=0
        to_keep_interface(j,z) = to_cut2(j,z);
        end
    end

    if to_cut1(j,z) ~= 0
        if to_cut2(j,z) == 0
        to_keep_interface(j,z) = to_cut1(j,z);
        end
        if to_cut2(j,z) ~=0
            if to_cut2(j,z)> to_cut1(j,z)
                to_keep_interface(j,z) = to_cut2(j,z);
            else
                to_keep_interface(j,z) = to_cut1(j,z);
            end
        end
    end

 end
end


joinv = [to_keep2;to_keep_interface; to_keep1];

figure()
imagesc(joinv);
shading interp;
colorbar
% set(gca,'YDir','reverse')
% set(gca,'XDir','reverse')


clearvars -except healthy_side cancer_side mask_final
join1 joinv join2b join1b join1 join2 a b c d e f g
```

References

[1] A. Moglia, A. Menciassi, P. Dario, and A. Cuschieri, “Capsule endoscopy: progress update and challenges ahead,” *Nat. Rev. Gastroenterol. Hepatol.*, vol. 6, no. 6, p. 353, 2009.

[2] Gavriel Iddan, Gavriel Meron, Arkady Glukhovsky, and Paul Swain, “Wireless capsule endoscopy,” *Nature*, vol. 405, no. 6785, 2000.

[3] S. M. Milluzzo, A. Bizzotto, P. Cesaro, and C. Spada, “Colon capsule endoscopy and its effectiveness in the diagnosis and management of colorectal neoplastic lesions,” *Expert Rev. Anticancer Ther.*, vol. 19, no. 1, pp. 71–80, 2019.

[4] M. Esaki *et al.*, “Capsule endoscopy findings for the diagnosis of Crohn’s disease: a nationwide case–control study,” *J. Gastroenterol.*, vol. 54, no. 3, pp. 249–260, 2019.

[5] A. Mata *et al.*, “A prospective trial comparing wireless capsule endoscopy and barium contrast series for small-bowel surveillance in hereditary GI polyposis syndromes,” *Gastrointest. Endosc.*, vol. 61, no. 6, pp. 721–725, 2005.

[6] M. Yu, “M2A capsule endoscopy. A breakthrough diagnostic tool for small intestine imaging.,” *Gastroenterol. Nurs. Off. J. Soc. Gastroenterol. Nurses Assoc.*, vol. 25, no. 1, pp. 24–27, 2002.

[7] C. Gheorghe, R. Iacob, and I. Bancila, “Olympus capsule endoscopy for small bowel examination,” *J. Gastrointest. Liver Dis.*, vol. 16, no. 3, p. 309, 2007.

[8] “Sonopill: The future of Capsule Ultrasound.” .

[9] G. Cummins *et al.*, “Gastrointestinal diagnosis using non-white light imaging capsule endoscopy,” *Nat. Rev. Gastroenterol. Hepatol.*, p. 1, 2019.

[10] M. Monici, “Cell and tissue autofluorescence research and diagnostic applications,” *Biotechnol. Annu. Rev.*, vol. 11, pp. 227–256, 2005.

[11] B. Wu, S. K. Gayen, and M. Xu, “Fluorescence spectroscopy using excitation and emission matrix for quantification of tissue native fluorophores and cancer diagnosis,” in *Photonic Therapeutics and Diagnostics X*, 2014, vol. 8926, p. 89261M.

[12] M. Hussein, L. Lovat, and R. Haidry, “Advances in diagnostic and therapeutic endoscopy,” *Medicine (Baltimore).*, 2019.

[13] D. C. G. De Veld, M. J. H. Witjes, H. Sterenborg, and J. L. N. Roodenburg, “The status of in vivo autofluorescence spectroscopy and imaging for oral oncology,” *Oral Oncol.*, vol. 41, no. 2, pp. 117–131, 2005.

[14] M. Kato, M. Kaise, J. Yonezawa, Y. Yoshida, and H. Tajiri, “Autofluorescence endoscopy versus conventional white light endoscopy for the detection of superficial gastric neoplasia: a prospective comparative study,” *Endoscopy*, vol. 39, no. 11, pp. 937–941, 2007.

[15] L. K. Wanders, J. E. East, S. E. Uitentuis, M. M. G. Leeflang, and E. Dekker, “Diagnostic performance of narrowed spectrum endoscopy, autofluorescence imaging, and confocal laser endomicroscopy for optical diagnosis of colonic polyps: a meta-analysis,” *Lancet Oncol.*, vol. 14, no. 13, pp. 1337–1347, 2013.

[16] S. Achilefu, “Lighting up tumors with receptor-specific optical molecular probes,” *Technol. Cancer Res. Treat.*, vol. 3, no. 4, pp. 393–409, 2004.

[17] R. Weissleder and V. Ntziachristos, “Shedding light onto live molecular targets,” *Nat. Med.*, vol. 9, no. 1, p. 123, 2003.

[18] S. F. Fulghum, “Autofluorescence imaging system for endoscopy.” Google Patents, Apr-2002.

[19] S. E. Cotterill, “Gut: The Inside Story of Our Body’s Most Under-rated Organ by Giulia Enders.” .

[20] “Gastrointestinal system anatomy | HealthEngine Blog.” [Online]. Available: https://healthengine.com.au/info/gastrointestinal-system. [Accessed: 07-Nov-2020].

[21] C. Ell, S. Remke, A. May, L. Helou, R. Henrich, and G. Mayer, “The first prospective controlled trial comparing wireless capsule endoscopy with push enteroscopy in chronic gastrointestinal bleeding.,” *Endoscopy*, vol. 34, no. 9, pp. 685–9, Sep. 2002.

[22] H. Sugano, K. Nakamura, and Y. Kato, “Pathological studies of human gastric cancer.,” *Acta Pathol. Jpn.*, vol. 32 Suppl 2, pp. 329–47, Jan. 1982.

[23] L. A. Torre, R. L. Siegel, E. M. Ward, and A. Jemal, “Global cancer incidence and mortality rates and trends - An update,” *Cancer Epidemiol. Biomarkers Prev.*, vol. 25, no. 1, pp. 16–27, 2016.

[24] M. Mirmozaffari, “Presenting an expert system for early diagnosis of gastrointestinal diseases,” *Int. J. Gastroenterol. Sci.*, vol. 1, no. 1, pp. 21–27, 2020.

[25] S. Komurcu, K. A. Nelson, D. Walsh, R. B. Ford, and L. A. Rybicki, “Gastrointestinal symptoms among inpatients with advanced cancer,” *Am. J. Hosp. Palliat. Med.*, vol. 19, no. 5, pp. 351–355, 2002.

[26] A. Jagadeesh, G. M. Sheela, B. P. Naidu, and P. V. Bramhachari, “Prognostic Molecular Markers for Gastrointestinal Cancer,” in *Recent Advancements in Biomarkers and Early Detection of Gastrointestinal Cancers*, Springer, 2020, pp. 45–53.

[27] “Treatment for Cancer - National Cancer Institute.” [Online]. Available: https://www.cancer.gov/about-cancer/treatment. [Accessed: 07-Nov-2020].

[28] “Understanding Colorectal Cancer | Knight Cancer Institute| OHSU.” [Online]. Available: https://www.ohsu.edu/knight-cancer-institute/understanding-colorectal-cancer. [Accessed: 07-Nov-2020].

[29] T. Matsuoka and M. Yashiro, “Precision medicine for gastrointestinal cancer: Recent progress and future perspective,” *World J. Gastrointest. Oncol.*, vol. 12, no. 1, p. 1, 2020.

[30] J. L. Ponsky and A. T. Strong, “A History of Flexible Gastrointestinal Endoscopy,” *Surg. Clin.*, vol. 100, no. 6, pp. 971–992, 2020.

[31] F. H. Opper, “The Growth of Gastroenterologic Knowledge During the Twentieth Century,” *JAMA*, vol. 273, no. 24, p. 1961, 1995.

[32] B. Schuman, “The development of the endoscope,” *Gastrointest. Dis. an Endosc. approach*, vol. 1, pp. 9–24, 1997.

[33] V. Subramanian *et al.*, “Comparison of high definition with standard white light endoscopy for detection of dysplastic lesions during surveillance colonoscopy in patients with colonic inflammatory bowel disease,” *Inflamm. Bowel Dis.*, vol. 19, no. 2, pp. 350–355, 2013.

[34] S. Schlegel *et al.*, “Endoscope with flexible Tip and Chip-on-the-Tip Camera,” in *World Congress on Medical Physics and Biomedical Engineering May 26-31, 2012, Beijing, China*, 2013, pp. 2111–2114.

[35] P. J. Trivedi and B. Braden, “Indications, stains and techniques in chromoendoscopy,” *Qjm*, vol. 106, no. 2, pp. 117–131, 2013.

[36] M. Kato *et al.*, “Magnifying endoscopy with narrow-band imaging achieves superior accuracy in the differential diagnosis of superficial gastric lesions identified with white-light endoscopy: a prospective study,” *Gastrointest. Endosc.*, vol. 72, no. 3, pp. 523–529, 2010.

[37] C. Hu, M.-H. Meng, and M. Mandal, “Efficient linear algorithm for magnetic localization and orientation in capsule endoscopy,” in *2005 IEEE Engineering in Medicine and Biology 27th Annual Conference*, 2006, pp. 7143–7146.

[38] H. Machida *et al.*, “Narrow-band imaging in the diagnosis of colorectal mucosal lesions: a pilot study,” *Endoscopy*, vol. 36, no. 12, pp. 1094–1098, 2004.

[39] M. Guelrud, I. Herrera, H. Essenfeld, and J. Castro, “Enhanced magnification endoscopy: a new technique to identify specialized intestinal metaplasia in Barrett’s esophagus,” *Gastrointest. Endosc.*, vol. 53, no. 6, pp. 559–565, 2001.

[40] S. Galandiuk, V. W. Fazio, and R. E. Petras, “Fluorescein endoscopy,” *Dis. colon rectum*, vol. 31, no. 11, pp. 848–853, 1988.

[41] M. B. Wallace *et al.*, “The safety of intravenous fluorescein for confocal laser endomicroscopy in the gastrointestinal tract,” *Aliment. Pharmacol. Ther.*, vol. 31, no. 5, pp. 548–552, 2010.

[42] R. Banerjee and D. Reddy, “Advances in endoscopic imaging: Advantages and limitations,” *J. Dig. Endosc.*, vol. 3, no. 5, p. 7, 2012.

[43] P. Sharma *et al.*, “The utility of a novel narrow band imaging endoscopy system in patients with Barrett’s esophagus,” *Gastrointest. Endosc.*, vol. 64, no. 2, pp. 167–175, 2006.

[44] S. C. Reddymasu and P. Sharma, “Advances in endoscopic imaging of the esophagus,” *Gastroenterol. Clin.*, vol. 37, no. 4, pp. 763–774, 2008.

[45] H. Osawa and H. Yamamoto, “Present and future status of flexible spectral imaging color enhancement and blue laser imaging technology,” *Dig. Endosc.*, vol. 26, pp. 105–115, 2014.

[46] N. Yoshida *et al.*, “Blue laser imaging, blue light imaging, and linked color imaging for the detection and characterization of colorectal tumors,” *Gut Liver*, vol. 13, no. 2, p. 140, 2019.

[47] C. K. Lee, S.-H. Lee, and Y. Hwangbo, “Narrow-band imaging versus I-Scan for the real-time histological prediction of diminutive colonic polyps: a prospective comparative study by using the simple unified endoscopic classification,” *Gastrointest. Endosc.*, vol. 74, no. 3, pp. 603–609, 2011.

[48] S. W. Jung *et al.*, “Flexible spectral imaging color enhancement (FICE) is useful to

discriminate among non-neoplastic lesion, adenoma, and cancer of stomach," *Dig. Dis. Sci.*, vol. 56, no. 10, p. 2879, 2011.

[49] N. Yoshida *et al.*, "The detection of surface patterns by flexible spectral imaging color enhancement without magnification for diagnosis of colorectal polyps," *Int. J. Colorectal Dis.*, vol. 27, no. 5, pp. 605–611, 2012.

[50] S. Beg, A. Wilson, and K. Ragunath, "The use of optical imaging techniques in the gastrointestinal tract," *Frontline Gastroenterol.*, vol. 7, no. 3, pp. 207–215, 2016.

[51] T. S. Kirtane and M. S. Wagh, "Endoscopic optical coherence tomography (OCT): advances in gastrointestinal imaging," *Gastroenterol. Res. Pract.*, vol. 2014, 2014.

[52] M. Mitsunaga *et al.*, "Fluorescence endoscopic detection of murine colitis-associated colon cancer by topically applied enzymatically rapid-activatable probe," *Gut*, vol. 62, no. 8, pp. 1179–1186, 2013.

[53] Y. Urano *et al.*, "Rapid Cancer Detection by Topically Spraying a g - Glutamyltranspeptidase – Activated Fluorescent Probe," vol. 3, no. 110, 2011.

[54] E. L. Bird-Lieberman *et al.*, "Molecular imaging using fluorescent lectins permits rapid endoscopic identification of dysplasia in Barrett's esophagus," *Nat. Med.*, vol. 18, no. 2, pp. 315–321, 2012.

[55] N. Sharma, N. Takeshita, and K. Y. Ho, "Raman spectroscopy for the endoscopic diagnosis of esophageal, gastric, and colonic diseases," *Clin. Endosc.*, vol. 49, no. 5, p. 404, 2016.

[56] "Jablonski Diagram | What is it? | Edinburgh Instruments." [Online]. Available: https://www.edinst.com/blog/jablonski-diagram/. [Accessed: 07-Nov-2020].

[57] E. U. Condon, "The Franck-Condon principle and related topics," *Am. J. Phys.*, vol. 15, no. 5, pp. 365–374, 1947.

[58] "File:Franck Condon Diagram.svg - Wikimedia Commons." [Online]. Available: https://commons.wikimedia.org/wiki/File:Franck_Condon_Diagram.svg. [Accessed: 07-Nov-2020].

[59] D. F. Swinehart, "The beer-lambert law," *J. Chem. Educ.*, vol. 39, no. 7, p. 333, 1962.

[60] A. Sassaroli and S. Fantini, "Comment on the modified Beer–Lambert law for scattering media," *Phys. Med. Biol.*, vol. 49, no. 14, p. N255, 2004.

[61] W.-F. Cheong, S. A. Prahl, and A. J. Welch, "A review of the optical properties of biological tissues," *IEEE J. Quantum Electron.*, vol. 26, no. 12, pp. 2166–2185, 1990.

[62] C. Sun, *Biophotonics for tissue oxygenation analysis*. Elsevier Ltd., 2015.

[63] L. A. Sordillo *et al.*, "Third therapeutic spectral window for deep tissue imaging," in *Optical Biopsy XII*, 2014, vol. 8940, p. 89400V.

[64] G. Thews, "Blood gas transport and acid-base balance," in *Human Physiology*, Springer, 1983, pp. 489–507.

[65] A. T. R. Williams, S. A. Winfield, and J. N. Miller, "Relative fluorescence quantum yields using a computer-controlled luminescence spectrometer," *Analyst*, vol. 108, no. 1290, pp. 1067–1071, 1983.

[66] M. R. Eftink and C. A. Ghiron, “Fluorescence quenching studies with proteins,” *Anal. Biochem.*, vol. 114, no. 2, pp. 199–227, 1981.

[67] G. A. Wagnieres, W. M. Star, and B. C. Wilson, “Invited Review ln Vivo Fluorescence Spectroscopy and Imaging for Oncological Applications,” vol. 68, no. 5, pp. 603–632, 1998.

[68] “Autofluorescence Imaging (AFI) - Optical Cancer Imaging LabOptical Cancer Imaging Lab.” [Online]. Available: http://biophotonics.bccrc.ca/index.php/research/technologies/afi/. [Accessed: 14-Nov-2020].

[69] L. Ehlen *et al.*, “Synergy of Fluorescence and Near-Infrared Spectroscopy in Detection of Colorectal Cancer,” *J. Surg. Res.*, vol. 242, pp. 349–356, 2019.

[70] L.-M. W. K. Song *et al.*, “Autofluorescence imaging,” *Gastrointest. Endosc.*, vol. 73, no. 4, pp. 647–650, 2011.

[71] R. C. Benson, R. A. Meyer, M. E. Zaruba, and G. M. McKhann, “Cellular autofluorescence--is it due to flavins?,” *J. Histochem. Cytochem.*, vol. 27, no. 1, pp. 44–48, 1979.

[72] Y. Yuanlong, Y. Yanming, L. Fuming, L. Yufen, and M. Paozhong, “Characteristic autofluorescence for cancer diagnosis and its origin,” *Lasers Surg. Med.*, vol. 7, no. 6, pp. 528–532, 1987.

[73] R. Adachi, T. Utsui, and K. Furusawa, “Development of the autofluorescence endoscope imaging system,” *Diagn. Ther. Endosc.*, vol. 5, no. 2, pp. 65–70, 1999.

[74] J. Haringsma *et al.*, “Autofluorescence endoscopy: feasibility of detection of GI neoplasms unapparent to white light endoscopy with an evolving technology,” *Gastrointest. Endosc.*, vol. 53, no. 6, pp. 642–650, 2001.

[75] W. L. Curvers *et al.*, “Endoscopic tri-modal imaging for detection of early neoplasia in Barrett’s oesophagus: A multi-centre feasibility study using high-resolution endoscopy, autofluorescence imaging and narrow band imaging incorporated in one endoscopy system,” *Gut*, vol. 57, no. 2, pp. 167–172, 2008.

[76] C. J. R. Sheppard, “Confocal microscopy. The Development of a Modern Microscopy,” *Encycl. Biomater. Biomed. Eng.*, no. October, pp. 41–47, 1990.

[77] N. Tamai, Y. Takeuchi, and H. Tajiri, “Second-generation autofluorescence imaging for colorectal neoplasia,” *Dig. Endosc.*, vol. 27, pp. 46–46, 2015.

[78] K. Woods, D. Kang, H. Neumann, M. Vieth, and E. Coron, “Confocal Endomicroscopy,” *Pathobiol. Hum. Dis. A Dyn. Encycl. Dis. Mech.*, vol. 12, no. 2, pp. 3890–3911, 2014.

[79] H. Neumann, R. Kiesslich, M. B. Wallace, and M. F. Neurath, “Confocal Laser Endomicroscopy: Technical Advances and Clinical Applications,” *Gastroenterology*, vol. 139, no. 2, pp. 388-392.e2, 2010.

[80] C. L. Leggett and E. C. Gorospe, “Application of confocal laser endomicroscopy in the diagnosis and management of Barrett’s esophagus,” *Ann. Gastroenterol.*, vol. 27, no. 3, pp. 193–199, 2014.

[81] A. Zambelli, V. Villanacci, E. Buscarini, G. Bassotti, and L. Albarello, “Collagenous colitis: a case series with confocal laser microscopy and histology correlation,” *Endoscopy*, vol. 40, no. 07, pp. 606–608, 2008.

[82] 1R Kiesslich *et al.*, “Local barrier dysfunction identified by confocal laser endomicroscopy predicts relapse in inflammatory bowel disease,” *Gut*, vol. 61, no. 8, pp. 1146–1153, 2012.

[83] H. Neumann and R. Kiesslich, “Endomicroscopy and endocytoscopy in IBD,” *Gastrointest. Endosc. Clin.*, vol. 23, no. 3, pp. 695–705, 2013.

[84] A. Hoffman, R. Atreya, T. Rath, and M. F. Neurath, “Use of fluorescent dyes in endoscopy and diagnostic investigation,” *Visc. Med.*, vol. 36, no. 2, pp. 95–103, 2020.

[85] S. Paramsothy and R. W. L. Leong, “Endoscopy: Fluorescein contrast in confocal laser endomicroscopy,” *Nat. Rev. Gastroenterol. Hepatol.*, vol. 7, no. 7, p. 366, 2010.

[86] M. Goetz and T. D. Wang, “Molecular imaging in gastrointestinal endoscopy,” *Gastroenterology*, vol. 138, no. 3, pp. 828–833, 2010.

[87] S. M.B. *et al.*, “Targeted imaging of esophageal neoplasia with a fluorescently labeled peptide: First-in-human results,” *Sci. Transl. Med.*, vol. 5, no. 184, 2013.

[88] M. Mitsunaga *et al.*, “Fluorescence endoscopic detection of murine colitis-associated colon cancer by topically applied enzymatically rapid-activatable probe,” pp. 1179–1186, 2013.

[89] H. Matsuzaki, M. Kamiya, R. J. Iwatate, D. Asanuma, T. Watanabe, and Y. Urano, “Novel Hexosaminidase-Targeting Fluorescence Probe for Visualizing Human Colorectal Cancer,” *Bioconjug. Chem.*, vol. 27, no. 4, pp. 973–981, Apr. 2016.

[90] P. Vinas, C. Lopez-Erroz, J. J. Marın-Hernandez, and M. Hernandez-Cordoba, “Determination of phenols in wines by liquid chromatography with photodiode array and fluorescence detection,” *J. Chromatogr. A*, vol. 871, no. 1–2, pp. 85–93, 2000.

[91] K. L. Goh, “Development and Application of Endoscopy,” *Indones. J. Gastroenterol. Hepatol. Dig. Endosc.*, vol. 2, no. 3, pp. 22–24, 2001.

[92] S. S. Brody, “Instrument to measure fluorescence lifetimes in the millimicrosecond region,” *Rev. Sci. Instrum.*, vol. 28, no. 12, pp. 1021–1026, 1957.

[93] G. Matz *et al.*, “Chip-on-the-tip compact flexible endoscopic epifluorescence video-microscope for in-vivo imaging in medicine and biomedical research,” *Biomed. Opt. Express*, vol. 8, no. 7, pp. 3329–3342, 2017.

[94] S. Cova, A. Longoni, and A. Andreoni, “Towards picosecond resolution with single-photon avalanche diodes,” *Rev. Sci. Instrum.*, vol. 52, no. 3, pp. 408–412, 1981.

[95] M. Ghioni, A. Gulinatti, I. Rech, F. Zappa, and S. Cova, “Progress in silicon single-photon avalanche diodes,” *IEEE J. Sel. Top. quantum Electron.*, vol. 13, no. 4, pp. 852–862, 2007.

[96] I. Gyongy *et al.*, “Fluorescence lifetime imaging of high-speed particles with single-photon image sensors,” in *High-Speed Biomedical Imaging and Spectroscopy IV*, 2019, vol. 10889, p. 108890O.

[97] N. A. W. Dutton, T. Al Abbas, F. M. Della Rocca, N. Finlayson, B. Rae, and R. K. Henderson, “Time of Flight Imaging and Sensing for Mobile Applications,” in *Low-Power Analog Techniques, Sensors for Mobile Devices, and Energy Efficient Amplifiers*, Springer, 2019, pp. 221–249.

[98] C. Charrat, C. Papaix, and S. Gesset, “X-ray detection circuit for a dental radiology sensor.” Google Patents, Jan-2019.

[99] C. Bruschini, H. Homulle, I. M. Antolovic, S. Burri, and E. Charbon, “Single-photon avalanche diode imagers in biophotonics: review and outlook,” *Light Sci. Appl.*, vol. 8, no. 1, pp. 1–28, 2019.

[100] G. Iddan, G. Meron, A. Glukhovsky, and P. Swain, “Wireless capsule endoscopy,” *Nature, Vol. 405, Issue 6785, pp. 417 (2000).*, vol. 405, p. 417, 2000.

[101] R. S. MACKAY and B. JACOBSON, “Endoradiosonde,” *Nature*, vol. 179, no. 4572, pp. 1239–1240, Jun. 1957.

[102] H. G. Noeller, “The use of a radiotransmitter capsule for the measurement of gastric pH,” *Ger. Med. Mon.*, vol. 6, no. 3, 1961.

[103] T. Nakamura and A. Terano, “Capsule endoscopy: past, present, and future,” *J. Gastroenterol.*, vol. 43, no. 2, pp. 93–99, 2008.

[104] C. Li, B. Zhang, C. Chen, and Y. Li, “OMOM capsule endoscopy in diagnosis of small bowel disease,” *J. Zhejiang Univ. Sci. B*, vol. 9, no. 11, pp. 857–862, 2008.

[105] K. Friedrich, S. Gehrke, W. Stremmel, and A. Sieg, “First clinical trial of a newly developed capsule endoscope with panoramic side view for small bowel: a pilot study,” *J. Gastroenterol. Hepatol.*, vol. 28, no. 9, pp. 1496–1501, 2013.

[106] Z. Fireman *et al.*, “Diagnosing small bowel Crohn’s disease with wireless capsule endoscopy,” *Gut*, vol. 52, no. 3, pp. 390–392, 2003.

[107] K. Schulmann *et al.*, “Feasibility and diagnostic utility of video capsule endoscopy for the detection of small bowel polyps in patients with hereditary polyposis syndromes,” *Am. J. Gastroenterol.*, vol. 100, no. 1, p. 27, 2005.

[108] A. Culliford, J. Daly, B. Diamond, M. Rubin, and P. H. R. Green, “The value of wireless capsule endoscopy in patients with complicated celiac disease,” *Gastrointest. Endosc.*, vol. 62, no. 1, pp. 55–61, 2005.

[109] M. Luján-Sanchis *et al.*, “Current role of capsule endoscopy in Crohn’s disease,” *World J. Gastrointest. Endosc.*, vol. 8, no. 17, p. 572, 2016.

[110] G. M. Eisen *et al.*, “The accuracy of PillCam ESO capsule endoscopy versus conventional upper endoscopy for the diagnosis of esophageal varices: a prospective three-center pilot study,” *Endoscopy*, vol. 38, no. 01, pp. 31–35, 2006.

[111] A. Pérez *et al.*, “Innovation in wireless in-body devices - the power of wireless -,” *BMC Public Health*, 2017. [Online]. Available: http://www.iracon.org/wp-content/uploads/2016/03/Sebastian-Schostek.pdf. [Accessed: 15-Nov-2020].

[112] D. R. Cave, “Reading wireless video capsule endoscopy,” *Gastrointest. Endosc. Clin.*, vol. 14, no. 1, pp. 17–24, 2004.

[113] G. Pan and L. Wang, “Swallowable wireless capsule endoscopy: Progress and technical challenges,” *Gastroenterol. Res. Pract.*, vol. 2012, 2012.

[114] “World’s First Gastrointestinal Videoendoscopes with Auto Fluorescence Imaging Capability.”

[115] S. Bang *et al.*, “First clinical trial of the ‘MiRo’ capsule endoscope by using a novel transmission technology: electric-field propagation,” *Gastrointest. Endosc.*, vol. 69,

no. 2, pp. 253–259, 2009.

[116] a. Uehara and K. Hoshina, “Capsule endoscope NORIKA system,” *Minim. Invasive Ther. Allied Technol.*, vol. 12, no. 5, pp. 227–234, 2003.

[117] S. P. Woods and T. G. Constandinou, “Wireless capsule endoscope for targeted drug delivery: mechanics and design considerations,” *IEEE Trans. Biomed. Eng.*, vol. 60, no. 4, pp. 945–953, 2012.

[118] S. Andersson-Engels, C. af Klinteberg, K. Svanberg, and S. Svanberg, “In vivo fluorescence imaging for tissue diagnostics,” *Phys. Med. Biol.*, vol. 42, no. 5, p. 815, 1997.

[119] M. Kfouri *et al.*, “Toward a miniaturized wireless fluorescence-based diagnostic imaging system,” *IEEE J. Sel. Top. Quantum Electron.*, vol. 14, no. 1, pp. 226–234, 2008.

[120] D. S. Ferreira, V. C. Pinto, J. H. Correia, and G. Minas, “Spectroscopic detection of gastrointestinal dysplasia using optical microsensors,” *IEEE Trans. Biomed. Eng.*, vol. 58, no. 9, pp. 2633–2639, 2011.

[121] T. D. O. Sullivan *et al.*, “Real-time , continuous , fluorescence sensing in a freely-moving subject with an implanted hybrid VCSEL / CMOS biosensor,” vol. 4, no. 8, pp. 1332–1341, 2013.

[122] M. A. W. Al-Rawhani, “Design and implementation of miniaturised capsule for autofluorescence detection with possible application to the bowel disease.” 31-Jul-2012.

[123] M. a. Al-Rawhani, J. Beeley, and D. R. S. Cumming, “Wireless fluorescence capsule for endoscopy using single photon-based detection,” *Sci. Rep.*, vol. 5, no. November, p. 18591, 2015.

[124] Z. Li, Z. Liao, and M. McAlindon, *Handbook of capsule endoscopy*. 2014.

[125] M. Ryou *et al.*, “An implantable wireless biosensor for the immediate detection of upper GI bleeding : a new fluorescein-based tool for diagnosis and surveillance (with video),” *YMGE*, vol. 74, no. 1, pp. 189-194.e1, 2011.

[126] P. Demosthenous, C. Pitris, J. Georgiou, and S. Member, “Infrared Fluorescence-Based Cancer Screening Capsule for the Small Intestine,” *IEEE Trans. Biomed. Circuits Syst.*, vol. 10, no. 2, pp. 467–476, 2016.

[127] K. Moore, “Zemax OpticStudio.” Apr, 2017.

[128] E. Gray, W. N, and M. Drive, “Data Sheet Data Sheet,” pp. 2–5, 2009.

[129] C. Accarino *et al.*, “A 64x64 SPAD array for portable colorimetric sensing, fluorescence and x-ray imaging,” *IEEE Sens. J.*, p. 1, 2019.

[130] T. Gotoda, “Endoscopic resection of early gastric cancer,” *Gastric cancer*, vol. 10, no. 1, pp. 1–11, 2007.

[131] M. Goetz *et al.*, “In vivo molecular imaging of colorectal cancer with confocal endomicroscopy by targeting epidermal growth factor receptor,” *Gastroenterology*, vol. 138, no. 2, pp. 435–446, 2010.

[132] K. Kelly, H. Alencar, M. Funovics, U. Mahmood, and R. Weissleder, “Detection of invasive colon cancer using a novel, targeted, library-derived fluorescent peptide,”

Cancer Res., vol. 64, no. 17, pp. 6247–6251, 2004.

[133] M. Bates, B. Huang, G. T. Dempsey, and X. Zhuang, "Multicolor super-resolution imaging with photo-switchable fluorescent probes," *Science (80-.).*, vol. 317, no. 5845, pp. 1749–1753, 2007.

[134] "Datasheet-ProteoGreen ™ -gGlu," p. 5860, 2017.

[135] C. N. C, "Datasheet - CellTracker ™ fluorescent probes," no. Figure 1, pp. 1–4.

[136] R. S. DaCosta, B. C. Wilson, and N. E. Marcon, "Light-induced fluorescence endoscopy of the gastrointestinal tract," *Gastrointest. Endosc. Clin.*, vol. 10, no. 1, pp. 37–69, 2000.

[137] H. Zeng, A. Weiss, R. Cline, and C. E. MacAulay, "Real-time endoscopic fluorescence imaging for early cancer detection in the gastrointestinal tract," *Bioimaging*, vol. 6, no. 4, pp. 151–165, 1998.

[138] H. Zeng, R. W. Cline, C. E. MacAulay, and B. W. Jaggi, "Imaging system for detecting diseased tissue using native fluorsecence in the gastrointestinal and respiratory tract." Google Patents, Jul-1997.

[139] H. Inomata *et al.*, "Efficacy of a novel auto-fluorescence imaging system with computer-assisted color analysis for assessment of colorectal lesions," *World J. Gastroenterol. WJG*, vol. 19, no. 41, p. 7146, 2013.

[140] J. Beynon, D. M. A. Foy, L. N. Temple, J. L. Channer, J. Virjee, and N. J. M. C. Mortensen, "The endosonic appearances of normal colon and rectum," *Dis. Colon Rectum*, vol. 29, no. 12, pp. 810–813, 1986.

[141] G. I. Zonios *et al.*, "Morphological model of human colon tissue fluorescence," *IEEE Trans. Biomed. Eng.*, vol. 43, no. 2, pp. 113–122, 1996.

[142] K. Izuishi *et al.*, "The histological basis of detection of adenoma and cancer in the colon by autofluorescence endoscopic imaging," *Endoscopy*, vol. 31, no. 07, pp. 511–516, 1999.

[143] M. Dandin, P. Abshire, and E. Smela, "Optical filtering technologies for integrated fluorescence sensors," *Lab Chip*, vol. 7, no. 8, pp. 955–977, 2007.

[144] Q. Chen *et al.*, "A CMOS image sensor integrated with plasmonic colour filters," *Plasmonics*, vol. 7, no. 4, pp. 695–699, 2012.

[145] S. Yokogawa, S. P. Burgos, and H. A. Atwater, "Plasmonic color filters for CMOS image sensor applications," *Nano Lett.*, vol. 12, no. 8, pp. 4349–4354, 2012.

[146] Z. Fan, H. Jiang, and J. Lin, "Micro-LED based high voltage AC/DC indicator lamp." Google Patents, May-2009.

[147] X. Xue, "High Power LED Lamp." Google Patents, Feb-2009.

[148] F. M. Della Rocca *et al.*, "Real-time fluorescence lifetime actuation for cell sorting using a CMOS SPAD silicon photomultiplier," *Opt. Lett.*, vol. 41, no. 4, pp. 673–676, 2016.

[149] N. Krstajić, J. Levitt, S. Poland, S. Ameer-Beg, and R. Henderson, "256× 2 SPAD line sensor for time resolved fluorescence spectroscopy," *Opt. Express*, vol. 23, no. 5, pp. 5653–5669, 2015.

[150] G. Giraud *et al.*, "Fluorescence lifetime biosensing with DNA microarrays and a

CMOS-SPAD imager," *Biomed. Opt. Express*, vol. 1, no. 5, pp. 1302–1308, 2010.

[151] P. Lalanne and P. Chavel, "Metalenses at visible wavelengths: past, present, perspectives," *Laser Photon. Rev.*, vol. 11, no. 3, p. 1600295, 2017.

[152] D. Sell, J. Yang, S. Doshay, R. Yang, and J. A. Fan, "Large-angle, multifunctional metagratings based on freeform multimode geometries," *Nano Lett.*, vol. 17, no. 6, pp. 3752–3757, 2017.

[153] Z.-B. Fan *et al.*, "Silicon nitride metalenses for close-to-one numerical aperture and wide-angle visible imaging," *Phys. Rev. Appl.*, vol. 10, no. 1, p. 14005, 2018.

[154] H. Pahlevaninezhad *et al.*, "Nano-optic endoscope for high-resolution optical coherence tomography in vivo," *Nat. Photonics*, vol. 12, no. 9, p. 540, 2018.

[155] K. Saptaji, "Machining of biocompatible materials : a review," pp. 2255–2292, 2018.